Rochester Institute of Technology
RIT Digital Institutional Repository

Theses

8-2016

Carbon Nanotube Arrays for Intracellular Delivery and Biological Applications

Masoud Golshadi
mxg1332@rit.edu

Follow this and additional works at: https://repository.rit.edu/theses

Recommended Citation
Golshadi, Masoud, "Carbon Nanotube Arrays for Intracellular Delivery and Biological Applications" (2016). Thesis. Rochester Institute of Technology. Accessed from

This Dissertation is brought to you for free and open access by the RIT Libraries. For more information, please contact repository@rit.edu.

R.I.T

Carbon Nanotube Arrays for Intracellular Delivery and Biological Applications

by

Masoud Golshadi

A dissertation submitted in partial fulfillment of the requirements for the degree of Doctor of Philosophy in Microsystems Engineering

Microsystems Engineering Program

Kate Gleason College of Engineering

Rochester Institute of Technology

Rochester, New York

August 2016

Carbon Nanotube Arrays for Intracellular Delivery and Biological Applications

by

Masoud Golshadi

Committee Approval:

We, the undersigned committee members, certify that we have advised and/or supervised the candidate on the work described in this dissertation. We further certify that we have reviewed the dissertation manuscript and approve it in partial fulfillment of the requirements of the degree of Doctor of Philosophy in Microsystems Engineering.

Dr. Michael G. Schrlau Date
Assistant Professor, Department of Mechanical Engineering, RIT (Advisor)

Dr. Ian M. Dickerson Date
Associate Professor, Department of Neuroscience, University of Rochester

---

Dr. Christiaan Richter Date
Assistant Professor, Department of Chemical Engineering, RIT
Associate Professor, Department of Industrial Engineering, Mechanical Engineering, and Computer Science, University of Iceland

---

Dr. Leslie K. Wright Date
Associate Professor, School of Life Sciences, RIT

Certified By:

Dr. Bruce Smith Date
Director, Microsystems Engineering Program

Dr. Doreen Edwards Date
Dean, Kate Gleason College of Engineering

ABSTRACT

Kate Gleason College of Engineering
Rochester Institute of Technology

Degree: Doctor of Philosophy **Program:** Microsystems Engineering
Author: Masoud Golshadi **Advisor:** Michael G. Schrlau
Dissertation Title: Carbon Nanotube Arrays for Intracellular Delivery and Biological Applications

Introducing nucleic acids into mammalian cells is a crucial step to elucidate biochemical pathways, modify gene expression in immortalized cells, primary cells, and stem cells, and intoduces new approaches for clinical diagnostics and therapeutics. Current gene transfer technologies, including lipofection, electroporation, and viral delivery, have enabled break-through advances in basic and translational science to enable derivation and programming of embryonic stem cells, advanced gene editing using CRISPR (Clustered regularly interspaced short palindromic repeats), and development of targeted anti-tumor therapy using chimeric antigen receptors in T-cells (CAR-T). Despite these successes, current transfection technologies are time consuming and limited by the inefficient introduction of test molecules into large populations of target cells, and the cytotoxicity of the techniques. Moreover, many cell types cannot be consistently transfected by lipofection or electroporation (stem cells, T-cells) and viral delivery has limitations to the size of experimental DNA that can be packaged.

In this dissertation, a novel coverslip-like platform consisting of an array of aligned hollow carbon nanotubes (CNTs) embedded in a sacrificial template is developed that enhances gene transfer capabilities, including high efficiency, low toxicity, in an

expanded range of target cells, with the potential to transfer mixed combinations of protein and nucleic acids. The CNT array devices are fabricated by a scalable template-based manufacturing method using commercially available membranes, eliminating the need for nano-assembly. High efficient transfection has been demonstrated by delivering various cargos (nanoparticles, dye and plasmid DNA) into populations of cells, achieving 85% efficiency of plasmid DNA delivery into immortalized cells. Moreover, the CNT-mediated transfection of stem cells shows 3 times higher efficiency compared to current lipofection methods. Evaluating the cell-CNT interaction elucidates the importance of the geometrical properties of CNT arrays (CNT exposed length and surface morphology) on transfection efficiency. The results indicate that densely-packed and shortly-exposed CNT arrays with planar surface will enhance gene delivery using this new platform. This technology offers a significant increase in efficiency and cell viability, along with the ease of use compared to current standard methods, which demonstrates its potential to accelerate the development of new cell models to study intractable diseases, decoding the signaling pathways, and drug discovery.

ACKNOWLEDGEMENT

This dissertation was completed with the help of so many and now it is my pleasure to thank all of them for their support, encouragement and blessings.

First of all, I would like to express my sincerest gratitude to my advisor, Dr. Michael G. Schrlau, for giving me the opportunity to work with him, for his valuable and endless guidance, and for his tireless support over the years. His pioneering vision, abundance of knowledge and sense of humor kept me motivated, and without his persistent mentoring, this dissertation would not have been accomplished. Thanks for all the birthday cakes, Thanksgiving and Christmas invitations, and the long arguments about cars.

I also would like to express my deepest appreciation to Dr. Ian M. Dickerson (University of Rochester), not only because of having the honor of working with him as a collaborator and a committee member during these years, but also for his insightful suggestions and persistent support. Your perseverance in pursuing the science, your mentoring attitude and skill, and your honest opinions provided me with an insight to believe in my research and gave me the courage to always push my boundaries one step forward. Thanks for introducing me to the car enthusiasts community, to the track days and auto-cross events, and for giving me the opportunity to enjoy my time at your garage by tuning the cars.

I would like to thank the other members of my dissertation committee, Dr. Christiaan Richter (RIT) and Dr. Leslie K. Wright (RIT), for their insights into my research and their overall support. Your thoughtful comments and recommendations served as an infrastructure for my research. Thanks for providing me all your resources, giving me a

positive vibe, and for being always available to discuss my research. I would also like to express my appreciation to Dr. Christoph Pröschel (University of Rochester) for providing the resources, and his constant support and insight on culturing and utilization of stem cells.

I would like to acknowledge Dr. Richard Hailstone (RIT) and Mr. Brian McIntyre (University of Rochester) for their assistance and advice on electron microscopy, and Mr. Matthew Cochrane (University of Rochester) for assistance with flow cytometry analysis. I would also thank Mr. Sean O'Brien (RIT), Mr. John Nash (RIT) and Mr. Richard Battaglia (RIT) for their time and dedication on answering my questions on nanomanufacturing equipments.

I would like to thank Cornell NanoScale Science and Technology Facility (CNF) and its staff, especially Mr. Michael Skvarla, Mr. Vincent Genova and Mr. Jerry Drumheller for their training, willingness to help my research moves forward, and for their professional and extended support about the nanomanufacturing equipments at CNF.

Thanks to the Department of Microsystems Engineering at RIT for giving me this once-in-a-lifetime opportunity. Thanks to all the distinguished faculty of the department from whom I have learned so much, especially Dr. Bruce Smith and Mrs. Lisa Zimmerman. I wish to thank the administrative staff and faculty members of the Department of Mechanical Engineering at RIT for general (and sometimes moral) support. Specifically, I would like to thank Dr. Risa Robinson, Dr. Edward Hensel, Dr. Wayne Walter, Dr. Alan Nye, Dr. Hany Ghoneim, Dr. Surendra Gupta, Mrs. Jill Ehmann,

Mrs. Hillary McCormick, Mrs. Venessa Mitchell, Mr. Jan Maneti, Mr. Robert Kraynik and Mr. William Finch.

Above All, I would like to express my heartily appreciation to my dearest parents, Mr. Jamshid Golshadi and Mrs. Maryam Askari, and also to my brother and sister, Majid and Fereshteh; none of this would have been possible without your support. You gave me all the encouragements, strength and beliefs throughout this journey. The words cannot thank you enough for all your sacrifices that brought me to this point; so, I can only say that I love you all.

Finally, I would like to thank the foundations and organizations that provided funding for this research. This work was supported in part by a grant from RIT to establish the American-German Partnership to Advance Biomedical and Energy Applications of Nanocarbon, the Texas Instruments / Douglas Harvey 2012 RIT Faculty Award, and a grant from the Schmitt Foundation from University of Rochester. Its was also supported in part by the Feinberg Foundation and Weizmann Institute of Science.

TABLE OF CONTENTS

LIST OF FIGURES

LIST OF TABLES

LIST OF ACRONYMS

AAO	Anodized Aluminum Oxide
AC	Alternating Current
AFM	Atomic Force Microscopy
ATP	Adenosine Triphosphate
C	Celsius
CAR	Chimeric Antigen Receptor
C-CVD	Catalytic Chemical Vapor Deposition
CNF	Carbon Nanofiber
CNP	Carbon Nanopipette
CNT	Carbon Nanotube
CRISPR	Clustered Regularly Interspaced Short Palindromic Receptor
CSFM	Complete Serum-Free Medium
CVD	Chemical Vapor Deposition
Da	Dalton
DMEM	Dulbecco's Modified Eagle Medium
EDS	Energy Dispersive X-Ray Spectroscopy
EGF	Epidermal Growth Factor
EGTA	Ethylene Glycol-Bis(β-Aminoethyl Ether)-N,N,N',N'-Tetraacetic Acid
ESC	Embryonic Stem Cell
EYFP	Enhanced Yellow Fluorescent Protein
FET	Field Effect Transistor
FN	Fibronectin

gRNA	Guide RNA
h/hrs	Hour/Hours
HDR	Homology-Directed Recombination
HEK293	Human Embryonic Kidney 293 Cell
HEPES	4-(2-Hydroxyethyl)-1-Piperazineethanesulfonic Acid
hESC	Human Embryonic Stem Cell
ICP	Inductive Coupled Plasma
iPSC	Induced Pluripotent Stem Cell
L	Length
L_s	Slip Length
LN	Laminin
M	Molarity
MRI	Magnetic Resonance Imaging
MWCNT	Multi-Wall Carbon Nanotube
mβcd	Methyl-β-Cyclodextrin
NO	Nitric Oxide
NSC	Neural Stem Cell
Pa	Pascal
PBS	Phosphate Buffered Saline
PDGF	Platelet-Derived Growth Factor
PCR	Polymerase Chain Reaction
PECVD	Plasma Enhanced Chemical Vapor Deposition
PEG	Poly(Ethylene Glycol)

PEO	Poly(Ethylene Oxide)
PI	Propidium Iodide
PLL	Poly-L-Lysine
Q	Volumetric Flow
RIE	Reactive Ion Etching
ROS	Reactive Oxygen Species
sccm	Standard Cubic Centimeters per Minute
SEM	Scanning Electron Microscopy
SERS	Surface-Enhanced Raman Spectroscopy
SpA	Staphylococcal Protein A
SPM	Scanning Probe Microscopy
SSC	Side Scatter
SWCNT	Single-Wall Carbon Nanotube
TCR	T-Cell Receptor
TEM	Transmission Electron Microscopy
V	Voltage
W	Watt
YFP	Yellow Fluorescent Protein
μ	Dynamic Viscosity
ΔP	Pressure Drop

CHAPTER 1

Introduction

Carbon nanotubes (CNTs) are structures of carbon atoms linked as a molecule into a long, hollow cylinder form. Because of their unique chemical, mechanical, electrical, and optical properties and hollow structure, CNTs have been studied and employed in a variety of applications such as cellular biology, electrochemical sensing, fluid transportation and energy storage systems. Therefore, the manufacturing and utilization of the unique properties of CNTs in a variety of configurations and nanostructures has been among the areas that attracted the attention of researches in recent years. In this chapter, a novel device consisting of an array of vertically aligned CNTs is introduced which has the potential to be used as a new platform for high efficient intracellular delivery and other biological applications. To this end, the motivations behind this research are first presented and the CNT properties are then categorized and explained.

1.1. Motivation

1.1.1. CRISPR/Cas9-Mediated Genome Engineering

The rapid development of CRISPR/Cas9-mediated (clustered regularly interspaced short palindromic repeats) genome engineering [1] has opened the doors to unprecedented genetic manipulation of human cells. However, genome engineering using homology-directed recombination (HDR) with the CRISPR/Cas9n system requires the delivery of multiple genetic elements into the target cell population. As illustrated in Figure 1.1, these components include: two guide-RNA (gRNA) expression plasmids, a plasmid expressing the Cas9n enzyme and single-stranded DNA template (HDR-template) that encodes the sequence that is to be inserted into the genome. The transduction of these multiple components using current transfection methods remains inefficient and cumbersome, resulting in laborious down-stream screening steps to arrive at a homogenous population of genetically targeted cells [1].

The CRISPR/Cas9 process is particularly inefficient in pluripotent stem cells; both embryonic stem cells (ESC) and induced pluripotent stem cells (iPSCs). These stem cells are important for the production of disease-relevant cell types that are otherwise not readily accessible, such as cells from the brain, and due to population heterogeneity often need to be made from the patient. There is therefore a need to conduct experiments with iPSCs genetically matched to the patient that differ only by the gene mutation of interest. The advent of CRISPR/Cas9n HDR technology now provides a unique opportunity to overcome this limitation [1, 2]: by targeted genome engineering of patient-derived iPSCs to reverse known mutations. To this end, a syngeneic cell line can be generated that

matches the original iPSC line, with the exception of the mutation(s) of interest. However, co-delivery and transduction of all CRISPR/Cas9n HDR components is very inefficient in pluripotent stem cells. In addition, selection of genetically engineered clonal cell populations is difficult in pluripotent stem cells (ESCs and iPSCs) as the survival of dissociated iPSCs is poor. Therefore, a new method for high efficient delivery of CRISPR/Cas9 complex into cells such as ESCs and iPSCs with high cell viability is of particular interest to be able to properly utilize this gene editing tool for various biomedical applications and life sciences.

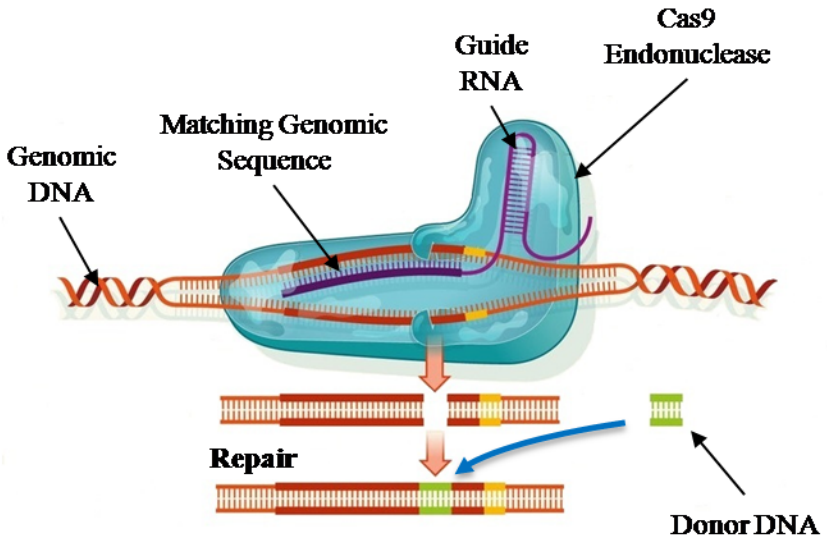

Figure 1.1: Schematic illustration of the CRISPR/Cas9 components.

1.1.2. Cancer Immunotherapy

Cancer cells use several strategies to escape and suppress the immune system including expression of weakly immunogenic antigens, downregulating or modulating the antigen expression to evade immune cell detection, and inhibiting the effector immune cell function through synthesis of various immune suppressants [3, 4]. These can result in a

failure to initiate and maintain adequate antitumour immunity, and consequently facilitate tumour survival and progression.

T-cells (also known as T-lymphocytes) are among the widely distributed cells in tissues and tumors, which have a key role in cell-mediated immunity and immune system responses. Enhancing the function of the T-cells through genetic modification has demonstrated the augmentation of the immune response for targeting specific tumors and cancer cells [5, 6]. In other words, the antigen specificity of T-cells can be manipulated by genetic modification and redirected to successfully target antigens that are expressed by tumours. In particular, these modifications can be either by altering the specificity of the T-cell receptor (TCR) or through introducing antibody-like recognition in chimeric antigen receptors (CARs). These approaches provide T-cells with more specificity and efficiency in term of targeting tumors.

Preparation and delivery of genetically modified T-cells starts by harvesting the T-cells from a patient. The genetic modification of the T-cell is done by transduction of the cells with viral vector (typically gamma retrovirus or lentivirus), which defines the most critical step in manufacturing process. The modified T-cells are then transferred back to the patient body, as illustrated in Figure 1.2. Despite the demonstrated clinical success of this technique as a personalized immunotherapy method, the cost and complexity of the manufacturing process associated with the utilization of viral vectors and transduction methods restricts their production and inhibits their potential applications. This necessitates the development of a novel and cost effective transfection method that can facilitate a high efficient transduction process [7].

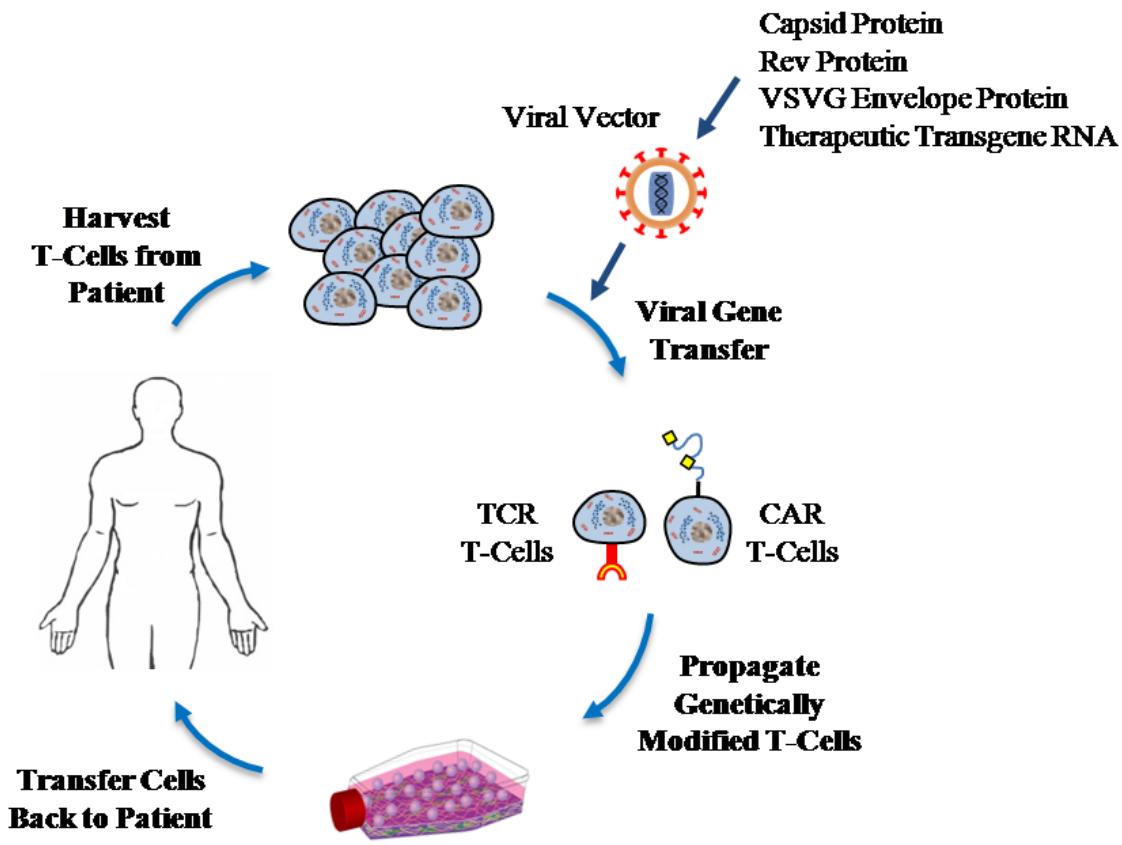

Figure 1.2: Manufacturing and delivery process of genetically modified T-cells therapy.

1.2. Carbon Nanotubes and Carbon Nanostructures

Over the past century, carbon fiber research has progressed from carbon fibers and filaments to carbon nanofibers and nanotubes [8]. The field has progressed from hollow graphitic nanofibers to the higher-ordered structure of carbon nanotubes. In the first decade after the discovery of multi-walled CNTs in 1991 [9], the majority of research focused on the fabrication, characterization, and determination of properties for CNTs and related structures. In the twenty-first century, one of the main focuses has been on applying their unique qualities for applications in biological or biomedical and sensing areas.

To simplify our discussion of a broad field, earlier proposed nomenclature is adopted to describe all hollow tube-like carbon structures with at least one dimension of 100 nm or less as carbon nanotubes [10]. Likewise, all solid fiber-like carbon structures with at least one dimension of 100 nm or less is described as carbon nanofibers (CNFs).

Since the 1990's, carbon nanostructures, such as CNTs and CNFs, have proven to be one of the most versatile nanostructures in engineering, science, and medicine. Carbon nanostructures have made broad and significant societal impacts, from enhancing material composites and miniaturizing electronics to providing more efficient means of storing energy and facilitating the early detection and treatment of disease. The diversity and versatility of carbon nanostructures are what make them attractive and versatile for many applications: carbon nanostructures are nanoscopic in size, have high length-to-width aspect ratio, have a high surface to volume ratio, can have hollow geometry, are chemically inert but can be easily modified to possess different surface chemistry, are mechanically robust, have conducting or semi-conducting properties, and have unique optical properties.

One of the most exciting applications for carbon nanostructures, and nanotechnology in general, is in the field of biomedicine, where their versatility has the potential to improve the detection of biological threats, efficiently and compactly monitor environmental conditions and screen the health of patients, and detect the early onset of disease. With their unique properties, carbon nanostructures can be used for various biomedical applications; from *in vivo* targeted drug delivery and regenerative tissue scaffolds to single cell probes and implanted sensors.

1.3. CNT Properties

The unique mechanical, electrical, chemical, thermal, and optical properties of CNTs and CNFs are well reviewed [11-13] and will not be discussed here in great detail. In addition to these properties, CNTs and CNFs have extremely large length-to-diameter aspect ratios and high surface-to-volume ratios. Their characteristics depend primarily on their structure and can vary significantly between the type and origin of the carbon material.

CNTs exhibit high tensile strength, stiffness, and ductility. For instance, single-wall CNTs (SWCNTs) have tensile strengths as high as 100 times that of steel, making them the strongest known material [14]. CNTs also behave elastically. When pushed against a hard surface, CNTs bend and buckle without fracture and return to their original shape when force is removed [15, 16]. CNTs and related structures exhibit a wide range of electrical characteristics. For example, SWCNTs can be metallic and semiconducting depending on their helicity whereas multi-wall CNTs (MWCNTs) exhibit a range of electronic behavior (metallic, semiconducting, and semimetallic) [12]. CNTs with defect sites, such as those grown using template-based synthesis methods, are good electrical conductors yet can be annealed to further improve conductivity [17]. Additionally, the reactivity of carbon surfaces varies greatly with surface microstructure, cleanliness, and functional groups [18]. Thus, carbon nanostructures provide a diverse platform to attach biomolecules for a variety of drug delivery, biological interfacing, and sensing applications.

1.4. Biomedical Applications of CNTs

The unique properties of CNTs and other carbon nanostructures make them well suited for a broad range of sensing applications. For example, the mechanical properties of CNTs enables them to be used, among other things, as strain gauges [19, 20], pressure transducers [21-23], torsional sensors [24, 25], textile-based sensors [26], atomic mass sensors [27], fluid flow sensors [28] and displacement sensors [29]. The thermal responses of CNTs can be used as thermometers [30, 31], environmental monitors [32, 33] and infrared sensors [34], while their optical properties have found uses as strain gauges [35], pressure gauges [36], and photodetectors [37]. Reviews of additional CNT-based biological sensors can be found in literature [38-40].

1.5. Research Objectives

Gene transfer into eukaryotic cells is an important tool for studying cellular biochemistry, developing transgenic models, and manipulating pluripotent stem cells. Current gene transfer technology including lipofection and electroporation suffer an inverse relationship between high-efficiency transfer and cellular toxicity, and cannot efficiently transduce important cell types such as primary neurons or stem cells. Viruses, on the other hand, can deliver nucleic acids to a broad range of cells, but suffer from cell toxicity and have a packaging size limit that precludes utilization of modern gene-editing techniques such as CRISPR/Cas9. To overcome the foregoing limitations of conventional agent transfer methods, microinjection using single-tipped devices is used to deliver genetic material into target cells. One of the biggest disadvantages of these single-tipped

devices is the low transfection rate due to serial approach of nanoinjection, and incapability of probing multiple cells in parallel, making the process time-consuming, and resulting in significant toxicity from physical damage to the cells. As a result single-tipped nanodevices have limited qualitative and quantitative abilities for analyzing populations of cells. These limitations necessitate the development of a new multifunctional platform capable of transfecting populations of cells with high efficiency and low cytotoxicity. The platform should be able to deliver a variety of cargo sizes into cells in a relatively short period of time. Additionally, it should be easy to use and relatively cheap to manufacture to have superior advantages over the current transfection techniques.

To this end, template-based nanofabrication method will be employed to produce a novel coverslip-like device consisting of a vertically aligned, protruding array of thousands of individually addressable CNTs that are both hollow and conductive, as illustrated in Figure 1.3. Heterogeneous cells can be cultured on top such that the CNTs are in contact with the adhered cells, providing electrical and fluid interfacing with each cell, individually. In this configuration, several CNTs will be integrated with each individual cell to enable high efficient intracellular transfection of populations of cells. Positioned under a standard fluorescence microscope, thousands of cells can be monitored while performing controlled transfection. The device will readily fit in a standard cell culture plates and under fluorescence microscopes, expediting technological dissemination and facilitating broad utilization, and is manufactured with simple, scalable processes to facilitate commercialization.

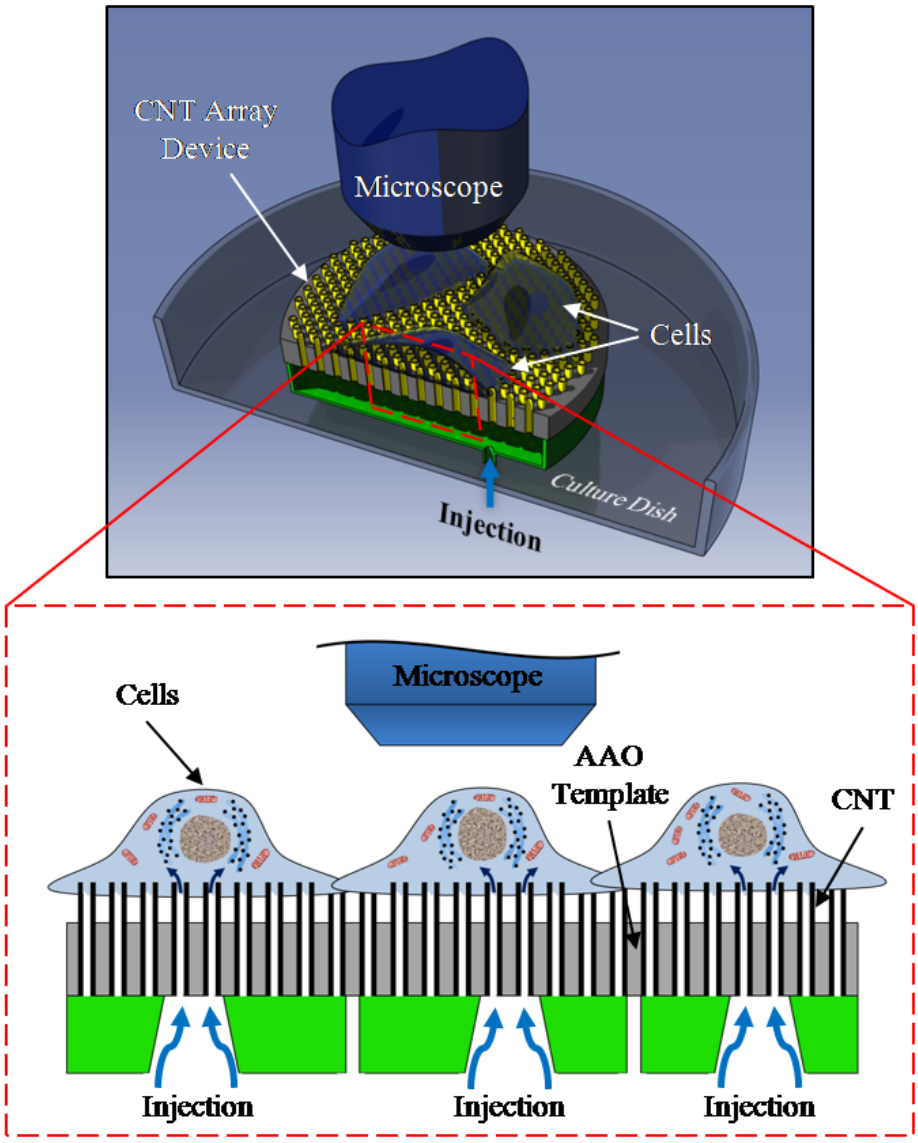

Figure 1.3: Schematic illustration of the concept of vertically aligned CNT-based array platform for intracellular transfection of population of cells and biological applications.

1.6. Dissertation Overview

This dissertation presents the manufacturing, characterization and implementation of a new CNT-based platform for intracellular delivery and biological applications, and the results have been structured in 9 chapters. Chapter 1 introduces the motivations behind

the research and the proposed CNT-based array device for intracellular delivery. Chapter 2 presents the literature review of the previous work on CNT array fabrication and template-based manufacturing, along with the current tools and techniques for intracellular transfection. The advantages of the methods provide a cornerstone for fabrication of the CNT array platform, while the shortcomings motivate the research. It also contains a comprehensive review of the CNT properties and available CNT-based tools for cellular study and biological applications. Chapter 3 describes the template-based manufacturing of the CNTs using commercially available templates. It discusses a detail fabrication and characterization of CNTs and the effect of process parameters on resultant CNTs. Chapter 4 presents the manufacturing process of the CNT-based array device by comparing various nanofabrication methods for partial exposure of the CNTs. The chapter also includes the fluidic characterization of the CNT array device for two different fluid transportation mechanisms. Chapter 5 demonstrates the application of the CNT array device for high efficient gene delivery into populations of cells. Chapter 6 discusses the effect of geometrical properties of the CNT arrays on intracellular gene delivery to optimize the transfection efficiency for an intended application. Chapter 7 demonstrates the successful utilization of the CNT array device for gene delivery into hard-to-transfect cells such as primary and stem cells. The chapter compares the transfection efficiency using the CNT array device with the current transfection methods. Chapter 8 provides a summary of the research along with the available opportunities to expand this research in a short or long term future. Finally, chapter 9 contains all the references used in this dissertation.

CHAPTER 2

Background

Building upon the unique properties of hollow CNTs and to create a multifunctional platform for intracellular transfection and biomolecular detection, arrays of vertically aligned CNTs were employed. Template-based chemical vapor deposition (CVD) is used to synthesize the CNT array inside the pores of anodized aluminum oxide (AAO) membranes as a sacrificial template. This method provides an effective process to fabricate millions of aligned CNTs without the need for nanoassembly. In this process, the choice of template dictates certain physical features of the CNT, such as length and outer diameter, while the CVD process affects other features, such as tube wall thickness, carbon deposition rate and carbon morphology. To this end, a comprehensive literature review on various CNT-based devices for biological applications and the template-based manufacturing of CNT using AAO membranes is presented in this chapter. Additionally, the fabrication process of AAO membranes and the mechanism behind the oxide growth is reviewed. Since the CNT array platform will be used to transfect population of cells, current transfection techniques are introduced and the advantages and disadvantages of each technique are discussed. Finally, a review on the vertically aligned array devices for intracellular transfection of cells is presented.

2.1. CNT and CNF-Based Devices

Carbon nanostructured devices come in many configurations depending on the desired transduction and application. Configurations include scaffolds with nanotubes randomly dispersed on their surfaces, substrates or electrodes consisting of aligned nanotube arrays or forests, probes tipped with individual or bundled nanotubes, transistors made up of a single nanotube or networks of nanotubes, or even three dimensional nanotube-based electromechanical devices [41].

2.1.1. Devices with Randomly Oriented CNTs

Several sensor configurations are manufactured from randomly oriented CNTs, from conductive CNT films and CNT-coated electrode surfaces to transistor-based sensors. CNT films and composites are well suited for macro- and microscale sensing platforms, such as smart wearable fabrics [42] and lab-on-chip devices [43], where concentrations of analytes are above μM. Smaller electrodes, with tips ranging from hundreds on nanometers to hundreds of micrometers, have been coated with CNTs to enhance their sensitivity.

SWCNTs (Fig. 2.1a) were coated onto flame-etched carbon fiber nanoelectrodes and utilized as electrochemical sensors (Fig. 2.1b) [44]. The CNT-modified electrode, with tips ranging from 100-300 nm, exhibited overall detection capabilities in the nM range, an order of magnitude lower than conventional carbon fiber electrodes of similar geometry. These small electrodes would be well suited for electrochemical applications in ultra-low fluid volumes or biological systems such as tissue or cells.

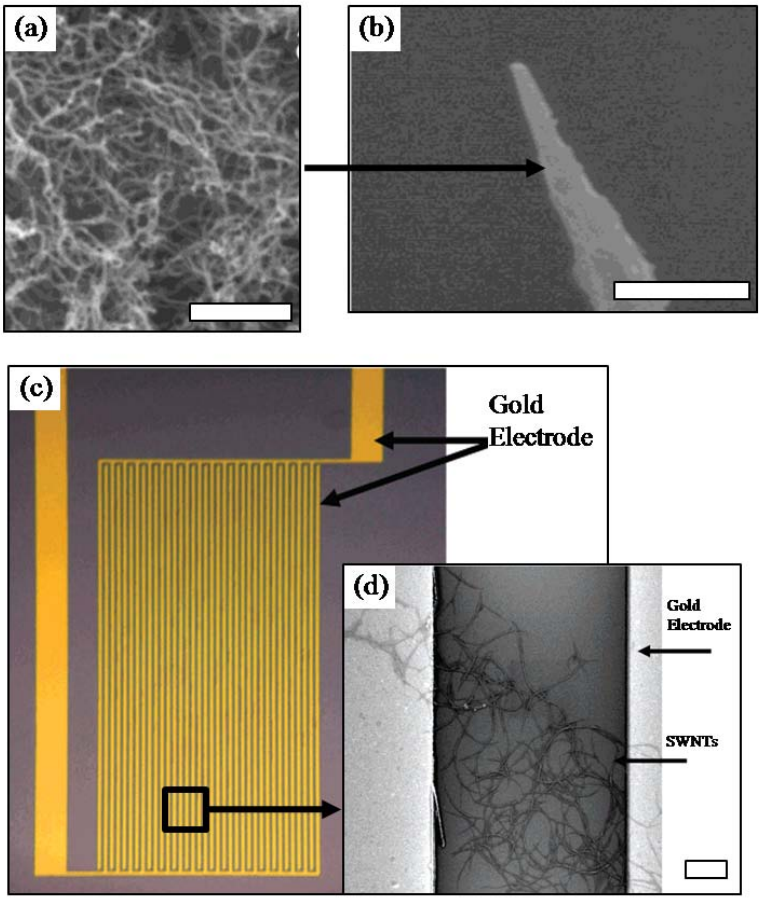

Figure 2.1: Devices with randomly oriented CNTs. (a,b) CNT-coated carbon fiber nanoelectrode. Adapted from Chen et al. (2003). (c, d) CNT-based FET. Adapted from Li et al. (2003) (Scale bars: 2 μm).

The size and high sensitivity of CNT-based field-effect transistor (FET) sensors makes them well suited to detect trace analytes in restricted spaces. FETs, first developed in 1998 [45, 46], have been made either by depositing or growing SWCNTs onto a SiO_2/Si substrate then patterning connective electrodes or, in reverse order, patterning electrodes and depositing SWCNTs over top. The former is the more common method and has been used extensively by a few research groups. In this method, semiconducting SWCNTs are grown on SiO_2/Si substrates by CVD from catalyst particles or islands. The result produces randomly oriented nanotubes across the substrate. Electrical contacts are

then patterned over the nanotube dispersion using shadow mask evaporation or electron beam- or photo-lithographic processes. The resulting sensor can consist of either single [47, 48] or networked [49] CNT-based FET sensors. The latter method has been used to create larger interdigitated electrode (Fig. 2.1c) with reproducible performance, where, as shown in Figure 2.1d, networks of randomly dispersed nanotubes lay on the electrodes to bridge the fingers.

2.1.2. Devices with Vertically Aligned CNTs and CNFs

Sensing devices and cell culture scaffolds have been made from vertically aligned (normal to the substrate) CNT and CNF forests and patterned arrays. The multiple detection sites of vertically aligned CNT arrays improves the signal-to-noise ratios and temporal responses orders of magnitude better than conventional flat electrodes of similar size and material [50]. When grown in patterns, vertically aligned arrays enable deterministic spatial resolution for a variety of sensing applications, e.g., plated living cells.

Although different substrates and growth methods are used, vertically aligned CNT or CNF devices are manufactured using a similar strategy, as shown in Figure 2.2. The device occasionally utilizes non-conducting substrates such as SiO_2/Si but typically utilizes a conducting substrate, either in the form of a metal wire, sheet, or plate or a substrate with a deposited metal film (Fig. 2.2a). Catalyst, such as Fe or Ni films or nanoparticles, is then deposited on the substrate (Fig. 2.2b). For deterministic arrays, the catalyst films are patterned. Plasma enhanced chemical vapor deposition (PECVD) is

used to grow the CNTs or CNFs from the catalyst and vertically orient the tubes on the substrate (Fig. 2.24c). These devices can be used as is so that the substrate and nanotubes act as the sensor (Fig. 2.2d) or embedded in an insulating film to only expose the ends of the nanotubes. In the latter, the insulating layer can be applied such that the nanotube tips protrude (Fig. 2.2e) or polished so the tips are flush (Fig. 2.2f).

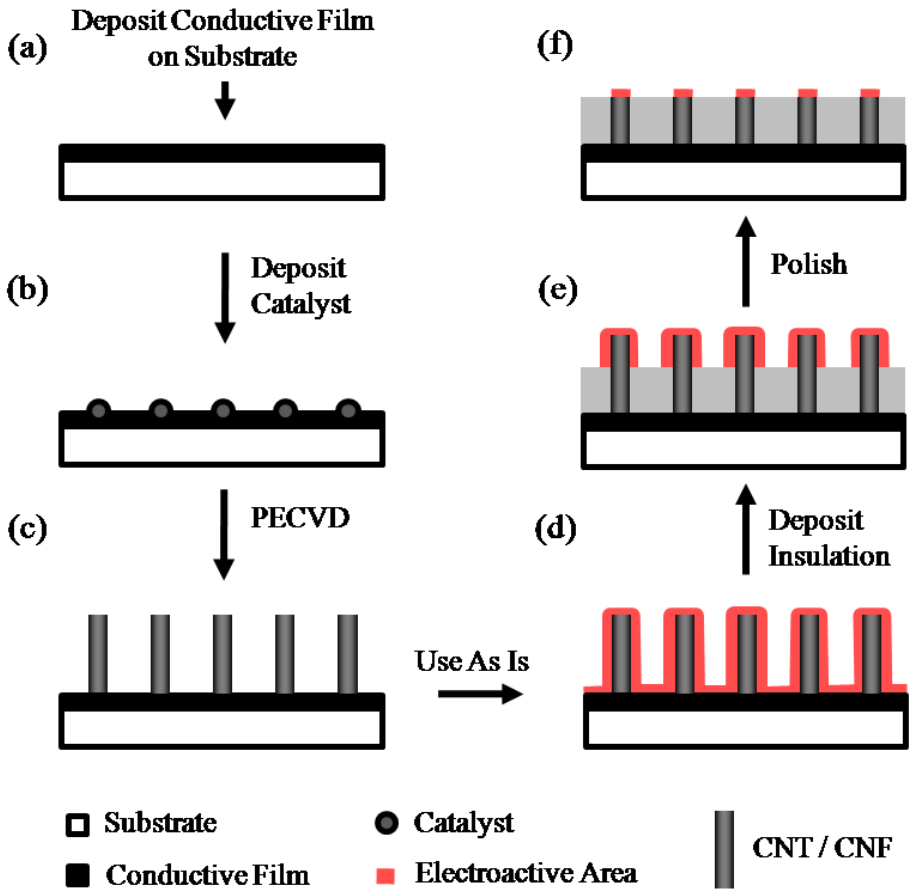

Figure 2.2: Fabrication of vertically aligned CNT arrays and device configurations.

Methods were developed to grow vertically aligned CNTs from Fe nanoparticles embedded into the pores of mesoporous silica [51] and CNFs from Ni films sputtered onto glass [52]. These methods produced large-scale, well-aligned vertical carbon

nanostructures that were isolated from one another. Methods were developed to grow vertically aligned CNTs and CNFs arrays at predetermined locations by patterning the catalyst on substrates (Fig. 2.3a) [53, 54]. These methods have since been utilized to produce an assortment of vertically aligned carbon nanostructures using PECVD for applications ranging from nanoelectrode ensembles for biosensing to needle arrays for the parallel delivery of reagents to multiple single cells.

As shown in Figure 2.3b, arrays of conically shaped CNFs (200 nm tip diameter, 6-20 μm long, deterministic nanofiber separation) were produced from Ni catalyst dots deterministically patterned on Si substrates [55]. The planar arrangement, vertical alignment, and small dimensions of the CNFs made them well suited to penetrate multiple cells simultaneously and deliver surface-adsorbed DNA into the cells [56]. A similar technique was later utilized to produce a nanoelectrode array of CNFs (30-160 nm diameter, ~5 μm long, deterministic nanofiber separation) from patterned Ni catalyst dots on Cr-coated Si wafer [50].

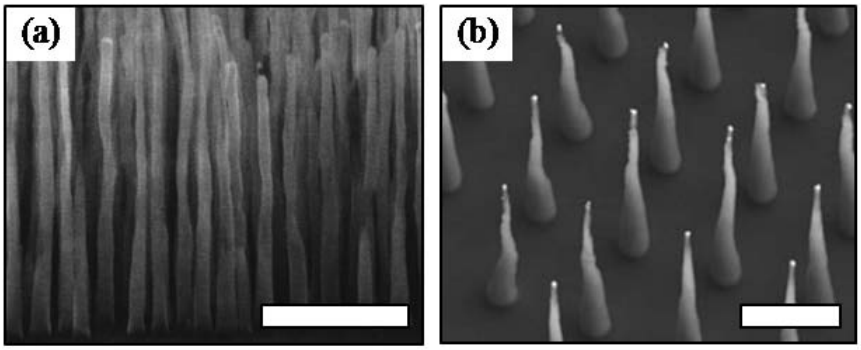

Figure 2.3: Vertically aligned arrays of carbon nanostructures. (a) CNT array (Scale bar: 2 μm). Adapted from Ren et al. (1999). (b) Patterned CNF array (Scale bar: 10 μm). Adapted from Melechko et al. (2003).

CNT electrode ensembles consisting of a dense array of CNTs (15-80 nm diameter, 30-100 μm long, 100-200 nm nanotube separation) were produced from an ion sputtered Fe catalyst film on an Al-coated Si wafer [57]. As depicted in Figure 2.2d, the CNTs and the conducting substrate act as the electrode and increase the electroactive surface area. Nanoelectrodes were made from carbon nanopipettes (10-15 nm tip diameter, several micrometers long) on Pt substrates [58] and low density arrays of vertically aligned CNTs (50-80 nm diameter, 10-12 μm long, >5 μm nanotube separation) from electrodeposited Ni nanoparticles on a Cr-coated Si substrate [59]. To limit the electroactive area to the tips of the CNTs or CNFs, these arrays can be coated with an epoxy to insulate the conductive substrate to expose needle-like tips or surface-polished to expose only the ends of the nanotubes.

2.1.3. Carbon Nanostructure-Tipped Devices

In contrast to CNT arrays, devices tipped with a single CNT or bundle of CNTs can deterministically interrogate a single feature on a substrate or region of interest, such as a single cell or intracellular location, with high spatial resolution. Carbon nanostructure-tipped devices have been utilized in several applications, including scanning probe microscopy (SPM), nanoscale electrochemistry, and cellular and intracellular studies. Their utilizations differ from other CNT-based devices in that they provide remote manipulation with nanoscale resolution and precise positioning of the sensor.

MWCNTs have been attached to the tips of atomic force microscope (AFM) cantilevers to take advantage of the precise manipulation capabilities of the AFM (Fig.

2.4a). By bringing the tip into contact with an adhesive and then a bundle of tubes dispersed on a surface, CNTs can be adhered onto the surface of the tip [15]. These devices, tipped with CNTs ranging from 5-200 nm diameters, were used for SPM of surfaces [60-64] and probing and delivering cargo to cells [65, 66]. CNTs have also been grown directly onto the tips of AFM cantilevers [67]. Although CNT-tipped AFM probes are relatively easy to use and have high spatial resolution due to the AFM, they are limited by fabrication, equipment, sensing and delivery capabilities.

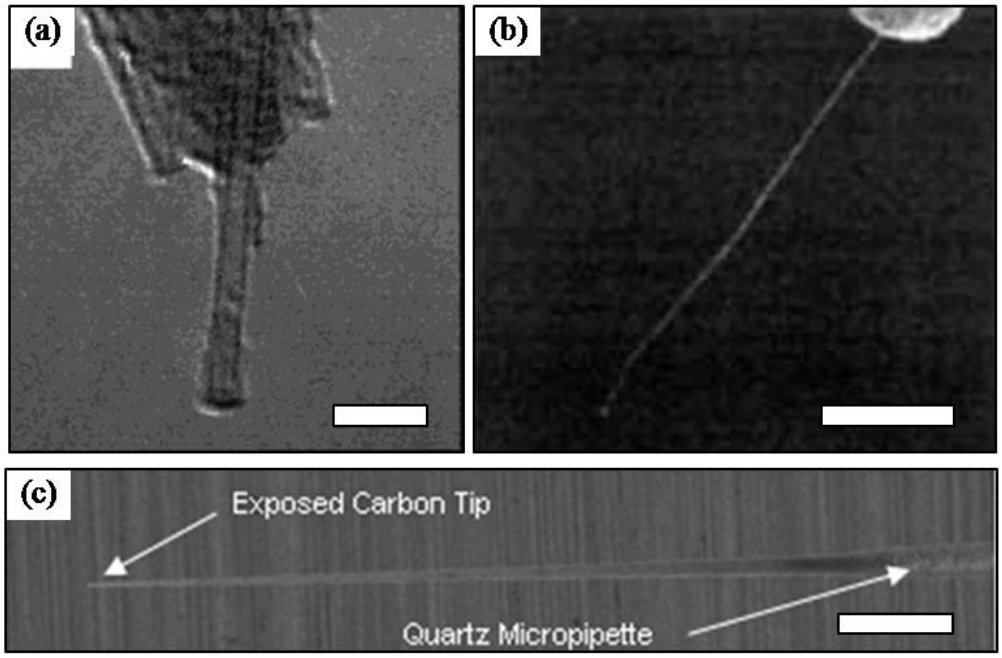

Figure 2.4: Probes tipped with carbon nanostructures. (a) CNT-tipped AFM probe (Scale bar: 10 μm). Adapted from Hafner et al. (2001). (b) CNT-tipped electrode (Scale bar: 90 μm). Adapted from Kaempgen and Roth (2005). (c) Carbon nanopipette (Scale bar: 5 μm). Adapted from Schrlau et al. (2008).

Instead of AFM tips, CNTs have been attached to the tips of thin wires using similar contact assembly methods. One of the earliest examples of such a probe was made by bringing the tip of a micron-sized Pt wire, coated with Ag-conducting epoxy, into contact

with aligned MWCNTs (Fig. 2.4b) [68]. The conductive surfaces were insulated with polyphenol. Afterwards, a 1 V negative potential in electrolyte was applied to expose only the CNT tip of the probe. It was demonstrated that these MWCNT bundle-tipped probes could be used as an electrochemical nanoelectrodes.

AC electric fields were used to capture bundles of CNTs at the tips of tungsten microelectrodes to form nanoprobes with a macroscopic handle [69]. Two tungsten microelectrodes were submerged in aqueous solutions containing either SWCNT or MWCNT so that their tips opposed each other. By applying an AC field across the two electrodes, CNTs were attracted to the regions with high field intensity to form narrow bundles at the electrode tip. Instead of AC fields, magnetic forces have been employed to position ferromagnetic CNTs at the tips of glass micropipettes [70]. Magnetic CNTs placed inside a glass micropipette were driven to its tip by magnetic fields, upon where the protruding CNT was fixed in place by epoxy. The magnetic positioning was later replaced with an evaporative fluid flow technique to reduce manufacturing complexity [71].

Glass micropipettes have also been used as templates for forming carbon nanopipettes. Using CVD, a carbon film was deposited onto all the surfaces of the glass micropipettes [72] or preferentially on the inner surfaces with catalyst [16] and CVD process controls [73]. After the glass was selectively removed from the pipette tip, an integrated CNT-like structure remained at the tip of the larger glass micropipette (Fig. 2.4c). Diameters as small as 10 nm have been achieved with this technique.

2.1.4. Enhancement and Selectivity

Several strategies have been developed to enhance the capabilities of carbon nanostructures. Their surfaces can be functionalized, modified, and customized to selectively detect molecules, chemicals, and biological material in liquid or gas phases. Non-covalent attachment can be utilized to preserve the structure of CNTs by adsorbing material onto their surface. Covalent attachment needs the surface of CNTs to have defect sites, often requiring the surface to be chemically activated in order to bind molecules to their surface. Alternatively, CNTs can be embedded or filled with material.

Surfaces of CNTs can be modified by non-covalent attachment. A simple method is to deposit material onto CNTs through incubation or drying steps. For example, CNT-coated glassy carbon electrodes were incubated in a combination of proteins and surfactants to enhance interfacial electron transfer [74] while single-stranded DNA were deposited and left to dry on top of CNT-based FETs in order to detect vapors [75].

A more elegant method is to use adsorption of aromatic compounds. In general, this strategy involves first attaching linker molecules to hydrophobic surfaces of carbon nanotubes via pi-pi stacking. Subsequently, nanoparticles, molecules, or proteins are then attached to linker molecule. For example, this method was used to selectively bind to streptavidin [76]. The surfactant poly(ethylene glycol) or PEG, was used to bind to hydrophobic CNTs to prevent the non-specific binding of proteins to their surface. However, when CNTs were coated with diamino-PEG, amine-reactive protein reagents (in their case amine-reactive biotin) could be bound to the CNTs. This gave the CNT selectivity by only permitting selective binding to high affinity molecules, in this case

streptavidin. These methods were used with several different linker molecules and selective reagents (proteins, receptors, even chemicals) to enhance the selectivity of FETs and chemical sensors [43, 48, 77].

Covalent functionalization is accomplished by chemically attaching molecules to the CNT surface and are reviewed in detail [78]. In general, CNTs that lack defect sites need to undergo processes, such as sonication, acid treatment, electrochemical oxidation, or plasma treatment, to activate their surface and provide hydrophilic surface functional groups for covalent attachment. CNTs and CNFs that have defect sites, such as those grown from template-based synthesis methods, will have binding sites but often still require a degree of surface activation.

A common approach is to use two linker molecules to covalently attach biomolecules to the surface of CNTs. CNTs are first activated by acid, electrochemistry, or other means to produce carboxyl functional groups on their surface. CNTs are then incubated in standard coupling agents, such as 1-ethyl-3-(3-dimethylaminopropyl) carbodiimide (EDC) and derivatives of N-hydroxysuccinimide (NHS) or 2[N-morpholina]ethane sulfonic acid (MES). The combination of the linker molecules allows biomolecules to bind to the CNT surface by forming linkages between the biomolecule amine groups and CNT carboxyl groups. This functionalization method has been successful in many applications, for instance, attaching peptide nucleic acid to CNTs to preferentially bind to DNA sequences [79], attaching DNA to the surface of magnetic CNTs for intracellular delivery [80], and binding glucose oxidize to CNTs for the electrochemical detection of glucose [81].

Several methods have been developed to make CNT-nanoparticle hybrids. The tips of CNT-based nanoelectrodes were coated with Au, Fe, and Ag nanoparticles using short-pulse, non-thermal corona discharge in liquids containing metal-salt solutions [82]. Metal nanoparticles can also be attached to CNT surfaces through electrostatic interactions. A positively charged polyelectrolyte was used to attach negatively charged Au nanoparticles to the negatively charged surface of acid treated nitrogen-doped MWCNTs [83]. Electrostatic functionalization was also utilized to attach gold nanoparticles to the surfaces of CNT-tipped probes to enable surface-enhanced Raman spectroscopy (SERS) [71, 84].

Besides attachment to CNT surfaces, nanoparticles can be embedded into CNTs or filled inside. For instance, CNTs grown by catalytic PECVD contain ferromagnetic nanoparticles enclosed in their tips. It was demonstrated how vertically aligned CNTs grown from Ni could be manipulated by external magnetic forces and be directed to spear cells [80]. Similar capabilities were demonstrated by embedding iron oxide nanoparticles into the walls of CNTs [85] or filling them with magnetic nanoparticles [86] or smaller carbon nanostructures [87] during template-based CNT synthesis processes.

2.2. CNT Fabrication

CNTs of various diameters, lengths, and structure can be fabricated using different methods, including electric arc discharge [88-91], laser ablation [92, 93], catalytic chemical vapor deposition (C-CVD) [94], catalytic PECVD [13], and template-based CVD [11, 95-97]. Electric arc discharge and laser ablation are very efficient methods for

producing high quality SWCNTs and MWCNTs in large quantities. Nanotubes are obtained by removing unwanted carbon particles and other material through complex purification and filtering processes. CNTs made in this fashion are free to be suspended and utilized in random dispersions. CNTs are also produced in quantity by CVD methods. In general, CVD involves the decomposition of hydrocarbon gases to controllably synthesize CNTs and CNFs. In C-CVD, the size of catalyst particle controls the uniform diameter of the carbon products. Catalyst particles can be prefabricated into patterned arrays to produce well-aligned CNT assemblies [51, 98]. The location, alignment, geometry, and structure of CNTs can be controlled during synthesis.

As an extension of CVD processing, CNTs can be produced by depositing carbon inside porous substrates like glass capillaries or AAO [95]. The template is removed to get aligned arrays [11, 99], individual nanotubes, or single integrated nanostructures [16, 72, 73]. Template-synthesis processing allows CNTs to be produced in various dimensions, geometries, and shapes, as well as produce customized nanotubes with wall-embedded nanoparticles [85] or nanoparticle-filled inner bores [86].

2.3. Template-Based Manufacturing of CNTs

Template-based manufacturing is a method of synthesizing a wide range of materials in micro and nano scale and with a desirable morphology. In this method, a central structure with nano-scale network is utilized as a template to form desirable nano-structures within its features. After template removal, the remaining products will have morphological shapes relative to those of the template, as shown in Figure 2.5. Pioneered by Charles R.

Martin in 1994 [95], membrane-based, or more generally template-based synthesis, has proven to be an effective, scalable, and versatile method for manufacturing of nano-structures. This method has since become one of the main techniques to form features such as nanotubes, nanorods, nanowires, and nanoparticles from metallic, semiconducting, and dielectric materials, and its use has been extended to physical guides for catalytic nanostructure growth and also lithography masks [100]. Using this nanomanufacturing technique eliminates the need for nanoassembly and reduces the fabrication cost. There are various types of porous templates that can be employed for the manufacturing of nanostructures such as track-etched polymeric membranes, AAO membranes, silica membranes and other nanoporous templates.

The track-etched membranes are produced by bombarding a nonporous sheet of the desired material (usually polymers) with nuclear fission fragments to create damage tracks in the material, and then chemically etching these tracks into pores (Fig. 2.5a) [101]. The process can provide randomly distributed cylindrical pores with diameters as small as 10 nm and the pore density of around 10^9 pore/cm^2 [101]. Moreover, silicon wafers can be prepared as a template using the well-known photolithography technique. For instance, individual SWCNTs have been synthesized using iron catalyst arranged in fabricated pores in silicon wafer [102].

AAO membranes, on the other hand, are self-organized and highly ordered porous structures that can be formed via oxidation on top of a pure aluminum layer through an electrochemical process (Fig. 2.5b). Pore diameters in range of 5 nm to several hundreds of nanometers with pore density as high as 10^{11} pore/cm^2 is achievable. Due to the flexibility of the fabrication process for achieving controllable pore diameter, length and

distribution, AAO membranes can be utilized for a variety of nanotechnology applications such as molecular filtering, fabricating nanowires and nanotubes, variety of sensors, electro-osmotic pumps and biological applications including cell culturing and tissue engineering [103, 104]. Highly ordered porous structure of AAO membranes along with controllability of their pore dimensions (diameter and length) and the ability to tolerate high temperature (up to 800 °C) are among their advantages in comparison to other templates. Moreover, the geometry of pores can be readily controlled to form not only uniform cylindrical shapes, but also pores with modulated diameter [104]. However, the fragility of these membranes can hinder their applications and needs to be addressed.

The aforementioned templates are utilized in a variety of fabrication processes and almost any type of material can be synthesized inside their pores. In electrochemical deposition, for instance, one side of the templates is covered by a conductive layer to be used as a cathode electrode and then, the volume of the pores is continuously filled up with the material in question, beginning from the pore bottom. Therefore, the shape and length of the deposited structure can be controlled by template morphology and deposition time, respectively [105].

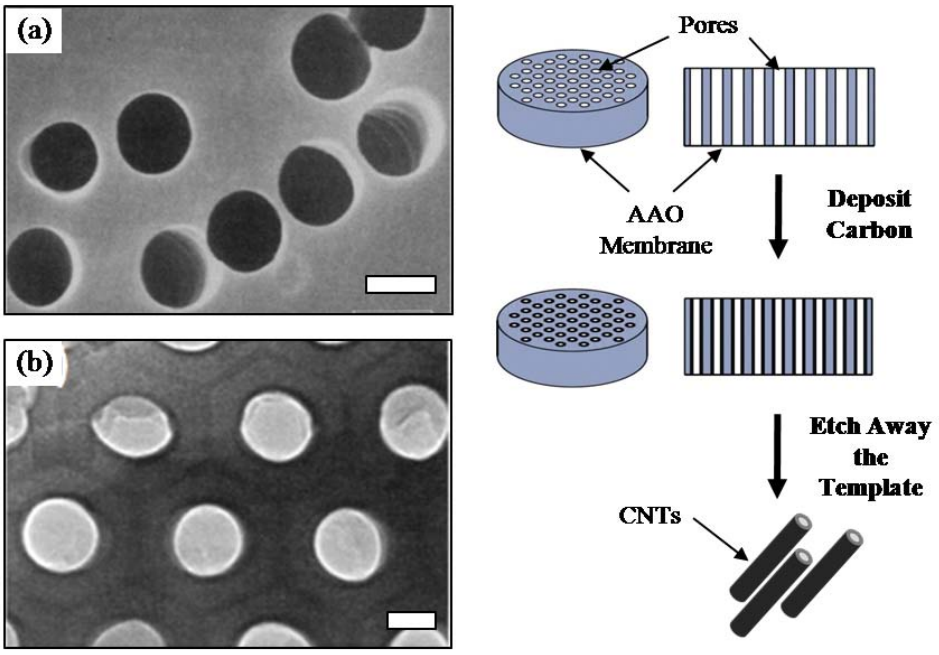

Figure 2.5: SEM micrographs of (a) track-etched (Scale bar: 1 μm) and (b) AAO templates (Scale bar: 50 nm). Adapted from Martin et al. (1994). (c) Schematic illustration of CNT fabrication by non-catalytic template assisted CVD. Carbon is deposited on AAO membranes by CVD. The AAO is chemically etched away to release the CNTs formed inside the AAO pores.

2.4. AAO Membranes

Metallic oxide layers have been used to prevent corrosion in seaplanes for about 90 years. Aluminum metal naturally reacts with atmospheric oxygen and creates a protective oxide layer. But there are two different types of oxide that can be grown on aluminum: the non-porous barrier oxide and the nano-porous alumina. The former type is thinner and has a protective characteristic against corrosion and wears while the latter one is thicker and has a porous structure. This porous oxide layer can be fabricated on aluminum sheets using a simple electrochemical process. Anodization mechanism and pore formation was first established and studied by Keller et al. in 1953 [106]. In this process, an aluminum sheet is connected to the anode electrode of an electrochemical cell and by controlling the

voltage and current density passing through the cell, pore diameter, pore density and thickness of the oxide layer can be controlled.

In general, the anodization process starts with a very pure aluminum sheet. First, the sheet is degreased and electropolished to eliminate any contamination and oxide layer from the surface. This is followed by annealing process in which the sheet is cooked in a temperature close to two-third of the aluminum melting point for several hours to release residual stresses and provide proper sites for nucleation in the next step. Since during the annealing process, the aluminum grain size increases and the surface becomes rougher with larger grain boundaries, lots of defect sites will be created for nucleation [103]. Then, anodization is done in an electrochemical cell to fabricate the desirable porous structure by controlling the electrolyte type and concentration, anodic voltage, cell temperature and anodization time. This process results in an ordered porous nanostructure which can be used as a template in other micro- or nanomanufacturing techniques. The anodization process can be done in one step or two steps. Masuda et al. was the first to establish the two-step anodization [107]. In this technique, after the first step, the porous oxide layer is removed from the surface and then, the second step is done in the same condition as the first one but in a shorter period. This technique results in a highly ordered structure of pores embedded inside hexagonal shaped cells (Fig. 2.5b) due to the fact that the second step utilizes the organized nucleation sites from the first step which will be explained in detail later.

It is worth noting that the pre-texturing of the aluminum sheet is the most important step of the whole process. This is because the pore nucleation mechanism is a combination of both random nucleation and nucleation due to surface defects such as

scratches, pits and grain boundaries. These nucleation sites can be produced on the surface by the tip of scanning probe microscope, the tip of atomic force microscope [108], focused ion beam lithography [108], or reactive ion etching [109]. Moreover, hexagonally arranged polystyrene spheres [110] or colloidal crystal nanospheres have been utilized as a stamp to form organized defects on the aluminum surface during the pre-texturing process [111]. Although these techniques can provide anodization sites free of imperfection and in a desirable order, they are very time consuming, are not cost effective and require special tools. Therefore, using the simple annealing process along with the two-step anodization is one of the most popular fabrication processes of AAO membranes among researchers.

Although the actual mechanism of pore formation in anodized aluminum oxide is not clear yet, there are several theories which try to explain this phenomenon [112, 113]. Figure 2.6 schematically illustrates the processes involve in the formation of the oxide layer. One of the first theories about AAO nucleation was presented by Thompson and Wood in 1970 [114]. According to their theory, during the surface preparation, small cracks and pits are created. As anodization starts, the pores grow over that cracks and surface imperfections which lead to variation of electric field on the surface in such a way that a higher electric field is formed at regions with a thinner oxide layer. Higher electric field adds to the local dissolution rate of the oxide in electrolyte causing the bottom of the pores to be deepened. The growth of barrier oxide is determined by the electric field at the metal/oxide interface while the local electric field at the oxide/electrolyte interface along with local heat determines the oxide dissolution rate at this point. The growth rate of the pores has been shown to be independent of the pore

bottom curvature while the dissolution rate increases as the radius of curvature decreases. It means that as the pore radius of curvature decreases due to oxide growth, the dissolution rate increases and enlarges the pore until the point that the curvature is too big; and therefore, dissolution slows down and the oxide growth dominates. These two competing processes keep the pore radius constant.

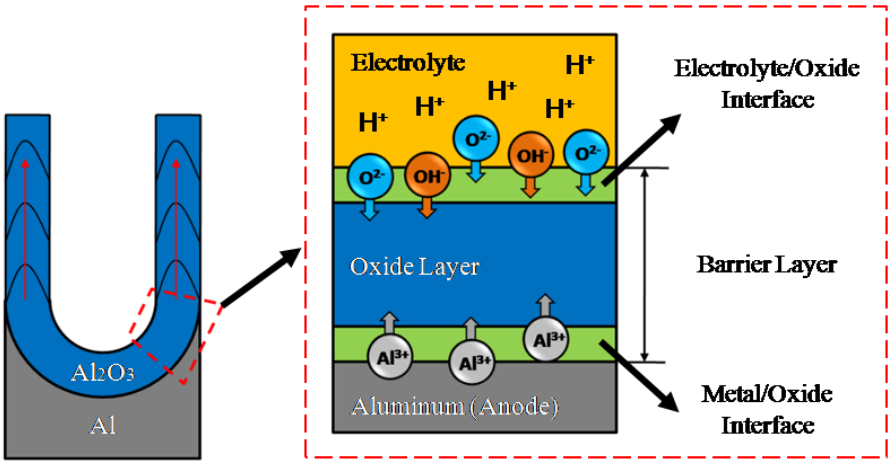

Figure 2.6: Schematic illustration of the processes involved in oxide formation over aluminum.

Li et al. introduced a new theory to better explain the pore formation in this process [112]. The baseline of their theory is also the electropolishing and creation of cracks and pits. By using SEM images, they illustrated that nanometer pits with density of around 10^{10}-10^{12} pits/cm^2 appear on the aluminum sheet surface after annealing and electropolishing. According to this theory, since the initial oxide layer on the surface is very thin and nonuniform, the electric field and ionic current density is larger at the pit bottom than between the pits. Therefore, the dissolution rate is higher at the pore bottom, leading to formation of nucleation sites. Aluminum ions, Al^{3+}, are formed at the metal/oxide interface by reaction (2.1) and migrate into the oxide layer. Meanwhile, the

O^{2-} ions produced at oxide/electrolyte interface through reaction (2.2) migrate toward metal/oxide interface, due to the electric field, and form Al_2O_3. At the oxide/electrolyte interface, the hydronium ions produced by reaction (2.2) dissolve the aluminum oxide through reaction (2.3) with a reaction constant rate smaller than oxide formation reaction, resulting in formation of the pore sidewalls. Also, the hydronium ions migrate toward the cathode to complete the circuit, releasing hydrogen gas through reaction (2.4). At the interface of the pore sidewall and hemispherical pore bottom, the reaction (2.2) happens while the reaction (2.3) does not occur, leading to formation of the sidewall from the bottom and evolution of the wall towards the top. It means that the new layer of oxide is created at the base and the older oxide goes upward. Formation of hydronium ions can happen by other reactions like (2.5), (2.6) and (2.7) which are dependent on the type of the electrolyte of the process. As explained before, these hydronium ions participate in the dissolution reaction of oxide; and therefore, selecting a proper electrolyte for balancing the oxide formation and dissolution reactions is crucial.

Reaction (2.1): $\mathrm{Al(s)} \rightarrow \mathrm{Al^{3+}(oxide)} + 3\mathrm{e^-}$

Reaction (2.2): $\frac{3}{2}\mathrm{H_2O(l)} \rightarrow 3\mathrm{H^+(aq)} + \frac{3}{2}\mathrm{O^{2-}(oxide)}$

Reaction (2.3): $\frac{1}{2}\mathrm{Al_2O_3(s)} + 3\mathrm{H^+(aq)} \rightarrow \mathrm{Al^{3+}(aq)} + \frac{3}{2}\mathrm{H_2O(l)}$

Reaction (2.4): $3\mathrm{H^+(aq)} + 3\mathrm{e^-} \rightarrow + \frac{3}{2}\mathrm{H_2(g)}$

Reaction (2.5): $\mathrm{HSO_4{}^-(aq)} \rightarrow \mathrm{SO_4{}^{2-}(oxide)} + \mathrm{H^+(aq)}$

Reaction (2.6): $\mathrm{H_2PO_4{}^-(aq)} \rightarrow \mathrm{HPO_4{}^{2-}(oxide)} + \mathrm{H^+(aq)}$

Reaction (2.7): $\mathrm{HP_2O_4{}^-(aq)} \rightarrow \mathrm{C_2O_4{}^{2-}(oxide)} + \mathrm{H^+(aq)}$

Fabrication of the desired AAO membranes with a specific pore density, pore diameter and thickness can be done by controlling and adjusting several factors such as electrolyte type, electrolyte concentration, anodization time, anodization voltage and cell temperature. Different studies have been done to investigate the effect of each factor on the resultant AAO membranes [115-117]. To fabricate porous oxide from an aluminum sheet, proper voltage and current density is required. Increasing the voltage can exponentially increase the current density; leading to higher oxidation rate. Moreover, increasing the temperature can also increase the current density. It should be noted that high oxidation rate due to higher current density causes the formation of nonuniform pores. Therefore, a slower process is desirable to reach a proper well-organized porous structure. In other words, longer anodization time can improve pore arrangement. Pore diameter can also be varied by voltage, temperature and time. Increasing the anodization potential, temperature and anodization time, increase the pore diameter. The relationship between pore diameter and voltage is linear while the effect of the other two factors can be linear or quadratic, depending on the electrolyte type and the type of anodization process which can be one-step or two-steps. Interestingly, neither temperature nor the time of anodization effect center-to-center distance between the pores. On the other hand, increasing the potential can linearly increase the interpore distance [103]. The higher the proportional constant, the faster the increase rate of pore diameter with potential. Since the porosity is a quadratic function of pore diameter and interpore distance, and because both of these parameters are linear functions of applied potential, one can conclude that the porosity is a quadratic function of the anodization voltage.

The pH of the solution is yet another effective factor on AAO pore formation. In order to form porous oxide over an aluminum sheet, the electrolyte should have a pH less than 5 to slow down the dissolution rate of the formed oxide by electrolyte. A pH of higher than 7 is utilized for the creation of non-porous barrier oxide. Therefore, electrolytes with basic characteristics tend to produce oxides that are harder, thicker, less porous and more wear resistant than those with more acidic properties [103].

Fabrication of AAO membranes is done under a variety of conditions. Recent review articles have highlighted the versatility of the manufacturing parameters and structural engineering [103, 104]. Table 2.1 is also summarizing the factors employed by different groups for AAO manufacturing.

Table 2.1: Various process parameters to fabricate AAO membranes with controlled pore diameters.

Electrolyte	Concentration (M)	Voltage (V)	Time (h)	Temperature (°C)	Pore Diameter (nm)	Ref.
Oxalic Acid	0.3	40	4 Steps	15	53-73	[118]
	0.3	20-60	0.5, 1, 2	35-50	20-100	[115]
	0.3-0.5	30-50	8	17	40-80	[116]
	0.2	40	2 Steps	18	43	[119]
Phosphoric Acid	0.3	195	16	0	300	[107]
	0.3	32-200	NS	0	80-480	[111]
Sulfuric Acid	0.5	18	NS	10	70	[120]
	1.9	15-70	0.3-1	0	10-50	[121]

2.5. Detection of Biomolecules Using CNTs

CNT-based sensors are attractive for detecting biomolecules commonly found in aqueous environments. For instance, researchers utilized vertically aligned CNT arrays [57] to bind DNA to the surface of CNTs [122], detected RNA, DNA, and DNA PCR amplicons in solution [50, 123, 124], and even delivered DNA plasmids into cells [56]. For the

detection applications, CNT-based devices were manufactured and DNA probes were covalently attached to the ends of CNTs using the EDC/sulfo-NHS method. When combined with the Ru(bpy)32+ mediated guanine oxidation method, the CNT-based sensor was capable of detecting less than a few attomoles of oligonucleotide targets, showing orders of magnitude improvement in sensitivity over other electrochemical detection of DNA immobilization [124], as well as detecting low number of PCR amplicon targets comparable to fluorescence-based DNA microarray techniques [123]. These detection capabilities were later summarized [50]. The electronic platform facilitates DNA and RNA detection and makes it possible to be integrated into hand-held microfluidic lab-on-chip devices.

Although their sensing capabilities were first demonstrated with the detection of gases and vapors, CNT-based FETs were soon utilized in electrolytes [125] to detect chemicals and biomolecules in aqueous environments. The development of such SWCNT-based FETs with the selective binding and recognition of target proteins was reported [48]. FETs were manufactured by dispersing a network of polyethylene oxide (PEO)-functionalized SWCNTs between two electrodes. The PEO coating, non-covalently bound to the CNT surface by pi-pi stacking, strongly prevented nonspecific binding. However, when its hydroxyl termini were activated, the receptors of specific targets could be conjugated to the PEO-coated CNTs to enable selective binding of target proteins. CNT-based FETs conjugated with staphylococcal protein A (SpA) were extremely sensitive to the addition of a protein that has a high affinity to SpA (i.e. IgG protein) but showed negligible response to others.

The *in situ* biomolecules detection has been done by SWCNT-based near-infrared sensors. These optical sensors detect the presence of specific targets by monitoring the fluorescence of functionalized SWCNTs at wavelengths that are transparent to biological tissue (900 – 1600 nm). In one application, a porous vessel containing glucose oxidase-coated SWCNTs was implanted beneath a human epidermal tissue sample [126]. The implanted sensor was capable of distinguishing between slight variations in local glucose concentration within the range of blood glucose. In contrast to flux-measuring electrochemical glucose sensors, concentration-measuring optical sensors were less prone to biofouling and significantly more stable over longer periods of time [127]. Detecting DNA hybridization and conformational polymorphism in cells with similar sensors has been also reported [128, 129].

2.6. Single Cell Probes and Sensors

CNT-tipped probes offer the ability to probe small aqueous environments, such as ultra-low volumes of liquids or single living cells. In contrast to CNT arrays or planar configurations, CNT-tipped probes are needle-like configurations that can be easily maneuvered to interrogate regions of interest in such things as fluid droplets, single cells, or living tissue.

As discussed earlier, CNT-tipped AFM cantilevers were some of the first CNT-tipped probes to be developed [15]. With high spatial resolution and precise manipulation, CNT-tipped AFM cantilevers were used in SPM applications [60-64] and were able to probe and deliver surface bound cargo to cells [65, 66]. Despite their relatively easy use

and high spatial resolution, these CNT-tipped probes were limited by laborious fabrication and inadequately suited for fluid delivery to and electrical sensing of discrete fluid volumes. In contrast, the development of CNT-tipped pencil-shaped probes and their utilization in biological sensing have progressed more rapidly. This is mostly due to their ability to readily fit standard cell physiology equipment such as optical microscopes, micromanipulators, cell injection systems, and electrophysiology amplifiers.

One of the earliest CNT-tipped biological sensor reported was a SWCNT-coated carbon fiber nanoelectrode (100-300 nm tip diameter, as shown in Figure 2b) [44]. Using cyclic voltammetry, the CNT-tipped electrode could detect dopamine, epinephrine, and norepinephrine at concentrations an order of magnitude lower than non-coated probes. The demonstration was significant because the dimensions of the CNT-tipped probe would make it possible to study the functions of living cells and tissue with minimal intrusion. Additionally, the pencil-like shape of the probe readily fit standard cell physiology equipment and facilitated its use.

Several pencil-shaped probes tipped with a single or bundle of CNTs were developed afterwards. Of note, it was reported that a probe tipped with a bundle of MWCNTs could be used as an electrochemical sensor [68]. This demonstration helped inspire the development of CNT-based probes to measure intracellular signals [130]. Referred to earlier as carbon nanopipettes (CNPs), these CNT-tipped probes were used to penetrate the membrane of single living cells and electrically measure changes in their transmembrane potential upon extracellular chemical and pharmacological stimulation. It was later shown that a CNT-tipped probe was capable of electrically stimulating and measuring intracellular and extracellular responses more efficiently than the electrolyte-

filled glass micropipettes typically used in cell electrophysiology [131]. It was found that similar CNT probes had comparable performance to conventional Ag/AgCl (silver/silver chloride) electrodes when employed to monitor both extracellular and intracellular neural activity [132]. Recently, CNT-tipped endoscopes have been developed to provide minimally invasive, multifunctional single cell analysis such as intracellular injection, electrochemistry, and SERS [71, 84, 133].

2.7. Intracellular Transfection Techniques

In recent years, growing interest towards manufacturing of nanoscale devices and methods for better monitoring and understanding of cellular behavior has enabled significant advances in biomolecular science, medical researches and therapeutic applications including gene therapy [134], cancer research [135], cell fate control [136] and direct interfacing with intracellular plasma [137, 138]. Such devices and methods should not only be biocompatible, but also facilitate simultaneous and parallel delivery of extracellular reagents into cells through bypassing the cell plasma membrane, with high cell viability and minimal effect on cell functionality.

Intracellular delivery of foreign molecules such as drugs and genetic materials can be accomplished by using chemical or biological reagents like liposomes [139], endosomes [140], or using viral vectors [141], electroporation [142], ionophoresis [143] and microfluidic techniques [144]. As illustrated in Figure 2.7, using lipofection, the genetic materials are transferred into the cells by packaging with liposomes; in electroporation, the cell lipid bilayer is punctured by an electric field to allow exogenous material to be

transferred inside the cell; by using viral vectors, the genetic materials are delivered by genetically modified viruses; and the microinjectors act as needles for intracellular delivery. Low efficiency of biomolecular delivery [145, 146] and invasiveness of some of these techniques [147, 148] limit their potential applications and impact.

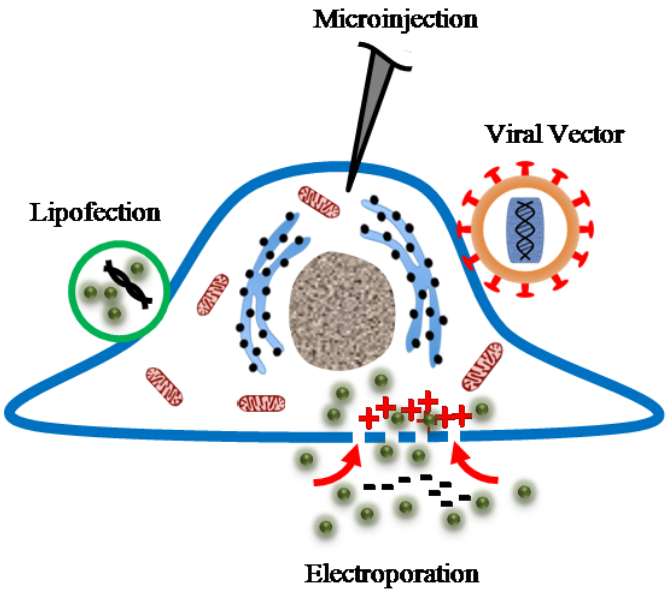

Figure 2.7: Schematic illustration of the current available intracellular gene transfection techniques.

Cellular injection is yet another delivery method in which nanowires or nanotubes penetrate cell membrane in order to deliver targeted reagents, promises a powerful tool for cellular biology in terms of controllability, compatibility and ability to directly address individual cells. Intracellular injection of biomolecules has been conducted by two main platforms of single-tipped [149, 150] and arrayed devices [151, 152]. For instance, a single-crystalline Au nanowire has been fabricated to deliver linear DNA fragment and plasmid into the nucleus of single living cell with high temporal and spatial selectivity [153]. Cytotoxicity and biocompatibility studies of these devices as a tool for

drug delivery show high cell viability in cell therapy and cancer treatment [154]. Bioprobes interfaced with an atomic force microscope consisting of microfluidic channel have been developed to introduce biomolecules into living cells in physiological environment [155, 156]. Vertically aligned nanowires and nanotubes have also been employed as yet another method for intracellular delivery of exogenous substances into the cell cytosol. This has been done by either attaching the biomolecules to the nanowires for cell uptake [157, 158] (Fig. 2.8a), transporting the reagent through the inner lumen of the nanotubes using electroporation [142, 159] (Fig. 2.8b), or through direct fluidic access into the cell cytoplasm using pressure gradient [160] or concentration gradient [161] in a microfluidic channel (Fig. 2.8c).

2.8. CNT-Based Platforms for Intracellular Delivery

CNT-based devices show significant promise in biological applications, such as single-cell probing and electrochemical sensing due to their small size and unique mechanical, chemical and electrical properties [162]. Both single-tipped and array device platforms have been fabricated using CNTs in order to utilize their multifunctional properties. For instance, biological probes consisting of individual CNTs have been developed to probe single living cells [16], controllably inject sub-attoliter volumes of fluids and particles into cells [163] and electrically measure membrane kinetics of cells [130]. These devices are minimally invasive to the cells and capable of delivering exogenous molecules into the cells, along with monitoring and studying cellular behavior through various detection techniques. However, their low injection throughput due to serial approach of

nanoinjection and incapability of probing multiple cells in parallel limit their qualitative and quantitative utilization to study multiple individual cells and cellular behavior in tissue form. Automated and robotic microinjection systems have also been developed to facilitate high throughput serial injection and monitoring of the injected cells [164, 165]. Yet the feasibility, reproducibility and accuracy of the systems rely on expensive tools such as nanomanipulator and complicated image processing software.

However, CNT-based array platforms can overcome the limitations of single-tipped tools [166] (Fig. 2.8d). These platforms can be used to deliver DNA or RNA into population of cells with relatively high efficiency and low cytotoxicity [167, 168]. CNT arrayed devices have also been used as an electrochemical electrode for sensing several biological reagents with known concentration [169, 170].

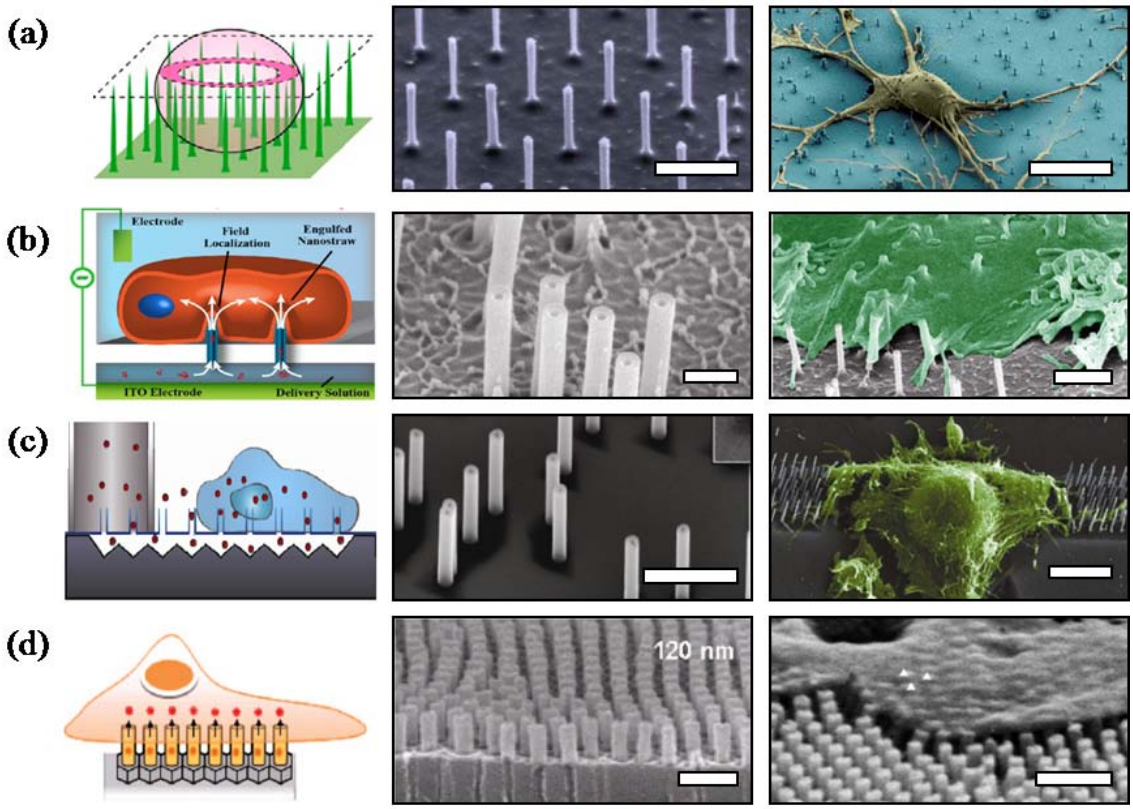

Figure 2.8: Vertically aligned array devices for intracellular delivery. (a) Array of silicon nanorods (Scale bar: 1 µm) for intracellular delivery of siRNA, peptides and plasmid DNA into primary neurons (Scale bar: 10 µm). Adapted from Shalek et al. (2010). (b) Array of aluminum oxide nano-straws (Scale bar: 100 nm) for intracellular delivery of fluorescence dye and plasmid DNA into CHO cells (Scale bar: 1 µm). Adapted from Xie et al. (2013). (c) Array of aluminum oxide nanotubes (Scale bar: 1 µm) for intracellular delivery into mouse fibroblasts (Scale bar: 5 µm). Adapted from Persson et al. (2011). (d) Array of aligned CNTs (Scale bar: 200 nm) for intracellular delivery of plasmid DNA into human mesenchymal stem cells (Scale bar: 200 nm). Adapted from Park et al. (2009).

CHAPTER 3

Template-Based Manufacturing of Carbon Nanotubes

Template-based chemical vapor deposition is an efficient one step process to synthesize CNTs for a wide range of applications. In this process, the choice of template dictates certain physical features of the CNT, such as length and outer diameter, while the process itself affects other features, such as tube wall thickness, carbon deposition rate and carbon morphology. In this chapter, various commercially available AAO templates are characterized to be utilized as a sacrificial template for carbon deposition. A systematic parametric study is conducted to determine how three key process parameters (deposition time, temperature, and gas flow rate) affect overall carbon mass deposition rate and CNT wall thickness and morphology. The findings show that process parameters can be independently utilized to produce CNTs with similar or differing cross-sectional dimensions and other useful features, each with distinct advantages.

3.1. Commercially Available AAO Membranes

In order to provide a universal, reproducible and cost effective fabrication process for a device that can be utilized in a variety of biological and biomedical applications,

commercially available AAO membranes were used as a sacrificial template. The membranes were characterized using scanning electron microscopy (SEM) to evaluate pore quality and measure pore diameter and interpore distance.

3.1.1. Experimental Procedure

Commercially available AAO membranes were used as a sacrificial template for carbon deposition. AAO membranes with 100 nm (Synkera UniKera, Cat. No.: SM-100-50-13, nominal pore diameter: 100±10 nm, nominal thickness: 50±1 μm), 150 nm (Synkera UniKera, Cat. No.: SM-150-50-13, nominal pore diameter: 150±10 nm, nominal thickness: 50±1 μm), and 200 nm nominal pore diameter (Whatman Anodisc 13, Cat. No.: 6809-7023, nominal pore diameter: 200 nm, nominal thickness: 60 μm) were utilized. To prevent curling of the membranes during the CVD process [97, 171], they were annealed 30 °C above synthesis temperature for 4 hours between two quartz plates before carbon deposition (Appendix, Fig. S1).

3.1.2. Results and Discussion

To provide a reproducible and cost effective fabrication process for a device that can be utilized in a variety of biological and biomedical applications, commercially available AAO membranes were used. Since the pore diameter of the AAO membrane dictates the outer diameter of resultant CNTs, pore diameters on both sides of the membrane were characterized by SEM. Three different AAO templates from two different manufacturers were investigated: Whatman AAO membranes with 200 nm nominal pore diameter and

Synkera AAO membranes with 100 nm and 150 nm nominal pore diameter. Figure 3.1 shows the SEM micrographs of the surfaces of these membranes along with a schematic of their pore structure. The average pore diameter and interpore distance (side-to-side) were found to be, respectively, 205±42 nm and 187±36 nm on one side (Fig. 3.1a-i), 286±48 nm and 80±24 nm on the other side (Fig. 3.2a-ii) for Whatman 200 nm templates (n=480), 146±29 nm and 90±14 nm on one side (Fig. 3.1b-i), 147±20 nm and 64±19 nm on the other side (Fig. 3.1b-ii) for Synkera 150 nm templates (n=250), 73±19 nm and 176±39 nm on one side (Fig. 3.1c-i) and 85±17 nm and 128±31 nm on the other side (Fig. 3.1c-ii) for Synkera 100 nm templates (n=330) (Appendix, Fig. S2, S3). Moreover, the pore density was found to be $11.6x10^8$, $22.1x10^8$, and $15.3x10^8$ pores/cm^2 for Whatman 200 nm, Synkera 150 nm and Synkera 100 nm AAO membranes, respectively. As the results show, the pore structure is more uniform and cylindrical for Synkera membranes with a shorter interpore distance, while the Whatman membranes have a barrel shaped pore formation and longer interpore spacing. Moreover, there is almost a 1 μm deep branch-shaped structure on one side of the Whatman AAO membranes (Fig. 3.1a-i) compared to Synkera, which is due to the difference between the fabrication processes of the two manufacturers. Although Synkera membranes provided more uniform pore diameters and spacing without the branched structure, subsequent CNT-based array devices were manufactured using Whatman membranes to facilitate production due to larger interpore spacing (mitigates lateral adhesion between exposed CNTs [172, 173]), and their lower cost (6X less than Synkera).

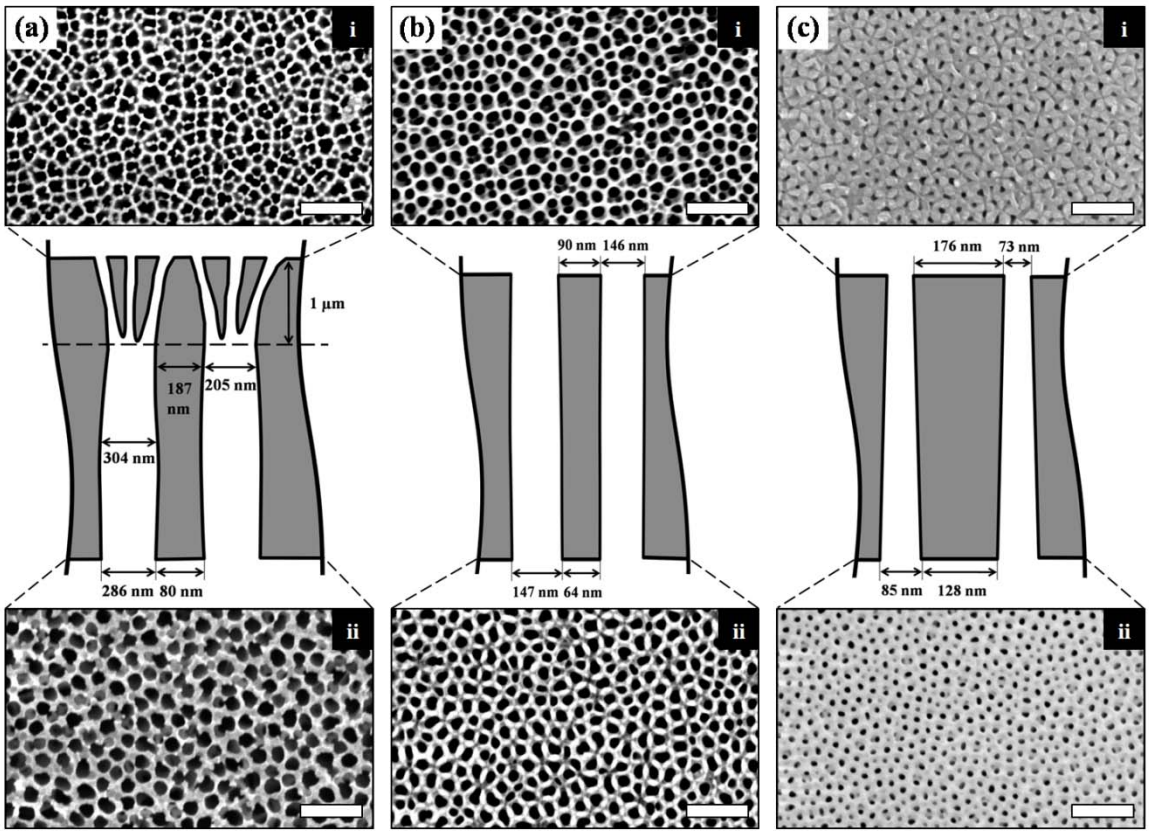

Figure 3.1: Commercially available AAO membrane pore structure. SEM micrographs of both surfaces along with the schematics of the pore structure for (a) Whatman 200 nm AAO membrane, (b) Synkera 150 nm AAO membrane, and (c) Synkera 100 nm AAO membrane (Scale bars: 1 µm).

3.2. Carbon Deposition and CNT Synthesis

Carbon nanostructures have emerged as a prominent class of nanomaterials possessing intriguing and unique mechanical, chemical, optical, and electronic properties [14, 162, 174-176]. Hollow tube-like carbon nanostructures with at least one dimension of 100 nm or less and whose properties distinctly depend on material structure, generally referred to as CNTs [10], consist of hollow carbon nanofibers, SWCNTs or MWCNTs, and carbon nanopipes. CNTs are of great interest in both fundamental and applied science fields and

have found utility in a wide range of applications such as electronic devices [177], reinforced material [178], energy storage [179] and field emission materials [180].

CNTs have played a key role and been applied in a variety of biomedical applications including tissue engineering [181], cellular [182] and neural interfacing [183], drug delivery devices [132], single cell probing [16], biomolecule separation [184] and biosensors [185]. These applications require CNTs with features and properties specific for their intended function. For instance, an array of highly aligned amorphous CNTs was employed as an electrochemical nanoelectrode interface to improve signal-to-noise ratio in molecular detection [186]. Yet, the lateral adhesion of the exposed CNTs (CNTs bending towards and adhering to each other to form bundles of CNTs) has remained a challenge for such arrayed devices. Lateral adhesion can reduce the signal-to-noise ratio, affecting the functionality and precision of the device. In another example, a biological probe consisting of an individual CNT was fabricated to probe single living cells and controllably inject sub-attoliter ($<10^{-18}$ L) volumes of fluids and particles into cells [16]. In these applications, fabricating mechanically robust CNTs for repeated cell membrane piercing and optimizing the channel size to facilitate mass transport are among the main challenges. Ultimately, the ability to tailor CNT features and properties for a specific application is highly desirable.

CNTs can be synthesized by a variety of different methods including electric arc discharge [187], laser ablation [188], CVD [11], and high pressure carbon monoxide disproportionation [189]. The fabrication methods of CNTs have been discussed in several books and review articles [190-193]. Of all synthesis techniques, CVD is one of the most economical and controllable processes to fabricate various types of CNTs on a

variety of substrates, making it a highly desirable method for research and industrial synthesis.

CNTs can be produced by different CVD methods such as thermally activated CVD [194], plasma-enhanced CVD [195], aerosol-assisted CVD [196] and fluidized-bed CVD [197]. Parametric studies have been reported for several CVD methods to provide better understanding of the influence of the manufacturing factors on geometrical and structural properties of CNTs. For instance, arrays of CNTs have been synthesized on iron-embedded silica substrates with CVD and the effect of temperature, growth time, gas ratio, and gas velocity on CNT length, diameter, inter-bundle spacing, density, and crystallinity has been evaluated [198-200]. Vertically aligned MWCNTs have been synthesized on quartz substrates using injection CVD to study the effect of temperature, injection duration, hydrogen concentration and gas flow on nanotube diameter, length, alignment and deposition profile [201, 202]. The growth of MWCNTs by catalytic CVD in a fluidized bed reactor has also been investigated to elucidate the effect of temperature, reaction time, system pressure and gas composition on CNT growth rate and properties [197, 203].

Another popular CVD-based fabrication technique is template-based manufacturing in which CNTs are formed by depositing carbon on a sacrificial template via thermal decomposition of a carbon-carrying precursor gas [11, 99, 204, 205]. Unlike other methods, template-based manufacturing provides the unique ability to control the outer diameter, length of the tubes and other nanostructures through template selection [95, 206] and the potential to tailor other properties, such as tube wall thickness and morphology through synthesis parameters. Moreover, the produced CNTs are embedded in the parent

matrix thus forming a robust platform to directly fabricate devices without the need for elaborate nanoassembly. It should be noted that the CNTs fabricated by this method are in the form of amorphous carbon shaped as nanoscale tubes. A range of templates can be utilized in template-based manufacturing, such as glass capillaries and most commonly AAO membranes [16, 207].

There are several variables in the template-based CVD process that may affect CNT formation, including the type, geometry, and dimensions of the template, type and dimensions of the CVD furnace, relative size and position of the template in the furnace, type of precursor gas (or gases), gas mixture and flow rate, and synthesis temperature and duration. According to Choy, small changes in temperature (~25 °C) can affect the reaction kinetics and, therefore, changes the deposition rate of carbon film [208]. Generally, the chemical reactions in the CVD process depend on the reaction rates and diffusion of gases [208]. This suggests that the gas flow rate could play an important role in carbon film deposition on the template. Adjusting the deposition duration, on the other hand, can change the reaction interval, leading to various thicknesses of the deposited carbon layer [199, 209]. Therefore, synthesis temperature, gas flow rate and deposition duration are among the main process parameters that potentially affect CNT formation.

Until now, only a few parametric studies have been conducted to understand CNT synthesis inside the pores of AAO membranes. For instance, the structural and thermal stability, and deformation of CNTs manufactured by AAO-based CVD, with and without utilization of catalyst, was studied by Sui et al. [210]. Subsequently, high temperature annealing was employed by Mattia et al. to graphitize as-grown amorphous CNTs into MWCNTs [17]. Jeong et al. investigated the effect of reaction gas and catalyst on the

growth of CNTs synthesized inside AAO pores [211]. Kim et al. reported a morphological study on vertically aligned CNTs grown inside AAO membranes by plasma enhanced CVD to investigate the influence of plasma intensity, temperature and gas composition [212]. A comprehensive study of template-based CNTs manufactured by CVD in AAO membranes was conducted by Ciambelli et al. [213, 214] and Sarno et al. [215] to analyze the degree of crystallinity and effect of deposition time, temperature, gas mixture and hydrogen feed on carbon content deposited on the entire template and carbon order of the synthesized CNTs. However, the effect of process parameters on carbon deposition rate and geometrical features of individual CNTs manufactured by AAO-based CVD has not been investigated. These particular features are of critical importance for the batch processing of such CNTs for many practical applications, such as biosensors and probes, tissue scaffolds, and bio-fluid filtration and separation.

To this end, a parametric study on the template-based manufacturing process of CNTs is presented. The main goal of this study was to empirically investigate and understand the influence of process parameters such as temperature, gas flow rate, and deposition duration on tube wall thickness, CNT morphology, and carbon mass deposition rate. Carbon was deposited on commercially available AAO templates using CVD without the utilization of catalyst. The wall thickness of the tubes was determined by transmission electron microscopy (TEM) and the mass of the deposited material was measured after the CVD process. SEM was used to visualize the surface of the templates after the CVD process. Raman spectroscopy was employed to analyze the carbon structure of the resultant CNTs.

3.2.1. Experimental Procedure

3.2.1.1. Template-Based Synthesis of CNTs

AAO membranes were placed upright in a custom quartz boat and positioned in the middle of a three-stage tube furnace (Carbolite, TZF17/600, inner tube diameter: 7 cm, tube length: 152 cm). The reactor temperature was slowly increased to the desired set-point temperature under 100 sccm of argon gas flow. After temperature stabilization, a 30/70 (vol%/vol%) ethylene/helium gas mixture was flown through the reactor tube for a predetermined time at various flow rates to deposit carbon film on all surfaces of the AAO membrane. The furnace was then slowly ramped down to room temperature under 100 sccm of argon flow (Appendix, Fig. S4).

The effect of furnace temperature, gas flow rate and deposition time on CNT wall thickness and structural features were studied in an orthogonal manor; in each set of experiments, one parameter was changed while the others remained unchanged. Orthogonal experiments were conducted for synthesis temperatures of 675, 700, 750 and 800 °C, gas flow rates of 20, 40, 60, 80, 100, 200, and 300 sccm and deposition times of 2.5, 5, 7.5, 10, 15 and 20 hours, resulting in AAO-embedded CNTs.

3.2.1.2. Sample Preparation

The mass of each AAO membrane was measured before and after the initial annealing process, and before and after the CVD process using a mass balance (Metter Toledo, XS204; 0.1 mg accuracy) to determine the mass of the total carbon deposited on the membrane for each experimental set.

AAO membrane was completely dissolved to release CNTs from the template in order to characterize geometric features and material structure. To release the CNTs from the template after synthesis, AAO membranes were completely dissolved in a heated reflux system containing 1 M aqueous NaOH solution at 80 °C for 5 hours (Appendix, Fig. S5). Released CNTs were triple-washed with distilled water, filtered (Sterlitech, polyester membrane filter, pore size: 0.1 µm) and stored in 70% ethanol. Each suspension was sonicated for 10 min to produce individual carbon nanotubes suspended in ethanol.

3.2.1.3. Electron Microscopy

The geometry, density, and integrity of individual CNTs and the condition of the template pores and surface after each stage of the CVD process were characterized by SEM (JEOL 6400V; 20 kV acceleration voltage). AAO membranes and individual CNTs were characterized without sputter coating.

The outer diameter and wall thickness of individual tubes was characterized by TEM (JEOL 100CX II; 100 kV acceleration voltage). TEM samples were produced by placing a 5 µL drop of the sonicated CNT-ethanol suspension on a lacey carbon film, 400-square copper mesh TEM grid. CNT outer diameters and wall thicknesses were measured from calibrated TEM micrographs using ImageJ software. Measurements were marked, labeled, and recorded at several points along an individual CNT. For each experiment, 20-50 CNTs were imaged and 400-1200 measurements were gathered. Each experiment was conducted in duplicate or triplicate to ensure the reproducibility of the results and the data were reported all together in the following graphs. The average measured wall thickness was reported along with its variation in forms of standard deviation.

3.2.1.4. Raman Spectroscopy

Raman spectra were measured with a Renishaw inVia system employing a laser operating at 532 nm (~ 2 mW) and an objective lens with a numeric aperture of 0.9 (50X magnification). Raman spectra were recorded with a lateral resolution (in the focal plane) of circa 2 µm and a spectral resolution of ~1.2 cm^{-1}. Peak fitting of the D- and G-bands was accomplished by fitting four Lorentzian curves to the obtained spectra. The ethanol-suspended CNTs were directly drop-casted on silica glass and measured after drying in air (ca. 15 minutes).

3.2.2. Results and Discussion

Three parameters in the AAO-based CVD process were adjusted to investigate their effects on CNTs. Table 3.1 summarizes the experiments conducted, the associated parameter settings, the resultant average mass of deposited carbon, and the CNT wall thickness. From previous experiments it has been established that CNTs and CNT-embedded devices can be successfully synthesized with the aforementioned AAO-based CVD technique using process parameters of 700 °C furnace temperature, 60 sccm carrier gas flow rate and 5 hours deposition time (Table 3.1, Experiment R2). Therefore, these settings became the relative baseline from which the process parameters (deposition time, temperature and precursor gas flow rate) were adjusted. It is worth noting that the measured temperature inside the tube furnace at the position of the templates was uniform for all flow rates tested and approximately 12 °C lower than the set point for any given temperature.

In total, 29 experiments were conducted and 9633 measurements recorded to generate data presented in Table 3.1. From TEM micrographs, the average outer diameter of the tubes from all CNTs manufactured in this study was found to be 304±54 nm. These values also represent the average diameter of the pores within the AAO membranes. However, from SEM micrographs of the membrane surface, the average pore diameter was found to be 205±42 nm on one side and 286±48 nm on the other side (Fig. 3.1a). This range of outer diameters and the observed variation between the ends of the tube coincide with measurements reported previously [214, 216] and detailed characterization of AAO membrane pores can be found elsewhere [217]. It should be noted that the quality of commercial AAO is generally low, resulting in wide variation in average pore diameter from membrane to membrane.

Table 3.1: Overview of carbon deposition experiments and measurements

	Experiment Number	Temperature (°C)	Flow Rate (sccm)	Deposition Time (h)	Avrg. Deposited Mass ± Standard Deviation (nm)	Avrg. Wall Thickness ± Standard Deviation (nm)
Effect of the Deposition Time	R1	700	60	2.5	0.9 ± 0.1	12 ± 2
	R2			5	2.4 ± 0.2	28 ± 5
	R3			7.5	5.2 ± 0.0	55 ± 13
	R4			10	6.3 ± 0.6	69 ± 8
	R5			15	6.9 ± 0.1	85 ± 12
	R6			20	7.4 ± 0.1	87 ± 11
Effect of the Temperature	R7	675	60	5	0.6 ± 0.0	12 ± 2
	R2	700			2.4 ± 0.2	28 ± 5
	R8	750			7.9 ± 1.2	80 ± 17
	R9	800			10.6 ± 0.7	84 ± 11
Effect of the Gas Flow Rate	R10	700	20	5	1.3 ± 0.0	18 ± 2
	R11		40		1.9 ± 0.2	26 ± 3
	R2		60		2.4 ± 0.2	28 ± 5
	R12		80		2.7 ± 0.4	30 ± 9
	R13		100		2.5 ± 0.5	28 ± 8
	R14		200		1.9 ± 0.6	21 ± 8
	R15		300		1.0 ± 0.0	13 ± 2

It is worth noting that the TEM measurements of the CNTs outer diameter are affected by elastic deformation of CNTs due to van der Waals interaction with substrate. This noticeable deformation depends on nanotube diameter and wall thickness and has been reported in previous studies [218-221]. The scattered plot of all measured outer diameters as a function of wall thickness in Figure 3.2 represents a general linear trend in which for every 10 nm increase in wall thickness, the outer diameter decreases by around 2 nm. This is due to the fact that CNTs with thicker walls are less affected by elastic deformation, resulting in more rounded tubes.

Atomic force microscopy (AFM, Veeco DI-3000, Olympus AC160TS-10 tip) in tapping mode was used to determine the percentage of deformation of the nanotubes. The

collected measurements for several CNTs were corrected based on calibration and measurement protocols for this particular AFM. The average of the measured width and height (14-20 measurements) was utilized as the average diameter for each tube and then, the percent of deformation was calculated. The results indicate that CNTs deform between 6% and 17% with thickest (87 nm) and thinnest walls (12 nm), respectively. However, elastic flattening of nanotubes does not affect the wall thickness measurements reported in this study.

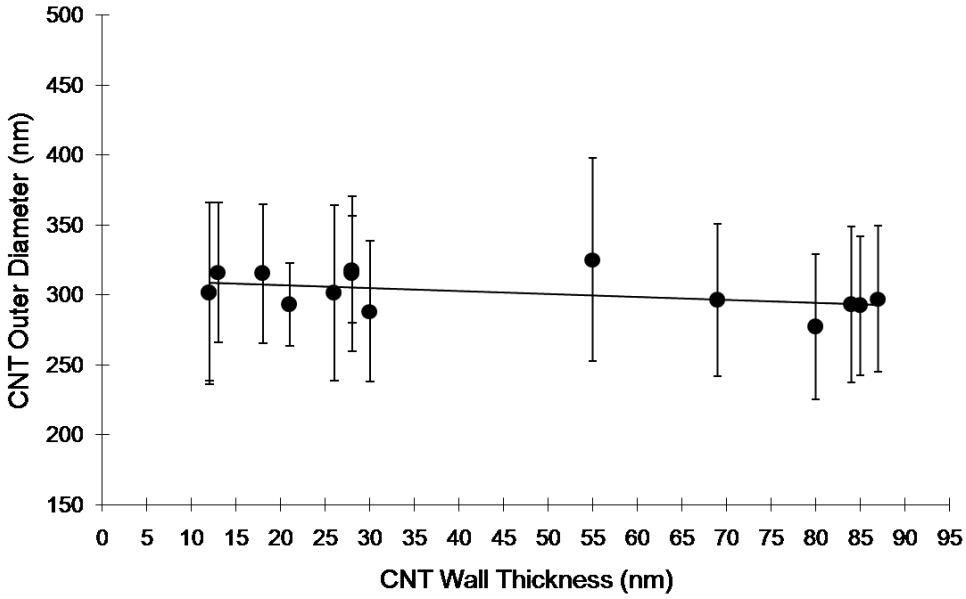

Figure 3.2: Measured CNT outer diameter as a function of wall thickness, indicating tube flattening for CNTs with thinner walls.

3.2.2.1. Influence of Deposition Time

The overall mass of carbon deposited on the AAO membrane and the resultant CNT wall thickness were measured as a function of deposition time. Figure 3.3 shows representative TEM micrographs of CNTs (Fig. 3.3a-d) and SEM micrographs of the membrane surface (Fig. 3.3e-h) for 2.5, 5, 7.5 and 10 hours of deposition time. The deposition time was also extended up to 20 hours.

As the TEM micrographs in Figure 3.3 indicate, CNT wall thickness increases as deposition time increases. The results match our expectations since the growth mechanism of CVD processes at constant temperature and atmospheric pressure is considered to be diffusion-limited [208]. Therefore, increasing the deposition time provides a longer constant diffusion reaction period, resulting in deposition of more mass over the templates and consequently, inside the pores. According to observations from SEM micrographs of the membrane surface after deposition (Fig. 3.3e-h), the pores on the surface become increasingly closed as deposition time increased. For deposition times longer than 7.5 hours (10, 15 and 20 hours), a layer of carbon covers the outer surfaces of the AAO membrane, resulting in blocked pores.

As measured from TEM micrographs (Fig. 3.3a-d), CNT wall thicknesses were 12±2 nm for 2.5 hours, 28±5 nm for 5 hours, 55±13 nm for 7.5 hours, 69±8 nm for 10 hours, 85±12 nm for 15 hours and 87±11 nm for 20 hours of deposition. Similarly, the deposited carbon mass increased from 0.9 to 2.4, 5.2, 6.3, 6.9 and then 7.4 mg for 2.5, 5, 7.5, 10, 15, and 20 hours of deposition, respectively. These trends can be seen in Figure 3.4a and b. In this study, measuring the mass of the membranes before and after the CVD process and comparing it with the growth rate of the wall thickness provides qualitative insight into the amount of carbon deposited inside the AAO pores versus over the template surface. This can also be supported with SEM micrographs by the appearance of covered or open pores. Furthermore, these results elucidate previous observations reporting generally that the overall carbon content deposited on the entire AAO template increases as CVD process time increases [214].

Figure 3.4a reveals three different time-based deposition regimes in template-based CVD: nucleation, normal deposition and carbon infiltration. In the nucleation regime, carbon atoms nucleate on the AAO surface, providing the growth sites for the carbon film (Region I in Fig. 3.4a). Evidence of the nucleation regime can be seen in TEM micrographs, where CNTs synthesized for 2.5 hours (Fig. 3.3a) have a noticeable roughness on the inner tube wall surfaces. However, a decrease in the roughness is observed between the two samples synthesized for 2.5 and 5 hours. In other words, the standard error of wall thickness within each tube is between 14-18% of the average measured wall thickness for the CNTs synthesized at 2.5 hours, while this value reduces to 3-12% for CNTs synthesized after 5 hours. This suggests the transition of deposition into a new regime. The normal deposition regime, defined as the carbon deposition dominated by precursor gas diffusion, encapsulates the range of deposition time between 5 and 7.5 hours (Region II in Fig. 3.4a). Here, the deposited mass and CNT wall thickness follow a similar trend due to the fact that the carbon is deposited on all the surfaces of the AAO membrane, including the inner lumen of the pores.

The deposition and wall thickness growth rates reach a peak at 7.5 hours, and then, start to decrease for longer deposition times. This reduction is due to the fact that increasing the wall thickness decreases the channel size from which the gas can pass through, resulting in less available reactant to be diffused and less deposition. Therefore, by assuming a constant diffusion of precursor inside the CVD chamber, the deposition of carbon occurs more on the template surface rather than the inner lumen of the pores, resulting in covered pores at the surface, which can be confirmed by SEM micrograph (Fig. 3.3h). Finally, despite the covering of pores by the surface carbon layer after 10

hours of deposition, and the increase in deposited mass, the thickness of the CNT walls increases up to 15 hours of deposition, after which it plateaus (Region III in Fig. 3.4a). This suggests that some precursor molecules infiltrate and pass through the carbon layer on the surface, thermally decompose, and are deposited inside the pores [222-224]. By increasing the thickness of the carbon layer over the outer surfaces of the AAO membrane, the precursor gas infiltration decreases, resulting in negligible changes in wall thickness after 15 and 20 hours of deposition, despite the increase in deposited mass. Also, a closer look at Figure 3.4c indicates that up to 2.5 hours of deposition, the wall thickness growth rate is higher compared to 5 and 7.5 hours, due to the available bare AAO surface area for carbon deposition and the catalytic effect of AAO membranes [225, 226].

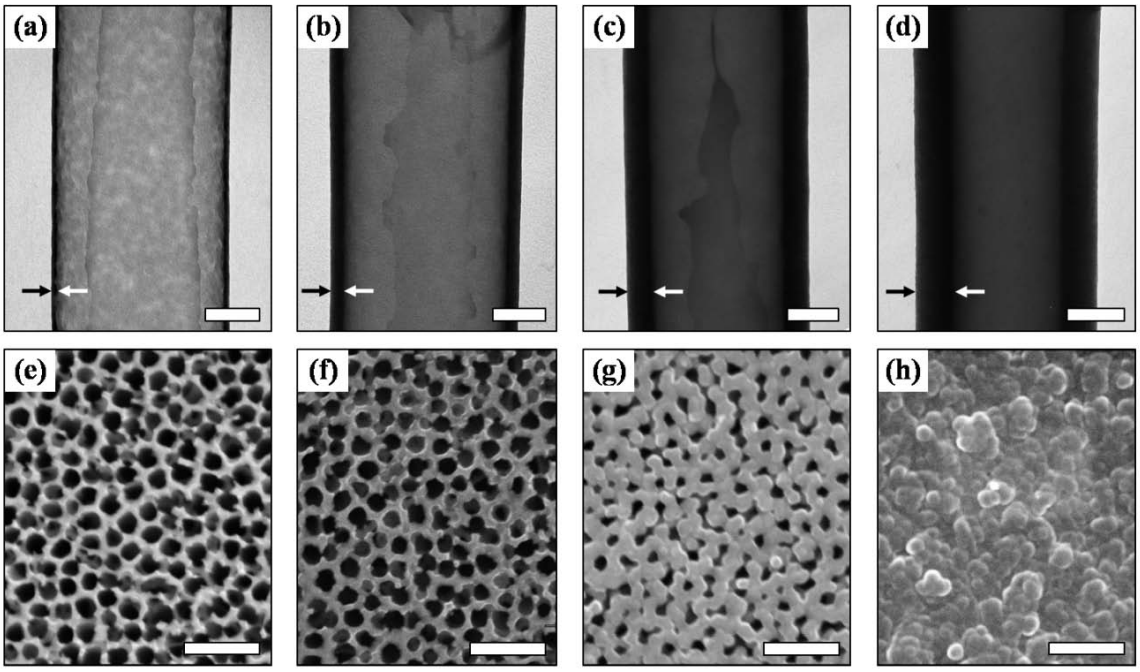

Figure 3.3: TEM micrographs of synthesized CNTs at 700 °C with 60 sccm of gas flow rate for (a) 2.5 hours, (b) 5 hours, (c) 7.5 hours and (d) 10 hours of deposition time (Scale bars: 100 nm). Arrows indicate CNT wall thickness. SEM micrographs of the surface of the AAO membrane after (e) 2.5 hours, (f) 5 hours, (g) 7.5 hours and (h) 10 hours of carbon deposition at 700°C with 60 sccm of gas flow rate (Scale bars: 1 μm).

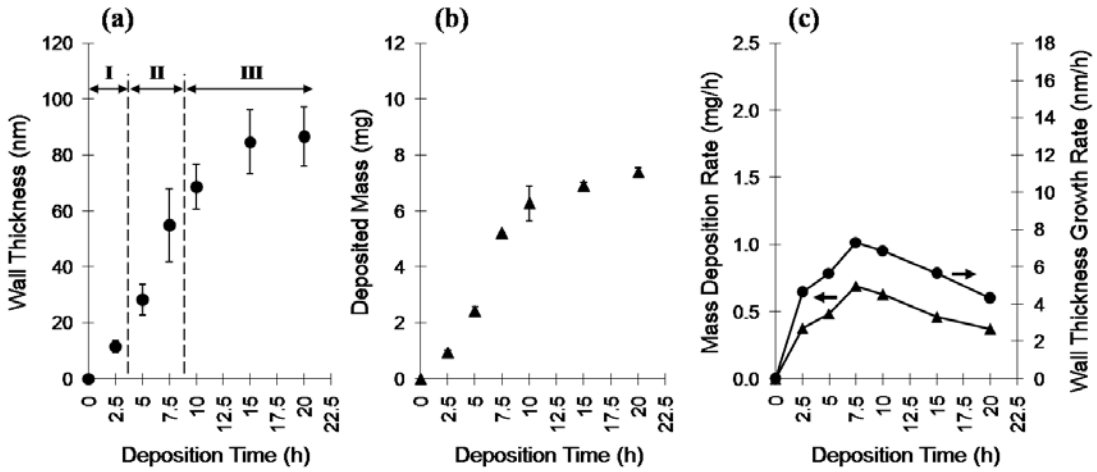

Figure 3.4: (a) CNT wall thickness and (b) deposited carbon mass as a function of deposition time. (c) Comparison between the mass deposition rate (left axis, triangles) and wall thickness growth rate (right axis, circles) as a function of deposition time.

3.2.2.2. Influence of Temperature

The mass of carbon deposited on the AAO membrane and the resultant CNT wall thickness was also measured as a function of furnace temperature. Since small changes in the temperature may change the reaction kinetics [208], the effect of temperature variation on CNT synthesis and structure was studied at different furnace temperatures of 675, 700, 750 and 800 °C. The lower temperature bound was chosen based on our experimental observations, where little, if any, carbon deposition occurred incrementally below 675 °C. The upper bound, on the other hand, was selected due to limitations experienced during the annealing process between the two quartz plates, where AAO membranes would fracture at temperatures above 800 °C.

Figure 3.5 shows representative TEM micrographs of CNTs (Fig. 3.5a-d) and SEM micrographs of the membrane surface (Fig. 3.5e-h) for furnace temperatures of 675, 700, 750, and 800 °C. As can be qualitatively seen in the TEM micrographs, CNT wall thickness increases as temperature increases. This is due to the fact that vapor deposition

reaction kinetics increase with temperature, causing faster deposition and resulting in tubes with thicker walls. These findings elucidate previous observations reporting that the overall carbon content deposited on the entire AAO template increases as CVD temperature increases [214, 215]. The SEM micrographs of the template surface show open pores at 675 and 700 °C, a combination of open and covered pores at 750 °C, and a thick layer of carbon covering the whole membrane surface at 800 °C.

Figure 3.6a indicates an approximate linear trend in deposited mass as a function of temperature as it increases from 0.6 to 2.4, 7.9, and 10.6 mg for 675, 700, 750, and 800 °C, respectively. However, this linear trend is not seen in Figure 3.6b for CNT wall thickness, where wall thickness increases from 12±2 nm at 675 °C to 28±5 nm at 700 °C, 80±17 nm at 750 °C, and 84±11 nm at 800 °C. A closer look at Figure 3.6c indicates that the variation of mass deposition rate between 700 to 750 °C, and 750 to 800 °C is almost negligible while there is a significant difference in wall thickness growth rate within the same temperature intervals. Supported by observations from SEM micrographs at 800 °C (Fig. 3.5h), the change in wall thickness growth rate is attributed to faster pore blockage by the carbon film deposited over the membrane outer surface. In other words, after 750 °C, carbon deposits on each side of the membrane starts to cover more of the pores on the outer surface, resulting in continued deposition of carbon on the membrane outer surfaces and less on the inside surfaces of the pores.

Variation of activation energy represents the existence of different deposition regimes [208, 227, 228]. For this, an Arrhenius plot of logarithm of wall thickness growth rate versus reciprocal temperature was generated for the studied temperature range and the activation energy between each temperature was calculated (Fig. 3.7). For the lower

temperature range of 675-700 °C, an activation energy of 262 kJ/mol was calculated, which is comparable to the reported values in other literature for a reaction-limited deposition regime in chemical vapor deposition processes using carbon precursors [229]. However, for the higher temperature range of 750-800 °C, activation energy decreases to 9 kJ/mol. This indicates that wall thickness growth is controlled by gas diffusion as a result of pores being covered by a carbon layer at higher temperatures, as shown in Fig. 3.5g-h. This carbon layer hinders the precursor gas from diffusing into the pores and decomposing to deposit carbon on the pore surface. Therefore, these results suggest a reaction-limited deposition regime for the lower temperature range and a diffusion-limited deposition regime for higher temperature range.

It should be noted that non-uniform carbon deposition has been found to occur when temperature is used to increase vapor deposition reaction kinetics [230]. Diffusion is considered to be a slow process; when the process temperature is raised to increase reaction kinetics and CVD reactions occur faster than diffusion, diffusion struggles to evenly distribute reactant species and maintain equilibrium throughout the process, resulting in non-uniform film thicknesses. In this study, non-uniformity at higher temperatures can be seen in the form of standard deviation in wall thicknesses from tube to tube. For instance, the standard deviation and standard error of the CNT wall thickness is 1.6 nm and 13 %, respectively, at 675 °C while they increases to 17.3 nm and 22 % at 750 °C. Non-uniformity was also observed when SEM micrographs of films deposited at lower temperatures (Fig. 3.5e, f) were compared to those of films deposited at higher temperatures (Fig. 3.5g, h). In particular, the random combination of open and covered

pores in Figure 3.5g shows the onset of non-uniform carbon deposition at higher temperatures.

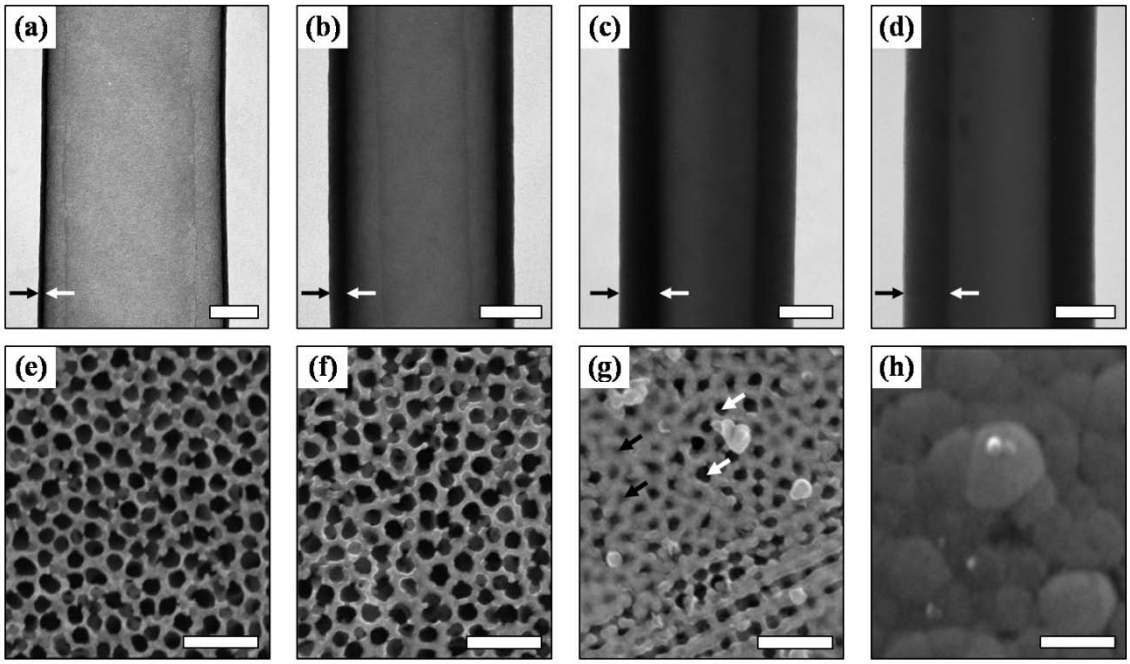

Figures 3.5: TEM micrographs of synthesized CNTs at (a) 675 °C, (b) 700 °C, (c) 750 °C, and (d) 800 °C with 60 sccm of gas flow rate for 5 hours (Scale bars: 100 nm). Arrows indicate CNT wall thickness. SEM micrographs of the surface of the AAO membrane after 5 hours of deposition with 60 sccm of gas flow rate at (e) 675 °C, (f) 700 °C, (g) 750 °C and (h) 800 °C (Scale bars: 1 μm). White arrows indicate observably open pores and black arrows indicate covered pores on membrane surface.

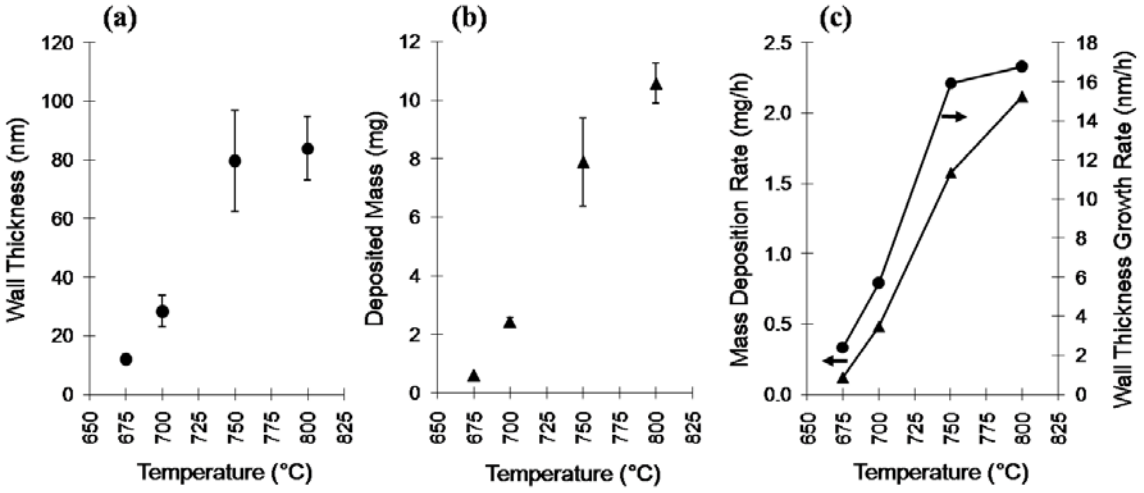

Figure 3.6: (a) CNT wall thickness and (b) deposited carbon mass as a function of temperature. (c) Comparison between the mass deposition rate (left axis, triangles) and wall thickness growth rate (right axis, circles) as a function of temperature.

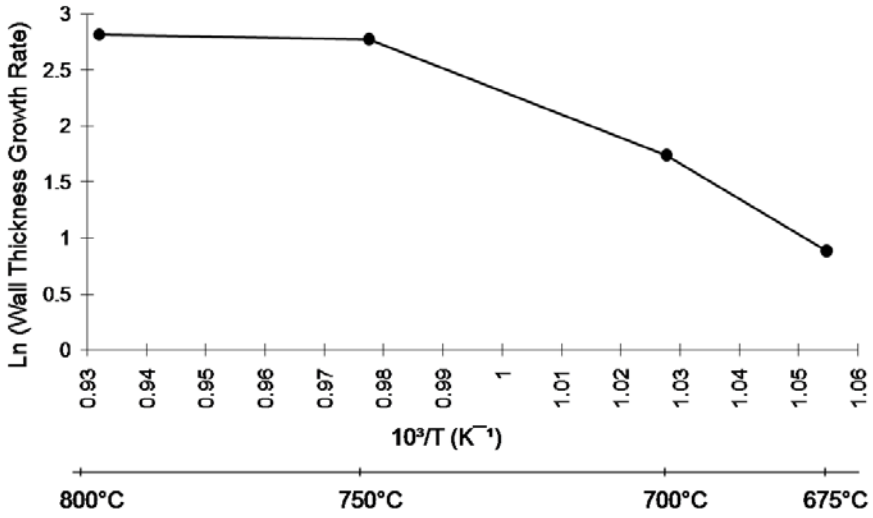

Figures 3.7: Arrhenius plot of the wall thickness growth rate, representing activation energies and alteration of deposition mechanism by temperature variation.

3.2.2.3. Influence of Precursor Gas Flow Rate

The overall mass of carbon deposited on the AAO membrane and the resultant CNT wall thickness was measured as a function of precursor gas flow rate. As mentioned earlier, the CVD process is a chemical reaction and the limitations of diffusion and reaction

kinetics can play an important role in resultant CNTs. Therefore, the flow rate of the precursor gas is yet another factor that can affect the geometrical and structural characteristics of the CNTs. The range of precursor flow rates was determined empirically. Difficulties in forming structurally intact CNTs when flow rates are below 20 sccm defined the lower bound while the formation of carbonaceous tar inside the reaction tube when flow rates exceeded 300 sccm defined the upper bound of the experiments. The observance of carbonaceous tar forming at high precursor gas flow rates was also reported independently in other literature [199].

Figure 3.8 shows representative TEM micrographs of CNTs (Fig. 3.8a-d) and SEM micrographs of the membrane surface (Fig. 3.8e-h) for 20, 40, 60, 80, 100, 200, and 300 sccm of 30 % ethylene in helium. Increasing the flow rate increases the wall thickness up to 80 sccm and then, due to lower mass deposition, the resultant wall thickness decreases. For CNTs manufactured with 20 sccm of gas flow rate, TEM micrographs reveal several dense carbon deposits randomly distributed along the length of each tube, indicating sporadic carbon nucleation amongst smooth CNT wall formation. These carbon deposits are not observed for flow rates in the 40-300 sccm range. However, for 300 sccm, as observed in TEM, the varied contrast in the CNT walls indicates a rough interior surface. Despite the variations of wall thickness and texture observed in TEM micrographs, SEM micrographs reveal that the pores of the template remained open for all of the conducted experiments.

The trend of wall thickness as a function of precursor gas flow rate is more clearly seen in Figure 3.9. As measured from TEM micrographs, CNT wall thicknesses were 18±2 nm for 20 sccm, 26±3 nm for 40 sccm, 28±5 nm for 60 sccm, 30±9 nm for 80 sccm,

28±8 nm for 100 sccm, 21±8 nm for 200 sccm and13±2 nm for 300 sccm of precursor gas flow rate. Similarly, the average deposited carbon mass was 1.3, 1.9, 2.4, 2.7, 2.5, 1.9, and 1 mg for 20, 40, 60, 80, 100, 200, and 300 sccm of gas flow rate, respectively. The effect of the gas flow rate on carbon deposition suggests two different deposition regimes: mass transport limitation and residence time limitation. For flow rates up to 80 sccm, mass transport limits deposition rate, where an increase in gas flow increases the availability of reactants resulting in increased carbon deposition (Region IV in Fig. 3.9a). At flow rates above 80 sccm, residence time limits deposition rate, where an increase in precursor gas flow further removes reactants from the template surface before thermal decomposition has occurred resulting in lower carbon deposition (Region V in Fig. 3.9a). A similar phenomenon has been seen in other CVD processes [199, 222].

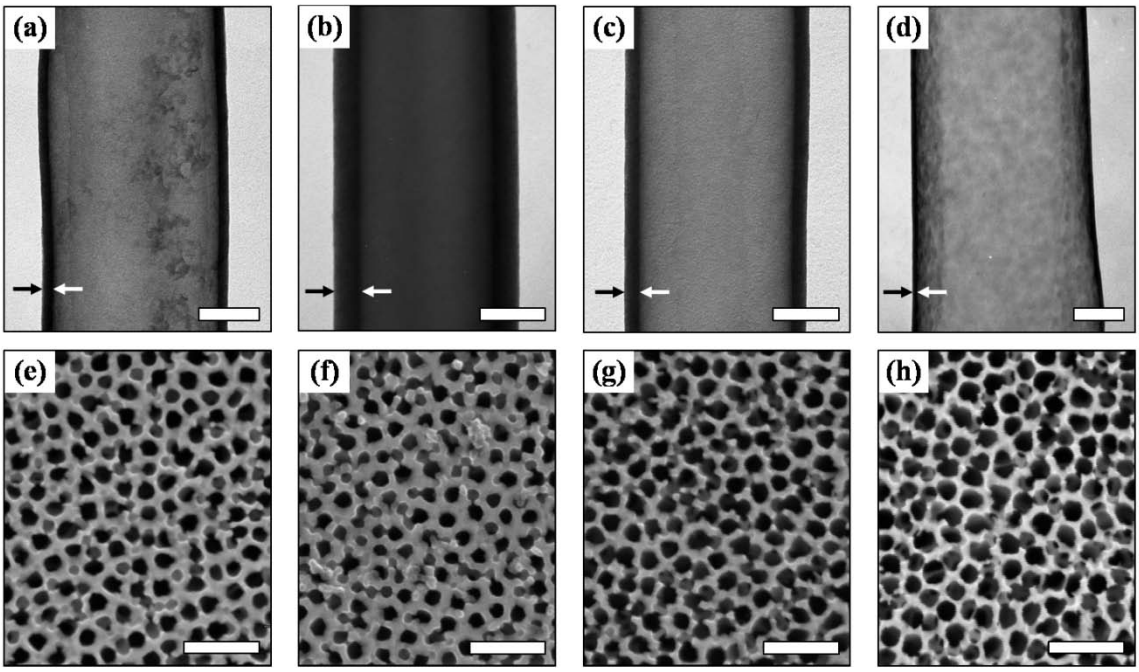

Figure 3.8: TEM micrographs of synthesized CNTs with (a) 20 sccm, (b) 80 sccm, (c) 100 sccm and (d) 300 sccm of the gas flow at 700 °C for 5 hours (Scale bars: 100 nm). Arrows indicate CNT wall thickness. SEM micrographs of the surface of the AAO membranes after 5 hours of deposition with (e) 20 sccm, (f) 80 sccm, (g) 100 sccm and (h) 300 sccm of gas flow rate at 700 °C (Scale bars: 1µm).

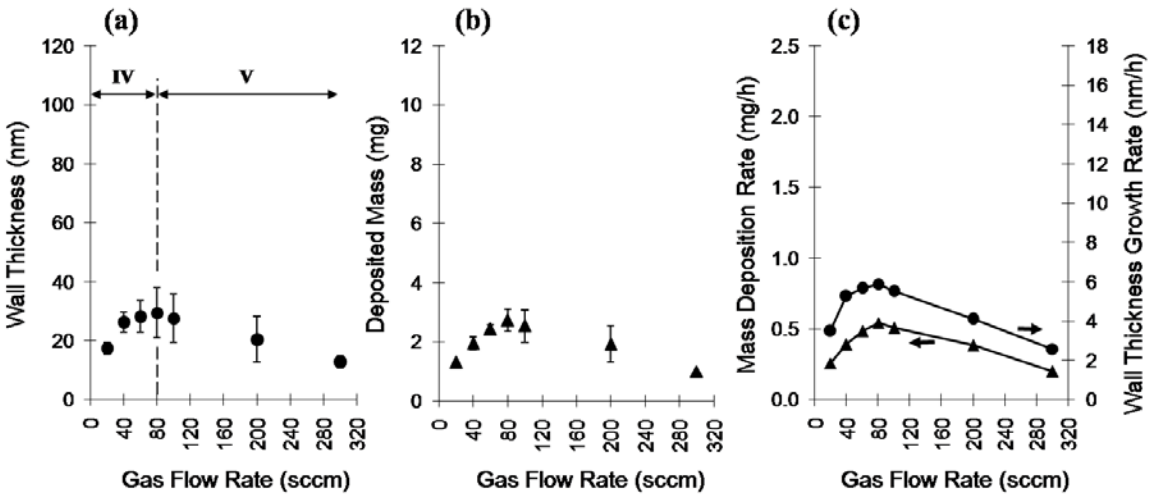

Figure 3.9: (a) CNT wall thickness and (b) deposited carbon mass as a function of gas flow rate. (c) Comparison between the mass deposition rate (left axis, triangles) and wall thickness growth rate (right axis, circles) as a function of gas flow rate.

3.2.2.4. Parametric Effects on Carbon Structure

Raman analysis shows that all CNTs are composed of dominantly amorphous carbon as representative for the used CVD process with a prominent D- and G-peak (Fig. 3.10) [231]. In particular, Raman spectra depicted in Figure 3.10 show that within one sample, both single CNTs (Fig. 3.10, Sample A) as well as CNT bundles (Fig. 3.10, Sample B) have within a narrow margin (peak position: ±1 1/cm, full-width at half maximum FWHM: ±10 1/cm) very comparable spectral features with well-defined D- and G-modes. The D-mode, located at around 1340 1/cm is a spectral feature strongly associated with structural disorder of carbon while the G-mode is the characteristic vibration for crystalline sp^2 hybridized carbon (E_{2g} symmetry) [232]. The featureless and broad peak between 2200 and 3100 1/cm is representative for overtones and combination modes and this result is, too, well in agreement with the presence of partially crystalline graphitic carbon [233].

We carried out a very systematic study of all the synthesis parameters and their impact on the structure of carbon as accessible by Raman spectroscopy. The results of this investigation are outlined in Table 3.2. Unlike the mass, tube thickness, and wall roughness, only very little spectral variation was found between all samples tested, indicating the tested synthesis conditions insignificantly affected the crystallinity of the CNTs within the studied range of parameters. Commonly, especially the synthesis temperature would be expected to impact carbon ordering (i.e., increase with higher temperature) [234]. Yet, in the current study, the temperature was only varied over a range of 125 °C; this is a small range compared to other studies where clear trends were only observed over large ranges of temperature (e.g., from 400 °C to 2400 °C [233], or 200 °C to 1200 °C [235]). Low crystallinity of CNTs manufactured inside the pores of AAO have also been reported for different synthesis parameters [214, 215].

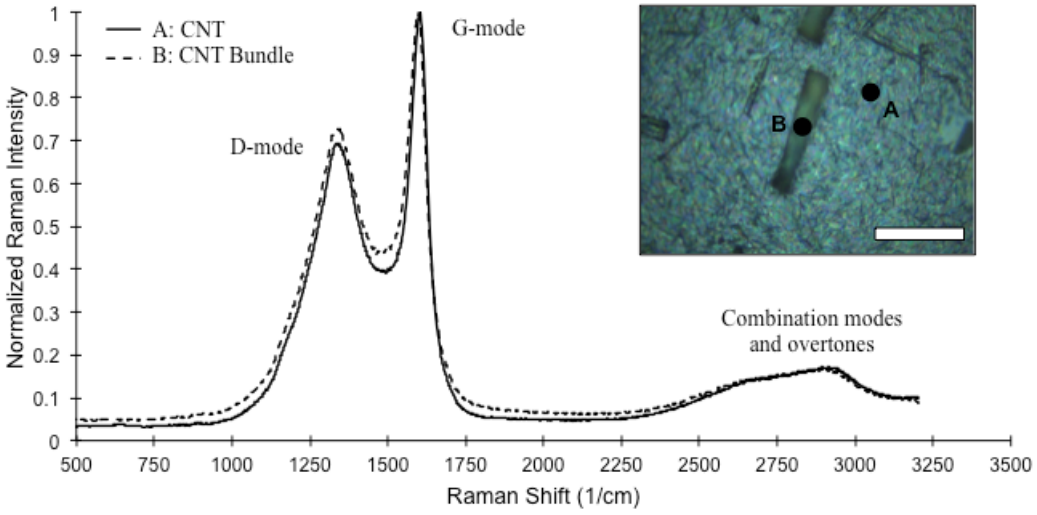

Figure 3.10: Raman spectrum of single and bundles of AAO-manufactured CNTs. Inset: Typical optical image of single CNT and CNT bundles (Scale bar: 50 µm).

Table 3.2: Overview of the results of Raman spectroscopy investigating the impact of synthesis parameters on the structure of CNTs.

		I_D/I_G Ratio	FHWM D-Mode ± Standard Deviation (cm^{-1})	FHWM G-Mode ± Standard Deviation (cm^{-1})	Peak Position D-Mode ± Standard Deviation (cm^{-1})	Peak Position G-Mode ± Standard Deviation (cm^{-1})
Deposition Time	Single CNT	2.23 ± 0.23	187.5 ± 7.9	60.6 ± 3.1	1344.0 ± 5.1	1601.9 ± 0.7
	CNT Bundle	2.36 ± 0.12	193.5 ± 3.1	63.0 ± 3.5	1342.2 ± 4.6	1599.1 ± 1.3
Temperature	Single CNT	2.13 ± 0.06	191.5 ± 3.1	60.3 ± 2.6	1341.6 ± 2.0	1601.3 ± 1.4
	CNT Bundle	2.27 ± 0.08	193.9 ± 3.7	62.0 ± 1.9	1339.7 ± 3.0	1598.1 ± 1.7
Gas Flow Rate	Single CNT	2.21 ± 0.08	191.9 ± 1.8	59.5 ± 0.9	1339.4 ± 1.0	1600.6 ± 0.8
	CNT Bundle	2.42 ± 0.14	195.6 ± 2.6	60.5 ± 1.3	1338.0 ± 1.0	1598.2 ± 1.0

3.2.3. Comparable Analysis of Parameters

The findings show that process parameters can be used to produce CNTs with similar or differing cross-sectional dimensions and other useful features as well as reveal reasons to select one parameter over another. As an example, thick-walled CNTs can be fabricated to improve mechanical robustness of the tubes for a particular application either by increasing (a) deposition time or (b) furnace temperature. However, in the second case, less precursor gas is consumed, making temperature a more economically viable parameter to use for commercialization than the deposition time. For instance, CNTs with average wall thicknesses of 80 nm can be fabricated at 750 °C after only 5 hours while 85 nm of average wall thickness is achievable at 700 °C after 15 hours of deposition. Moreover, a thicker carbon layer can be deposited over the outer surfaces of the template at higher temperature to facilitate CNT interfacing for subsequent device manufacturing. For instance, according to SEM micrographs of membrane cross-sections (Fig. 3.11), a 1 µm-thick carbon layer covers the membrane surface for the samples synthesized at 800 °C for 5 hours while, for samples synthesized at 700 °C for 20 hours, a 300 nm-thick carbon layer covers the membrane surface. It is worth noting that at 800 °C, the 1 µm

layer of carbon has around 50 µm layer of carbon soot on top, which needs to be removed before interfacing with CNT for any specific application.

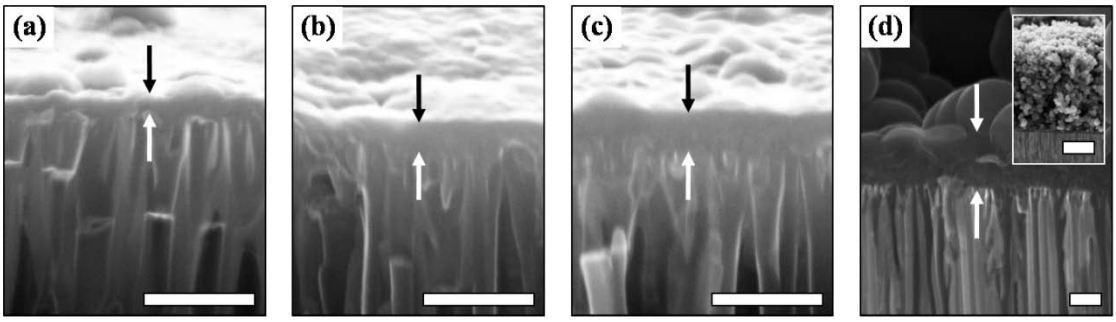

Figure 3.11: Cross-section SEM micrographs of templates after CNT synthesis at 700 °C for (a) 10 hours, (b) 15 hours, and (c) 20 hours, and after 5 hours of deposition at (d) 800 °C with 60 sccm of gas flow rate (Scale bars: 1 µm). Arrows indicate the carbon layer thickness. Inset: The carbon soot layer over the template surface after 5 hours of deposition at 800 °C with 60 sccm of gas flow rate (Scale bar: 25 µm).

The precursor gas flow rate can provide better control over the growth of CNT wall thickness than the temperature parameter since a small variation of temperature results in large alteration of CNTs wall thickness. For instance, below 80 sccm, a 20 sccm change in gas flow results in a 2 nm change in wall thickness. Better control over the internal tube diameter could find many useful applications such as filtering and desalinization. Additionally, CNTs with rough internal surfaces are achievable at flow rates higher than 80 sccm as determined by an increase in the wall thickness standard error from 28 % at 80 sccm to 37 % at 200 sccm. This unique feature may be potentially beneficial for applications requiring internal surface functionalization, such as nanotube-based nanofluidic sensing. Moreover, despite the variation of wall thickness brought on by adjusting the precursor gas flow rate, the pores remain open in all cases, providing open-access to membrane pores for micro-nanofluidic applications such as filtering, separation, and desalination.

It is worth noting that since the aforementioned parameters do not change the morphology of the fabricated tubes, the control of the geometrical and morphological features of the CNTs can be uncoupled. In other words, CNTs with desirable geometrical features can be produced with almost the same morphology and then, if desired, other processes, such as high temperature annealing, can be utilized to modify the morphological characteristics of the tubes. In this line, we also have demonstrated that the structure of carbon remains the same, that is, there is no significant change in carbon ordering in any of the samples within the studied range of parameters as seen from Raman spectroscopy.

CHAPTER 4

Vertically Aligned Array of Carbon Nanotubes

Vertical arrays of nanowires and nanotubes have recently been used in an increasing number of applications. These applications almost invariably rely on the physical features of these nanoelements, necessitating a better control over their geometrical properties to improve their performance. In this chapter, the manufacturing process of vertically aligned, hollow CNT arrays of different tube diameters, spacing, and length is presented, as needed for their intended application. A template-based manufacturing method was employed to form CNTs inside the pores of commercially available AAO using CVD. After removing the carbon layer from the surface of the membrane with oxygen plasma, the membrane surface was selectively removed by either reactive ion etching (RIE), wet chemical etching, or a combination of ion milling and wet etching to expose the CNTs embedded in the membrane. The results show that to reach longer individually addressable exposed CNTs, dry etching processes like RIE are more promising. The work provides a scalable and reliable manufacturing recipe for a CNT-based array device that can be used for various sensing and also biological and biomedical applications. Moreover, the performance of the CNT array on fluid transportation is characterized. To

this end, two different fluid transportation mechanisms, pressure driven and gradient driven, were utilized to transport fluid through arrays of CNTs.

4.1. Fabrication of Vertically Aligned CNT Arrays

In recent years, growing interest towards creating novel nanoscale devices for elucidating cellular behavior has enabled significant advances in biomolecular science, biomedical applications and new approaches to clinical diagnostics and therapeutics [16, 163, 236]. Of particular interest are vertically aligned arrays of nanowires or nanotubes for interfacing with living cells and tissues [151, 237]. Nanoarray devices have been employed to measure the force adherent cells exert on a surface [238] and as various biomolecular and chemical sensors [239, 240]. One of the unique features of nanoarrays is their ability to access the cell's cytosol [241-243] resulting in broad biomedical applications. Such applications include utilizing nanoarrays to observe intracellular biochemical activity [244], measure intracellular/extracellular signals [245], and deliver drugs, nanoparticles and biomolecules, such as quantum dots, nucleic acids and proteins, directly into cells [158, 161, 166, 246, 247].

The ever growing demand for vertically aligned nanostructured arrays in biomedical applications necessitates the ability to control the geometrical features of the nanostructures, such as length, diameter, orientation and packing density, since these features play a crucial role in the performance of the arrays. As biological and chemical sensors, the sensitivity of array electrode-based sensors can be increased by exposing more of the nanostructure in the array thus increasing the available surface area for

detection [170, 248]. In applications requiring cell-array interfacing, such as cell proliferation, differentiation, adhesion and migration [249, 250], in situ study of intracellular molecular processes [244] and efficient intracellular delivery [166, 251, 252] geometrical features influence how well the nanostructures interact with the cell membrane. Studies have found that transfection efficiency and intracellular access depend on the length of the nanostructures in the array [166, 253]. Optimizing the length and spacing of arrayed nanostructures promotes cell adhesion onto its surface and enables the nanostructures to penetrate the membrane without causing detrimental effects [243].

As will be discussed in next chapters, cells adhere well to tightly-packed arrays of short lengths of exposed CNTs, which promotes highly efficient delivery of macromolecules, quantum dots and plasmid DNA into tens of thousands of adherent cells simultaneously. As shown in Figure 4.1, these CNT-based array devices are manufactured using a three-step process: First, an AAO porous membrane is selected to serve as a sacrificial template. Next, CNTs are formed inside the AAO membrane using established template-based CVD processes discussed in chapter 3. Finally, carbon is removed from one side of the AAO membrane using oxygen plasma and then, the tips of the CNTs embedded in the AAO membrane are exposed using selective etching techniques. The resultant CNT-based array device consists of millions of vertically aligned, hollow and conductive CNTs protruding from the surface of a sacrificial membrane. The porous AAO membrane dictates the outer diameter and spacing between the CNTs, whereas the selective etching process controls the length of the exposed CNT tip. Dozens of these array devices can be manufactured without assembly in a single run, making the process amenable for further scale-up.

Here, the development and fabrication of the CNT-based array device is presented and several approaches are described to expose and control the length of the CNTs protruding from the device surface. Commercially available AAO membranes of varying pore sizes and interpore distances were utilized as the sacrificial template to produce CNT-based array devices. The CNT tips were exposed using either RIE, wet chemical etching, or a combination of ion milling and wet etching. The effect of etching process and associated process parameters on the exposed length of the CNTs are discussed and compared. Ultimately, this process strategy serves as a guide for manufacturing vertically aligned, hollow CNT arrays of different tube diameters, spacing, and length as needed for their intended application.

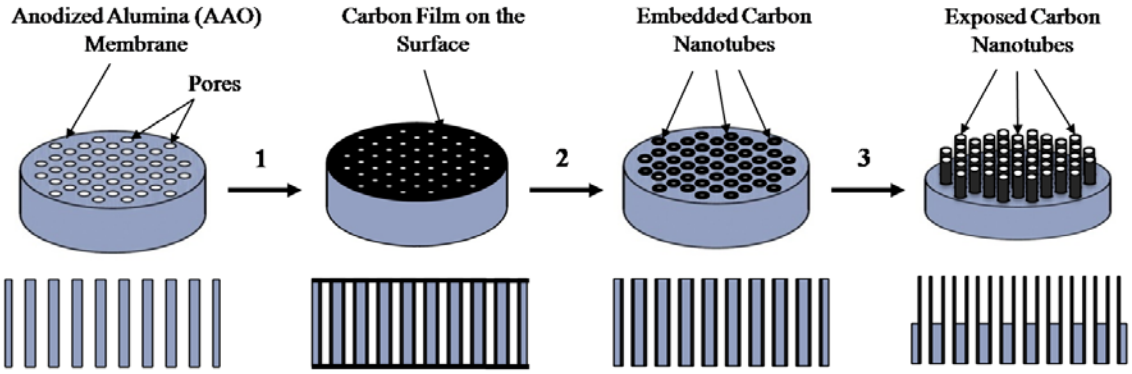

Figure 4.1: Schematic illustration of the CNT array device fabrication procedure. Fabrication process shows (1) carbon deposition by chemical vapor deposition, (2) removing the amorphous carbon layer by oxygen plasma from the surface, (3) exposing the CNT tips by either reactive ion etching, wet chemical etching, or a combination of ion milling and wet etching process.

4.1.1. Experimental Procedure

4.1.1.1. Template Preparation

Commercially available AAO membranes were used as a sacrificial template for carbon deposition. AAO membranes with 100 nm (Synkera UniKera, Cat. No.: SM-100-50-13, nominal pore diameter: 100±10 nm, nominal thickness: 50±1 µm), 150 nm (Synkera UniKera, Cat. No.: SM-150-50-13, nominal pore diameter: 150±10 nm, nominal thickness: 50±1 µm), and 200 nm nominal pore diameter (Whatman Anodisc 13, Cat. No.: 6809-7023, nominal pore diameter: 200 nm, nominal thickness: 60 µm) were utilized. To prevent curling of the membranes during the CVD process [97, 171], they were annealed 30 °C above synthesis temperature for 4 hours between two quartz plates before carbon deposition.

4.1.1.2. Carbon Deposition

Carbon film was deposited inside the pores of AAO templates to form CNTs using previously reported methods in chapter 3 [97]. In brief, AAO membranes were placed upright in a custom quartz boat and positioned in the middle of a three-stage tube furnace (Carbolite, TZF17/600, inner tube diameter: 7 cm, tube length: 152 cm). The reactor temperature was slowly increased to 700 °C under 100 sccm of argon gas flow. After temperature stabilization, 60 sccm of 30/70 (vol%/vol%) ethylene/helium gas was flown through the reactor tube for 5 hours to deposit carbon film on all surfaces of the AAO membrane. The furnace was then slowly ramped down to room temperature under 100 sccm of argon flow.

4.1.1.3. CNT Tip Exposure

It should be noted that the deposited carbon layer over the AAO template after CVD was removed by oxygen plasma at 250 W, 300 mTorr for 3.75 minutes under 100 sccm of oxygen flow (LAM 490) before every etching processes.

Reactive Ion Etching

Reactive Ion Etching (RIE, LAM 4600 Etcher) was employed to selectively etch AAO templates in order to partially expose the tips of embedded CNTs. Etching occurred using a combination of boron trichloride (BCl_3) and chlorine (Cl_2) gases (100 sccm combined flow) under constant chamber pressure (150 mTorr) at different RF power (200-400 W) for various durations (approximately 2-5.5 hours).

The effect of etching time, RF power and gas combination on CNT exposure length were studied in an orthogonal manor; in each set of experiments, one parameter was changed while the others remained unchanged. Orthogonal experiments were conducted for 100%/0%, 75%/25%, 50%/50%, 257%/75% and 0%/100% of BCl_3 and Cl_2 gases, respectively, RF power of 200, 300 and 400 W, and up to 315 minutes of etching time at 150 mTorr chamber pressure.

Wet Chemical Etching

Wet chemical etching using various acids and bases was employed to partially expose the CNTs. To this end, 0.5 M aqueous solution of sulfuric acid (H_2SO_4), hydrochloric acid

(HCl), phosphoric acid (H_3PO_4), acetic acid (CH_3COOH), formic acid (HCOOH) and also sodium hydroxide (NaOH) and potassium hydroxide (KOH) were utilized to dissolve the template at room temperature for 15 minutes. The samples were then rinsed for 15 minutes with distilled water and dried overnight before imaging.

The effect of etching time on CNT exposed length was studied for all three AAO membranes. Carbon deposited AAO membranes were submerged in 1 M aqueous NaOH solution for 4, 6, 8, 10, 12, 14 and 18 minutes at room temperature. The samples were then rinsed for 15 minutes with distilled water and dried overnight before imaging. The exposed length of the CNTs was measured using SEM micrograph.

The AAO membrane (Whatman 200 nm) etch rate was determined as a function of NaOH temperature (21 °C-90 °C), NaOH concentration (0.3, 1 and 1.5 M) and time. A full bare AAO membrane disc with 13 mm nominal diameter was fully dissolved in various concentrations and temperatures of aqueous NaOH solution in a heated reflux system, and the dissolution time was recorded.

Ion Milling and Wet Chemical Etching

The CNTs were also exposed by a combination of ion milling and wet etching processes. After CVD, the template surface was etched by ion milling at 800 V, 45 degree argon ion shower angle for 2 hours (AJA Ion Mill). The membranes were then etched in 1 M aqueous NaOH solution for 9 and 15 minutes to expose the tips. The samples were then rinsed for 15 minutes with distilled water and dried overnight before imaging.

4.1.1.4. Electron Microscopy

The exposed length of CNT tips, the surface morphology and the integrity of individual CNTs after each exposing process were examined and measured using scanning electron microscopy (SEM, Zeiss Auriga; 20 kV acceleration voltage). The samples were characterized without sputter coating.

4.1.2. Results and Discussion

4.1.2.1. CNT Tip Exposure

The AAO membrane was selectively removed to expose the tips of CNTs embedded inside the pores of the sacrificial template. Three selective etching approaches were investigated: (1) RIE, (2) wet etching, and (3) a combination of ion milling and wet etching. Table 4.1 summarizes the experiments conducted to expose the CNT tips, the associated parameter settings and the resultant average exposed length of the CNTs.

Table 4.1: Overview of experiments and measurements to partially expose the CNT tips

Type of the Process	Parameter	AAO Template	Etching Time (min)	RF Power (W)	Gas Combination (BCl3% / Cl2%)	Gas Flow Rate (sccm)	Chemical Etchant	CNT Exposed Length ± Standard Deviation (nm)
Reactive Ion Etching	Effect of the Etching Time	Whatman 200 nm	135	400	100% / 0%	100	NA	152 ± 77
			150					113 ± 26
			180					176 ± 34
			195					177 ± 44
			225					293 ± 97
			270					314 ± 115
			315					389 ± 169
		Synkera 150 nm	135	400	100% / 0%	100	NA	48 ± 26
			195					81 ± 20
			225					186 ± 52
	Effect of the RF Power	Whatman 200 nm	150	200	100% / 0%	100	NA	0
				300				0
				400				113 ± 26
	Effect of the Gas Mixture	Whatman 200 nm	150	400	0% / 100%	100	NA	0
					25% / 75%			0
					50% / 50%			0
					75% / 25%			0
					100% / 0%			113 ± 26
Wet Chemical Etching	Effect of the Etching Time	Whatman 200 nm	4	NA	NA	NA	1M NaOH	0
			8					0
			10					42 ± 12
			14					153 ± 22
			16					208 ± 46
		Synkera 150 nm	4	NA	NA	NA	1M NaOH	0
			6					0
			8					73 ± 21
			10					196 ± 32
			12					238 ± 89
			14					645 ± 123
		Synkera 100 nm	4	NA	NA	NA	1M NaOH	0
			6					0
			8					43 ± 15
			10					85 ± 33
			12					108 ± 25
			14					118 ± 44
			18					167 ± 56
Wet Chemical Etching after Ion Milling	Effect of the Etching Time	Whatman 200 nm	9	NA	NA	NA	1M NaOH	100 ± 27
			15					183 ± 48

4.1.2.2. Reactive Ion Etching

There are several parameters that can affect the etch rate of AAO membranes using RIE, including gas combination, gas flow rate, chamber pressure, RF power and etching time. Among these parameters, etching time, RF power and gas combination were identified in preliminary experiments as the most influential on AAO etch rate and were therefore chosen to study how they affected CNT exposure. The other settings were set based on the limitations of the equipment and preliminary experiments.

For the baseline RIE process (400 W, 100% BCl_3 at 100 sccm, 150 mTorr), the exposed CNT length was measured as a function of etching time for two different membranes, as shown in Figure 4.2. The results show that for Whatman AAO (200 nm pore diameter), CNTs are exposed at lengths of 152±77 nm, 113±26 nm, 176±34 nm, 177±44 nm, 293±97 nm, 314±115 nm and 389±169 nm from the AAO surface after 135, 150, 180, 195, 225, 270 and 315 minutes of RIE, respectively. For Synkera AAO (150 nm pore diameter), CNTs are exposed at lengths of 48±26 nm, 81±20 nm and 186±52 nm after 135, 195 and 225 minutes of RIE, respectively. For both membranes, CNT exposure length trends approximately linear as a function of time. However, the lower etch rate of the Synkera membrane suggests a more resistant crystalline structure to RIE etching due to their manufacturing process. For both membranes, the measured standard deviation increases as time increases, indicating a less planer CNT tip surface at longer etching times. This can be due to the nature of the RIE process in which a combination of physical and chemical etching reduces the selectivity of the results. Therefore, the CNTs will be etched but at a slower rate compared to aluminum oxide and the longer they are exposed to the plasma, the less uniform they will become.

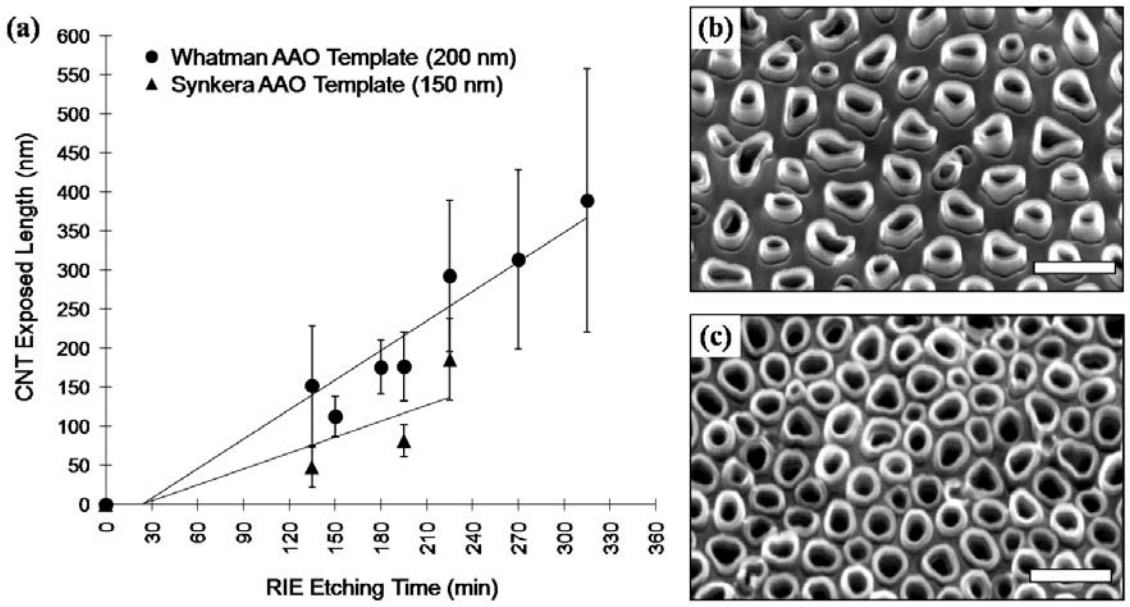

Figure 4.2: Effect of RIE etching time on CNT exposure. (a) CNT exposed length as a function of RIE etching time for Whatman (200 nm pore diameter, solid circle) and Synkera (150 nm pore diameter, solid triangle). SEM micrographs (35° tilt) of embedded exposed CNTs after 195 minutes of etching under 100 sccm of 100% BCl_3 at 400 W of RF power and 150 mTorr for (b) Whatman and (c) Synkera AAO templates (Scale bars: 500 nm).

The effect of RF power on the exposure of the CNT tips was also investigated. To this end, CNT-embedded Whatman AAO templates were etched at 200, 300 and 400 W under 100 sccm of 100% BCl_3 gas flow at 150 mTorr for 150 minutes. As illustrated in Figure 4.3, although increasing the RF power increases the AAO etch rate, which matches our expectation and also other studies [254, 255], no exposed CNTs can be measured at 200 and 300 W (Fig. 4.3a, b). However, CNTs are exposed 113±26 nm from the AAO surface at 400 W after 150 minutes (Fig. 4.3c). Note that the variation of CNT packing density in Figures 4.3a-c is due to the existence of branch-shaped structure of the pores on top of the Whatman AAO templates (Fig. 3.1a-i) which is completely etched away after 150 minutes of RIE at 400 W.

Combining BCl_3 and Cl_2 gases have been reported to etch aluminum oxide [254, 256-258]. Therefore, the effect of gas mixture on the CNT exposed length was studied. The SEM micrographs of the CNT embedded AAO membranes after 150 minutes of RIE are also presented in Figure 4.3. The membranes were etched with 50%/50% and 75%/25% of BCl_3/Cl_2 gases with total gas flow rate of 100 sccm at 400 W and 150 mTorr of chamber pressure (data not shown for higher percentage of chlorine gas). Although introduction of chlorine gas to the plasma can increase the AAO etch rate [254, 259], the results show that it also increases the carbon etch rate, such that the CNT tip exposure cannot be achieved (Fig. 4.3d, e). Therefore, to partially remove the AAO templates, 100% BCl_3 gas at 100 sccm of flow rate and 400 W of power was selected.

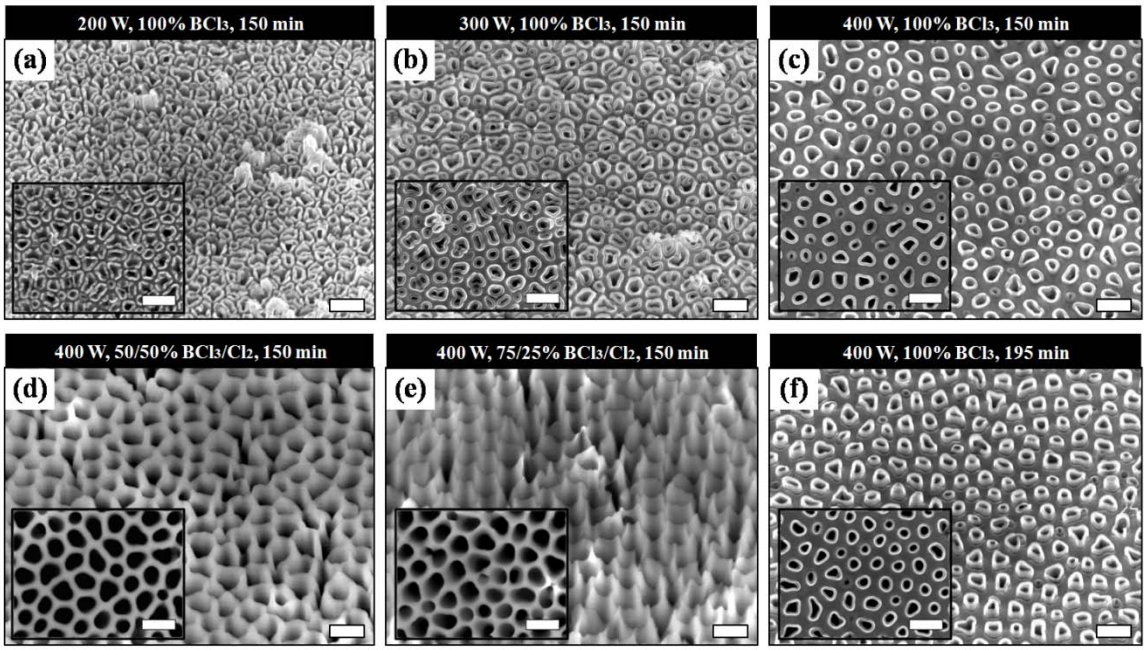

Figure 4.3: SEM micrographs of CNT embedded Whatman AAO membranes at 35° tilt, showing the effect of RF power, gas mixture and etching time on CNT exposure after RIE. AAO membranes etched under 100 sccm of 100% BCl_3 at (a) 200 W, (b) 300 W and (c) 400 W of RF power and 150 mTorr for 150 minutes and (f) 195 minutes. Also, AAO membranes etched for 150 minutes by adding (d) 50% and (e) 25% of Cl_2 gas to the mixture with total flow rate of 100 sccm, at 400 W of RF power and 150 mTorr. Insets: top view SEM micrographs of each parameter setting (Scale bars: 500 nm).

4.1.2.3. Wet Chemical Etching

To selectively remove the AAO templates and expose the CNT tips, wet etching processes were also utilized. The carbon deposited templates were first submerged in 0.5 M aqueous solution of 5 different acids (sulfuric acid (H_2SO_4), hydrochloric acid (HCl), phosphoric acid (H_3PO_4), acetic acid (CH_3COOH), formic acid (HCOOH)) and 2 bases (sodium hydroxide (NaOH) and potassium hydroxide (KOH)) for 15 minutes at room temperature to elucidate proper etchant. The SEM micrographs in Figure 4.4 show that the CNT tips are not visible after etching with acids (Fig. 4.4a-e). However, CNTs are exposed after etching with two bases (Fig. 4.4f, g). This indicates that only NaOH and KOH can etch the AAO templates in this relatively short time window. This is in agreement with the results from other studies [256, 260, 261].

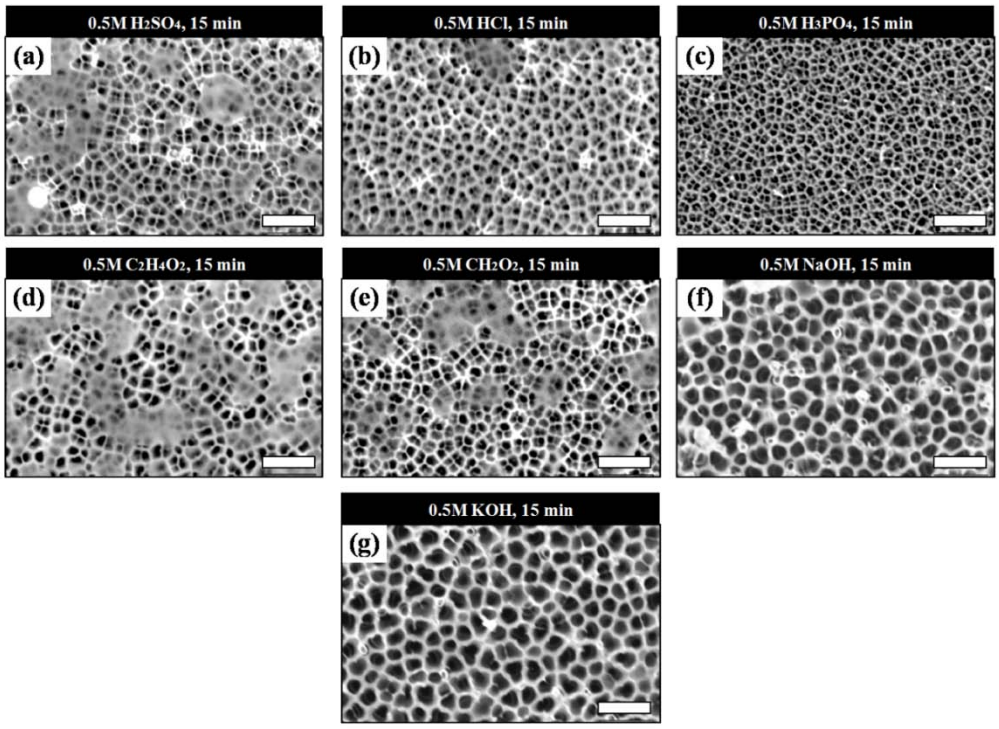

Figure 4.4: Effect of the type of wet chemical etchant on CNT exposure. SEM micrographs of CNT embedded Whatman AAO membranes after 15 minutes of etching in 0.5 M aqueous solution of (a) sulfuric acid, (b) hydrochloric acid, (c) phosphoric acid, (d) acetic acid, (e) formic acid, (f) sodium hydroxide and (g) potassium hydroxide at room temperature (Scale bars: 1 µm).

The effect of etching time on CNT tip exposure was studied using 1 M aqueous NaOH solution for all three membranes (Fig. 4.5b-j). As illustrated in Figure 4.5a, increasing the etching time, increases the CNT exposed length. However, the Synkera 150 nm AAO membrane shows a steeper trend compared to the Whatman membrane. Recalling the pore structure for Whatman and Synkera AAO membranes (Fig. 3.1), to expose the CNT tips using pure wet chemical etching, the Whatman membrane should be submerged in the etchant to first remove the 1 μm deep branch structure. Therefore, it takes longer to expose CNTs from the Wahtman AAO membrane compared to Synkera. Moreover, increased variability (standard deviation) at longer etching time indicates less uniform AAO membrane etching due to the isotropic nature of wet etching process. A comparison between the exposed CNTs after RIE (Fig. 4.3f) and wet etching with 1 M aqueous NaOH solution (Fig. 4.5d, g, j) indicates that the exposed CNTs are aggregated into bundles after being wet etched for longer than 14 minutes. This is likely due to the widening of the AAO pores during the wet etching step, which reduces the support of the AAO template for the exposed CNTs. Therefore, the nonuniform etching of the AAO templates, the Van der Waals attraction between the CNTs, and the surface tension of the wet solution during evaporation can cause lateral adhesion of the CNTs after exposure (Fig. 4.5a-inset). Similar results have been observed elsewhere [172, 173]. This suggests that to reach longer individually addressable exposed CNTs, dry etching processes like RIE are more promising.

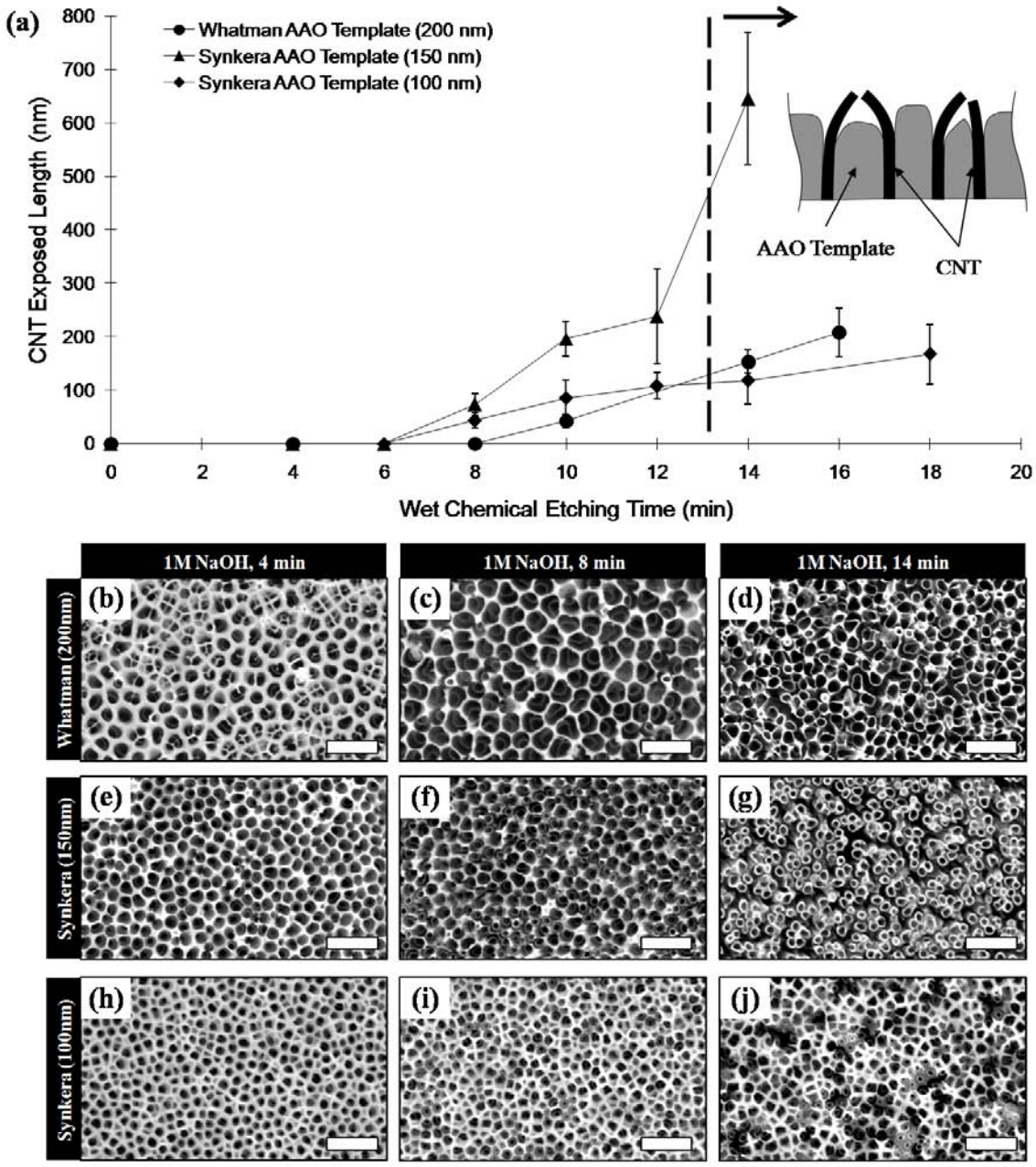

Figure 4.5: Effect of wet chemical etching time on CNT exposure. (a) CNT exposed length as a function of etching time in 1 M aqueous NaOH solution at room temperature for Whatman (200 nm pore diameter, solid circle), Synkera (150 nm pore diameter, solid triangle) and Synkera (100 nm pore diameter, solid diamond). Inset: The schematic of the lateral adhesion of CNTs after long wet etching due to pore widening and the loss of support from the etched AAO template. SEM micrographs of CNT embedded AAO membranes after wet chemical etching in 1 M aqueous NaOH solution for (b, e, h) 4, (c, f, i) 8 and (d, g, j) 14 minutes for (b-d) Whatman 200 nm, (e-g) Synkera 150 nm and (h-j) Synkera 100 nm AAO membranes (Scale bars: 1 μm).

The etch rate of Whatman AAO membranes in aqueous NaOH solution was studied to elucidate the effect of temperature, etching time and solution concentration on their etch rate. To this end, the required etching time was recorded for three different solution concentrations and at a range of temperatures from 21 °C (room temperature) to 90 °C. The experiment was conducted using AAO membranes without embedded CNTs to understand the etch rate and influence of aforementioned parameters. Determination of etching time was based on dissolution of a full AAO disc with 13 mm of nominal diameter. Figure 4.6 indicates the etching time of an AAO template (before carbon deposition) as a function of temperature for three solution concentrations of 0.3, 1 and 1.5 M. As can be expected, increasing the temperature and NaOH molarity increases the etching rate. The etch rates are almost 2 times faster or slower for 1.5M and 0.3M solution, respectively, in comparison to the 1M solution at room temperature. However, etching rate exponentially decays as temperature increases. Some, but not all, experiments were repeated to screen for reproducibility which have been indicated with error bars in Figure 4.6. For those repeated, good reproducibility were observed within the range of 2% to 13% error. For a given temperature and solution concentration, the approximate etch rate was determined from the experimental data assuming a linear etching mechanism. For instance, at room temperature and for 1M solution, an average membrane (58 μm thick) will be completely etched in around 22 minutes or at an approximate etch rate of 2.64 μm/min.

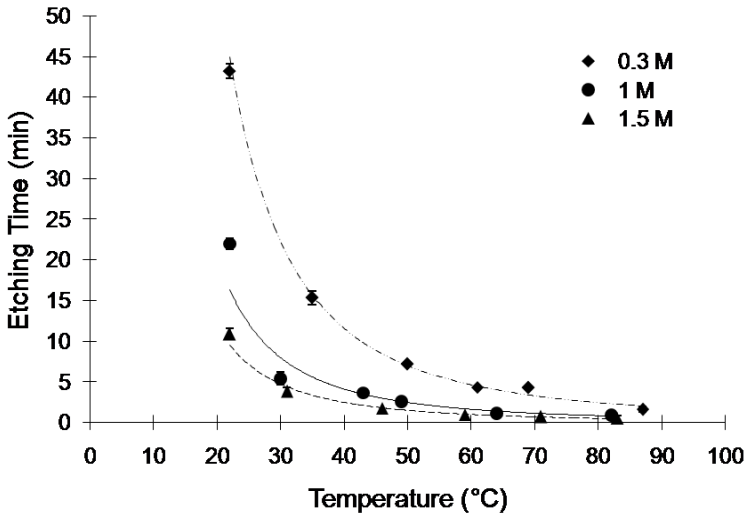

Figure 4.6: Effect of temperature and molarity on etch rate of a full AAO membrane disc.

4.1.2.4. Ion Milling and Wet Chemical Etching

To create individually addressable CNTs protruded from the AAO surface, a combination of ion milling and wet etching was followed. Note that there is a branch shaped structure with a depth of around 1 μm on top of the Whatman AAO template (Fig. 3.1a-i) that needs to be removed before CNT exposure. To this end, the surface of carbon deposited AAO templates were first etched away for 2 hours using ion milling and the CNTs were then exposed by wet etching in aqueous NaOH solution. Figure 4.7 shows the embedded CNTs after ion milling process, and also after ion milling followed by 9 and 15 minutes of wet etching with 1M aqueous NaOH solution, resulting in exposed CNTs of 100±27 nm and 183±48 nm, respectively. Despite the fact that ion milling removes a layer from the top surface of AAO template and provides a clean surface for wet etching, the surface has a non-planar morphology. Exposing the CNTs with wet etching after ion milling carries the same pore widening problem observed from wet etching alone, which caused

the CNTs to lose their support from the template and adhere to each other after a certain point, resulting in less controllability over the length of the exposed CNTs.

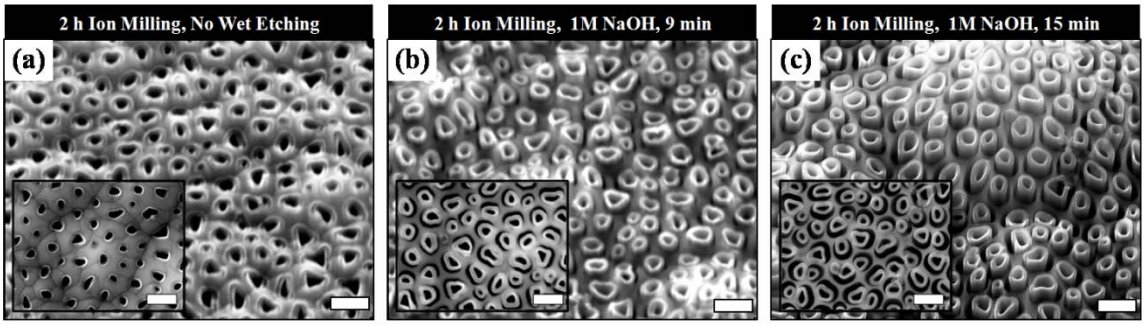

Figure 4.7: SEM micrographs (35° tilted view) of CNT embedded Whatman AAO membranes after (a) 2 hours of ion milling, and 2 hours of ion milling followed by (b) 9 minutes and (c) 15 minutes of wet etching using 1 M aqueous NaOH solution at room temperature. Insets: top view SEM micrograph of the same parameter setting (Scale bars: 500 nm).

4.1.3. Conclusion

Vertically aligned, hollow arrays of CNTs can be produced using a three-step template-based nanomanufacturing process. Carbon was deposited inside the pores of AAO templates using CVD to form CNTs. Three different etching processes were explored to expose the CNT tips by selectively removing the AAO template: RIE using BCl_3 and Cl_2 gases, wet chemical etching and ion milling. The results indicate that in RIE process, adding the chlorine gas to the combination expedites the carbon etch rate compare to AAO, preventing the CNT exposure. Moreover, increasing the RF power and etching time increase the CNT exposed length. A comparison of several chemical etchants revealed that the two bases, NaOH and KOH, could selectively etch the AAO templates in a relatively short time period. However, creating individually addressable CNTs using only wet etching is challenging due to formation of CNT bundles after etching. This could be due to the loss of support from the AAO templates and Van der Waals attraction

forces between CNTs. On the other hand, a combination of ion milling and wet etching served as a hybrid method to expose CNTs but with a non-planar surface morphology. Therefore, the RIE process is a more suitable method to fabricate individually addressable CNTs. Note that the main intend of these experiments were to evaluate the sensitivity of the manufacturing process of the CNT array device with respect to each process parameter, in a try and error fashion. More comprehensive design of an experiment is necessary as a future work to optimize the manufacturing process. The final outcome of this work provides a scalable and reliable manufacturing guideline for a CNT-based array device that can be used for various sensing, biological and biomedical applications.

4.2. Fluidic Characterization of Array of CNTs

To apply the CNT array platform for intracellular transfection and delivery, the flow behavior inside the channels plays an important role in device performance. To this end, two types of fluid transportation can be conducted: fluid flow due to pressure gradient and fluid flow due to concentration gradient. In the former case, the relationship between the required pressure and the flow rate is of important interest. In the latter case, the required time for diffusion of species through the CNT array needs to be investigated. Experiments conducted to characterize the fluidic performance of the device in both cases.

4.2.1. Experimental Procedure

4.2.1.1. Pressure Driven Flow

Fluid flow characteristics were investigated using a custom experimental setup capable of handling fluid pressures up to 60 psi. A syringe pump with 60 mL capacity and Luer-Lok fitting was used to drive water through the membrane using a programmable micro-injector device (World Precision Instruments, ALADDIN-1000). The CNT membrane was mounted in a commercially available stainless steel filter holder (Whatman, 1980001). A pressure transducer (Omega, PX409-500G10V) was connected between the syringe pump and the filter holder via a union tee. PTFE tape was applied to the pressure sensor threads to ensure a tight seal (Appendix, Fig. S6). The fluid pressure upstream of the membrane was monitored as a function of flow rate. A series of pressure measurements involving a minimum of six different CNT membranes were obtained for various nominal flow rates (0.3, 0.5, 0.7 and 1 mL/min). Volumetric flow rate was measured by weighing the exiting fluid every minute for 20 minutes. All experiments were conducted at room temperature (22 °C). The results were then compared to theoretical estimations from classical continuum fluid mechanics.

Note that for this experiment, CNTs were synthesized inside the pores of Whatman AAO membranes using the discussed process in chapter 3. Briefly, AAO membranes were annealed in air at 700 °C for 4 hours and placed in a 3-stage CVD tube furnace (Carbolite TZF17/600). After purging the furnace with Argon, 30/70 (vol%/vol%) ethylene/helium precursor gas was flowed at 60 sccm into the furnace at 675 °C for 5 hours to deposit a thin film of carbon on all surfaces of the AAO membrane, including the walls of the membrane pores to form CNTs embedded in the AAO template.

4.2.1.2. Fluid Diffusion

Tetramethylrhodamine (dextran) (Life technologies, D3308) diffusion through the device was studied using a custom injection stage (Appendix, Fig. S6) for 4 different concentrations of 2.5, 5, 10 and 20 μM in PBS. Solution diffusion was monitored and imaged by fluorescent microscopy every 1 second for a period of 14 minutes. The average fluorescent intensity along with the standard deviation of each image was analyzed by imageJ software. The fluorescent intensity was then correlated to the intensity of solutions with various concentrations to extract the concentration of solution diffused through the arrayed CNTs as a function of time.

Note that for this experiment, CNTs were synthesized inside the pores of Whatman AAO membranes using the discussed process in chapter 3. Briefly, AAO membranes were annealed in air at 730 °C for 4 hours and placed in a 3-stage CVD tube furnace (Carbolite TZF17/600). After purging the furnace with Argon, 30/70 (vol%/vol%) ethylene/helium precursor gas was flowed at 60 sccm into the furnace at 700 °C for 5 hours to deposit a thin film of carbon on all surfaces of the AAO membrane, including the walls of the membrane pores to form CNTs embedded in the AAO template.

4.2.2. Results and Discussion

4.2.2.1. Pressure Driven Flow

For compatibility and versatility in its targeted biological applications, the device should be able to transfer fluid using pressure driven flow, thus, the relationship between flow rate and the pressure drop across the CNT membrane is of key interest. According to

classical continuum fluid mechanics for an incompressible Newtonian fluid, the flow rate through a tube with inner diameter of d can be predicted by the Equation 4.1 (Hegan-Poiseuille) in which Q is the volumetric flow rate, μ is the dynamic viscosity of the fluid, ΔP is the pressure drop and L is the length of the pipe.

$$Q = \frac{\pi(\frac{d}{2})^4}{8\mu}\frac{\Delta P}{L} \qquad Eq.(4.1)$$

Previous fluid flow rate investigations through single CNTs showed that the experimental measurements exceed predictions from the no-slip Poiseuille relationship by up to several orders of magnitude [262, 263]. Therefore, the volumetric flow rate can be modified by the slip length phenomenon as Equation 4.2 where the slip length (L_s) describes the velocity discontinuity between the liquid and the solid boundary [264].

$$Q_s = \frac{\pi[(\frac{d}{2})^4 + 4(\frac{d}{2})^3 L_s]}{8\mu}\frac{\Delta P}{L} \qquad Eq.(4.2)$$

However, for channels with diameters larger than ~100 nm, the no-slip Poiseuille relationship can be employed (Ls ~ 0) [265, 266]. Since the inner diameter of carbon nanotubes manufactured in this work is approximately 150 nm, Equation 4.1 will be used to predict experimental measurements. It should be noted that Q in Equation 4.1 is the flow rate through a single nanotube and, as such, will be multiplied by the number of tubes in the active area of the membrane through which fluid is flowing when compared to experimental flow rates.

In order to measure fluid flow through embedded CNTs, manufactured CNT membranes were first mounted in a commercially available stainless steel 13 mm filter

holder. A fluid tight seal was achieved by applying enough torque at the both sides of the filter holder in such a way that the fragile membranes stay intact. Effectiveness of the mounting method was confirmed by inserting a circular film of aluminum foil in place of the membrane and verifying that no fluid flowed through the filter holder even at a pressure of 60 psi (twice the amount of pressure during any experimental run). To ensure steady state flow conditions, each experiment was conducted at a constant desired flow rate for 20 minutes and the data recorded in 1 minute intervals. An active area of 0.64 cm^2 was estimated for each membrane mounted in the filter holder. After fluid flow experiments, membranes were randomly inspected in the SEM to ensure that the tube openings were not blocked and remained open.

Several further precautions were taken to ensure accurate measurements. First, the transport path was purged of air bubbles. Second, the length and connections between the pressure transducer and filter holder were minimized to reduce associated head loss. In addition, the syringe pump and filter holder were leveled. Third, membranes were supported by a rigid metal grid with coarse apertures to prevent cracking under hydraulic loads and subsequent leakage. Forth, the fluid emerging from the CNT array was collected and weighed in 1 minute intervals to measure actual experimental flow rates and verify the flow rate settings of the syringe pump. Finally, to account for the above and overall system losses, the pressure drop required to transfer fluid through the system without any membrane in the filter holder was measured. At the flow rates used in this study (nominal flow rates of 0.3, 0.5, 0.7 and 1 mL/min), the losses produced a pressure drop of 0.03 psi. To demonstrate the functionality of the measurement system and evaluate its performance, the pressure drop across a single-bore glass capillary as a

function of flow rate was measured and compared; the experimental results correlated well (within 0.4% error) with theoretical estimations using Equation 4.1.

From SEM micrographs, the density of nanotubes across 0.64 cm^2 of active area was $7.36x10^8$ tubes/cm^2, and the thickness of the membrane was 58 μm (i.e., L). For water with viscosity of $1.03x10^{-3}$ Pa.s, the calculated pressure for the flow rate of 0.49 mL/min (the actual measured flow rate) through the CNT membrane with average inner pore diameter of around 150 nm should be 8.03 psi. The average steady state pressure measured in this case was 8.13 psi which shows very close agreement with theoretical value. Figure 4.8 compares experimental measurements (linear curve fit, solid line, n=6) and theoretical estimations from Equation 4.1 (dotted line) of pressure drop across the membrane as a function of flow rate. Recall, a pressure drop of approximately 0.03 psi was due to system losses. Since this number is only 0.002% of the smallest measured pressure, system losses were neglected and data was not adjusted to compensate.

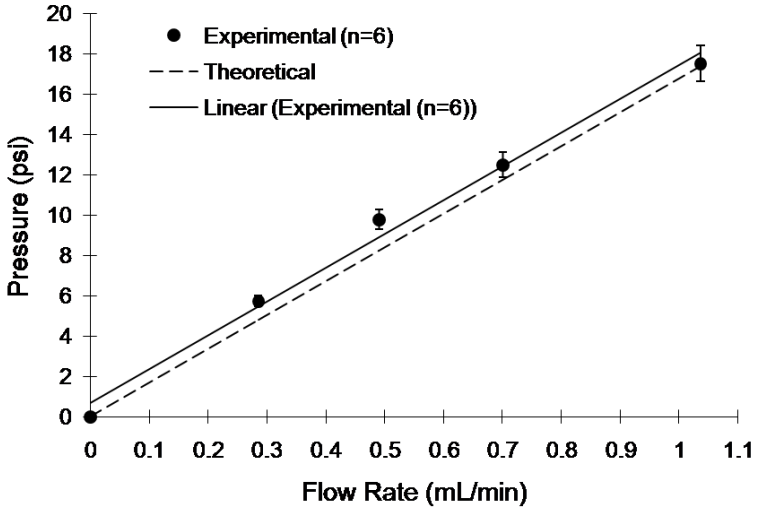

Figure 4.8: CNT membrane pressure drop as a function of water flow rate. The solid line indicates the linear fit of experimental data and the dashed line indicates the theoretical calculation based on Hegan-Poiseuille equation.

4.2.2.2. Fluid Diffusion

Transport of biomolecules through CNTs can also be conducted by solution composition and concentration gradient. Diffusion of fluorescent reagents such as membrane-impermeable dye (dextran) through the CNT array was investigated for four different solution concentrations. Figure 4.9 shows concentration of the diffused solution as a function of time for 2.5, 5, 10 and 20 µM solutions of dextran in phosphate buffered saline (PBS). Dextran diffusion starts after around 21, 17, 12 and 8 seconds and reaches to the maximum intensity after around 771, 562, 509 and 313 seconds for 2.5, 5, 10 and 20 µM solutions, respectively.

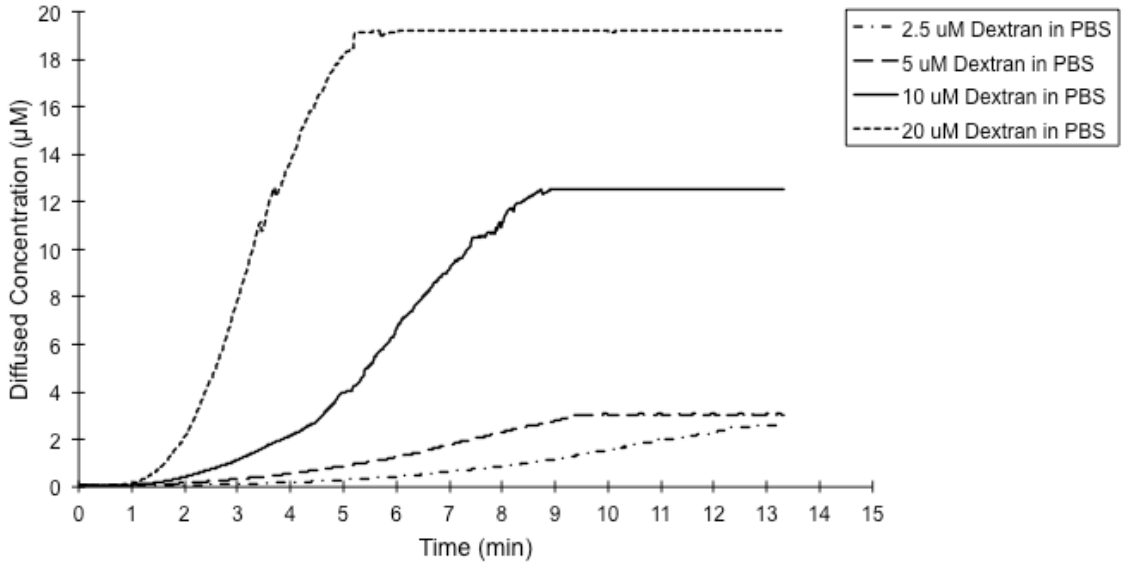

Figure 4.9: Concentration of dextran in PBS solution as a function of time during the transfusion through the device for 2.5, 5, 10 and 20 µM solutions.

CHAPTER 5

High Efficient Transfection of Cells through Carbon Nanotube Arrays

Introducing nucleic acids into mammalian cells is a crucial step to elucidate biochemical pathways, and to modify gene expression and cellular development in immortalized cells, primary cells, and stem cells. Current transfection technologies are time consuming and limited by the size of genetic cargo, the inefficient introduction of test molecules into large populations of target cells, and the cytotoxicity of the techniques. In this chapter, a novel method is presented to introduce genes and biomolecules into tens of thousands of mammalian cells through an array of aligned hollow CNTs, manufactured by template-based nanofabrication processes, to achieve rapid high efficiency transfer with low cytotoxicity. The utilization of CNT arrays for gene transfection overcomes molecular weight limits of current technologies and can be adapted to deliver drugs or proteins in addition to nucleic acids.

5.1. Intracellular Transfection

The most common methods used for transfecting mammalian cells include: Lipofection [139], which is simple but can have high toxicity and variable efficiency, particularly for

post mitotic cells; Electroporation [267], which requires significant investment in hardware and has variable efficiency and significant toxicity; Viral vectors [268], which are labor intensive to construct, can have high toxicity at high titers (necessary for increased efficiency) and have a limited DNA packing size; Biolistics (Gene Gun) [269], which can transfer multiple species of DNA but requires expensive hardware and has low efficiency and high toxicity. Intracellular microinjection has also been used for gene transfection and other delivery applications, either through glass micropipettes [270] or hollow nanostructures [16, 71, 149, 150, 155, 156, 163]. However, microinjection is carried out in a serial fashion, making it very time-consuming, even with automated systems [165, 271].

Recently, arrays of vertically aligned nanostructures have been developed for cell transfection [142, 151, 152, 157-161, 272]. In theses platforms, biomolecules are adsorbed on the surfaces of vertical nanowires or close-ended nanotubes that have been arranged in an array and protrude hundreds of nanometers to several micrometers from a substrate. After cells are cultured on top of the array, the adsorbed biomolecules find their way into cells over time [166, 272]. Alternatively, cells have been cultured on top of hollow nanotube arrays and transfected via fluid transport through the nanotube lumen [142, 161]. However, these transfection platforms require long incubation times with target cells (>24 hrs), have low transfection efficiency (< 30%) or require additional assistive transfection techniques (e.g. electroporation) to achieve higher efficiency (>67%) [142]. Moreover, there has been no demonstrated evidence that nanostructured arrays can be successfully utilized for high efficiency gene transfection in large quantities of cells, hindering broad application of the technology in the biomedical community.

In this chapter, the CNT-based array device (schematically depicted in Fig. 1.7) is utilized as a platform, which supports cell growth and enables high efficiency gene transfection through the lumens of CNTs into cells within a short period of time without any assistive technique. Template-based fabrication processes were developed to produce a device consisting of an array of closely-packed, hollow and open-ended CNTs embedded in a thin, 13-mm diameter sacrificial template. As discussed in chapter 3 and 4, the template was selectively etched away on one side to expose the tips of the embedded CNTs. The surface of the exposed CNT tips supports healthy cell growth similar to standard tissue culture plastic-wear. High efficiency gene transfer occurs rapidly into tens of thousands of cultured cells simultaneously through the CNTs by placing a nucleic acid solution on the back side of the device. Once transfected, cells can be left on the device or removed from the surface of the device and replated for subsequent growth, processing, and/or analysis. In addition to nucleic acids, the CNT array device can also deliver nanoparticles and macromolecules into large populations of cells simultaneously. The results presented here demonstrate the utility of CNT-based arrays as a rapid, versatile and efficient cellular delivery system to populations of cells.

5.2. Experimental Procedure

5.2.1. Device Manufacturing

CNT arrays were fabricated using commercially available AAO membranes (Whatman Anodisc 13). CNTs were formed inside the AAO membrane using previously established processes [97] discussed in chapters 3 and 4. Briefly, AAO membranes were annealed in air at 730 °C for 4 hours and placed in a 3-stage CVD tube furnace (Carbolite

TZF17/600). After purging the furnace with Argon, 30/70 (vol%/vol%) ethylene/helium precursor gas was flowed at 60 sccm into the furnace at 700 °C for 5 hours to deposit a thin film of carbon on all surfaces of the AAO membrane, including the walls of the membrane pores to form CNTs embedded in the AAO template. The carbon layer on one side of the membrane was then removed using oxygen plasma (LAM 490) at 300 mTorr, RF 250 W and oxygen flow rate of 100 sccm for 3.5 minutes. CNTs were then partially exposed by selectively etching the AAO template using RIE (LAM 4600) with boron trichloride (BCl_3) at 150 mTorr, RF 400 W and BCl_3 flow rate of 100 sccm for 180 minutes. The resultant CNT array consisted of millions of CNTs (average tip diameter of 205±42 nm, tube wall thickness of 28±5 nm, tube-to-tube spacing of 187±36 nm) protruding 176±34 nm from the surface of the 13 mm diameter AAO membrane. Dozens of CNT array devices were produced in a single manufacturing run and stored until needed for transfection.

5.2.2. Plasmid Preparation

The pEYFP mammalian expression vector mVenus-C1 [273] was maintained in *E.coli* DH5*a* cells. Plasmid DNA was isolated from overnight *E.coli* cultures using commercially available kits (QIAGEN Plasmid Plus Midi Kit).

5.2.3. Cell Culturing

Human embryonic kidney 293 cells (HEK293) and rat L6 myocyte were cultured in DMEM supplemented with 10% fetal bovine serum and 1% penicillin/streptomycin at

37 °C and 5% CO_2. CNT array devices were sterilized in ethanol, dried in air for 15 minutes and submerged in DMEM for 30 minutes. Forty-thousand cells were counted by hemocytometry and introduced on each device and cultured for 48 hours before transfection.

5.2.4. Cell Growth Study

CNT array devices were sterilized in ethanol, dried in air for 15 minutes and submerged in DMEM for 30 minutes. Sixty-thousand cells were plated on the device and on a control well in a 24-well tissue culture dish and stained with 5 μM calcein-AM/ethidium homodimer-1, (Life technologies, L3224) in PBS before imaging. The CNT devices and tissue culture plates were washed 3X with PBS before imaging to eliminate unattached and free floating cells. Cell spreading and proliferation were determined by fluorescence microscopy, analyzing 20 sample images at two different magnifications (10X and 50X) and quantified using ImageJ software. The number of live cells stained by calcein-AM per surface area and the projected area of spread cells was calculated (200 to 850 counts on average). For cell growth and spreading at each time step, statistical significance between the tissue culture plate and CNT array samples was determined by p-values obtained from t-tests.

5.2.5. Cell Transfection

Transfection of cells was performed on a custom stage and controlled environment under the fluorescent microscope. Before transfection of the tetramethylrhodamine (dextran)

and quantum dots (Qdots), HEK293 cells were counter-stained with 2 µM calcein-AM dye (Life technologies, L3224) to be visible under the fluorescent microscope. A 10 µM solution of membrane-impermeable 3,000MW dextran in PBS (Life technologies, D3308) was prepared and introduced into the inlet of the transfection stage and the process was monitored by fluorescent imaging every 0.5 second. As a control for impermeability of dextran, cells were cultured in a well of 12-well cultrue plate for 48 hours. The cells were then incubated in DMEM containing 10 µM dextran for 20 minutes. The cells were then rinsed, trypsinized and re-cultured in tissue culture plate. The dextran permeation was monitored using fluorescence microcopy.

Qdot transfection was conducted by preparing an 80 nM solution of carboxyl Qdots (Life technologies, Q21341MP) in PBS. Delivery process was monitored by fluorescence microscopy. The transfected HEK293 cells were then washed 3X with PBS to remove suspended Qdots, before imaging. Cells were then trypsinized and re-cultured on tissue culture plates for 5 hours, after which they were imaged again. As a control for impermeability of Qdots, cells were cultured in a well of 12-well cultrue plate for 48 hours. The cells were then incubated in DMEM containing 80 nM Qdots for 20 minutes. The cells were then rinsed, trypsinized and re-cultured in tissue culture plate. The Qdot permeation was monitored using fluorescence microcopy.

Cells were also transfected with 75 µM solution of propidium iodide (PI) in PBS. For these studies L6 cells were cultured on the CNT array device for 48 hours, after which they were stained with 2 µM calcein-AM dye to identify the live cells. PI delivery was conducted in our custom stage, keeping the cells hydrated in PBS. After 20 minutes, cells were trypsinized and collected in 100 µL of complete serum-free medium (CSFM,

DMEM supplemented with 2 mg/ml BSA, 25 mM HEPES pH 8.0, 1% penicillin/streptomycin, 1 ng/ml transferrin, 1.25 ng/ml insulin) for flow cytometry. As a control for impermeability of PI, forty-thausand cells were cultured in each well of a 24-well cultrue plate for 48 hours. The cells were then incubated in 0.6, 0.8, 10, 50, 75, 100 and 500 μM of PI in CSFM for 10, 20, 30, 40, 50 and 60 minutes. The cells were then rinsed, trypsinized and collected for flow cytometry. The PI permeation was quantified by the percentage of cells emitting red fluorescence.

For transfection of plasmid DNA, HEK293 cells were seeded and cultured on the device as described above for 48 hours. A 500 ng/μL solution of plasmid DNA encoding enhanced yellow fluorescent protein (EYFP) in modified patch clamp electrode buffer (148 mM KCl, 1 mM $MgCl_2$, 5 mM EGTA, 5 mM HEPES, 2 mM creatine, 5 mM Phosphocreatin (Sodium salt), 5 mM ATP (dipotassium), pH 7.2) [274] was prepared. Transfection was conducted using our custom stage (Appendix, Fig. S7) in a tissue culture incubator for 2 hours; after which the cells were trypsinized and transferred to a 6-well tissue culture plate and cultured for 48 hours. Expression of EYFP transfected cells was monitored by fluorescence microscopy before transfection, and every 24 hours after transfection for 2 days. Cells were then trypsinized and collected in 100 μL of CSFM for flow cytometry.

DNA transfection was conducted via lipofection for comparison. HEK 293 cells were seeded and cultured on a well of 24-well tissue culture plate for 48 hours. Lipofection was performed using commercial reagents and protocols (Polyplus Transfection, jetPRIME). In brief, 0.5 μg of plasmid DNA was added into 50 μL of jetPRIME buffer. After mixing, 1.3 μL of jetPRIME reagent was added to the mixture

and vortexed for 10 seconds. The final mixture was incubated at room temperature for 10 minutes, and then added to 0.5 mL of growth medium of the cells. The cells were incubated in the lipofection solution overnight. Cells were then trypsinized and collected in 100 µL of CSFM for flow cytometry.

5.2.6. Flow Cytometry

Flow cytometry was utilized to quantify transfection efficiency from a large poulation of cells. Analysis was carried out on a BD Biosciences Accuri C6 Flow Cytometer, using 488 excitation/670 nm emission to detect PI fluorescence, and 488 nm excitation/530 nm emission to detect calcein-AM and EYFP fluorescence. A cut-off percentage of 0.2% (PI) or 0.1% (EYFP) positive within the control untransfected sample was used to set the gates (Appendix, Fig. S8). Side scatter (SSC) data was also collected and plotted on the Y-axis vs. fluorescence intensity on X-axis. Transfection efficiency was reported as the ratio of the number of transfected live cells to the number of live cells.

5.2.7. Scanning Electron Microscopy

Following culture on CNT array device for 48 hours, L6 cells were fixed in 3% glutaraldehyde/0.1% sodium phosphate pH 7.4 for 30 min at room temperature, washed twice with PBS for 5 minnutes, and then dehydrated in a graded ethanol series at room temperature, first for 10 minutes in 30% ethanol/PBS, and then successively in 50%, 70%, 85%, 95% and 100% ethanol. CNT devices with fixed and dehydrated cells were then further dried in a critical point dryer (Tousimis PVT-3B), and coated with platinum in a

DC sputter coater (Denton Vacuum DESK-II). The cells were examined using a field emission SEM (Zeiss Auriga).

5.3. Results and Discussion

5.3.1. Vertically Aligned CNT Array Device

CNT array devices were fabricated using a template-based CVD approach, as depicted in chapter 4. CNTs were formed inside the pores of commercially available AAO membranes via CVD as described previously [97]. The selected membrane dictated the outer diameter, length of CNTs and spacing between the tubes, while the CNT wall thickness was controlled by CVD time, temperature, and gas flow rate. After removing the carbon film deposited on the membrane surface with oxygen plasma, one side of the AAO membrane was partially etched by RIE using boron trichloride plasma to expose the tips of CNTs embedded in the membrane. The exposed length of CNTs was controlled by RIE etching time, chamber pressure and RF power. The result is a densely packed array of aligned CNTs embedded inside the AAO template with relatively short exposed lengths, which are open on both sides of the membrane. Typical devices consisted of millions of CNTs (average outer and inner diameters approximately 200 nm and 140 nm, respectively) spaced on average 200 nm from each other, and protruding approximately 180 nm from the surface of the 13 mm diameter template (Fig. 5.1b, c).

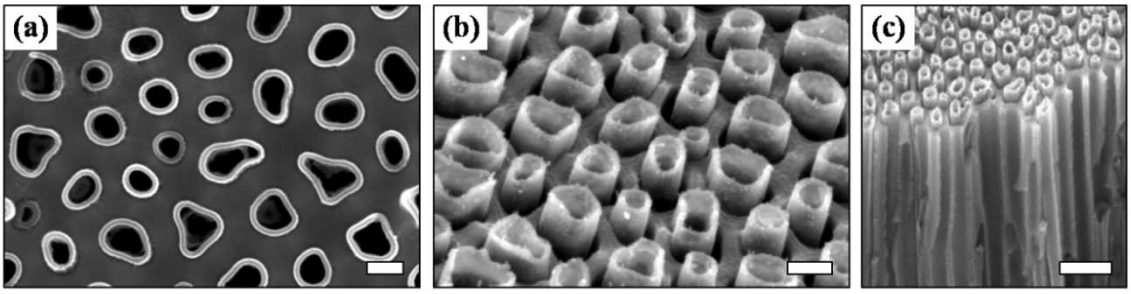

Figure 5.1: CNT array device for high efficient parallel intracellular transfection. SEM micrographs of exposed CNT array, (a) top view and (b) 35° tilted view (Scale bars: 200 nm). (c) Fractured edge of CNT device showing embedded CNTs with exposed tips extending through the plane of the device (Scale bar: 1 μm).

5.3.2. Cell-CNT Interaction

HEK293 and rat L6 myocyte cells were successfully cultured on top of CNT arrays using established cell culture protocols (Fig. 5.2a, b). Figure 5.2a shows the typical morphology of cells adhering to the surface of the CNT array, where a cell covers the protruding tips of approximately 900 CNTs. As observed in Figure 5.2b, the basal cell membrane is in intimate contact with the tightly packed textured surface of the short protruding CNT tips.

Cells grew and proliferated on CNT arrays at the same rate as standard tissue culture plates (Fig. 5.2c, d). HEK293 cells (40,000 cells/mL) were seeded in parallel on a CNT array device and a similar-sized (13 mm) well of a tissue culture plate. Cells were cultured for 48 hours during which the numbers of living cells were counted using fluorescence microscopy and the surface area covered by the cells was calculated. As shown in Figure 5.2c, d, there was no statistically significant difference in cell coverage or number of live cells between cells cultured on the CNT array or on tissue culture plastic over the 48 hours period. Cells were then trypsinized and re-cultured on tissue culture plastic for an additional 24 hours to score cell viability. As confirmed by SEM

imaging after trypsinization, all cells were collected from the device surface. Using the live/dead cell viability assay (calcein-AM/ethidium homodimer-1), 97% of re-cultured cells were alive, indicating the CNT array supports cell culture comparable to standard tissue culture plates and without cytotoxic effects. These results are in agreement with our previous work showing the low toxicity of single CNT-tipped probes in single cell analysis [16, 71, 163, 275]. Although not shown here, cells have also been successfully cultured on the device for up to 96 hours.

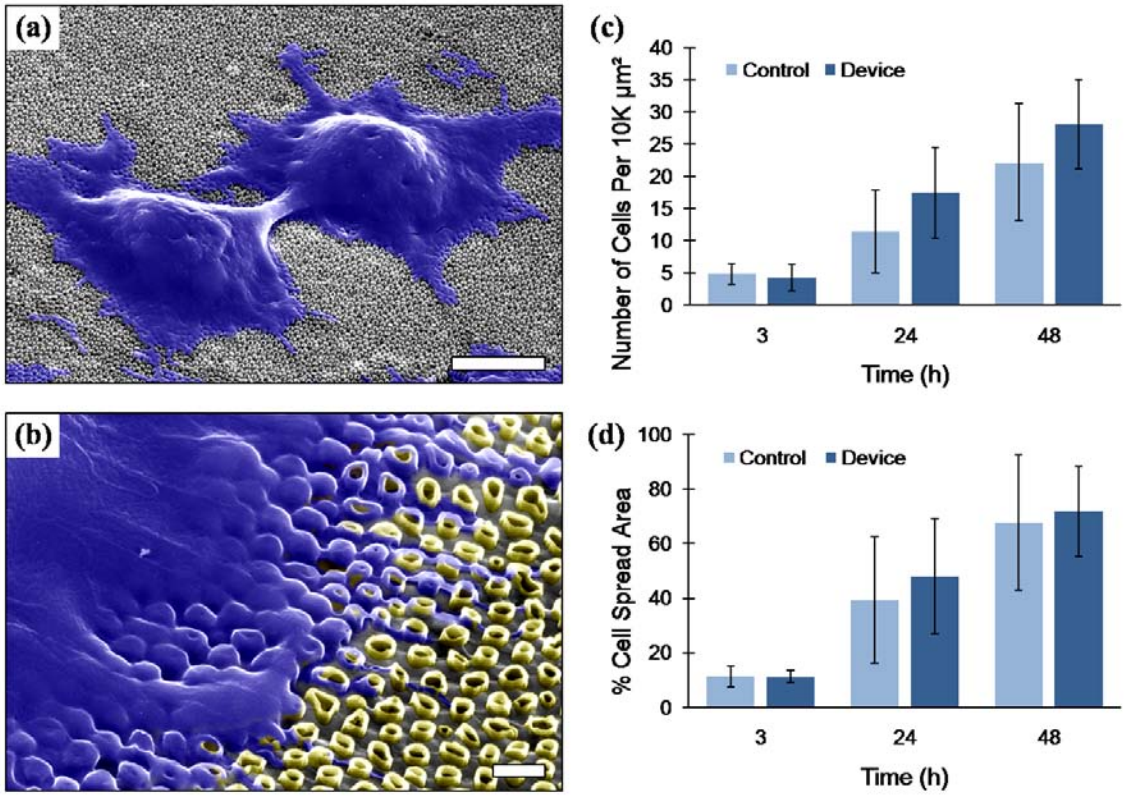

Figure 5.2: Interaction and proliferation of cells on the CNT array device. (a) SEM micrographs of L6 cells (false colored blue) cultured on CNT device after 48 hours (Scale bar: 5µm), and (b) high magnification micrograph of cell-CNT interface, showing engulfment of CNTs (false colored yellow) by basal membrane of L6 cells (Scale bar: 500 nm). (c, d) Cell proliferation study of HEK293 cells on CNT array compared with tissue culture plate shows live cell number and area covered by cells monitored at 3, 24 and 48 hours after seeding. Error bars indicate the standard deviation of 20 sampled images for each case. No significant difference in cell growth or cell area was observed between control plastic and CNT devices (T-test resulted in p-values of 0.63, 0.20 and 0.29 for (c), and 0.95, 0.55 and 0.63 for (d), comparing control with CNT array device after 3, 24 and 48 hours, respectively.)

5.3.3. High Efficiency Transfection of Population of Cells

The CNT array device was utilized to deliver cell-impermeable molecules, such as macromolecules, nanoparticles and nucleic acid into cells cultured directly on its surface. These molecules are unable to efficiently penetrate through the cell plasma membrane without a transport technique or reagent [276]. HEK293 cells were cultured on top of the CNT array for 48 hours. The device was then removed from the culture media and positioned under an upright fluorescent microscope on a custom perfusion stage to prevent cell dehydration during transfection. To demonstrate delivery into cells through the device, a 10 µM droplet of tetramethylrhodamine (dextran) dye was placed under the device and allowed to diffuse through the CNTs and into HEK293 cells cultured on the top surface of the device. The cells and delivery were observed in real time under a fluorescent microscope (Fig. 5.3a-b). As shown in Figure 5.3b, dye delivery through the CNT array device occurred within 16 minutes and cells remained viable throughout the process.

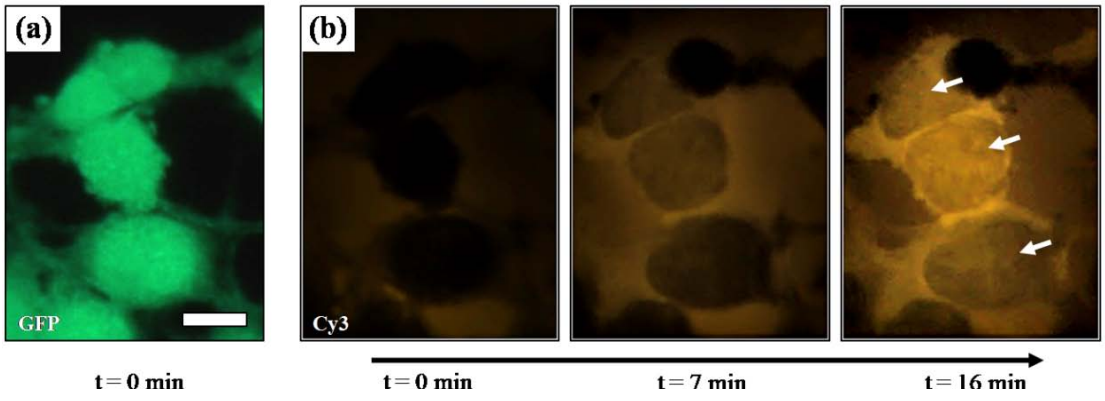

Figure 5.3: Intracellular transfection of cells with membrane-impermeable dye using CNT array. (a) Magnified fluorescent images of five HEK293 cells during transfection, showing the live cells stained by calcein-AM dye imaged by GFP fluorescent filter at t=0 minute, and (b) same cells during the CNT-mediated transfection of 10 µM tetramethylrhodamine (dextran) imaged by Cy3 fluorescent filter at t=0, 7 and 16 minutes (Scale bar: 5 µm). The background fluorescence is due to diffusion of dextran into the growth medium through open CNTs (with no cells blocking the exit opening).

Control experiments were conducted to ensure impermeability of dextran molecule. To this end, HEK293 cells were cultured on a standard tissue culture plate (Fig. 5.4a) and incubated in growth medium containing 10 µM dextran, the same dextran concentration utilized for transfection. Cells were incubated for 20 minutes (the required time for intracellular delivery of biomolecules with the device) (Fig. 5.4b), then rinsed, trypsinized and re-cultured in tissue culture plate. Evaluation of the cells by fluorescence microscopy showed no intracellular fluorescence in cells (Fig. 5.4c), indicating membrane impermeability of dextran.

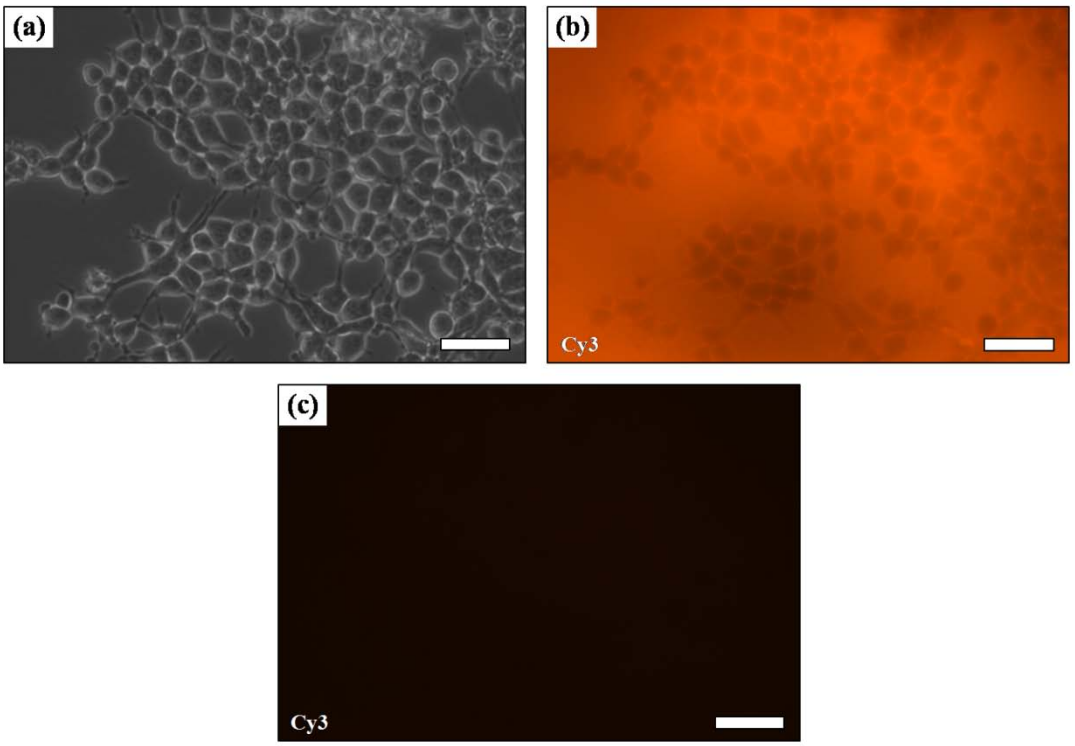

Figure 5.4: Permeation control of tetramethylrhodamine (dextran) into cells. (a) Brightfield image of HEK293 cells cultured on culture plate for 48 hours before introduction of dextran, (b) fluorescent image of cells incubated in 10 µM solution of dextran (dark spots indicate untransfected cells) after 20 minutes, and (c) fluorescent image of the same cells after rinsing with PBS indicating impermeability of dextran (Scale bars: 50 µm).

Cells cultured on the CNT array device can be transfected, removed from the device, and cultured in standard tissue culture plates. Using the transfection and cell culturing protocols described above, HEK293 cells were seeded on top of the device for 48 hours and stained with live assay (calcein-AM), as shown in Figure 5.5a. A solution of 80 nM carboxyl Qdots (15-20 nm diameter) in PBS was prepared and introduced on the back side of the device over our custom stage for 20 minutes. The transfected HEK293 cells were then washed three times with PBS to remove suspended Qdots before imaging. Cells were then trypsinized and re-cultured on tissue culture plates for 5 hours, after which they were imaged again (Fig. 5.5c). As shown in Figures 5.5b, c, fluorescent Qdots are distinctly visible inside calcein-stained HEK293 cells after delivery (Fig. 5.5b), and 5 hours after transfection and re-culturing (Fig. 5.5c). Results show efficient transfer of fluorescent Qdots. Cells remained viable before, during, and after both the delivery and re-culturing process, as determined using the live/dead assay.

Since the cells can uptake molecules from solution through endocytosis [277, 278], control experiments were conducted to ensure impermeability of Qdots. To this end, cells were cultured on a standard tissue culture plate and incubated in growth medium containing 80 nM Qdots, the same Qdot concentration utilized for transfection. Cells were incubated for 20 minutes (the required time for intracellular delivery of biomolecules with the device), then rinsed, trypsinized and re-cultured in culture plate and evaluated by fluorescence microscopy. No intracellular Qdots were observed in these control cells, indicating membrane impermeability of Qdots.

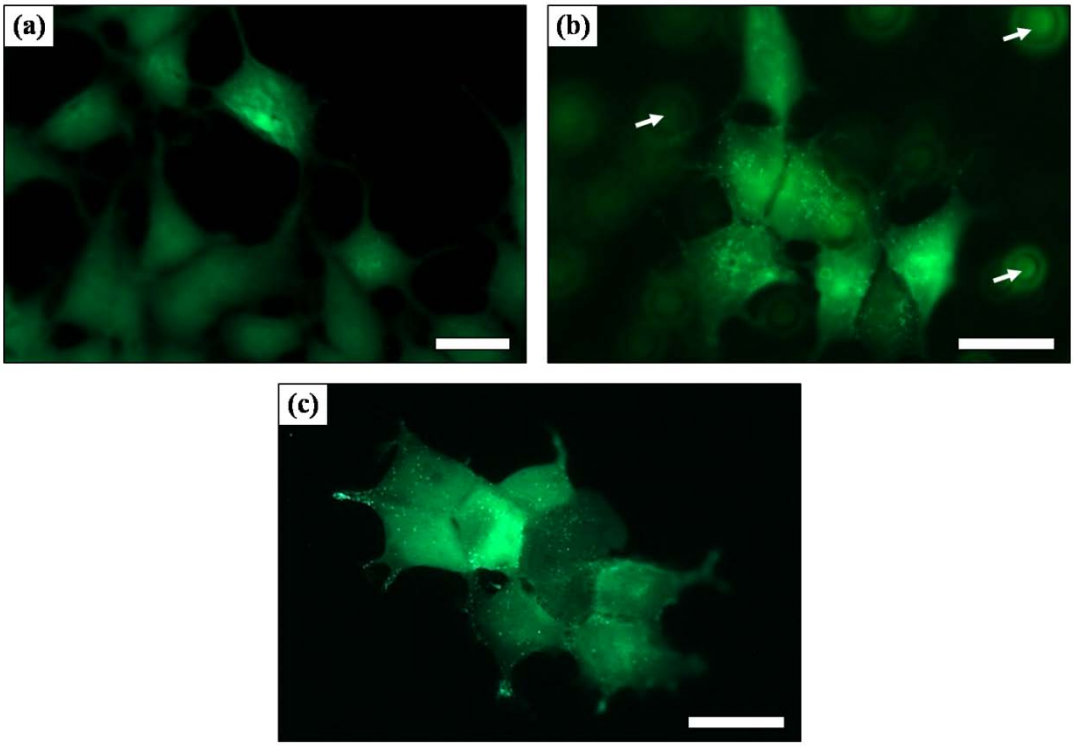

Figure 5.5: Intracellular transfection of cells with quantum dots by CNT array. (a) Fluorescent images of live HEK 293 cells cultured on CNT array for 48 hours and stained with calcein-AM dye imaged by GFP fluorescent filter, (b) cells during the transfection with Qdots (white arrows show the free floating Qdots), and (c) same cells trypsinized and re-cultured in culture plate for 5 hours after transfection (Scale bar: 20 µm). The bright punctuate green transfected Qdots are detectable on a uniform background of calcein-AM staining.

To facilitate large-scale transfection, a platform was developed consisting of a media-filled cylinder on which a CNT array, with cells cultured on its surface, would be inverted and placed on top. Once in place, injection solution could be applied to the backside of the inverted CNT array while keeping the cells bathed in growth media during the transfection. Using the custom platform, populations of cells were efficiently transfected with fluorescent dye. Forty-thousand L6 cells were seeded on the CNT array and cultured for 48 hours. Cells were stained with calcein-AM dye to identify live cells (Fig. 5.6a). The device was then inverted and placed on the transfection platform to keep cells hydrated. A 50 µL drop of 75 µM propidium iodide, a red membrane-impermeable

dye, was placed on the backside of the device and allowed to diffuse through the CNTs and into the cells for 20 minutes. Cells were imaged (Fig. 5.5a-c), and then trypsinized to stop transfection and collected for flow cytometry. Using fluorescence microscopy, almost all the cells appear to be both alive (stained green with calcein-AM) and transfected with dye (red fluorescence) (Fig. 5.6b). These results were confirmed by flow cytometry analysis, where 98% of the cells stained green (alive, data not shown) and 99% of the viable cells were transfected with PI (Fig. 5.6d). These results demonstrate that the CNT array is able to transfect mamalian cells with high efficiency and minimal impact on cell viability within a short period of time.

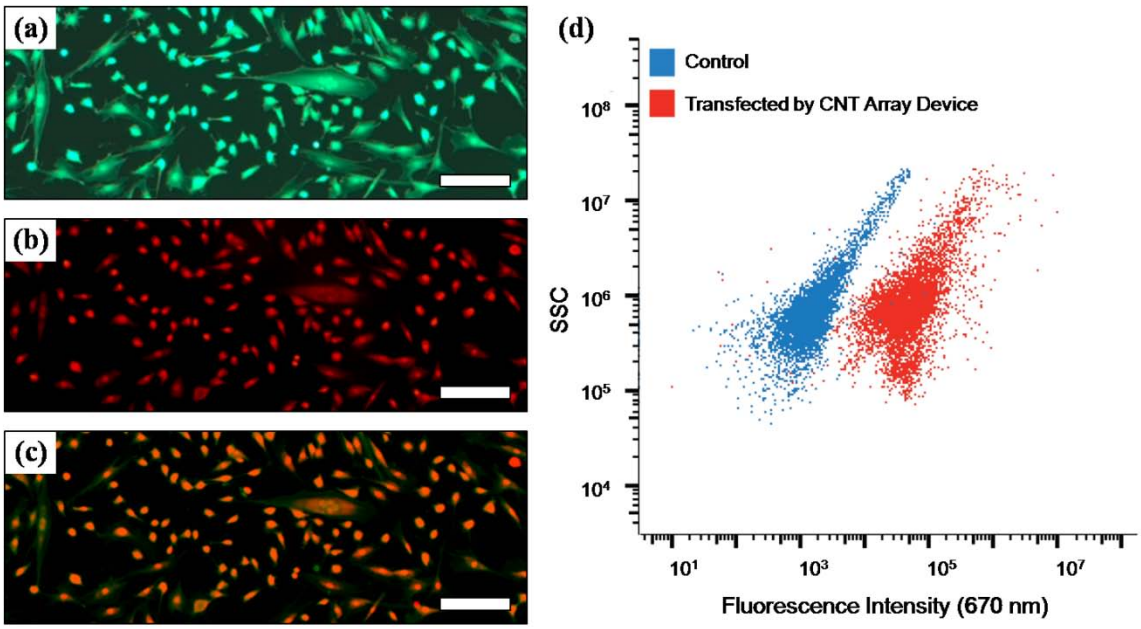

Figure 5.6: High efficiency dye transfer into cells using CNT array. (a) L6 cells plated on CNT array and stained with 2 µM calcein-AM dye, and (b) transfected with 75 µM propidium iodide after 14 minutes, and (c) merged fluorescent image of a and b (Scale bars: 200 µm). (d) Flow cytometry results of L6 cells transfected with propidium iodide using CNT array device. Transfection indicated by rightward shift in the 670 nm fluorescence intensity of injected cell population (red) compared to control uninjected (blue) cells. Nine thousand cells were counted for each sample population.

Control experiments were conducted to ensure impermeability of PI at the concentrations in which the cells were transfected. To this end, 40,000 L6 cells were cultured on standard tissue culture plates for 48 hours. Cells were incubated in CSFM containing various concentrations of PI for up to 60 minutes. Cells were then trypsinized and collected for flow cytometry. For each incubation time, 30,000 cells were analyzed by flow cytometry. As shown in Figure 5.7, the results indicate that for 10 µM PI (concentration represents the extreme scenario, where the entire 50 µL injection volume of 75 µM PI entered into the serum-free medium reservoir), the PI does not permeate into cells incubated even up to 40 minutes (double the time used to inject cells through the CNT array). The 10 µM PI permeated only 5% of the cells incubated for 60 minutes. However, for highe concentration of the PI, the permeation is inevitable.

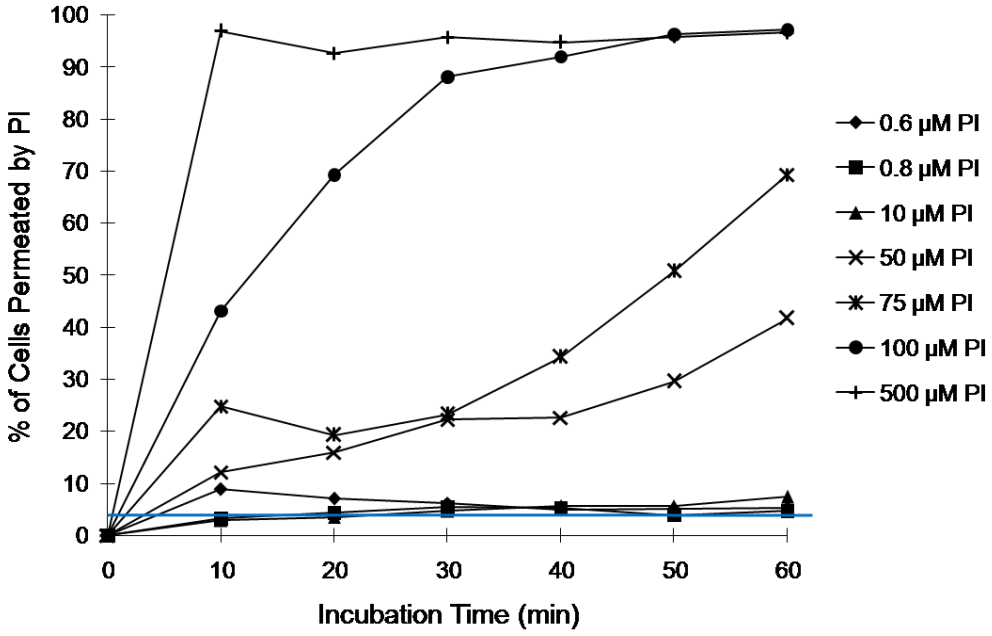

Figure 5.7: Permeation of propidium iodide dye into L6 cells at various concentrations. Blue line indicates the control (cells with no staining).

The CNT array can efficiently transfer plasmid DNA into large populations of cells. Forty-thousand HEK293 cells were seeded on the device and cultured for 48 hours. The device was inverted and placed in the custom transfection fixture containing growth media to keep cells hydrated. A 50 µL drop of 500 ng/µL plasmid DNA encoding enhanced YFP was placed on the backside of the device and allowed to diffuse through the CNTs and into the cells for 2 hours in a tissue culture incubator. Cells were then trypsinized to stop transfection, collected, transferred to tissue culture plate and cultured for two days. The EYFP expression in cultured cells was confirmed by fluorescence microscopy (Fig. 5.8a-c). Due to variation of EYFP expression level, a gradation of fluorescence was observed, indicated as a continuum of low to high fluorescence intensity in the transfected population. The cells were then trypsinized and collected for flow cytometry. Quantification of transfection efficiency by flow cytometry showed that out of 25,000 counted cells, 84% of them were alive and expressing EYFP (Fig. 5.8d). These results demonstrate that the CNT array is able to transfer DNA into tens of thousands of cells with high efficiency and high cell viability.

DNA transfection was also conducted via lipofection for comparison. HEK 293 cells were seeded and cultured on a well of 24-well tissue culture plate for 48 hours. Lipofection was performed using commercial reagents and protocols. The flow cytometry results of the lipofected cells, indicating that 90.8% of the cells were transfected (Appendix, Fig. S9). This demonstrates that the CNT array device can achieve gene transfection efficiency comparable to well-established transfection methods, e.g. lipofection, but can do so within a shorter amount of time.

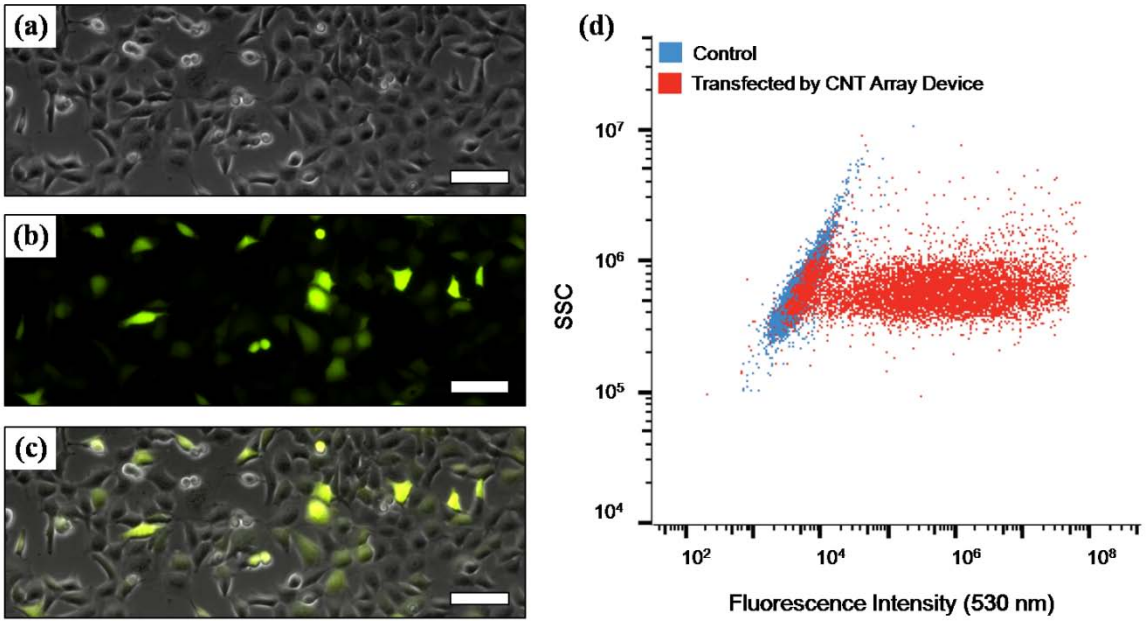

Figure 5.8: High efficiency plasmid transfection of cells using CNT array. (a) Phase image of HEK293 cells, and (b) fluorescent images of transfected cells with EYFP plasmid DNA, 48 hours after transfection, and (c) the merged phase and fluorescent image of a and b (Scale bars: 100 µm). (d) Flow cytometry results of HEK293 cells transfected with plasmid DNA encoding YFP by CNT array device. Transfection indicated by rightward shift in the 530 nm fluorescence intensity of injected cell population (red) compared to control uninjected (blue) cells. Twenty-five thousand cells were counted for each sample population.

5.4. Conclusion

The array of hollow CNTs described in the current studies is able to deliver macromolecules, nanoparticles, and DNA into tens of thousands of cells simultaneously with high efficiency and low toxicity. The CNT device provides the ability to accommodate a wide range of sizes of biomolecules, from 0.66 kDa (propidium iodide), 3 kDa (tetramethylrhodamine-dextran) to 3900 kDa (6000 bp plasmid DNA). This wide range of cargo size suggests that the CNT array will have broad use for transferring DNA, proteins or drugs into cells. Results show highly efficient delivery of dye (99%) and plasmid DNA (84%) into tens of thousands of cells from two different cell lines, demonstrating the robustness of the hollow CNT arrays for efficient biomolecular

delivery, with low toxicity. The CNT device is easily manufactured and utilizes standard cell culture consumables and procedures, making it amenable for broad application. By applying a sample solution to the backside of the CNT array and delivering the cargo molecules through the hollow CNT, the delivery concentration and cell-cargo contact time can be precisely controlled, and, serial delivery of multiple biomolecules is possible.

The CNT array device is well tolerated by cells, which adhere and grow with characteristics similar to tissue culture plastic, suggesting applications for cells that are resistant to current transfection protocols such as macrophages, primary neurons and stem cells. Additionally, gene transfer by CNT array is not associated with cell distress, and may thus have significantly fewer side-effects on cellular physiology than standard transfection methods, speeding development of new cell models to study intractable diseases, discovery of signaling pathways, and drug discovery.

CHAPTER 6

Effect of Geometrical Properties of Carbon Nanotube Arrays on Intracellular Gene Transfection

Vertical arrays of nanostructures are emerging as promising platforms for cellular biology, probing and manipulating live cells and intarcellular deliver. These broad ranges of applications require different types of interfaces, almost invariably relying on the physical and geometrical properties of the nanowire or nanotube arrays. This necessitates a need for a better understanding of the affect of their geometrical properties on cellular behavior. In this chapter, arrays of vertically aligned CNTs are used for gene transfection into populations of cells. The effect of CNT exposed length and surface morphology on transfection efficiency is studied. The results indicate that relatively short exposed CNTs with planar-surface morphology promote intracellular gene transfection through hollow CNTs into populations of cells. This provides a guideline for optimization of transfection efficiency using arrays of vertically aligned CNTs.

6.1. Nanoarray Features and Cellular Interface

The ever increasing utilization of arrays of vertical nanowires and nanotubes for biological applications has demonstrated a new perspective for cellular investigation

during the last decade [151, 237, 279, 280]. The small dimensions of these nanostructures and their minimal cell perturbation make them a promising tool for applications including biomolecule detection [239, 240, 281], mechanosensing [282-284], biomolecule transport [159, 160, 285], cell recording [286-288], and axonal guidance [289, 290]. To this end, various arrays of nanowires and nanotubes fabricated out of different materials, with a broad range of geometrical properties and surface chemistry are desired to fulfill the requirements of each application due to the interaction of nanostructural elements with biological entities.

Intracellular delivery of macromolecules and genetic materials is yet another application of these platforms which is emerging as an important field of research to overcome the limitations of current transfection techniques and allow understanding of cell heterogeneity in complex biological systems [142, 161, 166]. The limiting step in current analysis of cellular physiology is the inefficient introduction of test molecules into target cells with physiologic characteristics representative of *in vivo* pathophysiology.

Vertically aligned structures of such nanowires and nanotubes have demonstrated high efficient delivery of biomolecules into population of cells [246, 272]. Various parameters such as cell type, geometrical properties of the arrays (lengths, diameters, spacing between the elements), material and even fabrication method seem to influence the interaction of cells with these nanostructures and therefore, affect the transfection efficiency [158, 249, 253, 291-293]. For instance, surface morphology can greatly affect the cell function through activation of signaling pathways due to the cytoskeleton rearrangement [294]. Spacing between the nanoelements can either change the chemical

cues in the cellular environment or changes the cytoskeleton dynamics, affecting the cell motility [295].

There have been attempts to improve the interface between the nanowires or nanotubes and cells through proper selection of geometrical properties [243, 251]. However, the studies show that penetration of these nanostructures through cell lipid bilayer and have a direct access to the cell cytosol is very unlikely [252, 253]. This means that despite the rapidly expanding utilization of vertical nanowires and nanotubes for cellular transfection, the effect of their geometrical properties on transfection efficiency still needs more exploration.

As discussed in previous chapter, high efficient transfection of populations of cells with different macromolecules and nanoparticles, and also plasmid DNA was demonstrated using an array of vertically aligned CNTs with high cell viabilitys. The results show that densely packed and shortly exposed CNTs with a uniform and co-planar surface are the key features to achieve high transfection rate and high cell viability. This is in contrast with the results reported in other literature in which high aspect ratio nanowires or nanotubes (height > 1 μm) with longer spacing (> 2 μm) is preferable for better cell penetration and intracellular delivery [243, 251, 253].

In this chapter, the effect of CNT exposed length and surface roughness on transfection efficiency of population of cells is examined. To this end, arrays of CNTs were fabricated using template-based manufacturing method discussed in chapter 3 and 4. As illustrated in Figure 6.1, first, carbon was deposited on the surface of commercially available porous AAO membranes to form CNTs. The carbon layer was removed from

the top surface of the template using oxygen plasma. Finally, the tips of the CNTs were exposed using RIE process. Arrays of CNTs were fabricated through 1 step (Fig. 6.1c) or 2 steps (Fig. 6.1d-f) manufacturing processes in which the RIE parameters such as RF power, chamber pressure and plasma mixture were modified to adjust the exposed length of the CNTs and introduce the surface roughness. Cells were grown on the array device for 48 hours, after which were transfected with plasmid DNA encoding enhanced YFP and the transfection efficiency was quantified using flow cytometry. Cell growth and proliferation was also studied as a function of CNT exposed length and surface roughness. Moreover, the cell-CNT interaction was evaluated using SEM. The final results indicate that a shortly exposed and densely packed aligned array of CNTs with a co-planar surface morphology is a more promising nanostructure to achieve high gene transfection efficiency into populations of cells.

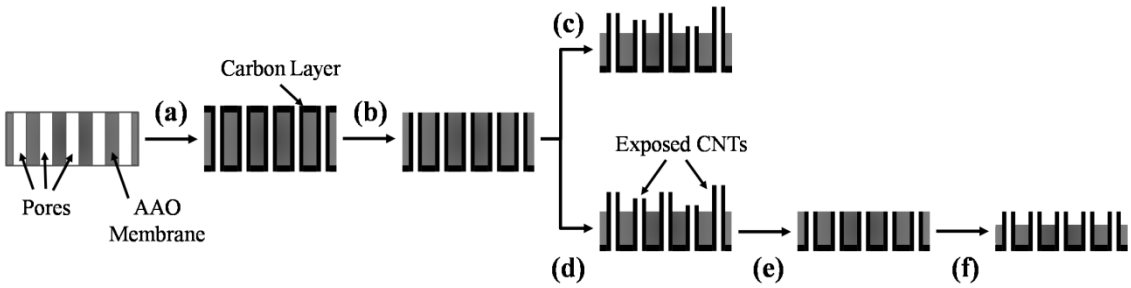

Figure 6.1: Schematic illustration of the CNT array device fabrication procedure. Fabrication process shows (a) carbon deposition by chemical vapor deposition, (b) removing the amorphous carbon layer by oxygen plasma from the surface, (c, d) exposing the CNT tips by reactive ion etching, (e) trimming the exposed CNTs by oxygen plasma, and (f) re-exposing the CNT tips by reactive ion etching.

6.2. Experimental Procedure

6.2.1. Carbon Deposition

CNT arrays were fabricated using commercially AAO membranes (Whatman Anodisc 13). CNTs were formed inside the AAO membrane using previously established processes [97], discussed in chapter 3. Briefly, AAO membranes were annealed in air at 730 °C for 4 hours and placed in a 3-stage CVD tube furnace (Carbolite TZF17/600). After purging the furnace with Argon, 30/70 (vol%/vol%) ethylene/helium precursor gas was flowed at 60 sccm into the furnace at 700 °C for 5 hours to deposit a thin film of carbon on all surfaces of the AAO membrane, including the walls of the membrane pores to form CNTs embedded in the AAO template.

6.2.2. CNT Tip Exposure

CNT tips were exposed using an alteration of peviously discussed process in chapter 4. After the CVD, the carbon layer on one side of the membrane was removed using oxygen plasma (LAM 490) at 300 mTorr, RF 250 W and oxygen flow rate of 100 sccm for 3.75 minutes. CNTs were partially exposed by selectively etching the AAO template using RIE (PlasmaTherm720/740 Etcher). To introduce CNT tip roughness, the AAO templates were partially removed using a 1 step manufacturing process. Here, the CNTs were exposed using RIE with 100% boron trichloride (BCl_3) gas at 15 mTorr, RF 250 W and 100 sccm of total gas flow rate for 2, 2.5, 3, 3.5 and 4 hours. On the other hand, to create a uniform and co-planar exposed CNTs, a 2 steps manufacturing process was followed. First, the AAO templates were etched with 80%/20% mixture of boron trichloride (BCl_3) and argon (Ar) gas, respectively, at 15 mTorr, RF 250 W and 100 sccm of total gas flow

rate for 6 hours. The exposed CNTs were trimmed using oxygen plasma at 300 mTorr, RF 250 W and oxygen flow rate of 100 sccm for 3.5 minutes. Then, the CNTs with a co-planar tips were exposed again using RIE with 80%/20% mixture of BCl_3 and Ar gas, respectively, at 15 mTorr, RF 250 W and 100 sccm of total gas flow rate for 2, 4 and 6 hours. The resultant CNT array consisted of millions of CNTs (average tip diameter of 205±42 nm, tube wall thickness of 28±5 nm, tube-to-tube spacing of 187±36 nm) protruding from the surface of the 13 mm diameter AAO membrane. Dozens of CNT array devices were produced in a single manufacturing run and stored until needed for transfection.

6.2.3. Plasmid Preparation

The pEYFP mammalian expression vector mVenus-C1 [273] was maintained in *E.coli* DH5*a* cells. Plasmid DNA was isolated from overnight *E.coli* cultures using commercially available kits (QIAGEN Plasmid Plus Midi Kit).

6.2.4. Cell Culturing

HEK293 cells were cultured in DMEM supplemented with 10% fetal bovine serum and 1% penicillin/streptomycin at 37 °C and 5% CO_2. CNT array devices were sterilized in ethanol, dried in air for 15 minutes and submerged in DMEM for 30 minutes. Seventy five-thousand cells were counted by automated cell counter (Life technologies, Countess II) and introduced on each device and cultured for 48 hours before transfection.

6.2.5. Cell Growth Study

CNT array devices were sterilized in ethanol, dried in air for 15 minutes and submerged in DMEM for 30 minutes. Seventy five-thousand HEK293 cells were plated on the CNT array, and on a control well in a 12-well tissue culture dish and stained with 5 µM calcein-AM/ethidium homodimer-1, (Life technologies, L3224) in PBS before imaging. The CNT devices and tissue culture plates were washed 3X with PBS before imaging to eliminate unattached and free floating cells. Cell spreading and proliferation were determined by fluorescence microscopy, analyzing 20 sample images at two different magnifications (10X and 20X) and quantified using ImageJ software. The number of live cells stained by calcein-AM per surface area and the projected area of spread cells was calculated (up to 600 counts on average). The results were normalized based on the control experimet in standard tissue culture plate.

6.2.6. Cell Transfection

Transfection of cells with plasmid DNA was performed using previously established protocol [246], discussed in chapter 5. To this end, HEK293 cells were seeded and cultured on the device as described above for 48 hours. A 500 ng/µL solution of plasmid DNA encoding enhanced YFP in modified patch clamp electrode buffer (148 mM KCl, 1 mM $MgCl_2$, 5 mM EGTA, 5 mM HEPES, 2 mM creatine, 5 mM Phosphocreatin (Sodium salt), 5 mM ATP (dipotassium), pH 7.2) [274] was prepared. Transfection was conducted using a custom stage (Appendix, Fig. S7) in a tissue culture incubator for 2 hours; after which the cells were trypsinized and transferred to a 12-well tissue culture plate and cultured for 48 hours. Expression of EYFP transfected cells was monitored by

fluorescence microscopy before transfection, and every 24 hours after transfection for 2 days. Cells were then trypsinized and collected in 100 µL of complete serum-free medium (CSFM, DMEM supplemented with 2 mg/ml BSA, 25 mM HEPES pH 8.0, 1% penicillin/streptomycin, 1 ng/ml transferrin, 1.25 ng/ml insulin) for flow cytometry.

DNA transfection was conducted via lipofection for comparison. HEK 293 cells were seeded and cultured on a well of 12-well tissue culture plate for 48 hours. Lipofection was performed using commercial reagents and protocols (Polyplus Transfection, jetPRIME). In brief, 0.8 µg of plasmid DNA was added into 75 µL of jetPRIME buffer. After mixing, 2 µL of jetPRIME reagent was added to the mixture and vortexed for 10 seconds. The final mixture was incubated at room temperature for 10 minutes, and then added to 1 mL of growth medium of the cells. The cells were incubated in the lipofection solution overnight. Cells were then trypsinized and collected in 100 µL of CSFM for flow cytometry.

6.2.7. Flow Cytometry

Flow cytometry was utilized to quantify transfection efficiency from a large poulation of cells. Analysis was carried out on a BD Biosciences Accuri C6 Flow Cytometer, using 488 nm excitation/530 nm emission to detect EYFP fluorescence. A cut-off percentage of 0.1% (EYFP) positive within the control untransfected sample was used to set the gates (Appendix, Fig. S10, S11). Side scatter (SSC) data was also collected and plotted on the Y-axis vs. fluorescence intensity on X-axis. Transfection efficiency was reported as the ratio of the number of transfected live cells to the number of live cells.

6.2.8. Scanning Electron Microscopy

Following culture on CNT array device for 48 hours, HEK293 cells were fixed in 3% glutaraldehyde/0.1% sodium phosphate pH 7.4 for 30 minutes at room temperature, washed twice with PBS for 5 minutes, and then dehydrated in a graded ethanol series at room temperature, first for 10 minutes in 30% ethanol/PBS, and then successively in 50%, 70%, 85%, 95% and 100% ethanol. CNT devices with fixed and dehydrated cells were then further dried in a critical point dryer (Tousimis PVT-3B), and coated with platinum in a DC sputter coater (Denton Vacuum DESK-II). The cells were examined using a field emission scanning electron microscope (Zeiss Auriga).

6.3. Results and discussion

6.3.1. CNT Array Device Fabrication and Characterization

Vertically aligned arrays of CNTs were fabricated by exposing the CNT tips using RIE process. To this end, the AAO templates were selectively etched with a plasma mixture of BCl_3 and Ar for various etching times. A detailed study of the effect of RIE parameters on CNT exposed length was discussed in chapter 4. To introduce surface roughness and also control the exposed length of the CNT tips, two different fabrication protocols were followed. In the first manufacturing protocol, called 1 step technique, the CNTs were exposed by RIE, right after CVD and removal of the top carbon layer (Fig. 6.1c) to create exposed CNTs with non-planar surface morphology. On the other hand, using the second manufacturing protocol, called 2 steps technique, after the first RIE process, the exposed CNTs were trimmed using oxygen plasma. The planar tip-shaped CNTs were exposed again using a second RIE step (Fig. 6.1d-f). The exposed CNTs show a more planar

surface morphology while variation of the etching time can control the CNT exposed length. Figure 6.2 shows the exposed length of the CNTs as a function of RIE etching time for both protocols along with the SEM micrographs of the array devices fabricated with each protocol. The results show that for 1 step manufacturing protocol, CNTs are exposed at lengths of 336±176 nm, 311±139 nm, 350±132 nm, 436±92 nm and 536±164 nm from the AAO surface after 2, 2.5, 3, 3.5 and 4 hours of RIE, respectively. Also, for 2 steps manufacturing protocol, CNTs are exposed at lengths of 138±40 nm, 427±66 nm and 566±72 nm from the AAO surface after 2, 4 and 6 hours of RIE, respectively. This indicates that increasing the etching time, increases the CNT exposed length in an approximately linear manor (Fig. 6.2a). However, the measured standard deviations of the exposed CNTs for the 2 steps manufacturing protocol is almost 58% lower, on average, compared to the 1 step protocol. This suggests that the 2 steps technique provides more planar surface morphology compared to the 1 step protocol. This variation of surface morphology can also be observed in SEM micrographs (Fig. 6.2b-g). Note that after etching the AAO template using 1 step protocol for 2 hours of RIE, very long and widely dispersed CNTs have been exposed (Fig. 6.2b), while increasing the etching time, increases the number of exposed CNTs (Fig. 6.2c, d). However, a closer look at the CNT tips reveals a non-uniform and non-planar morphology due to the relatively lower RIE power and chamber vacuum. On the other hand, trimming the CNT tips with the second oxygen plasma provides a flat and planar surface for the second RIE process. Therefore, the CNTs fabricated by the 2 steps protocol have more uniform and planar tips (Fig. 6.2e-g).

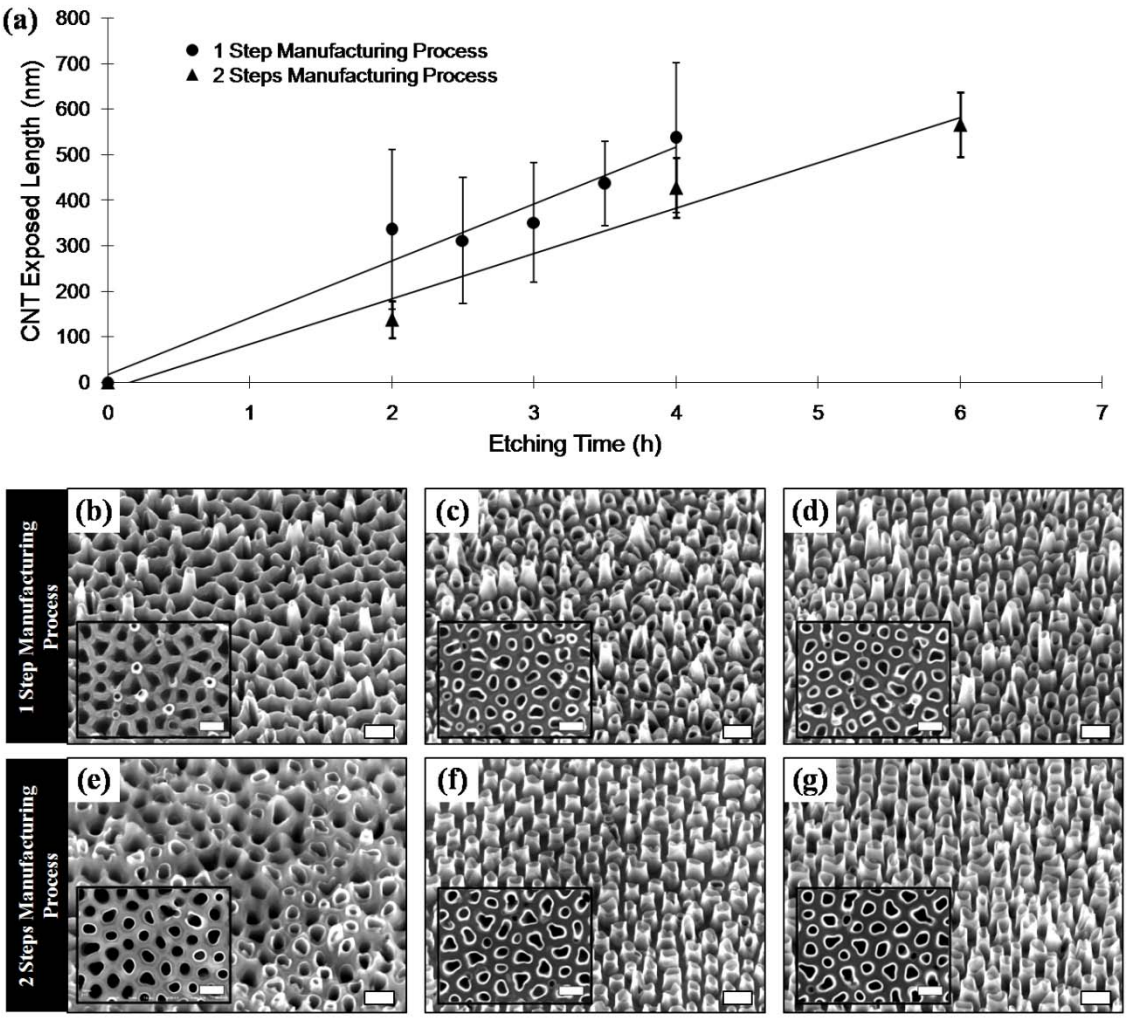

Figure 6.2: Exposing the CNT tips using two different fabrication protocols. (a) Exposed length of CNTs as a function of reactive ion etching time for 1-step (solid circle) and 2-steps (solid triangle) manufacturing processes. SEM micrographs (35° tilt) of exposed CNTs after the first RIE process for (b) 2 hours, (c) 3 hours, (d) 4 hours, and after the second RIE exposure for (e) 2 hours, (f) 4 hours and (g) 6 hours. Insets: top view SEM micrographs of each parameter setting (Scale bars: 500 nm).

6.3.2. Cell-CNT Interaction

Cells grew and proliferated on CNT arrays and the effect of surface roughness and CNT exposed length on cell growth was studied. HEK293 cells (75,000 cells) were seeded in parallel on a CNT array device, and a well of a tissue culture plate. Cells were cultured for 48 hours after which the numbers of living cells were counted using fluorescence

microscopy by staining with calcein-AM/ethidium homodimer-1, and the surface area covered by the cells was calculated, as shown in Figure 6.3. Note that the results were normalized based on the number of cells and cell spread area of the control experiment (1 corresponds to the control). The higher number of cells and the area coverage for a surface with a planar morphology suggests that it promotes cell growth and proliferation compared to the rough surface (Fig. 6.3a, b). Moreover, the results indicate that CNTs with a smoother exposed tips improve proliferation compared to the control well. On the other hand, increasing the CNT exposed length with a planar surface morphology, increases the number of cells and spread area up to a point (CNT exposed length of around 400 nm), after which it drops down, while this trend almost plateaus (considering the standard deviation) for exposed CNTs with rough surface. This could be due to the fact that longer exposed CNTs with such a relatively high packing density prevents the receptor binding [296], focal adhesion [294, 297] and van der Waals interaction [298] between the cell membrane and the substrate. This results in deformation of the nanotubes around the CNTs until it eventually makes contact with the substrate surface [293]. This phenomenon can be observed in SEM micrographs of the cells on the CNT arrays (Fig. 6.3c-k). The widely dispersed CNTs with long exposed tips causes the cells to distord and deform around the tubes, and be attached to the substrate surface (Fig. 6.3c-e). However, increasing the number of exposed CNTs and their exposed length causes the cells to be sitted on top of a "bed of tubes" in such a way that they can not make any contact to the substrate below to create focal adhesion, resulting in less CNT engolfement (Fig. 6.3i-k). Therefore, a shortly exposed CNTs with a planar surface

morphology provides a promising platfom for the cells to grow and proliferate, while engolfing the CNTs without detrimental effect [246].

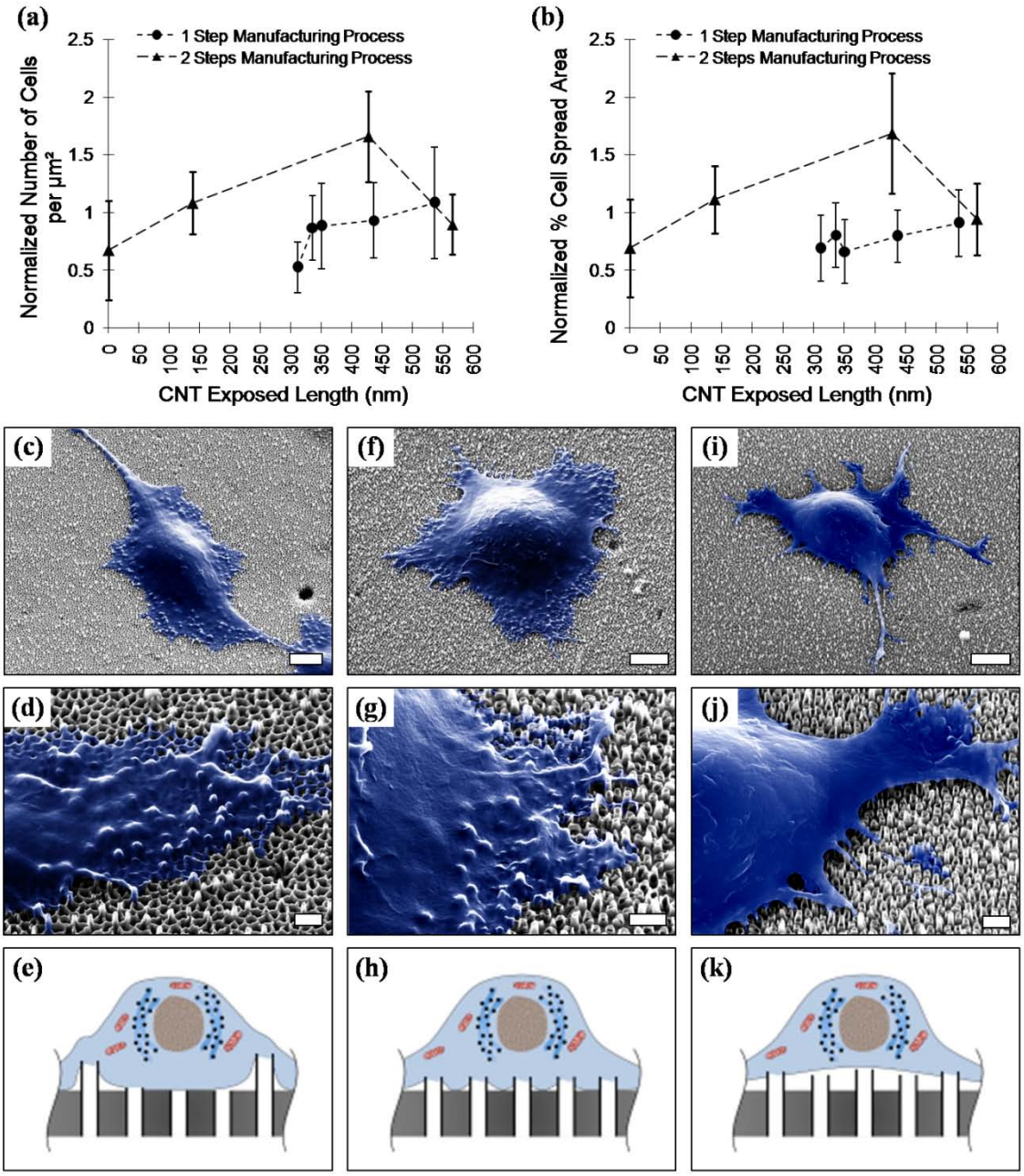

Figure 6.3: Proliferation and interaction of cells on the CNT array devices. (a, b) Cell proliferation study of HEK293 cells on CNT arrays showing the effect of exposed length of CNT tips and the surface roughness on live cell number and area covered by cells monitored 48 hours after seeding. Error bars indicate the standard deviation of 20 sampled images for each case. (X-axis error bars have been removed for clarity). SEM micrographs (35° tilt) of HEK293 cells (false colored blue) 48 hours after culturing on the CNT array devices manufacturing by 1-step protocol after (c,d) 2 hours, (f, g) 3 hours and (i, j) 4 hours of RIE process (Scale bars: 5µm). High magnification SEM micrographs of cell-CNT interface, showing (d) the extensive deformation of the cell membrane, (g) engulfment of CNTs by basal membrane, and (j) cell membrane detachment from the CNT array device surface. (Scale bars: 1µm). (e, h, k) Schematic illustration of cell-CNT interaction for each parameter setting.

6.3.3. Transfection Efficiency

The CNT arrays were used to transfer plasmid DNA into large populations of cells and the effect of surface morphology and CNT exposed length were studied on transfection efficiency, as shown in Figure 6.4. To this end, seventy five-thousand HEK293 cells were seeded on the device and cultured for 48 hours. The device was inverted and placed in the custom transfection fixture containing growth media to keep cells hydrated (Fig. 6.4b). A 50 µL drop of 500 ng/µL plasmid DNA encoding enhanced YFP was placed on the backside of the device and allowed to diffuse through the CNTs and into the cells for 2 hours in a tissue culture incubator. Cells were then trypsinized to stop transfection, collected, transferred to tissue culture plate and cultured for two days. The EYFP expression in cultured cells was confirmed by fluorescence microscopy (Fig. 6.4c, d). Note that due to variation of EYFP expression level, a gradation of fluorescence was observed, indicated as a continuum of low to high fluorescence intensity in the transfected population. The cells were then trypsinized and collected for flow cytometry. DNA transfection was also conducted via lipofection as a control experiment using commercial reagents and protocols. The results show that for the CNT array devices fabricated by 1 step process with exposed CNTs at lengths of 336 nm, 311 nm, 350 nm, 436 nm and 536 nm, the transfection efficiencies were 1.25%, 19.7%, 24.2%, 26.2% and 14.9%, respectively, with 99.7% transfection efficiency for the lipofection control. Also, for the CNT array devices fabricated by 2 steps process with exposed CNTs at lengths of 0 nm, 138 nm, 427 nm and 566 nm, the transfection efficiencies were 4%, 11.5%, 48.8% and 36.9%, respectively, with 64.6% transfection efficiency for the lipofection control.

The transfection efficiencies of the CNT array devices were normalized based on the lipofection efficiency to provide a better measure for comparison (1 corresponds to the lipofection control) (Fig. 6.4a). Quantification of transfection efficiencies by flow cytometry (up to 50,000 counts) shows that increasing the exposed length of the CNT tips up to around 400 nm, increases the transfection efficiency, after which, it reduces. On the other hand, CNT tips with a planar surface morphology show about 127% higher transfectin efficiency, on average, compared to the CNTs with non-planar tip structure. The results suggest that relatively short exposed CNTs with uniform and planar surface morphology enhances the gene transfection efficiency of populations of cells. Moreover, the peack transfection effeicincy occurs at the point that cells show higher number and spreading area, with CNTs being engolfed by the cell membrane (Fig. 6.3).

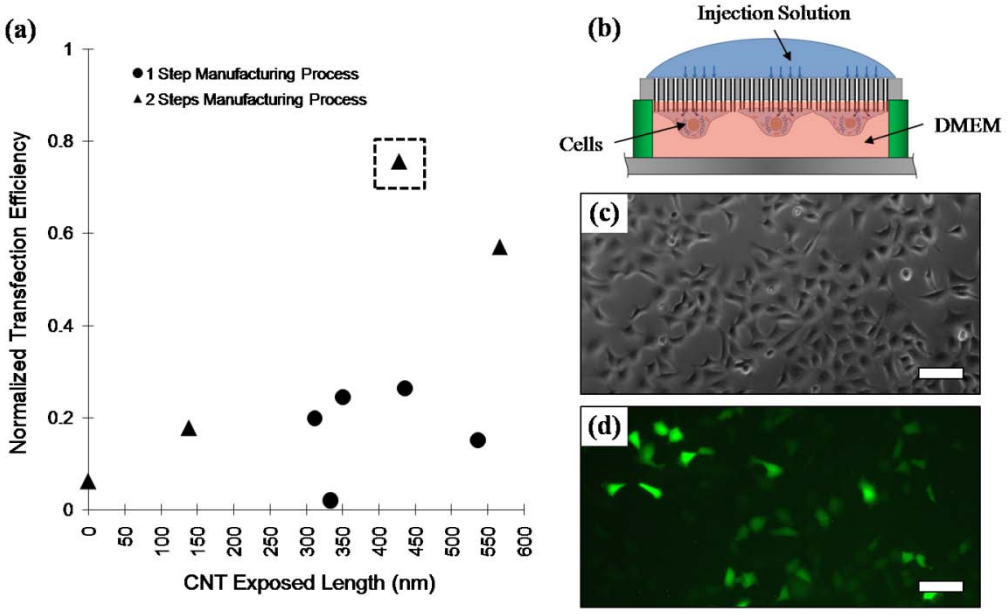

Figure 6.4: (a) The efficiency of transfected HK293 cells by plasmid DNA encoding YFP as a function of CNT exposed length for CNT devices with non-planar (1-step manufacturing process, solid circle) and planar (2-steps manufacturing process, solid triangle) CNT tip morphology (Transefection efficiencies have been normalized based on lipofection control experiemnt). (b) The schematic illustration of the transfection setup. (c) Phase image of HEK293 cells, and (d) fluorescent image of transfected cells with EYFP plasmid DNA, 48 hours after transfection for the CNT array device marked by the dashed square (Scale bars: 100 µm).

6.4. Conclusion

Vertically aligned array of CNTs were used for gene transfection of population of cells. To optimize the transfection efficiency, the effect of geometrical properties of the CNTs such as their exposed length, and the surface morphology created by the CNT exposed tips on cell transfection efficiency were studied. Arrays of hollow CNTs were fabricated via 2 different manufacturing methods. First, the carbon was deposited inside the pores of commercially available AAO membranes as a sacrificial layer. After removing the carbon layer from one side of the membrane by oxygen plasma, the CNTs were exposed using RIE. Using 100% BCl_3 plasma at relatively low RF power and chamber vacuum in 1 step, devices with non-planar surface morphology were fabricated. On the other hand, introducing Ar gas to the mixture and exposing the CNTs with 2 steps method (first exposure with RIE, trimming the CNTs with oxygen plasma, and re-exposing with RIE), created the CNTs with planar and uniform exposed tips. The exposed length of the CNTs was controlled by changing the RIE etching time. Cell proliferation and gene transfection efficiency were studied as a function of CNT exposed length and surface morphology. Increasing the CNT exposed length, increases the transfection efficiency up to certain point, after which, it drops down due to the fact that the cells can not make proper contact to the substrate through focal adhesion and receptor binding. The results also show that relatively short exposed CNTs with planar and uniform surface morphology provide a substrate over which the cells can properly grow and proliferate without cytotoxicity. Moreover, CNTs exposed with these properties are engulfed with cell membrane in such a way that the gene transfection efficiency can be improved. Note that the main intend of these experiments were to evaluate the sensitivity of the transfection efficiency with

respect to the geometrical features of exposed CNTs, in a try and error fashion. More comprehensive design of an experiment is necessary as a future work to optimize the transfection efficiency of cells using the CNT array device.

CHAPTER 7

Intracellular Gene Delivery into Hard-to-Transfect Cells through Carbon Nanotube Arrays

Gene delivery into the cell types that are resistant to the current transfection techniques is of particular importance for various biological and biomedical applications including gene editing, cellular programming and developing transgenic models. Vertical arrays of nanowires or nanotubes provide a new approach for gene delivery into hard-to-transfect cells such as stem cells and primary cells. In this chapter, an efficient transfection of these cell types using an array of vertically aligned and hollow CNTs is presented. This new platform demonstrates gene delivery into stem cells with almost 3 times higher efficiency compare to current techniques along with low cytotoxicity. This new platform has the potential to overcome size limits of current gene transfer technologies, and can be adapted to deliver drugs or proteins in addition to nucleic acids into difficult-to-transfect cells.

7.1. Gene Transfection of Resistant Cell Lines

Gene transfer into eukaryotic cells is an important tool for studying cellular biochemistry, developing transgenic models, and manipulating pluripotent stem cells [151, 299, 300].

To this end, several tools and techniques such as lipofection [301], electroporation [302], viral vector [303, 304] and gene gun [305] are available to introduce specific and controlled perturbations to cells by delivering various biological effectors like DNAs, RNAs, peptides, and proteins [306-308]. Current gene transfer technologies suffer an inverse relationship between high-efficiency transfer and cellular toxicity, and cannot efficiently transduce important cell types such as primary neurons, macrophages and stem cells. For instance, lipofection is a relatively simple transfection technique, but is toxic and non-efficient for post-mitotic cells. Viruses, on the other hand, can deliver nucleic acids to a broad range of cells, but suffer from cell toxicity and have a packaging size limit that precludes modern gene-editing techniques such as CRISPR/Cas9 [309, 310].

Nanoscale devices consisting of an array of vertical nanowires or nanotubes have been an emerging strategy that can interact with cells and transfer genetic material without chemical, viral or electrical assistance [160, 246, 272]. This strategy has the ability to deliver various biological molecules, and the potential for broad target cell compatibility and less disruption of cellular homeostasis, as discussed in chapter 6. Intracellular delivery can be done by coating the vertical rods or tubes with the cargo (nucleic acids or proteins) [166, 244, 272], or by transferring the solution containing the cargo through the open tubes over the period of several hours [160, 161]. Vertical arrays of nanotubes have been used to transfer genetic material to immortalized cell lines, but reported efficiency is quite variable (7%-70%) [161, 272, 311], and early devices have been less successful working with primary cells, and have not been used with ESC. Stem cells represent a particularly important target for nanotube devices, as high efficiency gene transfer is currently possible only by viral vectors, and nanotube devices could

alleviate concerns over lingering virus in genetically modified stem cells for therapeutic gene editing use [312].

In chapters 5 and 6, high efficient gene transfection of populations of immortalized cells with high cell viability was demonstrated using arrays of aligned CNTs. The platform has been designed so that the CNTs are closely packed and shortly exposed. This configuration allows cells to envelope the nanotubes and does not distort the cells, which enable them to grow efficiently, and be transfected with high efficiency and low toxicity. To extend this transfection method to the cell lines resistant to standard techniques, in this chapter, the cell growth and transfection results of cell types such as primary cells and stem cells are presented. Five different cell types that are resistant to standard DNA transfection techniques were investigated: macrophages (RAW264.7), human embryonic stem cells (H7-hESC), human neuronal stem cells (H7-hESC derived neural stem cells), human primary neurons (POC16-7 P1 cortical neurons) and cultured primary human skin cells. First, several surface coatings were examined to promote attachment and growth of these cells on the CNT array devices. Cell growth was scored by cell morphology on the CNT device, assayed by fluorescence microscopy and SEM, and compared to the control experiment in a tissue culture dish using standard plating conditions. The nanotubes were also examined by SEM to ensure that they are not blocked by the coatings. The ESCs and the primary human skin cells were grown on the array device for 48 hours, after which were transfected with plasmid DNA encoding enhanced YFP and the transfection efficiency was quantified using fluorescence microscopy and flow cytometry. The effect of CNT exposed length on transfection efficiency of these two cell types was studied. The results show that the gene transfection

efficiency on ESCs achieved by CNT array device is up to 3 times higher compare to the current lipofection method.

7.2. Experimental Procedure

7.2.1. CNT Array Device Fabrication

CNT arrays were fabricated using commercially available AAO membranes (Whatman Anodisc 13). CNTs were formed inside the pores of AAO membrane using previously established processes [97], discussed in chapters 3 and 4. Briefly, AAO membranes were annealed in air at 730 °C for 4 hours and placed in a 3-stage CVD tube furnace (Carbolite TZF17/600). After purging the furnace with Argon, 30/70 (vol%/vol%) ethylene/helium precursor gas was flowed at 60 sccm into the furnace at 700 °C for 5 hours to deposit a thin film of carbon on all surfaces of the AAO membrane, including the walls of the membrane pores to form CNTs embedded in the AAO template. The carbon layer on one side of the membrane was removed using oxygen plasma (LAM 490) at 300 mTorr, RF 250 W and oxygen flow rate of 100 sccm for 3.75 minutes. CNTs were partially exposed by selectively etching the AAO template using RIE (PlasmaTherm720/740 Etcher) in 2 steps. First, the AAO templates were etched with 80%/20% mixture of boron trichloride (BCl_3) and argon (Ar) gas, respectively, at 15 mTorr, RF 250 W and 100 sccm of total gas flow rate for 6 hours. The exposed CNTs were trimmed using oxygen plasma at 300 mTorr, RF 250 W and oxygen flow rate of 100 sccm for 3.5 minutes. Then, the CNTs with a co-planar tips were exposed again using RIE with 80%/20% mixture of BCl_3 and Ar gas, respectively, at 15 mTorr, RF 250 W and 100 sccm of total gas flow rate for 2, 4

and 6 hours. Dozens of CNT array devices were produced in a single manufacturing run and stored until needed for transfection.

7.2.2. Plasmid Preparation

The pEYFP mammalian expression vector mVenus-C1 [273] was maintained in *E.coli* DH5*a* cells. Plasmid DNA was isolated from overnight *E.coli* cultures using commercially available kits (QIAGEN Plasmid Plus Midi Kit).

7.2.3. Cell Culturing

Macrophages (RAW264.7) and primary human skin cells were cultured in DMEM supplemented with 10% fetal bovine serum and 1% penicillin/streptomycin at 37 °C and 5% CO_2. Seventy five-thousand cells were counted by automated cell counter (Life technologies, Countess II) and introduced on each device and cultured for 48 hours. Human embryonic stem cells (H7 (WA07)-hESC), human neuronal stem cells (H7-derived NSCs) and human primary neurons (POC16-7 P1 cortical neurons) were cultured in complete mTeSR1 medium (STEMCELL Technologies, 05850) at 37 °C and 5% CO_2. The H7-hESCs were plated on the CNT array device at 30-50% of the cell density prior to passage and H7-derived NSCs were plated as single cells at 200,000 cells/m^2. Note that the CNT array devices were sterilized in ethanol, and dried in air for 15 minutes before cell seeding.

7.2.4. Cell Growth Study

To promote cell adhesion, 4 different surface coatings at various concentrations were prepared and utilized following the manufacturer protocols: matrigel (Corning, Matrigel matrix 354248), recombinant human laminin-521 (ThermoFisher Scientific, A29249), a combination of poly-L-lysine (PLL, Sigma-Aldrich, P8920) and laminin (LN, Sigma-Aldrich, L2020) at 0.2, 1 and 5 µg/mL, and a combination of fibronectin (FN, Sigma-Aldrich, F1141) and laminin (LN, Sigma-Aldrich, L2020) at 5 µg/mL. Cells were plated on the coated CNT array device and on a control tissue culture dish for 48 hours; after which, stained with 200 nM calcein AM (Life technologies, L3224) and 5 ng/mL Hoechst (Sigma-Aldrich, H6024) in PBS and imaged by fluorescence microscopy. The CNT arrays were then imaged by SEM to examine tube blockage due to surface coating.

7.2.5. Cell Transfection

Transfection of cells with plasmid DNA was performed using previously established protocol [246], discussed in chapter 5. To this end, H7-hESC and primary human skin cells were seeded and cultured on the device as described above for 48 hours. A 500 ng/µL solution of plasmid DNA encoding enhanced YFP in modified patch clamp electrode buffer (148 mM KCl, 1 mM $MgCl_2$, 5 mM EGTA, 5 mM HEPES, 2 mM creatine, 5 mM Phosphocreatin (Sodium salt), 5 mM ATP (dipotassium), pH 7.2) [274] was prepared. Transfection was conducted using our custom stage in a tissue culture incubator for 1.5 (for H7-hESC) and 2 hours (for primary human skin cells); after which the cells were trypsinized and transferred to a 12-well tissue culture plate and cultured for 48 hours. Expression of EYFP transfected cells was monitored by fluorescence

microscopy before transfection, and every 24 hours after transfection for 2 days. Cells were then trypsinized and collected in 100 µL of complete serum-free medium (CSFM, DMEM supplemented with 2 mg/ml BSA, 25 mM HEPES pH 8.0, 1% penicillin/streptomycin, 1 ng/ml transferrin, 1.25 ng/ml insulin) for flow cytometry.

DNA transfection was conducted via lipofection for comparison. H7-hESC and primary human skin cells were seeded and cultured on a well of 12-well tissue culture plate for 48 hours. Lipofection was performed using commercial reagents and protocols (Polyplus Transfection, jetPRIME). In brief, 0.8 µg of plasmid DNA was added into 75 µL of jetPRIME buffer. After mixing, 2 µL of jetPRIME reagent was added to the mixture and vortexed for 10 seconds. The final mixture was incubated at room temperature for 10 minutes, and then added to 1 mL of growth medium of the cells. The cells were incubated in the lipofection solution overnight. Cells were then trypsinized and collected in 100 µL of CSFM for flow cytometry.

7.2.6. Flow Cytometry

Flow cytometry was utilized to quantify transfection efficiency from a large poulation of cells. Analysis was carried out on a BD Biosciences Accuri C6 Flow Cytometer, using 488 nm excitation/530 nm emission to detect EYFP fluorescence. A cut-off percentage of 0.1% (EYFP) positive within the control untransfected sample was used to set the gates (Appendix, Fig. S12, S13). Side scatter (SSC) data was also collected and plotted on the Y-axis vs. fluorescence intensity on X-axis. Transfection efficiency was reported as the ratio of the number of transfected live cells to the number of live cells.

7.2.7. Scanning Electron Microscopy

Following culture on CNT array device for 48 hours, cells were fixed in 3% glutaraldehyde/0.1% sodium phosphate pH 7.4 for 30 minutes at room temperature, washed twice with PBS for 5 minutes, and then dehydrated in a graded ethanol series at room temperature, first for 10 minutes in 30% ethanol/PBS, and then successively in 50%, 70%, 85%, 95% and 100% ethanol. CNT devices with fixed and dehydrated cells were then further dried in a critical point dryer (Tousimis PVT-3B), and coated with platinum in a DC sputter coater (Denton Vacuum DESK-II). The cells were examined using a field emission SEM (Zeiss Auriga).

7.3. Results and Discussion

In previous studies discussed in chapters 5 and 6, immortalized cells such as HEK293 and rat L6 myocyte cells have not required pre-coating for adhesion to the CNT device [246]. However, cells such as primary neurons and stem cells often require a surface coating to adhere to a substrate. Therefore, different coating regimes were examined to enhance cell adherence, and cells were scored by morphology using fluorescence microscopy. The CNT devices were coated with various concentrations of substrates known to promote adhesion of primary neurons and stem cells, which act as an artificial basement membrane, including matrigel, recombinant human laminin-521, a combination of poly-L-lysine (PLL) and laminin (LN), and a combination of fibronectin (FN) and laminin (LN). Cells were plated on the coated devices and grown for 48 hours, and then stained on the device with calcein-AM (live cells) and Hoechst dye (nuclei) and imaged with fluorescence microscopy. As control, parallel experiments were carried out with

cells plated in duplicate wells of a tissue culture dish using standard plating conditions. The results show that the H7-hESCs adhered best when plated on a thin layer of matrigel or 0.5 μg/cm^2 recombinant laminin-521, as illustrated in Figure 7.1. They exhibit typical and tightly packed colony morphology with prominent nucleoli on both glass coverslip (Fig. 7.1a, b) and CNT array (Fig. 7.1c-f) surfaces. The neuronal stem cells (NSCs) also adhered well on CNT coated with a thin layer of matrigel. The fluorescent images indicate similar neural rosette morphology on matrigel thin-layer coated glass coverslip (Fig. 7.1g, h) and CNT array (Fig. 7.1i, j) surfaces. The CNTs were also images by SEM after coating and the micrographs show that the coating materials do not block the nanotubes (Fig. 7.1k-m).

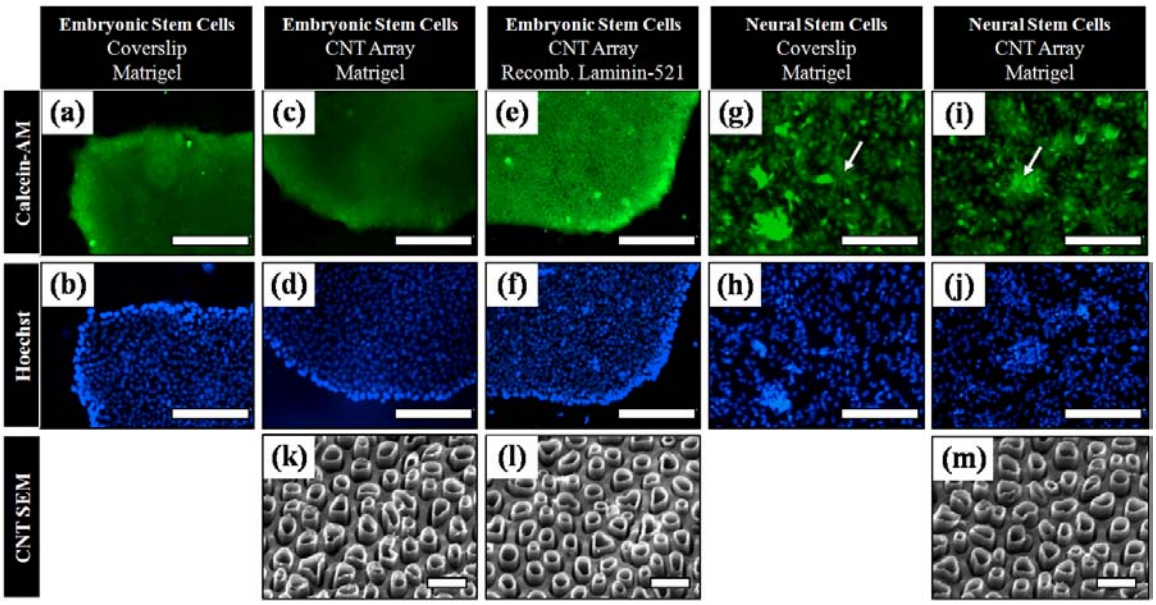

Figure 7.1: Attachment and growth of (a-f) H7 human embryonic stem cells and (g-j) H7-derived neural stem cells on CNT array device and standard coverslip for different surface coatings (Scale bars: 200 μm). Live cells imaged after calcein-AM and Hoechst labeling. H7 hESCs exhibit a typical, tightly packed colony morphology with prominent nucleoli on both (a, b) glass coverslip and (c-f) CNT array device. The white arrows show neural rosette morphology on matrigel thin-layer coated (g, h) glass coverslip and (i, j) CNT array surface. SEM micrographs (35° tilt) of CNTs after surface coating with (k, m) matrigel and (l) human recombinant laminin-521, indicating nanotubes with no blockage (Scale bars: 500 nm).

The primary neurons adhered best with the combination of PLL and LN. According to Figure 7.2, CNT arrays with no surface coating show low cell attachment with very poor cell survival (<1%) (Fig. 7.2a-c). However, increasing the concentration of PLL and LN from 0.2 to 5 µg/mL, improves the cell attachment (Fig. 7.2d-i), with highest cell survival rate at 5 µg/mL of PLL and LN (Fig. 7.2j-l). Note that the macrophages and primary human skin cells did not require any surface coating for proper attachment to the array of CNTs.

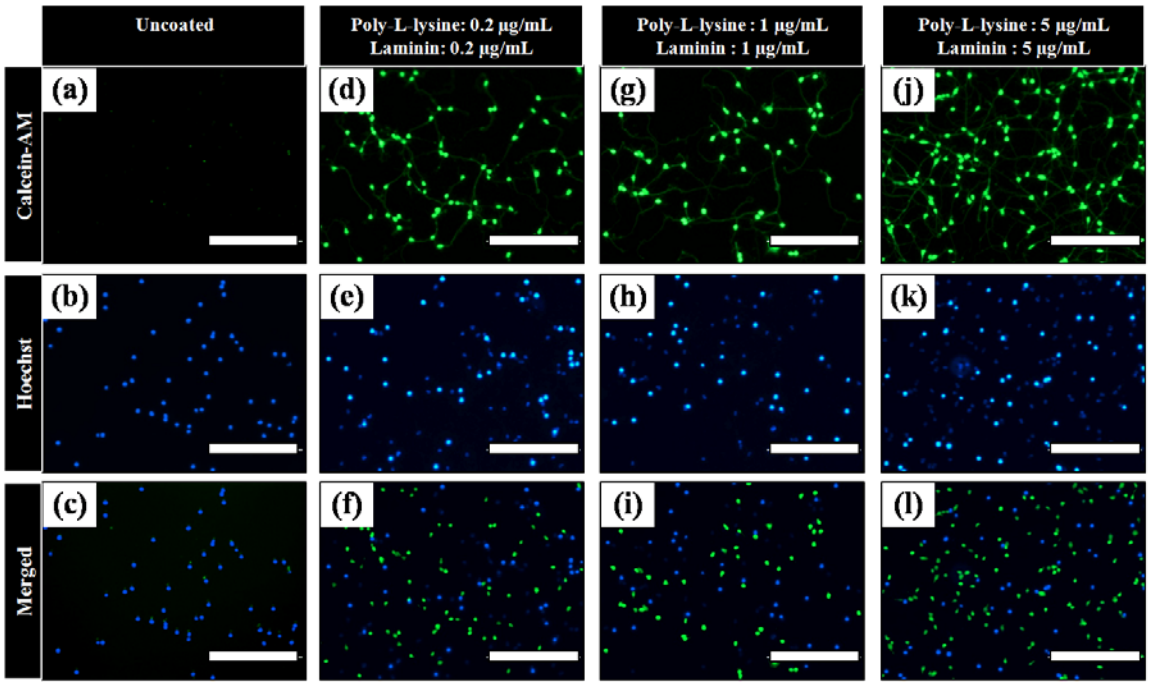

Figure 7.2: Attachment and growth of POC16-7 P1 cortical neurons on CNT array device (a-c) without surface coating, and with a coating of (d-f) a combination of 0.2 µg/mL of poly-L-lysine and 0.2 µg/mL of laminin, (g-i) a combination of 1 µg/mL of poly-L-lysine and 1 µg/mL of laminin, and (j-l) with a combination of 5 µg/mL of poly-L-lysine and 5 µg/mL of laminin (Scale bars: 200 µm). Live cells imaged after calcein-AM and Hoechst labeling.

The cells were also imaged by SEM to observe their interaction with array of CNTs, as illustrated in Figure 7.3. The micrographs show that primary neurons properly attach to the CNT arrays and efficiently proliferate, such that they create axons connecting each

of the cells to one another (Fig. 7.3a). Also, the NSCs show neural rosette morphology indicating their proper growth over the coated device (Fig. 7.3b). However, the macrophages are attached properly to the CNT arrays without any coating (Fig. 7.3c).

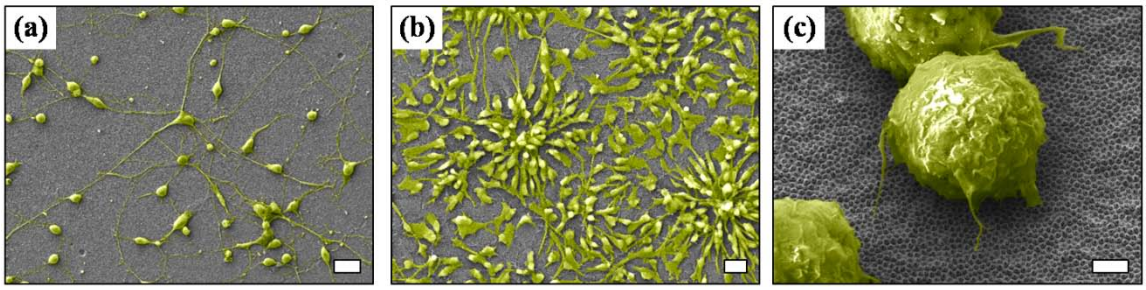

Figure 7.3: Cell attachment to the CNT array device and cell-CNT interface. SEM micrographs (35° tilt) of (a) POC16-7 P1 cortical neurons plated on CNT array device coated with poly-L-lysine and laminin (Scale bar: 20 µm), (b) H7-derived neural stem cells plated on CNT array device coated with matrigel (Scale bar: 20 µm) and (c) RAW264.7 macrophage cells plated on CNT array device without surface coating (Scale bar: 2 µm). All cells are false colored in yellow.

Two different cell types were selected to be transfected by plasmid DNA using the CNT arrays and the effect of CNT exposed length on transfection efficiency was studied, as shown in Figure 7.4. To this end, H7-hESC and primary human skin cells were seeded on the device and cultured for 48 hours. The device was inverted and placed in the custom transfection fixture containing special growth media for each cell type to keep the cells hydrated. A 50 µL drop of 500 ng/µL EYFP plasmid DNA was placed on the backside of the device and allowed to diffuse through the CNTs and into the cells for 1.5 (for H7-hESCs) and 2 hours (primary human skin cells) in a tissue culture incubator. Cells were then trypsinized to stop transfection, collected, transferred to tissue culture plate and cultured for 2 days. The EYFP expression in cultured cells was confirmed by fluorescence microscopy (Fig. 7.4b-k). The cells were then trypsinized and collected for flow cytometry. DNA transfection was also conducted via lipofection as a control

experiment using commercial reagents and protocols. The results show that for the CNT array devices with exposed CNTs at lengths of 0 nm, 138 nm, 427 nm and 566 nm, the transfection efficiencies were 1±0.5%, 1.5±0.8%, 1.2±1.1% and 1.8±1.1%, respectively, with 0.4±0.3% transfection efficiency for the lipofection control for H7-hESCs (2 experiemnts); and they were 1.6%, 5.8%, 4.8% and 2.9%, respectively, with 7.9% transfection efficiency for the lipofection control for primary human skin cells (1 experiment).

The transfection efficiencies of the CNT array devices were normalized based on the lipofection efficiency to provide a better measure for comparison (1 corresponds to the lipofection control) (Fig. 7.4a). Quantification of transfection efficiencies by flow cytometry (up to 100,000 counts) shows that transfection efficiency is almost 3 times higher, on average, uisng vertically aligned CNT array compare to lipofection, which indicates that the CNT array can promote tansfection for H7-hESCs. Moreover, lipofected ESCs shows tranfected cells only at the edge of the island colonies (Fig. 7.4f), while the CNT array transfects ESCs even inside the colonies (Fig. 7.4b-e). Moreover, the highest transfection efficiency occurs at the longest exposed CNTs (around 600 nm). Although the transfection efficiency of the primary human skin cells are lower compare to the lipofection method, the peack transfection efficiency using CNT arrays happens at the shortest CNT exposed lenght (around 140 nm) (Fig. 7.4h).

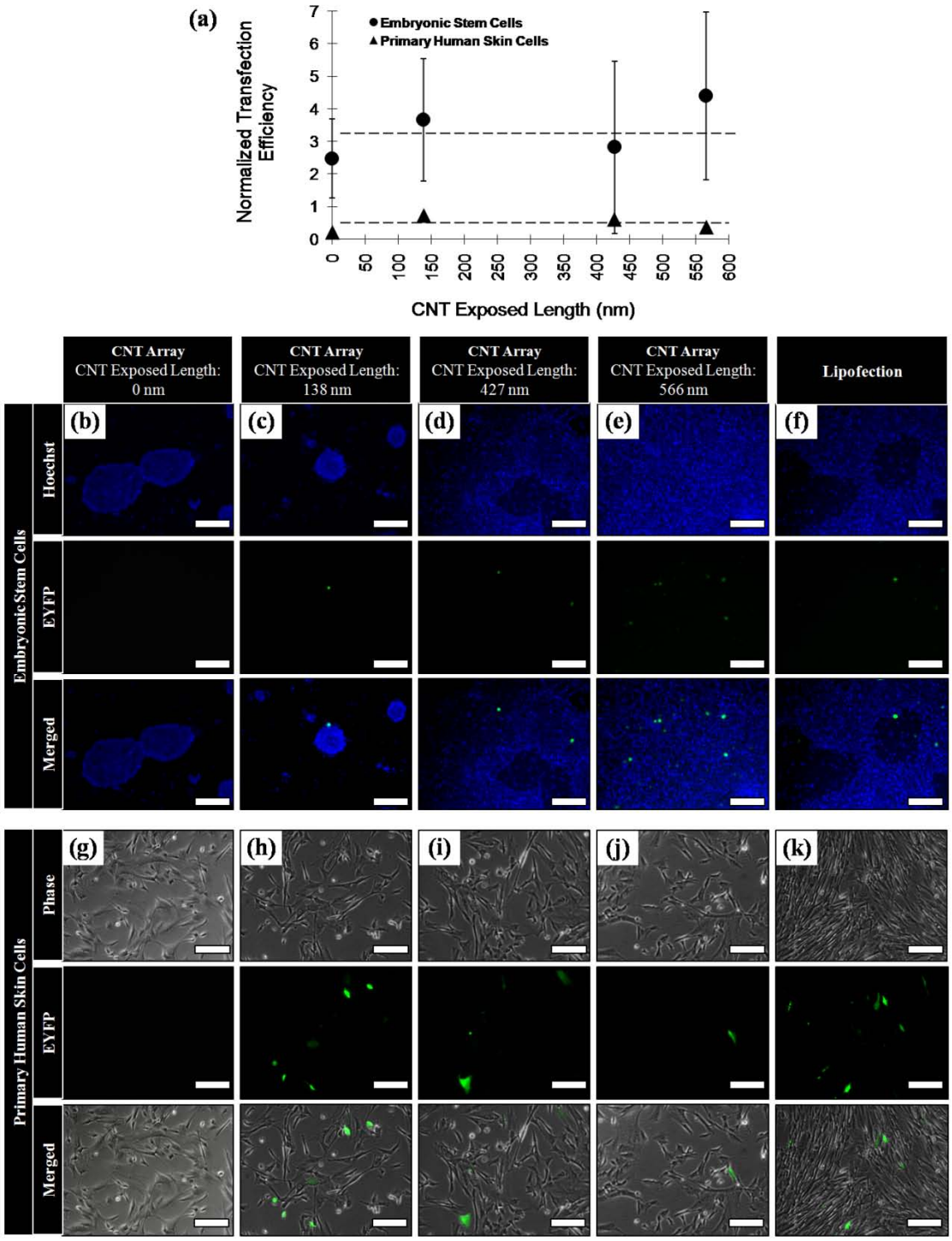

Figure 7.4: (a) The efficiency of transfected H7 human embryonic stem cells (solid circle) and primary human skin cells (solid triangle) by plasmid DNA encoding YFP as a function of CNT exposed length. Transefection efficiencies have been normalized based on lipofection control experiemnt (Error bars are the result of two experiments). Fluorescent images of transfected (b-f) H7 human embryonic stem cells and (g-k) primary human skin cells showing the EYFP expression after transfection using the CNT array device and conventional lipofection method (Scale bars: 200 μm).

7.4. Conclusion

Vertically aligned arrays of CNTs were used to deliver gene into hard-to-transfect cells. Several cell types which are resistant to current transfection techniques were seeded and cultured over the CNT arrays. To promote cell attachment, the device surface was coated with several materials. Results show that the ESCs attach well to the surface coated with matrigel or recombinant laminin-521. The NSCs adhere best to the surface coated with a thin layer of matrigel. Primary neurons show high survival rates and great cell attachment by using a combination of PLL and LN. However, the macrophages and primary human skin cells were cultured on the CNT arrays without any coatings. The primary human skin cells and the H7-hESCs were transfected by plasmid DNA using the CNT array device. The transfection results of the H7-hESCs show that the efficiency of gene delivery is almost 3 times higher, on average, compared to current lipofection method. However, the transfection efficiency of primary skin cells using the CNT array device is lower compared to lipofection control. It should be noted that the cells qualitatively look healthier under the microscope after being transfected by CNT array device compared to lipofection. However, more experiments need to be conducted to quantitatively validate this point.

To evaluate the pluripotency of the stems cells after transfection, several assays and techniques can be used. To this end, the SCOREcard assay can be utilized for hESCs, through which it assesses pluripotency and trilineage differentiation potential using quantitative polymerase chain reaction technique [313, 314]. This provides the ability to compare the gene expression profiles of hESCs to a common reference set, which elucidates that the cells have not been differentiated. The in vitro sphere formation assay

can also be employed for hESCs and NSCs as a marker free methodology to identify the stem-like cells from differentiated cells [315, 316]. To better quantify the success of the transfection process, western blot method can be used to identify the proteins resulted from transfection of the tagged plasmid DNA into either hESCs, NSCs or even primary cells [317].

A combination of geometrical properties of the presented CNT array device (shortly exposed and densely packed CNTs) with a proper surface coating provides a platform for gene transfection of hard-to-transfect cells such as stem cells, primary cells and macrophages. Since high efficiency gene transfer to stems cells is currently limited to viral infection, which has severe size limits on the genetic material that can be transferred, the CNT array device can bypass the genetic size restriction and toxicity of the current methods, provide a new technique for high gene delivery with low toxicity. Therefore, it can be optimized for delivery of large CRISPR/Cas9 plasmids into stem cells, which would allow for faster construction of transgenic animal models and development of new therapeutic reagents. This new technology offers a significant increase in efficiency, cell viability, and ease of use compared to current standard methods, and has the potential to enable highly efficient transduction of human cells that are otherwise difficult to transduce, and as a result has the potential to accelerate the development of disease models and drug discovery.

CHAPTER 8

Conclusions and Future Opportunities

Vertically aligned array of CNTs presented in this research is a remarkable platform for intracellular transfection and biological applications. The CNT array device consists of millions of vertically aligned hollow CNTs, embedded inside the pores of a sacrificial template without the need for nanoassembly. CNT arrays provide fluidic nanochannels through which various solutions, particles and biomolecules can be transported. It was demonstrated that high efficient delivery of fluorescent dyes, Qdots and genetic materials like plasmid DNA can be conducted into populations of cells using CNT array device with high cell viability. In addition, the CNT array device can support growth of stem cells and primary cells, and transfect them with genetic material and superior efficiency compared to current methods, demonstrating the fact that it provides a platform technology for applications in diverse areas.

In order to investigate and apply CNT array device in cell studies, this research involved establishing collaborations at the intersection of mechanical engineering, nanotechnology, and cellular biology. This involved designing and efficiently fabricating CNT arrays, utilizing the technology in cell biology, and extending the applications into other fields. This chapter summarizes this research on carbon nanotube arrays for

intracellular delivery and biological applications and its impact on multidisciplinary research. The chapter concludes the dissertation by highlighting some future opportunities.

8.1. Research Summary

The ever increasing utilization of arrays of vertical nanowires and nanotubes for biological applications has demonstrated a new perspective for elucidating cellular behavior and enabled significant advances in biomolecular science, biomedical applications and new approaches to clinical diagnostics and therapeutics. On the other hand, the discovery of CNTs and the development of CNT-based platforms motivated researchers to use their multifunctional properties such as small dimensions, mechanical robustness and electrical conductivity to probe cells for such purposes as intracellular delivery and measuring cell signals. By combining the multifunctional properties of CNTs in a vertically aligned array configuration, in this research, a novel CNT-based platform was introduced for intracellular transfection of population of cells capable of in situ monitoring of cellular deliver, biomolecular sensing and cellular electrophysiology. The CNT array device can overcome the limitations of current gene transfection techniques by high efficient delivery of various particles, biomolecules and genetic materials into populations of cells with high cell viability, in a relatively short period of time and with minimal labor investment.

Chapter 1 presents the motivations behind this research and its objectives to fabricate a novel cover-slip like CNT-based platform for intracellular delivery and biological

applications. Although the envisioned applications were difficult and complex, CNT-based nanostructure research was inspired by the potential to make significant contributions to medicine and life science. However, the shortcomings of prior work and the multifunctional properties of CNT motivated this research toward an alternative, CNT-based array platform for high efficient intracellular transfection, which was introduced at the end of the chapter.

Chapter 2 reviews the literatures related to the CNT-based array platform along with a comprehensive review of the current carbon nanostructures and CNT-based tools for various biological applications. Various template-based CNT manufacturing methods were introduced. The advantages of using AAO membranes as a sacrificial template for CNT fabrication and the detailed manufacturing process of the AAO membranes were discussed. Moreover, the advantages and disadvantages of current cell transfection techniques such as lipofection, electroporation and viral vectors were explained. Finally, the current vertically aligned array devices for intracellular transfection were introduced.

Chapter 3 describes the template-based fabrication of CNTs by CVD process using AAO membranes as sacrificial template. Various commercially available AAO membranes from two different manufacturers (Whatman and Synkera) were characterized in detail. The Whatman AAO membranes were used to form CNTs and manufacture the CNT devices due to its longer interpore distance and cheaper price. Carbon deposition over the AAO membranes was carried by CVD process. The effect of deposition time, temperature and precursor gas flow rate on carbon deposition and CNT wall thickness were studied. Increasing the deposition time and temperature increases the carbon deposition and CNT wall thickness, while they both reach to a peak at a certain

point by increasing the gas flow rate. No morphological differences were observed between the CNTs fabricated with different CVD parameters.

Chapter 4 illustrates the fabrication of the CNT array device after carbon deposition described in chapter 3. The CNTs were exposed using three different etching processes: RIE, wet chemical etching, and a combination of ion milling and wet etching. The effect of fabrication parameters on CNT tip exposure were studied as a function of etching time, RF power and plasma mixture for RIE process, as a function of etching time, etchant temperature and molarity for wet chemical etching process, and as a function of etching time for ion milling process. Results show that to create individually addressable exposed CNTs, dry etching processes such as RIE are more promising. Moreover, the fluidic performance of the CNT array device was characterized for two different fluid transportation mechanisms: active fluid transportation due to pressure gradient, and passive fluid transportation due to concentration gradient.

Chapter 5 demonstrates high efficient transfection of population of cells (84% - 98%) using CNT array device. Two different cell lines were transfected by various fluorescent dye, Qdots and plasmid DNA using the CNT array device, covering the delivery of a range of cargo sizes (2 – 20 nm) in a relatively short period of time (20 minutes – 2 hours). The unique geometrical configuration of the CNT array device (densely packed and shortly exposed CNTs), supported the cells growth and provided a platform for high efficient transfection of population of cells without cytotoxicity.

Chapter 6 discusses the effect of geometrical properties of exposed CNTs on transfection efficiency. Cell proliferation and transfection was studied as a function of

CNT surface morphology and CNT exposed length. The results suggest that relatively short CNTs with a co-planar surface morphology can promote cell growth and improve intracellular delivery of genetic materials.

Chapter 7 demonstrates the utilization of CNT array device for intracellular delivery of hard-to-transfect cells such as primary neurons, macrophages and stem cells. Using various surface coatings, these cells types can be grown on the CNT array device without blocking the nanotubes. Transfection of stem cells with plasmid DNA indicates that the CNT array device can promote transfection efficiency 3 times higher than current techniques such as lipofection. This suggests that the CNT array device can be used for intracellular delivery of biomolecules into cells that are resistant to the current transfection techniques, drawing a new perspective for gene editing and cell programming researches.

The CNT array device presented in this research demonstrated its capability in transfecting several cell lines, including hard-to-transfect cells such as primary cells and stem cells. The device could deliver various cargos with different molecular sizes (2 – 20 nm) and electrical charges (positive and negative) into the cells, in a relatively short period of time (20 minutes – 2 hours). High efficient transfection, high cell viability after transfection and its ease of use, categorize the CNT array device as a new platform for intracellular delivery. Moreover, using the carbon as the material to form the tubes provides a functional flexibility for the device, not only because of its biocompatibility that supports cell growth and cell attachment, but also for its electrical conductivity that offers the potential to be used as an implantable or electrochemical sensor. The unique geometrical features of the CNT array device (shortly exposed and densely packed tubes)

along with its multifunctional potential, and capability of in-situ imaging during the cell transfection, set it apart from other array platforms.

8.2. Future Opportunities

The fabrication of vertically aligned array of CNTs in a coverslip-like platform that can deliver genetic material into populations of cells with high efficiency and low cell toxicity provides a new tool and methodology for various biological applications, such as cell programming and biological sensing. This identifies a range of opportunities to expand this research and explore potential avenues, since the processes and techniques utilized in the research provide a means to produce unique devices in other fields. In short term, scaling-up the manufacturing process by using more efficient nanofabrication methods, making the CNT array device reusable, and improving the transfection efficiency by better understanding of the transfection mechanism are among the main goals. On the other hand, utilizing the CNT array device as an electrochemical or implantable biosensor, as a gene editing tool using CRISPR/Cas9, or an efficient way for cell programming in CAR T-cell therapy can be seen as the future perspective of this unique platform.

8.2.1. CNT Array Device Manufacturing Scale-Up

As explained in chapters 3 and 4, the fabrication process of the CNT array device, briefly, includes annealing the AAO membranes, carbon deposition by CVD, removing the top carbon layer by oxygen plasma and exposing the CNT tips using RIE process.

Considering this manufacturing process, and the availability of the equipments such as CVD furnace, oxygen plasma etcher and RIE machine, 60 devices can be fabricated in 2 weeks (an average of around 4 devices per day). To scale-up the manufacturing process and fabricate more and bigger CNT array devices, several avenues can be explored.

During the CVD process, the AAO membranes are placed upright in a custom quartz boat and positioned in the middle of a three-stage tube furnace. The number of AAO membranes is limited by the consistency of the temperature at the middle stage of the tube furnace, since the variation of the temperature can affect the carbon deposition. To this end, a study needs to be conducted to evaluate the effect of membrane position on carbon deposition and CNT wall thickness. Considering these results, more AAO membranes can be placed in the tube furnace to form CNTs; therefore, more devices can be synthesized in a single run.

The AAO templates that have been used in this research are circular membranes with 13 mm of diameter. Both introduced manufacturers (Whatman and Synkera), provide variety of AAO templates with various sizes and pore characteristics, including custom membranes, as illustrated in Table 8.1. By using bigger AAO membranes (e.g. 47 mm), more cells can be transfected in one attempt, improving the overall efficiency of the transfection process using CNT array devices. Moreover, availability of the AAO membranes with different pore diameters and interpore distances provide possibility of tailoring the nanotube features for targeted cell lines and application.

Table 8.1: Available ranges of commercial AAO membranes

Manufacturer	Synkera							Whatman			
Parameter	Standard						Custom	Standard			Custom
Pore Diameter (nm)	18	35	55	80	100	150	100-200	20	100	200	-
Thickness (μm)	50 and 100						15-150	60			-
Format and size	Round Shape: 13, 25, 47 mm Square Shape: 10x10 mm						Custom shape up to 120 mm in size	Round Shape: 13, 21, 43 mm			-

The RIE process, during which the AAO templates are selectively etched, is the most time consuming step of the manufacturing process due to the fact that the AAO membranes are among the most robust ceramic materials. Therefore, the RIE can be substituted by the inductively coupled plasma (ICP) process. ICP is basically an RIE process in which a much higher density of plasma can be generated, resulting in higher etch rate and more isotropic etching profile [318-320]. Moreover, other etching methods such as wet chemical etching can be explored to create a more streamlined manufacturing process.

In order to commercialize the CNT array device, an estimation of the cost for each device has been presented in Table 8.2, for the devices that are manufactured today (current), devices that could be fabricated with existing facilities but after engineering new solutions (extended), and devices that could be manufactured with an industrial sized equipment and/or more efficient processes (market ready). To this end, the cost of the AAO membranes can be estimated as $5 per template, CVD gas usage as about $15 per week, and oxygen plasma and RIE equipment as about $400 and $625 per week,

respectively. Also, the personnel cost to fabricate the devices is about $600 per week. This means that the cost of each CNT membrane can be reduced from $107 to $13, and ultimately into $7 per devices for the current, extended and market ready estimations, respectively.

Table 8.2: Cost estimation of CNT array device manufacturing for commercialization.

Item	Purpose	Production Cost ($/Week)		
		Current (16 Devices/Week)	Extended (200 Devices/Week)	Market Ready (1000+ Devices/Week)
Membrane	Device Substrate	80	1000	5000
Annealing and CVD Gases	Carbon Deposition	15	15	15
Oxygen Plasma	Surface Carbon Removal	400	400	400
RIE	Exposing CNT Tips	625	625	625
Personnel	Manufacturing	600	600	600
TOTAL		1,720 (107.5/Device)	2,640 (13.2/Device)	6,640 (6.6/Device)

8.2.2. Device Cleaning and Reusability

To reduce the fabrication cost of the CNT array devices and to increase the number of experiments that can be conducted by each device, attempts have been done to reuse the CNT arrays. In pilot studies, the devices were cleaned and sterilized after the first use and been utilized for the second gene transfection. To this end, HEK293 cells were first transfected with 500 ng/µL of EYFP plasmid DNA for 120 minutes, as discussed in chapter 5. In brief, CNTs were formed inside the pores of Whatman AAO membranes at 700 °C for 5 hours under 60 sccm flow of 30/70 (vol%/vol%) ethylene/helium precursor gas. The carbon layer on one side of the membrane was removed using oxygen plasma at 300 mTorr, RF 250 W and oxygen flow rate of 100 sccm for 3.5 minutes. CNTs were then partially exposed by selectively etching the AAO template using RIE with boron

trichloride (BCl_3) at 150 mTorr, RF 400 W and BCl_3 flow rate of 100 sccm for 180 minutes. HEK293 cells were seeded and cultured on the device as for 48 hours, and then transfected using a 500 ng/µL solution of EYFP plasmid DNA in modified patch clamp electrode buffer for 120 minutes.

The used CNT devices were then cleaned using three different protocols after trypsinizing all the cells. A CNT array device was cleaned in air at 700 °C for 4 hours using a high temperature tube furnace. Two other devices were cleaned using an alteration of previously published protocols [321, 322]. To this end, one CNT array device was first stored in 100% ethanol and the other in 1 mL PBS containing 20 µL of azide, overnight, after which, they were both submerged in 10% detergent for 30 minutes. After rinsing 3X with distilled water for 5 minutes, the devices were submerged in 4% bleach for 30 minutes, and then rinsed 3X with distilled water for 5 minutes. Finally, they were autoclaved on dry cycle. Figure 8.1 shows the SEM micrographs of the CNTs for all three devices after cleaning processes. The micrographs show that the surface of the devices is clean and the tubes are open in all cases (Fig. 8.1a-c). However, the CNT array device that cleaned at high temperature, was curled after the process (Appendix, Fig. S14), hindering its reusability, while the other two devices remained planar for next set of experiment.

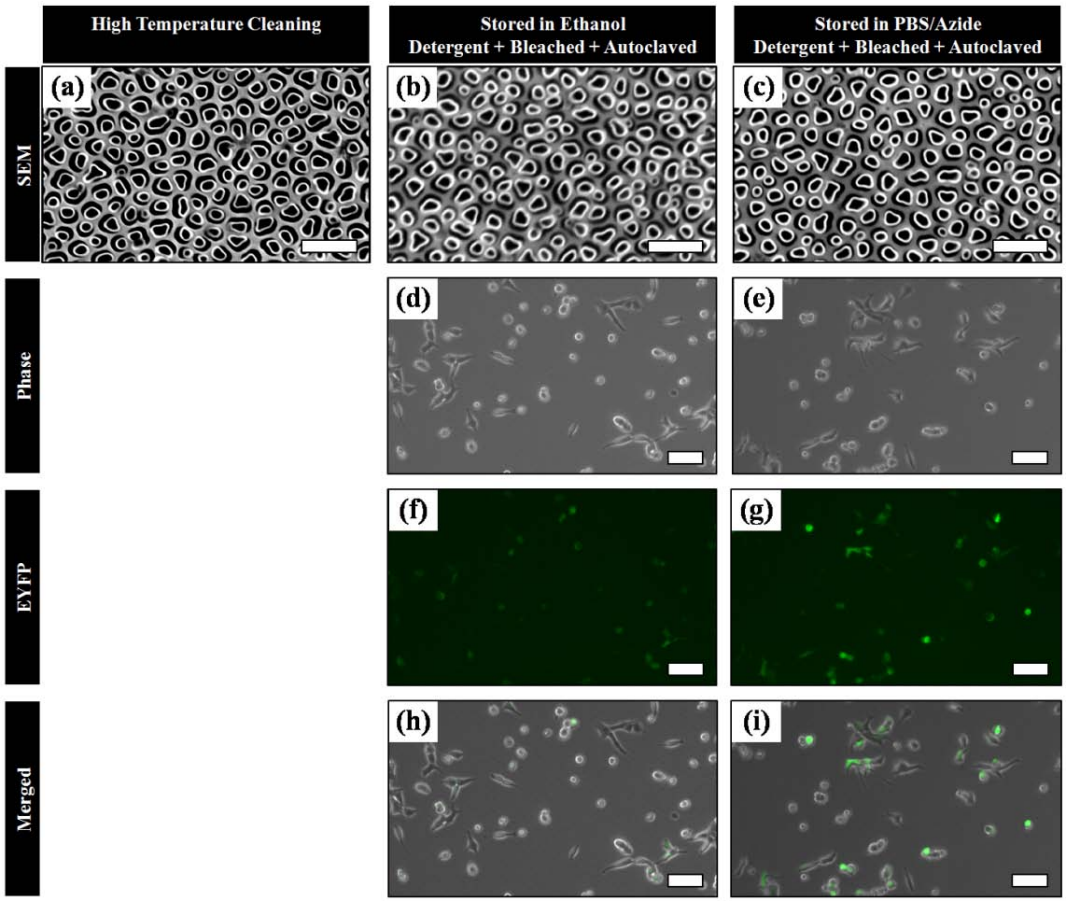

Figure 8.1: Reusability of the CNT array devices. SEM micrographs (top view) of CNT array devices after the first use for transfecting cells with plasmid DNA, cleaned (a) at high temperature, (b) by storing in ethanol or (c) in PBS/azide solution, followed by autoclaving after a post-process cleaning in detergent and bleach, indicating nanotubes with no blockage (Scale bars: 1 μm). (d, e) Phase images of HEK293 cells, and (f, g) fluorescent images of transfected cells with EYFP plasmid DNA, 48 hours after transfection for the second use of cleaned CNT array devices, indicating the possibility of reusing them (Scale bars: 100 μm). The CNT array device cleaned at high temperature couldn't be used for the second transfection due to curling of the membrane after cleaning.

CNT array devices cleaned with chemical and autoclave process were reused to transfect HEK293 cells. The cells were cultured on the devices for 48 hours, as described in chapter 5, and then transfected with 500 ng/μL of EYFP plasmid DNA for 120 minutes. The cells were then trypsinized to stop transfection, cultures on a tissue culture plate for 2 days and monitored using fluorescence microscope (Fig. 8.1d-i). The cells were then

collected for flow cytometry to quantify the transfection efficiency. The results show that 2.4% from 53% of the live collected cells are transfected for the stored device in ethanol, while 66.3% from 28% of the live collected cells are transfected for the stored device in PBS/azide solution. This indicates that although submerging the device in PBS/azide solution overnight can better clean the device compare to the ethanol, the solution has higher cytotoxicity on transfected cells. On the other hand, the overall low transfection efficiencies suggest that despite observing a clean tube surface, the CNTs might still be blocked. Considering the fact that this pilot study has been only conducted once, and although it shows that the CNT array devices can be reused, further experiments need to be conducted to achieve a proper cleaning protocol.

8.2.3. Transfection Mechanism of Cells Using CNT Array

To optimize the transfection efficiency and tailor the CNT array device for targeted cell line, the transfection mechanism needs to be studied. Two potential mechanisms for CNT-mediated transfection are: (1) direct fluidic transfer involving puncture of the cell membrane by the CNT, or (2) enhanced endocytosis as a result of cells resting on top of the bed of CNTs, which in turn do not penetrate the cell membrane, but instead act to concentrate the cargo at the cell surface and enhance endocytosis or macropinocytosis. To this end, clathrin-mediated endocytosis and pinocytosis can be inhibited by incubating cells in cytocholasin D, an inhibitor of actin polymerization that effectively blocks clathrin-mediated endocytosis [323]. Clathrin-independent endocytosis can be inhibited by incubating cells with flipin or methyl-β-cyclodextrin (mβcd), which interferes with access to cholesterol in the lipid membrane [324-326], or with Pitstop2, a protein that

blocks clathrin-independent endocytosis [327]. Conversely, endocytosis can be enhanced by incubating cells with epidermal growth factor (EGF) or platelet-derived growth factor (PDGF) [328-330]. Inhibitors or enhancers can be added to the media in the cylinder of the injection stage, bathing cells while transfecting with cargo, and inhibition or enhancement of cargo transfer can be assessed by flow cytometry. Cargo trafficking can also be monitored by fluorescence microscopy, to match cargo with sub-cellular compartments. To this end, cells cab be stained with dye while cargo is injected, using Hoechst dye to identify nuclei, and Molecular Probes'ER-tracker dye (FITC or Red) to identify endoplasmic reticulum and LysoTracker dye (Green, Red, Deep Red) to identify lysosomes. Sequential images can be acquired and merged to determine convergence of signals for sub-cellular compartment and fluorescent cargo.

Alternatively, cargo may be transferred into cells by direct fluidic access. As explained in chapter 5 and 6, the transfection efficiencies were significantly higher when cargo was diluted in buffer compatible with intracellular ion concentrations, such as this buffer used to fill patch-clamp electrodes: 1 mM MgCl2, 1 mM EGTA, 150 mM KCl, 5 mM HEPES, 0.4 mM Phosphocreatin (Sodium salt), 0.7 mM K2-ATP, 0.3 mM β-hydroxybutyric acid, pH 7.2. Derivative buffers, lacking the energy source (ATP, phosphocreatine) or containing only buffered ATP and phosphocreatine can be tested to elucidate if the enhanced effect of this buffer can be substituted by the energy components alone. An energy requirement could suggest active transport mechanism of cargo uptake.

Therefore, if nanotube transfer is mediated by endocytosis, using one of the inhibitors can inhibit cargo transfer. Alternatively, if cargo is transported by direct fluidic

transfer, there will be much more dependence on injection buffer composition, as this buffer will come in direct contact with the cytoplasm. It is particularly important to monitor where the cargo is delivered after transfection. If cargo is routed through endosomes to lysosomes, lysosome function can be disrupted by incubating cells in 20 μM leupeptide or 10 nM bafilomycin [331] prior to transfection, and monitor cargo trafficking. If cargo is trafficked to lysosome, a significant increase in injection efficiency in presence of lysosomal inhibitors can be predicted.

8.2.4. Improve the Transfection Efficiency Using the CNT Array Device

Understanding the mechanism behind intracellular transfection of cells through CNTs can significantly affect the approaches that can be taken to optimize the efficiency. However, the following methods can be considered as the general guidelines for improving the transfection efficiency:

- As described in previous section, if transfection mechanism is mediated by endocytosis, using enhancers such as EGF or PDGF [328-330], and chloroquine [332] can improve the transfection efficiency. On the other hand, if the mechanism is due to direct fluidic access, a buffer that is more compatible with cytoplasm can be utilized.
- Despite demonstration of intracellular delivery of various cargos with different molecular charges in this research, the interactions between cargo and nanotube may be ionic. Therefore, negative or positive molecules may be observed to be either aided or impeded during the transfection. To this end, counter ions can be

added to the injection buffer to mask the charge, promoting the transportation of the cargo through CNTs.

- To provide a more direct access to the intracellular environment, physical or chemical approached can be explored. After seeding and culturing the cells on the device, the cells can be pushed toward the CNTs using centrifugal force. To this end, CNT array devices coated with cells can be put in a centrifuge before transfection. On the other hand, using chemicals such as a very mild detergent (Triton X-100 at 0.17 mM) [333] or a mixture of localized dimethyl sulfoxide and latrunculin A [311] can create self-sealing transient membrane pores, enhancing the intracellular transportation of targeted molecules.
- Surface functionalization of the CNT array device can promote cell adhesion and engulfment of CNTs by cell lipid bilayer, resulting in higher transfection efficiency [334]. For example, functionalizing the nanoarrays with aminosilane can provide a stable intracellular access for transfection [251].

8.2.5. Vertically Aligned CNT Array as an Electrochemical Sensor

Aerobic cells produce reactive oxygen species (ROS), such as nitric oxide (NO), peroxynitrite and their precursor, and superoxide as part of their normal oxygen metabolism. When the need arises, they can deliberately change their normal metabolism to produce the higher levels of superoxide and ROS needed for such functions as communication, apoptotic gene expression and defense against bacteria and virus. Although there are various sources that contribute to ROS, approximately 90% of it comes from mitochondria [335]. However, excess ROS, either produced by active or

passive means, is damaging to cells and amplifies cell damage over long periods of time. To reduce the damaging effects, intracellular enzymes and antioxidants eliminate the excess ROS or repair any damage that has been done. However, oxidative stress occurs if an acute or chronic imbalance exists between the two. Of major concern with regards to oxidative stress is the role of NO, an ROS that has been linked to many physiological or pathological situations. Nitric oxide is very interesting because it affects cells differently as a function of concentration and environmental conditions.

Unfortunately, due to the complex pathways involve and series of reactions that take place, the majority of oxidative stress mechanisms in cells and the roles of NO and other free radicals, are not fully understood or quantified. What is known of intracellular ROS is either quantified inside the cell with molecular fluorescent probes, or as it diffuses through the cell membrane with extracellular electrochemistry. In fact, over the last several years, electrochemistry has become the method of choice to help understand the intracellular generation of ROS and its role in oxidative stress, processes that are suspected to play a significant part in many human pathologies including aging, cancer, Parkinson and Alzheimer diseases, autoimmune pathologies and arthritis [335].

Whether randomly dispersed or grown onto conductive surfaces, the electrical properties and modifiable surfaces of CNTs enable them to be used as electrochemical sensors. Compared to conventional electrodes, CNT-based electrochemical sensors offer higher ratio of surface-area to volume which increases the signal-to-noise ratio for sensitive detection. CNT-based electrodes can be further modified by surface activation to enhance interfacial electron transfer, selectively detect analytes, or attach reagents that prevent non-specific binding but allow specific binding of analytes [336].

Randomly dispersed CNT films can be used as electrochemical sensors. For instance, ferrocene was non-covalently attached to acid-treated SWCNT films to detect glutamate [43]. The combination of SWCNTs and ferrocene provided enhanced surface area, direct electron transfer, and catalytic effect. Electrodes can also be coated with CNTs to enhance performance. As described in chapter 1, CNT-coated carbon nanoelectrodes outperformed conventional carbon fiber electrodes of similar geometry [44]. CNT coating can also enhance other electrodes, such as glassy carbon and Pt microelectrodes. It was found that CNT-coated glassy carbon electrodes offered superior performance to non-coated electrodes [337].

CNT arrays can be used directly as electrochemical sensors [59]. The low-density array exhibited sigmoidal behavior during cyclic voltammetry and provided high signal-to-noise ratio. The electrochemical sensor was used to detect glucose (as well as ascorbic acid, uric acid, and acetaminophen) by attaching glucose oxidase to the CNT surface through the EDC/sulfo-NHS linker moiety [81]. The sensor was later used to detect lead in low-electrolyte conditions [338] and trace cadmium(II) and lead(II) at sub-ppb level (detection limit of 0.04 μg/L) [339].

Electrochemical sensors have also been developed from arrays of CNTs that protrude an insulating surface. Starting with carbon nanopipettes grown on a Pt-wire substrate [340], a nanoelectrode array with protruding conical carbon tips was produced that exhibited sigmoidal electrochemical behavior [58]. By oxidizing the protruding nanoscopic tips, the sensor was able to electrochemically distinguish between ascorbic acid (oxidation-shifted peak) and dopamine. Electrochemical sensors of a similar configuration using PECVD-grown CNT arrays have also been reported [341].

Due to the conductivity of the CNT arrays, the presented device in this research can be used as an electrochemical sensor. To this end, the electrochemical performance of the device can be characterized in a two-electrode configuration (working vs reference) by cyclic voltammetry and amperometry using a model oxidation-reduction (Red-Ox) species, such as Ferri/Ferrocyanide, in aqueous environments vs a standard Ag/AgCl reference electrode. The detection limits of the probe can be determined as a function of species concentration. The performance, detection limits, and reliability can be compared to microelectrodes and other CNT-based electrochemical probes [342, 343]. The reliability and reproducibility of current-voltage measurements as functions of manufacturing variability and final effective electrode detection area can be determined.

The CNT-based probe can also be utilized in controlled bench top tests to detect and measure NO. In this case, the device can be submerged, first in a standard supporting electrolyte (0.1 M KCl), then in intracellular buffer, and configured as a working electrode, in two-electrode electrochemical system. Bench top testing will mimic scenarios to be encountered in intracellular electrochemistry. Amperometry can be utilized to detect and measure the oxidation of NO in buffer as a function of concentration (maximum sensitivity is 700 mV vs. Ag/AgCl [344]). Controlling the amount of NO_2 bubbled in water can produce various concentrations of NO. Therefore, the oxidation potential can be adjusted according to potentiometric findings in model Red-Ox experiments. The reliability and reproducibility of current-voltage measurements as functions of manufacturing variability and final effective electrode detection area can be evaluated and compared to those determined in model experiments. The detection limits of NO can be compared, to those published for extracellular electrochemistry [345].

The CNT array device can also measure intracellular NO, electrochemically. Cells can be cultured on tissue culture plate. The device can be connected to a low-current potentiostat such that it acts as the working electrodes. Using Ag/AgCl reference electrode and amperometry, with the optimum NO oxidation potential applied between the two electrodes, Brandykinin can be added to the extracellular solution by a pipette to simulate NO release, as illustrated in Figure 8.2. Changes in current can be recorded and correlated to NO concentration.

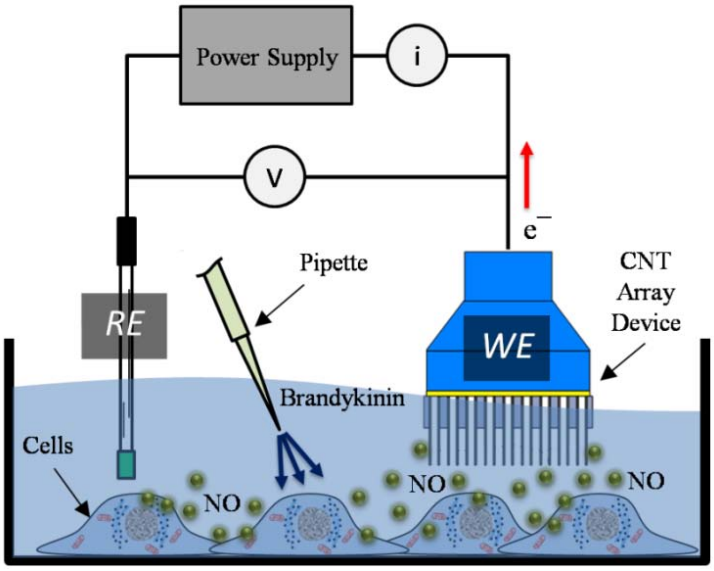

Figure 8.2: Schematic illustration of the electrochemical setup for extracellular NO detection using CNT array device. In this 2-electrode cell, the WE and RE are used for voltage and current measurement.

8.2.6. CNT Array Device as an Implantable Sensor

The ability to track implanted cells and to monitor the progress of tissue formation *in vivo* is important especially in large biological organisms and tissue engineering [346]. Labeling implanted cells would not only help in evaluating the viability of the tissue but would also help in understanding the distribution and migration pathways of transplanted cells. Traditional methods such as intravital microscopy or flow cytometry are extremely

time-consuming and challenging. However, there remains a need for contrasting agents that are biocompatible, and stable over long periods of time, and provide high image contrast between labeled and unlabeled specimens. Preliminary work has suggested CNTs are feasible imaging contrast agents for optical imaging [347], magnetic resonance imaging (MRI) [348], and radio-tracking [349].

Carbon nanoparticle contrasting agents have also been employed to monitor physiological events of single cells such as ion transport, enzyme/cofactor interactions, protein secretion, and matrix adhesion. Tissue and cellular responses have been observed using other nanoparticle contrast agents such as inflammation of pancreatic islets [350], apoptosis [351-353], and angiogenesis [354, 355]. The ability to monitor apoptosis and angiogenesis with relatively high spatial resolution would be advantageous not only to cell and tissue culturing but also monitoring disease progress and therapeutic responses. To complement intracellular nanocarbon-based contrasting agents, nanosensors could be employed to provide continuous monitoring of the performance of the cultured tissues.

One method of monitoring tissue *in vivo* would be to use implantable sensors capable of relaying information outside the body. Such a sensor would provide real time data related to the physiological relevant parameters such as pH [356], pO_2, and glucose levels [81, 127]. There are several advantages to use nanosensors for evaluating tissues *in vivo*. First, because the sensing element is nanosized and the overall probe miniaturized, implanting within tissue would not adversely disturb the system. Second, due to the large surface-to-volume ratio, a relatively large active area is available for immobilizing numerous biological and chemical compounds including DNA [357] and proteins [358] for improved sensitivity.

MWCNT electrodes have been developed to monitor the electrochemical oxidation of insulin, a pancreas-produced hormone that plays a key role in the regulation of carbohydrates and fat metabolism in the body [359]. This provides a possible method to evaluate the quality of pancreatic islets prior to their transplantation. By coating similar MWCNT electrodes with platinum microparticles, thiols containing amino acids can be detected in rat striatal [360]. CNT-based sensors can be incorporated into flexible biocompatible substrates to facilitate *in vivo* sensing. For instance, free cholesterol in blood can be measured using MWCNT electrodes placed on a biocompatible substrate [361] while flexible pH sensors can be formed from polyaniline and nanotube composites [362].

Carbon nanostructured surfaces and scaffolds have been shown to not hinder but promote cell growth. For example, neural cells [127] and mouse fibroblast cells [81] were successfully cultured on CNT scaffolds. The findings encourage the application of nanostructured carbon devices as implantable sensors and tissue scaffolds. For instance, ectopic formation of bone tissue was observed after MWCNT scaffolds were implanted in muscle tissue, suggesting the carbon nanostructured substrates could encourage cells to grow within the body [363].

Recent advances in micro and nanofabrication techniques have provided promising new device platforms and implantable interfaces for studying neural communication. For instance, MWCNT-coated stainless steel electrodes were implanted and utilized for wide-frequency stimulation in deep brain structures, showing superior performance to uncoated electrodes [364]. An emerging but promising platform, however, are arrays of carbon nanostructures patterned on rigid or flexible substrates. In related examples, arrays of

addressable CNFs have been used for highly resolved neural stimulation and recording, providing multiple channels of electrical, chemical and mechanical information [56, 363]. In related work, vertically aligned CNFs were employed for extracellular stimulation and recording of neuroelectrical activity. Here, it was reported that despite the small size of these fibers, CNFs could inject sufficient charge to stimulate organotypic hippocampal tissue [365, 366].

As an extension to the results presented in this research, CNT array device can be used to transfect cells in tissue form for further *in vivo* monitoring of the cells. Moreover, owing to the conductivity of CNTs and the small size of the nanotubes, the CNT array device can be used as an implantable sensor. Since the biocompatibility of the device has been demonstrated in previous chapters by monitoring the cell proliferation, the CNT array device provides a promising platform to be used as an implantable sensor for *in vivo* monitoring of reagents and biomolecules such as insulin or blood cholesterol.

To this end, pilot studies were conducted to characterize the electrical conductivity of the embedded CNT arrays, and also to coat the back side of the membranes with conductive material to provide a better electrical contact with CNTs. First, CNTs were formed inside the pores of AAO templates, as described in chapter 3. In brief, Whatman AAO membranes were annealed in air at 700 °C for 4 hours and placed in a 3-stage CVD tube furnace. After purging the furnace with Argon, 30/70 (vol%/vol%) ethylene/helium precursor gas was flowed at 60 sccm into the furnace at 675 °C for 5 hours to deposit a thin film of carbon on all surfaces of the AAO membrane.

To measure electrical resistance of the CNT arrays, both sides of the devices were coated with 20 µm of copper paste to provide better electrical contact. The coated CNT arrays were clamped between two electrodes in a custom stage (Appendix, Fig. S15) and the electrical resistance of the CNTs was measured using a potentiostat. To this end, 5 CNT array devices were tested and 10-15 measurements were recorded for each device. As shown in Figure 8.3, the results indicate a linear I-V curve with an average resistance of around 0.2±0.1 Ω among all the tested devices. This suggests th at the CNTs fabricated with presented CVD process has metallic electrical characteristics; a behavior that can be due to the amorphous CNT morphology, as discussed in chapter 3. More experiments are required to properly determine the electrical characteristics of these CNTs.

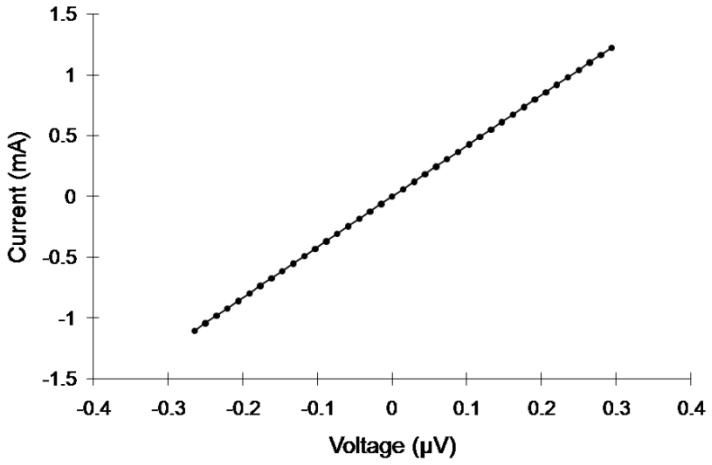

Figure 8.3: The current-voltage curve of the CNT array device, indicating the linear metallic behavior of embedded CNTs.

To provide a better and more robust electrical contact with embedded CNTs for further sensing applications, sputter coating and metal evaporation methods were utilized. CNT array devices were mounted on a proper stage and sputtered with Au/Pd for 6

minutes. The surface of the device was covered by a TEM grid to pattern the coating, simultaneously. As indicated in Figure 8.4, the line scanning EDS show that a 20 nm Au/Pd coating can be sputtered, coating the device without blocking the CNTs (Fig. 8.4a, b). Metal evaporation was also utilized to deposit a conductive layer on one side of the CNT device. Using a CHA flash evaporator, a 1 μm layer of aluminum was deposited over the device. The SEM micrographs of the device surface indicate that although the deposited aluminum layer blocks the tubes, a thick layer of conductive material can be deposited in a relatively short period of time (Fig. 8.4c, d). The results suggest that sputter coating can be used for coating the CNT array device with a thin layer of conductive material without blocking the CNTs, while metal evaporation can be used for deposition of a thicker conductive layer which blocks the tubes, providing different characteristics for intended applications of the CNT array device.

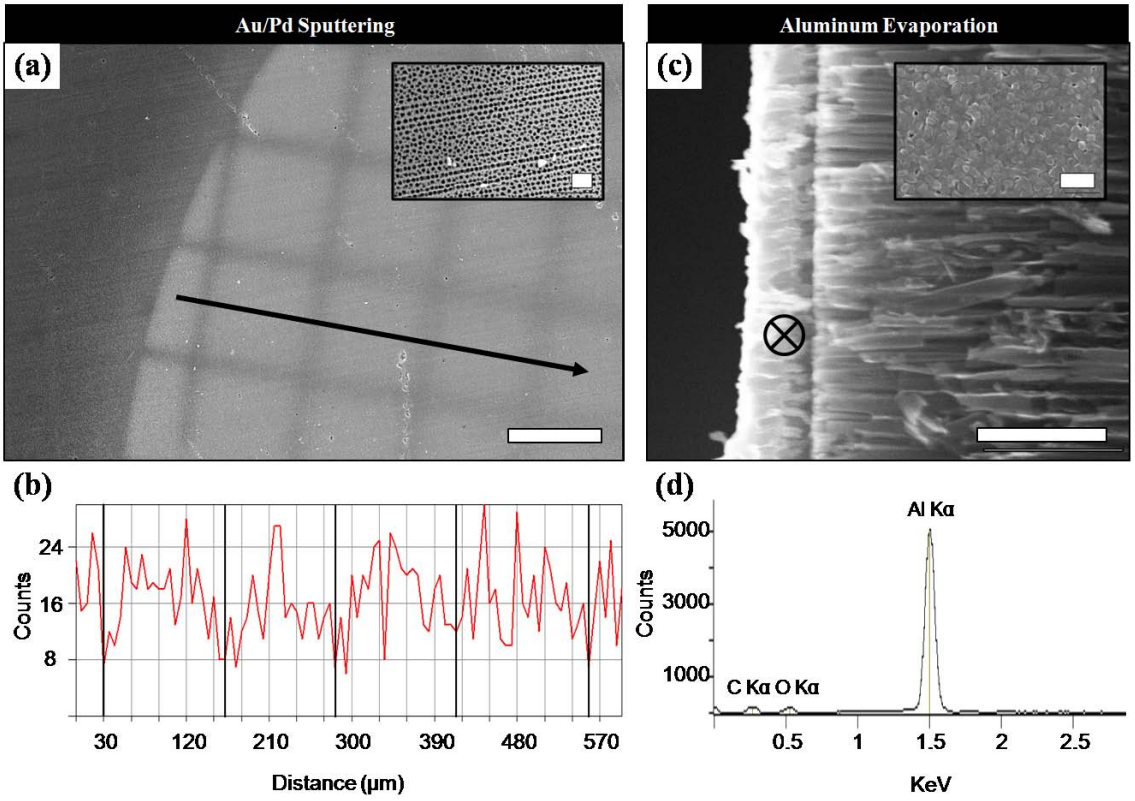

Figure 8.4: Coating the back side of the CNT array device with a conductive layer to provide better electrical connection with embedded CNTs. (a) SEM micrograph of the CNT arrays after 6 minutes of patterned sputter coating with Au/Pd (Scale bar: 100 μm). Inset: High magnification SEM micrograph (top view) of the CNT arrays, indicating nanotubes with no blockage (Scale bar: 1 μm). (b) Line-scan EDS (black arrow in a) of the Au/Pd coated CNT array surface, indicating the possibility of patterning the coating. (c) SEM micrograph (side view) of the CNT arrays after deposition of an aluminum layer using metal evaporation (Scale bar: 2.5 μm). Inset: High magnification SEM micrograph (top view) of the CNT arrays, indicating blocked nanotubes after metal deposition (Scale bar: 1 μm). (d) EDS analysis of the deposited aluminum layer (black cross in c), indicating the Al Kα peak.

8.2.7. Intracellular Delivery of CRISPR/Cas9 Complex Using CNT Array Device

The rapid development of CRISPR/Cas9-mediated genome engineering has opened the doors to unprecedented genetic manipulation of human cells. Gene editing using this technique requires the delivery of multiple genetic elements into the target cell population. Since this new method consists of complex and large components such as Cas9 enzyme and guide RNA, current transfection techniques have difficulties in delivery of these

large molecules. Moreover, maintaining the cellular viability during and after transfection is among the main challenges for the current techniques.

The CNT array device has demonstrated its capability of intracellular delivery of various biomolecules with different sizes while supporting the growth of primary and stem cells. Therefore, this platform can be utilized for delivery of large and multicomponent genetic tools such as CRISPR/Cas9 in stem cells with high efficiency and high cell viability. Bypassing the size limitations and high efficient transfection of cells using the CNT array device can lead into reduction of off-target mutation after delivery of the CRISPR/Cas9 complex, which is one of its biggest potential advantages compare to current transfection techniques.

8.2.8. T-Cell Therapy Using CNT Array Device

T-cells play a central role in cell-mediated immunity. By genetically modifying the T-cells either through altering the specificity of the T-cell receptor (TCR) or through introducing antibody-like recognition in chimeric antigen receptors (CARs), the immune response can be augmented and specific tumors can be targeted. The potential of these approaches has been demonstrated by their successful use in clinical trials. Currently, modification of the T-cells is conducted by employing viral vectors which is labor intensive, time-consuming and extremely expensive.

Building upon the capability of the CNT array device in transfection of populations of cells with high efficiency and cell viability, T-cells can be transduced in a relatively short period of time and with a less expensive protocol. However, many primary immune

cells do not adhere to any surfaces, and therefore, are grown and tranduced instead in suspension. To transfect the T-cells using CNT array device, first, they need to be adhered to the CNTs. To this end, the surface of the device can be coated with poly-L-lysine, or T-cell specific antibodies can be attached to the CNTs or by a linker to the AAO membrane using amino coupling [367, 368] to attract the cells toward the device surface.

CHAPTER 9

References

[1] F. A. Ran, P. D. Hsu, J. Wright, V. Agarwala, D. A. Scott, and F. Zhang, "Genome engineering using the CRISPR-Cas9 system," *Nat. Protocols,* vol. 8, pp. 2281-2308, 11//print 2013.

[2] M. Li, K. Suzuki, N. Y. Kim, G. H. Liu, and J. C. Izpisua Belmonte, "A cut above the rest: targeted genome editing technologies in human pluripotent stem cells," *J Biol Chem,* vol. 289, pp. 4594-9, Feb 21 2014.

[3] A. Pinzon-Charry, T. Maxwell, and J. A. Lopez, "Dendritic cell dysfunction in cancer: a mechanism for immunosuppression," *Immunology and cell biology,* vol. 83, pp. 451-461, 2005.

[4] T. Blankenstein, P. G. Coulie, E. Gilboa, and E. M. Jaffee, "The determinants of tumour immunogenicity," *Nature Reviews Cancer,* vol. 12, pp. 307-313, 2012.

[5] M. L. Davila, I. Riviere, X. Wang, S. Bartido, J. Park, K. Curran, *et al.*, "Efficacy and toxicity management of 19-28z CAR T cell therapy in B cell acute lymphoblastic leukemia," *Science translational medicine,* vol. 6, pp. 224ra25-224ra25, 2014.

[6] M. V. Maus, S. A. Grupp, D. L. Porter, and C. H. June, "Antibody-modified T cells: CARs take the front seat for hematologic malignancies," *Blood,* vol. 123, pp. 2625-2635, 2014.

[7] M. Sharpe and N. Mount, "Genetically modified T cells in cancer therapy: opportunities and challenges," *Disease Models and Mechanisms,* vol. 8, pp. 337-350, 2015.

[8] R. Saito, G. Dresselhaus, and M. S. Dresselhaus, *Physical Properties of Carbon Nanotubes* London World Scientific Publishing Co., 1998.

[9] S. Iijima, "Helical Microtubules of Graphitic Carbon," *Nature,* vol. 354, pp. 56-58, Nov 7 1991.

[10] C. R. Martin and P. Kohli, "The emerging field of nanotube biotechnology," *Nature Reviews Drug Discovery,* vol. 2, pp. 29-37, Jan 2003.

[11] G. Che, B. B. Lakshmi, C. R. Martin, E. R. Fisher, and R. S. Ruoff, "Chemical vapor deposition based synthesis of carbon nanotubes and nanofibers using a template method," *Chemistry of Materials,* vol. 10, pp. 260-267, Jan 1998.

[12] P. M. Ajayan, "Nanotubes from carbon," *Chemical Reviews,* vol. 99, pp. 1787-1799, Jul 1999.

[13] A. V. Melechko, V. I. Merkulov, T. E. McKnight, M. A. Guillorn, K. L. Klein, D. H. Lowndes, *et al.*, "Vertically aligned carbon nanofibers and related structures: Controlled synthesis and directed assembly," *Journal of Applied Physics,* vol. 97, pp. -, Feb 15 2005.

[14] R. S. Ruoff, D. Qian, and W. K. Liu, "Mechanical properties of carbon nanotubes: theoretical predictions and experimental measurements," *Comptes Rendus Physique,* vol. 4, pp. 993-1008, 2003.
[15] H. J. Dai, J. H. Hafner, A. G. Rinzler, D. T. Colbert, and R. E. Smalley, "Nanotubes as nanoprobes in scanning probe microscopy," *Nature,* vol. 384, pp. 147-150, Nov 14 1996.
[16] M. G. Schrlau, E. M. Falls, B. L. Ziober, and H. H. Bau, "Carbon nanopipettes for cell probes and intracellular injection," *Nanotechnology,* vol. 19, pp. -, Jan 9 2008.
[17] D. Mattia, M. P. Rossi, B. M. Kim, G. Korneva, H. H. Bau, and Y. Gogotsi, "Effect of graphitization on the wettability and electrical conductivity of CVD-carbon nanotubes and films," *Journal of Physical Chemistry B,* vol. 110, pp. 9850-9855, May 25 2006.
[18] P. H. Chen and R. L. McCreery, "Control of electron transfer kinetics at glassy carbon electrodes by specific surface modification," *Analytical Chemistry,* vol. 68, pp. 3958-3965, Nov 15 1996.
[19] Z. L. Li, P. Dharap, S. Nagarajaiah, E. V. Barrera, and J. D. Kim, "Carbon nanotube film sensors," *Advanced Materials,* vol. 16, pp. 640-+, Apr 5 2004.
[20] R. J. Grow, Q. Wang, J. Cao, D. W. Wang, and H. J. Dai, "Piezoresistance of carbon nanotubes on deformable thin-film membranes," *Applied Physics Letters,* vol. 86, pp. -, Feb 28 2005.
[21] J. R. Wood, M. D. Frogley, E. R. Meurs, A. D. Prins, T. Peijs, D. J. Dunstan, *et al.*, "Mechanical response of carbon nanotubes under molecular and macroscopic pressures," *Journal of Physical Chemistry B,* vol. 103, pp. 10388-10392, Nov 25 1999.
[22] C. Stampfer, T. Helbling, D. Obergfell, B. Schoberle, M. K. Tripp, A. Jungen, *et al.*, "Fabrication of single-walled carbon-nanotube-based pressure sensors," *Nano Letters,* vol. 6, pp. 233-237, Feb 2006.
[23] C. Hierold, A. Jungen, C. Stampfer, and T. Helbling, "Nano electromechanical sensors based on carbon nanotubes," *Sensors and Actuators a-Physical,* vol. 136, pp. 51-61, May 1 2007.
[24] J. C. Meyer, M. Paillet, and S. Roth, "Single-molecule torsional pendulum," *Science,* vol. 309, pp. 1539-1541, Sep 2 2005.
[25] T. Cohen-Karni, L. Segev, O. Srur-Lavi, S. R. Cohen, and E. Joselevich, "Torsional electromechanical quantum oscillations in carbon nanotubes," *Nature Nanotechnology,* vol. 1, pp. 36-41, Oct 2006.
[26] K. Laxminarayana and N. Jalili, "Functional nanotube-based textiles: Pathway to next generation fabrics with enhanced sensing capabilities," *Textile Research Journal,* vol. 75, pp. 670-680, Sep 2005.
[27] K. Jensen, K. Kim, and A. Zettl, "An atomic-resolution nanomechanical mass sensor," *Nature Nanotechnology,* vol. 3, pp. 533-537, Sep 2008.
[28] S. Ghosh, A. K. Sood, and N. Kumar, "Carbon nanotube flow sensors," *Science,* vol. 299, pp. 1042-1044, Feb 14 2003.
[29] L. J. Hall, V. R. Coluci, D. S. Galvao, M. E. Kozlov, M. Zhang, S. O. Dantas, *et al.*, "Sign change of Poisson's ratio for carbon nanotube sheets," *Science,* vol. 320, pp. 504-507, Apr 25 2008.

[30] J. R. Wood, Q. Zhao, M. D. Frogley, E. R. Meurs, A. D. Prins, T. Peijs, *et al.*, "Carbon nanotubes: From molecular to macroscopic sensors," *Physical Review B,* vol. 62, pp. 7571-7575, Sep 15 2000.

[31] L. Shi, C. H. Yu, and J. H. Zhou, "Thermal characterization and sensor applications of one-dimensional nanostructures employing microelectromechanical systems," *Journal of Physical Chemistry B,* vol. 109, pp. 22102-22111, Dec 1 2005.

[32] T. Kawano, H. C. Chiamori, M. Suter, Q. Zhou, B. D. Sosnowchik, and L. W. Lin, "An electrothermal carbon nanotube gas sensor," *Nano Letters,* vol. 7, pp. 3686-3690, Dec 2007.

[33] L. T. Liu, X. Y. Ye, K. Wu, R. Han, Z. Y. Zhou, and T. H. Cui, "Humidity Sensitivity of Multi-Walled Carbon Nanotube Networks Deposited by Dielectrophoresis," *Sensors,* vol. 9, pp. 1714-1721, Mar 2009.

[34] B. Pradhan, R. R. Kohlmeyer, K. Setyowati, H. A. Owen, and J. Chen, "Advanced carbon nanotube/polymer composite infrared sensors," *Carbon,* vol. 47, pp. 1686-1692, Jun 2009.

[35] M. D. Frogley, Q. Zhao, and H. D. Wagner, "Polarized resonance Raman spectroscopy of single-wall carbon nanotubes within a polymer under strain," *Physical Review B,* vol. 65, pp. -, Mar 15 2002.

[36] M. S. Amer, M. M. El-Ashry, and J. F. Maguire, "Study of the hydrostatic pressure dependence of the Raman spectrum of single-walled carbon nanotubes and nanospheres," *Journal of Chemical Physics,* vol. 121, pp. 2752-2757, Aug 8 2004.

[37] R. F. Khairoutdinov, L. V. Doubova, R. C. Haddon, and L. Saraf, "Persistent photoconductivity in chemically modified single-wall carbon nanotubes," *Journal of Physical Chemistry B,* vol. 108, pp. 19976-19981, Dec 30 2004.

[38] A. Merkoci, M. Pumera, X. Llopis, B. Perez, M. del Valle, and S. Alegret, "New materials for electrochemical sensing VI: Carbon nanotubes," *Trac-Trends in Analytical Chemistry,* vol. 24, pp. 826-838, Oct 2005.

[39] S. N. Kim, J. F. Rusling, and F. Papadimitrakopoulos, "Carbon nanotubes for electronic and electrochemical detection of biomolecules," *Advanced Materials,* vol. 19, pp. 3214-3228, Oct 19 2007.

[40] N. Sinha, J. Z. Ma, and J. T. W. Yeow, "Carbon nanotube-based sensors," *Journal of Nanoscience and Nanotechnology,* vol. 6, pp. 573-590, Mar 2006.

[41] Y. Hayamizu, T. Yamada, K. Mizuno, R. C. Davis, D. N. Futaba, M. Yumura, *et al.*, "Integrated three-dimensional microelectromechanical devices from processable carbon nanotube wafers," *Nature Nanotechnology,* vol. 3, pp. 289-294, May 2008.

[42] B. S. Shim, W. Chen, C. Doty, C. L. Xu, and N. A. Kotov, "Smart Electronic Yarns and Wearable Fabrics for Human Biomonitoring made by Carbon Nanotube Coating with Polyelectrolytes," *Nano Letters,* vol. 8, pp. 4151-4157, Dec 2008.

[43] X. J. Huang, H. S. Im, D. H. Lee, H. S. Kim, and Y. K. Choi, "Ferrocene functionalized single-walled carbon nanotube bundles. Hybrid interdigitated construction film for L-glutamate detection," *Journal of Physical Chemistry C,* vol. 111, pp. 1200-1206, Jan 25 2007.

[44] R. S. Chen, W. H. Huang, H. Tong, Z. L. Wang, and J. K. Cheng, "Carbon fiber nanoelectrodes modified by single-walled carbon nanotubes," *Analytical Chemistry*, vol. 75, pp. 6341-6345, Nov 15 2003.

[45] S. J. Tans, A. R. M. Verschueren, and C. Dekker, "Room-temperature transistor based on a single carbon nanotube," *Nature*, vol. 393, pp. 49-52, May 7 1998.

[46] R. Martel, T. Schmidt, H. R. Shea, T. Hertel, and P. Avouris, "Single- and multi-wall carbon nanotube field-effect transistors," *Applied Physics Letters*, vol. 73, pp. 2447-2449, Oct 26 1998.

[47] J. Kong, N. R. Franklin, C. W. Zhou, M. G. Chapline, S. Peng, K. J. Cho, *et al.*, "Nanotube molecular wires as chemical sensors," *Science*, vol. 287, pp. 622-625, Jan 28 2000.

[48] R. J. Chen, S. Bangsaruntip, K. A. Drouvalakis, N. W. S. Kam, M. Shim, Y. M. Li, *et al.*, "Noncovalent functionalization of carbon nanotubes for highly specific electronic biosensors," *Proceedings of the National Academy of Sciences of the United States of America*, vol. 100, pp. 4984-4989, Apr 29 2003.

[49] J. Li, Y. J. Lu, Q. Ye, M. Cinke, J. Han, and M. Meyyappan, "Carbon nanotube sensors for gas and organic vapor detection," *Nano Letters*, vol. 3, pp. 929-933, Jul 2003.

[50] J. Koehne, J. Li, A. M. Cassell, H. Chen, Q. Ye, H. T. Ng, *et al.*, "The fabrication and electrochemical characterization of carbon nanotube nanoelectrode arrays," *Journal of Materials Chemistry*, vol. 14, pp. 676-684, Feb 21 2004.

[51] W. Z. Li, S. S. Xie, L. X. Qian, B. H. Chang, B. S. Zou, W. Y. Zhou, *et al.*, "Large-scale synthesis of aligned carbon nanotubes," *Science*, vol. 274, pp. 1701-1703, Dec 6 1996.

[52] Z. F. Ren, Z. P. Huang, J. W. Xu, J. H. Wang, P. Bush, M. P. Siegal, *et al.*, "Synthesis of large arrays of well-aligned carbon nanotubes on glass," *Science*, vol. 282, pp. 1105-1107, Nov 6 1998.

[53] Z. F. Ren, Z. P. Huang, D. Z. Wang, J. G. Wen, J. W. Xu, J. H. Wang, *et al.*, "Growth of a single freestanding multiwall carbon nanotube on each nanonickel dot," *Applied Physics Letters*, vol. 75, pp. 1086-1088, Aug 23 1999.

[54] V. I. Merkulov, D. H. Lowndes, Y. Y. Wei, G. Eres, and E. Voelkl, "Patterned growth of individual and multiple vertically aligned carbon nanofibers," *Applied Physics Letters*, vol. 76, pp. 3555-3557, Jun 12 2000.

[55] A. V. Melechko, T. E. McKnight, D. K. Hensley, M. A. Guillorn, A. Y. Borisevich, V. I. Merkulov, *et al.*, "Large-scale synthesis of arrays of high-aspect-ratio rigid vertically aligned carbon nanofibres," *Nanotechnology*, vol. 14, pp. 1029-1035, Sep 2003.

[56] T. E. McKnight, A. V. Melechko, G. D. Griffin, M. A. Guillorn, V. I. Merkulov, F. Serna, *et al.*, "Intracellular integration of synthetic nanostructures with viable cells for controlled biochemical manipulation," *Nanotechnology*, vol. 14, pp. 551-556, May 2003.

[57] J. Li, A. Cassell, L. Delzeit, J. Han, and M. Meyyappan, "Novel three-dimensional electrodes: Electrochemical properties of carbon nanotube ensembles," *Journal of Physical Chemistry B*, vol. 106, pp. 9299-9305, Sep 12 2002.

[58] R. D. Lowe, R. C. Mani, R. P. Baldwin, and M. K. Sunkara, "Nanoelectrode ensembles using carbon nanopipettes," *Electrochemical and Solid State Letters,* vol. 9, pp. H43-H47, 2006.
[59] Y. Tu, Y. H. Lin, and Z. F. Ren, "Nanoelectrode arrays based on low site density aligned carbon nanotubes," *Nano Letters,* vol. 3, pp. 107-109, Jan 2003.
[60] J. H. Hafner, C. L. Cheung, and C. M. Lieber, "Direct growth of single-walled carbon nanotube scanning probe microscopy tips," *Journal of the American Chemical Society,* vol. 121, pp. 9750-9751, Oct 20 1999.
[61] J. H. Hafner, C. L. Cheung, T. H. Oosterkamp, and C. M. Lieber, "High-yield assembly of individual single-walled carbon nanotube tips for scanning probe microscopies," *Journal of Physical Chemistry B,* vol. 105, pp. 743-746, Feb 1 2001.
[62] S. Akita, H. Nishijima, Y. Nakayama, F. Tokumasu, and K. Takeyasu, "Carbon nanotube tips for a scanning probe microscope: their fabrication and properties," *Journal of Physics D-Applied Physics,* vol. 32, pp. 1044-1048, May 7 1999.
[63] E. Yenilmez, Q. Wang, R. J. Chen, D. W. Wang, and H. J. Dai, "Wafer scale production of carbon nanotube scanning probe tips for atomic force microscopy," *Applied Physics Letters,* vol. 80, pp. 2225-2227, Mar 25 2002.
[64] A. Patil, J. Sippel, G. W. Martin, and A. G. Rinzler, "Enhanced functionality of nanotube atomic force microscopy tips by polymer coating," *Nano Letters,* vol. 4, pp. 303-308, Feb 2004.
[65] I. U. Vakarelski, S. C. Brown, K. Higashitani, and B. M. Moudgil, "Penetration of living cell membranes with fortified carbon nanotube tips," *Langmuir,* vol. 23, pp. 10893-10896, Oct 23 2007.
[66] X. Chen, A. Kis, A. Zettl, and C. R. Bertozzi, "A cell nanoinjector based on carbon nanotubes," *Proceedings of the National Academy of Sciences of the United States of America,* vol. 104, pp. 8218-8222, May 15 2007.
[67] J. H. Hafner, C. L. Cheung, and C. M. Lieber, "Growth of nanotubes for probe microscopy tips," *Nature,* vol. 398, pp. 761-762, Apr 29 1999.
[68] M. Kaempgen and S. Roth, "Ultra microelectrodes from MWCNT bundles," *Synthetic Metals,* vol. 152, pp. 353-356, Sep 20 2005.
[69] N. A. Kouklin, W. E. Kim, A. D. Lazareck, and J. M. Xu, "Carbon nanotube probes for single-cell experimentation and assays," *Applied Physics Letters,* vol. 87, pp. -, Oct 24 2005.
[70] J. R. Freedman, D. Mattia, G. Korneva, Y. Gogotsi, G. Friedman, and A. K. Fontecchio, "Magnetically assembled carbon nanotube tipped pipettes," *Applied Physics Letters,* vol. 90, pp. -, Mar 5 2007.
[71] R. Singhal, Z. Orynbayeva, R. V. Kalyana Sundaram, J. J. Niu, S. Bhattacharyya, E. A. Vitol, *et al.*, "Multifunctional carbon-nanotube cellular endoscopes," *Nature Nanotechnology,* vol. 6, pp. 57-64, Jan 2011.
[72] B. M. Kim, T. Murray, and H. H. Bau, "The fabrication of integrated carbon pipes with sub-micron diameters," *Nanotechnology,* vol. 16, pp. 1317-1320, Aug 2005.
[73] R. Singhal, S. Bhattacharyya, Z. Orynbayeva, E. Vitol, G. Friedman, and Y. Gogotsi, "Small diameter carbon nanopipettes," *Nanotechnology,* vol. 21, pp. -, Jan 8 2010.

[74] Y. M. Yan, W. Zheng, M. N. Zhang, L. Wang, L. Su, and L. Q. Mao, "Bioelectrochemically functional nanohybrids through co-assembling of proteins and surfactants onto carbon nanotubes: Facilitated electron transfer of assembled proteins with enhanced faradic response," *Langmuir,* vol. 21, pp. 6560-6566, Jul 5 2005.

[75] C. Staii, A. T. Johnson, M. Chen, and A. Gelperin, "DNA-Decorated Carbon Nanotubes for Chemical Sensing," *Nano Letters,* vol. 5, pp. 1774-1778, 2005.

[76] M. Shim, N. W. S. Kam, R. J. Chen, Y. M. Li, and H. J. Dai, "Functionalization of carbon nanotubes for biocompatibility and biomolecular recognition," *Nano Letters,* vol. 2, pp. 285-288, Apr 2002.

[77] R. J. Chen, Y. G. Zhang, D. W. Wang, and H. J. Dai, "Noncovalent sidewall functionalization of single-walled carbon nanotubes for protein immobilization," *Journal of the American Chemical Society,* vol. 123, pp. 3838-3839, Apr 25 2001.

[78] J. L. Bahr and J. M. Tour, "Covalent chemistry of single-wall carbon nanotubes," *Journal of Materials Chemistry,* vol. 12, pp. 1952-1958, 2002.

[79] K. A. Williams, P. T. M. Veenhuizen, B. G. de la Torre, R. Eritja, and C. Dekker, "Nanotechnology - Carbon nanotubes with DNA recognition," *Nature,* vol. 420, pp. 761-761, Dec 26 2002.

[80] D. Cai, J. M. Mataraza, Z. H. Qin, Z. P. Huang, J. Y. Huang, T. C. Chiles, *et al.*, "Highly efficient molecular delivery into mammalian cells using carbon nanotube spearing," *Nature Methods,* vol. 2, pp. 449-454, Jun 2005.

[81] Y. H. Lin, F. Lu, Y. Tu, and Z. F. Ren, "Glucose biosensors based on carbon nanotube nanoelectrode ensembles," *Nano Letters,* vol. 4, pp. 191-195, Feb 2004.

[82] S. Bhattacharyya, D. Staack, E. A. Vitol, R. Singhal, A. Fridman, G. Friedman, *et al.*, "Localized Synthesis of Metal Nanoparticles Using Nanoscale Corona Discharge in Aqueous Solutions," *Advanced Materials,* vol. 21, pp. 4039-+, Oct 26 2009.

[83] K. Y. Jiang, A. Eitan, L. S. Schadler, P. M. Ajayan, R. W. Siegel, N. Grobert, *et al.*, "Selective attachment of gold nanoparticies to nitrogen-doped carbon nanotubes," *Nano Letters,* vol. 3, pp. 275-277, Mar 2003.

[84] S. Haque, S. Md, M. I. Alam, J. K. Sahni, J. Ali, and S. Baboota, "Nanostructure-based drug delivery systems for brain targeting," *Drug Development and Industrial Pharmacy,* vol. 38, pp. 387-411, Apr 2012.

[85] D. Mattia, G. Korneva, A. Sabur, G. Friedman, and Y. Gogotsi, "Multifunctional carbon nanotubes with nanoparticles embedded in their walls," *Nanotechnology,* vol. 18, pp. -, Apr 18 2007.

[86] G. Korneva, H. H. Ye, Y. Gogotsi, D. Halverson, G. Friedman, J. C. Bradley, *et al.*, "Carbon nanotubes loaded with magnetic particles," *Nano Letters,* vol. 5, pp. 879-884, May 2005.

[87] T. D. B. Nguyen-Vu, H. Chen, A. M. Cassell, R. J. Andrews, M. Meyyappan, and J. Li, "Vertically aligned carbon nanofiber architecture as a multifunctional 3-D neural electrical interface," *Ieee Transactions on Biomedical Engineering,* vol. 54, pp. 1121-1128, Jun 2007.

[88] D. S. Bethune, C. H. Kiang, M. S. Devries, G. Gorman, R. Savoy, J. Vazquez, *et al.*, "Cobalt-Catalyzed Growth of Carbon Nanotubes with Single-Atomic-Layerwalls," *Nature,* vol. 363, pp. 605-607, Jun 17 1993.

[89] C. Journet, W. K. Maser, P. Bernier, A. Loiseau, M. L. delaChapelle, S. Lefrant, *et al.*, "Large-scale production of single-walled carbon nanotubes by the electric-arc technique," *Nature*, vol. 388, pp. 756-758, Aug 21 1997.
[90] T. W. Ebbesen and P. M. Ajayan, "Large-Scale Synthesis of Carbon Nanotubes," *Nature*, vol. 358, pp. 220-222, Jul 16 1992.
[91] D. T. Colbert, J. Zhang, S. M. Mcclure, P. Nikolaev, Z. Chen, J. H. Hafner, *et al.*, "Growth and Sintering of Fullerene Nanotubes," *Science*, vol. 266, pp. 1218-1222, Nov 18 1994.
[92] A. Thess, R. Lee, P. Nikolaev, H. J. Dai, P. Petit, J. Robert, *et al.*, "Crystalline ropes of metallic carbon nanotubes," *Science*, vol. 273, pp. 483-487, Jul 26 1996.
[93] T. Guo, P. Nikolaev, A. G. Rinzler, D. Tomanek, D. T. Colbert, and R. E. Smalley, "Self-Assembly of Tubular Fullerenes," *Journal of Physical Chemistry*, vol. 99, pp. 10694-10697, Jul 6 1995.
[94] S. Amelinckx, X. B. Zhang, D. Bernaerts, X. F. Zhang, V. Ivanov, and J. B. Nagy, "A Formation Mechanism for Catalytically Grown Helix-Shaped Graphite Nanotubes," *Science*, vol. 265, pp. 635-639, Jul 29 1994.
[95] C. R. Martin, "Nanomaterials - a Membrane-Based Synthetic Approach," *Science*, vol. 266, pp. 1961-1966, Dec 23 1994.
[96] T. Kyotani, L. F. Tsai, and A. Tomita, "Formation of Ultrafine Carbon Tubes by Using an Anodic Aluminum-Oxide Film as a Template," *Chemistry of Materials*, vol. 7, pp. 1427-1428, Aug 1995.
[97] M. Golshadi, J. Maita, D. Lanza, M. Zeiger, V. Presser, and M. G. Schrlau, "Effects of synthesis parameters on carbon nanotubes manufactured by template-based chemical vapor deposition," *Carbon*, vol. 80, pp. 28-39, 2014.
[98] M. Terrones, N. Grobert, J. Olivares, J. P. Zhang, H. Terrones, K. Kordatos, *et al.*, "Controlled production of aligned-nanotube bundles," *Nature*, vol. 388, pp. 52-55, Jul 3 1997.
[99] G. L. Che, B. B. Lakshmi, E. R. Fisher, and C. R. Martin, "Carbon nanotubule membranes for electrochemical energy storage and production," *Nature*, vol. 393, pp. 346-349, May 28 1998.
[100] A. Huczko, "Template-based synthesis of nanomaterials," *Applied Physics A*, vol. 70, pp. 365-376, 2000.
[101] J. Hulteen, "A general template-based method for the preparation of nanomaterials," *Journal of Materials Chemistry*, vol. 7, pp. 1075-1087, 1997.
[102] J. Kong, H. T. Soh, A. M. Cassell, C. F. Quate, and H. Dai, "Synthesis of individual single-walled carbon nanotubes on patterned silicon wafers," *Nature*, vol. 395, pp. 878-881, 1998.
[103] G. E. J. Poinern, N. Ali, and D. Fawcett, "Progress in nano-engineered anodic aluminum oxide membrane development," *Materials*, vol. 4, pp. 487-526, 2011.
[104] A. M. Md Jani, D. Losic, and N. H. Voelcker, "Nanoporous anodic aluminium oxide: advances in surface engineering and emerging applications," *Progress in materials science*, vol. 58, pp. 636-704, 2013.
[105] T. Whitney, P. Searson, J. Jiang, and C. Chien, "Fabrication and magnetic properties of arrays of metallic nanowires," *Science*, vol. 261, pp. 1316-1319, 1993.

[106] F. Keller, M. Hunter, and D. Robinson, "Structural features of oxide coatings on aluminum," *Journal of the Electrochemical Society,* vol. 100, pp. 411-419, 1953.
[107] H. Masuda, K. Yada, and A. Osaka, "Self-ordering of cell configuration of anodic porous alumina with large-size pores in phosphoric acid solution," *Japanese Journal of Applied Physics,* vol. 37, p. L1340, 1998.
[108] S. Shingubara, "Fabrication of nanomaterials using porous alumina templates," *Journal of Nanoparticle Research,* vol. 5, pp. 17-30, 2003.
[109] D.-G. Choi, H. K. Yu, S. G. Jang, and S.-M. Yang, "Colloidal lithographic nanopatterning via reactive ion etching," *Journal of the American Chemical Society,* vol. 126, pp. 7019-7025, 2004.
[110] Y. Matsui, K. Nishio, and H. Masuda, "Highly Ordered Anodic porous alumina by imprinting using Ni molds prepared from ordered array of polystyrene particles," *Japanese Journal of Applied Physics,* vol. 44, p. 7726, 2005.
[111] S. Fournier-Bidoz, V. Kitaev, D. Routkevitch, I. Manners, and G. A. Ozin, "Highly ordered nanosphere imprinted nanochannel alumina (NINA)," *Advanced Materials,* vol. 16, pp. 2193-2196, 2004.
[112] F. Li, L. Zhang, and R. M. Metzger, "On the growth of highly ordered pores in anodized aluminum oxide," *Chemistry of Materials,* vol. 10, pp. 2470-2480, 1998.
[113] D. Barkey and J. McHugh, "Pattern formation in anodic aluminum oxide growth by flow instability and dynamic restabilization," *Journal of the Electrochemical Society,* vol. 157, pp. C388-C391, 2010.
[114] G. Wood and J. O'Sullivan, "The anodizing of aluminium in sulphate solutions," *Electrochimica Acta,* vol. 15, pp. 1865-1876, 1970.
[115] W. J. Stępniowski and Z. Bojar, "Synthesis of anodic aluminum oxide (AAO) at relatively high temperatures. Study of the influence of anodization conditions on the alumina structural features," *Surface and Coatings Technology,* vol. 206, pp. 265-272, 2011.
[116] N.-Q. Zhao, X.-X. Jiang, C.-S. Shi, J.-J. Li, Z.-G. Zhao, and X.-W. Du, "Effects of anodizing conditions on anodic alumina structure," *Journal of Materials Science,* vol. 42, pp. 3878-3882, 2007.
[117] S. Chu, K. Wada, S. Inoue, M. Isogai, Y. Katsuta, and A. Yasumori, "Large-scale fabrication of ordered nanoporous alumina films with arbitrary pore intervals by critical-potential anodization," *Journal of the Electrochemical Society,* vol. 153, pp. B384-B391, 2006.
[118] S.-K. Hwang, J. Lee, S.-H. Jeong, P.-S. Lee, and K.-H. Lee, "Fabrication of carbon nanotube emitters in an anodic aluminium oxide nanotemplate on a Si wafer by multi-step anodization," *Nanotechnology,* vol. 16, p. 850, 2005.
[119] J. S. Suh and J. S. Lee, "Highly ordered two-dimensional carbon nanotube arrays," *Applied Physics Letters,* vol. 75, pp. 2047-2049, 1999.
[120] W. De Azevedo, D. De Carvalho, H. Khoury, and E. De Vasconcelos, "Spectroscopic characteristics of doped nanoporous aluminum oxide," *Materials Science and Engineering: B,* vol. 112, pp. 171-174, 2004.
[121] S. Z. Chu, K. Wada, S. Inoue, M. Isogai, and A. Yasumori, "Fabrication of Ideally Ordered Nanoporous Alumina Films and Integrated Alumina Nanotubule Arrays by High-Field Anodization," *Advanced Materials,* vol. 17, pp. 2115-2119, 2005.

[122] C. V. Nguyen, L. Delzeit, A. M. Cassell, J. Li, J. Han, and M. Meyyappan, "Preparation of nucleic acid functionalized carbon nanotube Arrays," *Nano Letters,* vol. 2, pp. 1079-1081, Oct 2002.
[123] J. Koehne, H. Chen, J. Li, A. M. Cassell, Q. Ye, H. T. Ng, *et al.*, "Ultrasensitive label-free DNA analysis using an electronic chip based on carbon nanotube nanoelectrode arrays," *Nanotechnology,* vol. 14, pp. 1239-1245, Dec 2003.
[124] J. Li, H. T. Ng, A. Cassell, W. Fan, H. Chen, Q. Ye, *et al.*, "Carbon nanotube nanoelectrode array for ultrasensitive DNA detection," *Nano Letters,* vol. 3, pp. 597-602, May 2003.
[125] M. Kruger, M. R. Buitelaar, T. Nussbaumer, C. Schonenberger, and L. Forro, "Electrochemical carbon nanotube field-effect transistor," *Applied Physics Letters,* vol. 78, pp. 1291-1293, Feb 26 2001.
[126] P. W. Barone, S. Baik, D. A. Heller, and M. S. Strano, "Near-infrared optical sensors based on single-walled carbon nanotubes," *Nature Materials,* vol. 4, pp. 86-U16, Jan 2005.
[127] P. W. Barone, R. S. Parker, and M. S. Strano, "In vivo fluorescence detection of glucose using a single-walled carbon nanotube optical sensor: Design, fluorophore properties, advantages, and disadvantages," *Analytical Chemistry,* vol. 77, pp. 7556-7562, Dec 1 2005.
[128] D. A. Heller, E. S. Jeng, T. K. Yeung, B. M. Martinez, A. E. Moll, J. B. Gastala, *et al.*, "Optical detection of DNA conformational polymorphism on single-walled carbon nanotubes," *Science,* vol. 311, pp. 508-511, Jan 27 2006.
[129] E. S. Jeng, A. E. Moll, A. C. Roy, J. B. Gastala, and M. S. Strano, "Detection of DNA hybridization using the near-infrared band-gap fluorescence of single-walled carbon nanotubes," *Nano Letters,* vol. 6, pp. 371-375, Mar 2006.
[130] M. G. Schrlau, N. J. Dun, and H. H. Bau, "Cell Electrophysiology with Carbon Nanopipettes," *Acs Nano,* vol. 3, pp. 563-568, Mar 2009.
[131] E. D. de Asis, J. Leung, S. Wood, and C. V. Nguyen, "High spatial resolution single multiwalled carbon nanotube electrode for stimulation, recording, and whole cell voltage clamping of electrically active cells," *Applied Physics Letters,* vol. 95, pp. -, Oct 12 2009.
[132] S. R. Yeh, Y. C. Chen, H. C. Su, T. R. Yew, H. H. Kao, Y. T. Lee, *et al.*, "Interfacing Neurons both Extracellularly and Intracellularly Using Carbon - Nanotube Probes with Long-Term Endurance," *Langmuir,* vol. 25, pp. 7718-7724, 2009.
[133] Z. Orynbayeva, R. Singhal, E. A. Vitol, M. G. Schrlau, E. Papazoglou, G. Friedman, *et al.*, "Physiological validation of cell health upon probing with carbon nanotube endoscope and its benefit for single-cell interrogation," *Nanomedicine : nanotechnology, biology, and medicine,* vol. 8, pp. 590-598, Sep 1 2012.
[134] H. Hatakeyama, H. Akita, and H. Harashima, "A multifunctional envelope type nano device (MEND) for gene delivery to tumours based on the EPR effect: a strategy for overcoming the PEG dilemma," *Advanced Drug Delivery Reviews,* vol. 63, pp. 152-160, 2011.

[135] B. Panchapakesan, R. Caprara, V. Velasco, J. Loomis, B. King, P. Xu, *et al.*, "Micro-and nanotechnology approaches for capturing circulating tumor cells," *Cancer Nanotechnology*, vol. 1, pp. 3-11, 2010.
[136] R. Z. Wu, S. N. Bailey, and D. M. Sabatini, "Cell-biological applications of transfected-cell microarrays," *Trends in cell biology*, vol. 12, pp. 485-488, 2002.
[137] E. Peer, A. Artzy-Schnirman, L. Gepstein, and U. Sivan, "Hollow nanoneedle array and its utilization for repeated administration of biomolecules to the same cells," *Acs Nano*, vol. 6, pp. 4940-4946, 2012.
[138] C. Xie, L. Hanson, W. Xie, Z. Lin, B. Cui, and Y. Cui, "Noninvasive neuron pinning with nanopillar arrays," *Nano Letters*, vol. 10, pp. 4020-4024, 2010.
[139] T. M. Allen and P. R. Cullis, "Liposomal drug delivery systems: from concept to clinical applications," *Advanced Drug Delivery Reviews*, vol. 65, pp. 36-48, 2013.
[140] S. Febvay, D. M. Marini, A. M. Belcher, and D. E. Clapham, "Targeted cytosolic delivery of cell-impermeable compounds by nanoparticle-mediated, light-triggered endosome disruption," *Nano Letters*, vol. 10, pp. 2211-2219, 2010.
[141] J. Mikkilä, A.-P. Eskelinen, E. H. Niemelä, V. Linko, M. J. Frilander, P. i. Törmä, *et al.*, "Virus-Encapsulated DNA Origami Nanostructures for Cellular Delivery," *Nano Letters*, vol. 14, pp. 2196-2200, 2014.
[142] X. Xie, A. M. Xu, S. Leal-Ortiz, Y. Cao, C. C. Garner, and N. A. Melosh, "Nanostraw–Electroporation System for Highly Efficient Intracellular Delivery and Transfection," *Acs Nano*, vol. 7, pp. 4351-4358, 2013.
[143] F. T. M. de Carvalho Vicentini, L. N. Borgheti-Cardoso, L. V. Depieri, D. de Macedo Mano, T. F. Abelha, R. Petrilli, *et al.*, "Delivery systems and local administration routes for therapeutic siRNA," *Pharmaceutical research*, vol. 30, pp. 915-931, 2013.
[144] A. Sharei, J. Zoldan, A. Adamo, W. Y. Sim, N. Cho, E. Jackson, *et al.*, "A vector-free microfluidic platform for intracellular delivery," *Proceedings of the National Academy of Sciences*, vol. 110, pp. 2082-2087, 2013.
[145] A. F. Adler and K. W. Leong, "Emerging links between surface nanotechnology and endocytosis: impact on nonviral gene delivery," *Nano Today*, vol. 5, pp. 553-569, 2010.
[146] I. Y. Wong, B. D. Almquist, and N. A. Melosh, "Dynamic actuation using nano-bio interfaces," *Materials Today*, vol. 13, pp. 14-22, 2010.
[147] M. Javorovic, H. Pohla, B. Frankenberger, T. Wölfel, and D. J. Schendel, "RNA transfer by electroporation into mature dendritic cells leading to reactivation of effector-memory cytotoxic T lymphocytes: a quantitative analysis," *Molecular Therapy*, vol. 12, pp. 734-743, 2005.
[148] J. Labanauskiene, J. Gehl, and J. Didziapetriene, "Evaluation of cytotoxic effect of photodynamic therapy in combination with electroporation in vitro," *Bioelectrochemistry*, vol. 70, pp. 78-82, 2007.
[149] X. T. Zheng and C. M. Li, "Single cell analysis at the nanoscale," *Chemical Society Reviews*, vol. 41, pp. 2061-2071, 2012.
[150] Y. Gao, T. Longenbach, E. A. Vitol, Z. Orynbayeva, G. Friedman, and Y. Gogotsi, "One-dimensional nanoprobes for single-cell studies," *Nanomedicine*, vol. 9, pp. 153-168, 2014.

[151] R. Elnathan, M. Kwiat, F. Patolsky, and N. H. Voelcker, "Engineering vertically aligned semiconductor nanowire arrays for applications in the life sciences," *Nano Today,* vol. 9, pp. 172-196, 2014.
[152] B. He, Y. Yang, M. Yuen, X. Chen, C. Lee, and W. Zhang, "Vertical nanostructure arrays by plasma etching for applications in biology, energy, and electronics," *Nano Today*, vol. 8, pp. 265-289, 2013.
[153] S. M. Yoo, M. Kang, T. Kang, D. M. Kim, S. Y. Lee, and B. Kim, "Electrotriggered, Spatioselective, Quantitative Gene Delivery into a Single Cell Nucleus by Au Nanowire Nanoinjector," *Nano Letters,* vol. 13, pp. 2431-2435, 2013.
[154] M. Singh, D. Movia, O. K. Mahfoud, Y. Volkov, and A. Prina-Mello, "Silver nanowires as prospective carriers for drug delivery in cancer treatment: an in vitro biocompatibility study on lung adenocarcinoma cells and fibroblasts," *European Journal of Nanomedicine,* vol. 5, pp. 195-204, 2013.
[155] T. Shibata, K. Nakamura, S. Horiike, M. Nagai, T. Kawashima, T. Mineta, *et al.*, "Fabrication and characterization of bioprobe integrated with a hollow nanoneedle for novel AFM applications in cellular function analysis," *Microelectronic engineering,* vol. 111, pp. 325-331, 2013.
[156] A. Meister, M. Gabi, P. Behr, P. Studer, J. n. Vo¨rös, P. Niedermann, *et al.*, "FluidFM: combining atomic force microscopy and nanofluidics in a universal liquid delivery system for single cell applications and beyond," *Nano Letters,* vol. 9, pp. 2501-2507, 2009.
[157] W. Kim, J. K. Ng, M. E. Kunitake, B. R. Conklin, and P. Yang, "Interfacing silicon nanowires with mammalian cells," *Journal of the American Chemical Society,* vol. 129, pp. 7228-7229, 2007.
[158] A. K. Shalek, J. T. Gaublomme, L. Wang, N. Yosef, N. Chevrier, M. S. Andersen, *et al.*, "Nanowire-mediated delivery enables functional interrogation of primary immune cells: application to the analysis of chronic lymphocytic leukemia," *Nano Letters,* vol. 12, pp. 6498-6504, 2012.
[159] N. Sköld, W. Hällström, H. Persson, L. Montelius, M. Kanje, L. Samuelson, *et al.*, "Nanofluidics in hollow nanowires," *Nanotechnology,* vol. 21, p. 155301, 2010.
[160] H. Persson, J. P. Beech, L. Samuelson, S. Oredsson, C. N. Prinz, and J. O. Tegenfeldt, "Vertical oxide nanotubes connected by subsurface microchannels," *Nano Research,* vol. 5, pp. 190-198, 2012.
[161] J. J. VanDersarl, A. M. Xu, and N. A. Melosh, "Nanostraws for direct fluidic intracellular access," *Nano Letters,* vol. 12, pp. 3881-3886, 2011.
[162] Y. Gogotsi and V. Presser, *Carbon nanomaterials,* 2nd Edition ed.: CRC Press, 2013.
[163] M. G. Schrlau, E. Brailoiu, S. Patel, Y. Gogotsi, N. J. Dun, and H. H. Bau, "Carbon nanopipettes characterize calcium release pathways in breast cancer cells," *Nanotechnology,* vol. 19, p. 325102, 2008.
[164] G. Becattini, L. S. Mattos, and D. G. Caldwell, "A Fully Automated System for Adherent Cells Microinjection," *Biomedical and Health Informatics, IEEE Journal of,* vol. 18, pp. 83-93, 2014.

[165] L. Mattos, E. Grant, R. Thresher, and K. Kluckman, "New developments towards automated blastocyst microinjections," in *Robotics and Automation, 2007 IEEE International Conference on*, 2007, pp. 1924-1929.
[166] S. Park, Y.-S. Kim, W. B. Kim, and S. Jon, "Carbon nanosyringe array as a platform for intracellular delivery," *Nano Letters*, vol. 9, pp. 1325-1329, 2009.
[167] D. G. Mann, T. E. McKnight, J. T. McPherson, P. R. Hoyt, A. V. Melechko, M. L. Simpson, *et al.*, "Inducible RNA interference-mediated gene silencing using nanostructured gene delivery arrays," *Acs Nano*, vol. 2, pp. 69-76, 2007.
[168] D. B. Peckys, A. V. Melechko, M. L. Simpson, and T. E. McKnight, "Immobilization and release strategies for DNA delivery using carbon nanofiber arrays and self-assembled monolayers," *Nanotechnology*, vol. 20, p. 145304, 2009.
[169] J. H. Kim, G. Withey, C.-H. Wu, and J. Xu, "Carbon Nanotube Array for Addressable Nano-Bioelectronic Transducers," *Sensors Journal, IEEE*, vol. 11, pp. 1274-1283, 2011.
[170] G. Withey, A. Lazareck, M. Tzolov, A. Yin, P. Aich, J. Yeh, *et al.*, "Ultra-high redox enzyme signal transduction using highly ordered carbon nanotube array electrodes," *Biosensors and Bioelectronics*, vol. 21, pp. 1560-1565, 2006.
[171] W. Lee and S.-J. Park, "Porous anodic aluminum oxide: anodization and templated synthesis of functional nanostructures," *Chemical Reviews*, vol. 114, pp. 7487-7556, 2014.
[172] A. Yin, H. Chik, and J. Xu, "Postgrowth processing of carbon nanotube arrays-enabling new functionalities and applications," *Nanotechnology, IEEE Transactions on*, vol. 3, pp. 147-151, 2004.
[173] R. Bandyopadhyaya, E. Nativ-Roth, O. Regev, and R. Yerushalmi-Rozen, "Stabilization of individual carbon nanotubes in aqueous solutions," *Nano Letters*, vol. 2, pp. 25-28, 2002.
[174] H. Dai, "Carbon nanotubes: synthesis, integration, and properties," *Accounts of Chemical Research*, vol. 35, pp. 1035-1044, 2002.
[175] W. Y. Jang, N. Kulkarni, C. Shih, and Z. Yao, "Electrical characterization of individual carbon nanotubes grown in nanoporous anodic alumina templates," *Applied Physics Letters*, vol. 84, pp. 1177-1179, 2004.
[176] J.-P. Salvetat-Delmotte and A. Rubio, "Mechanical properties of carbon nanotubes: a fiber digest for beginners," *Carbon*, vol. 40, pp. 1729-1734, 2002.
[177] Q. Cao, S.-j. Han, G. S. Tulevski, Y. Zhu, D. D. Lu, and W. Haensch, "Arrays of single-walled carbon nanotubes with full surface coverage for high-performance electronics," *Nature Nanotechnology*, vol. 8, pp. 180-186, 2013.
[178] P. M. Ajayan, L. S. Schadler, C. Giannaris, and A. Rubio, "Single-walled carbon nanotube–polymer composites: strength and weakness," *Advanced Materials*, vol. 12, pp. 750-753, 2000.
[179] Z. Liu, Q. Xue, C. Ling, Z. Yan, and J. Zheng, "Hydrogen storage and release by bending carbon nanotubes," *Computational Materials Science*, vol. 68, pp. 121-126, 2013.
[180] S. Fan, M. G. Chapline, N. R. Franklin, T. W. Tombler, A. M. Cassell, and H. Dai, "Self-oriented regular arrays of carbon nanotubes and their field emission properties," *Science*, vol. 283, pp. 512-514, 1999.

[181] B. S. Harrison and A. Atala, "Carbon nanotube applications for tissue engineering," *Biomaterials*, vol. 28, pp. 344-53, Jan 2007.
[182] A. O. Fung, C. Tsiokos, O. Paydar, L. H. Chen, S. G. Jin, Y. B. Wang, *et al.*, "Electrochemical Properties and Myocyte Interaction of Carbon Nanotube Microelectrodes," *Nano Letters*, vol. 10, pp. 4321-4327, 2010.
[183] L. Bareket-Keren and Y. Hanein, "Carbon nanotube-based multielectrode arrays for neuronal interfacing: progress and prospects," *Frontiers in Neural Circuits*, vol. 6, 2013.
[184] S. Qian and S. W. Joo, "Analysis of self-electrophoretic motion of a spherical particle in a nanotube: effect of nonuniform surface charge density," *Langmuir*, vol. 24, pp. 4778-4784, 2008.
[185] C. B. Jacobs, M. J. Peairs, and B. J. Venton, "Review: Carbon nanotube based electrochemical sensors for biomolecules," *Analytica Chimica Acta*, vol. 662, pp. 105-127, 2010.
[186] G. D. Withey, A. D. Lazareck, M. B. Tzolov, A. Yin, P. Aich, J. I. Yeh, *et al.*, "Ultra-high redox enzyme signal transduction using highly ordered carbon nanotube array electrodes," *Biosensors & Bioelectronics*, vol. 21, pp. 1560-1565, 2006.
[187] C. Journet, W. K. Maser, P. Bernier, A. Loiseau, M. L. de la Chapelle, S. Lefrant, *et al.*, "Large-scale production of single-walled carbon nanotubes by the electric-arc technique," *Nature*, vol. 388, pp. 756-758, 1997.
[188] T. Guo, P. Nikolaev, A. Thess, D. T. Colbert, and R. E. Smalley, "Catalytic Growth of Single-Walled Nanotubes by Laser Vaporization," *Chemical Physics Letters*, vol. 243, pp. 49-54, 1995.
[189] M. J. Bronikowski, P. A. Willis, D. T. Colbert, K. A. Smith, and R. E. Smalley, "Gas-phase production of carbon single-walled nanotubes from carbon monoxide via the HiPco process: A parametric study," *Journal of Vacuum Science & Technology A*, vol. 19, pp. 1800-1805, 2001.
[190] K. Awasthi, A. Srivastava, and O. N. Srivastava, "Synthesis of carbon nanotubes," *Journal of Nanoscience and Nanotechnology*, vol. 5, pp. 1616-1636, 2005.
[191] C. H. See and A. T. Harris, "A review of carbon nanotube synthesis via fluidized-bed chemical vapor deposition," *Industrial & Engineering Chemistry Research*, vol. 46, pp. 997-1012, 2007.
[192] M. Terrones, "Science and technology of the twenty-first century: synthesis, properties, and applications of carbon nanotubes," *Annual Review of Materials Research*, vol. 33, pp. 419-501, 2003.
[193] Z. Ren, Y. Lan, and Y. Wang, *Aligned Carbon Nanotubes: Physics, Concepts, Fabrication and Devices*: Springer, 2012.
[194] C. J. Lee and J. Park, "Growth model of bamboo-shaped carbon nanotubes by thermal chemical vapor deposition," *Applied Physics Letters*, vol. 77, pp. 3397-3399, 2000.
[195] M. Chhowalla, K. B. K. Teo, C. Ducati, N. L. Rupesinghe, G. A. J. Amaratunga, A. C. Ferrari, *et al.*, "Growth process conditions of vertically aligned carbon nanotubes using plasma enhanced chemical vapor deposition," *Journal of Applied Physics*, vol. 90, pp. 5308-5317, 2001.

[196] M. Pinault, M. Mayne-L'Hermite, C. Reynaud, V. Pichot, P. Launois, and D. Ballutaud, "Growth of multiwalled carbon nanotubes during the initial stages of aerosol-assisted CCVD," *Carbon,* vol. 43, pp. 2968-2976, 2005.
[197] D. Venegoni, P. Serp, R. Feurer, Y. Kihn, C. Vahlas, and P. Kalck, "Parametric study for the growth of carbon nanotubes by catalytic chemical vapor deposition in a fluidized bed reactor," *Carbon,* vol. 40, pp. 1799-1807, 2002.
[198] C. J. Lee, J. Park, Y. Huh, and J. Y. Lee, "Temperature effect on the growth of carbon nanotubes using thermal chemical vapor deposition," *Chemical Physics Letters,* vol. 343, pp. 33-38, 2001.
[199] M. J. Bronikowski, "CVD growth of carbon nanotube bundle arrays," *Carbon,* vol. 44, pp. 2822-2832, 2006.
[200] W. Z. Li, J. G. Wen, and Z. F. Ren, "Effect of temperature on growth and structure of carbon nanotubes by chemical vapor deposition," *Applied Physics A-Materials Science & Processing,* vol. 74, pp. 397-402, 2002.
[201] C. Singh, M. S. Shaffer, and A. H. Windle, "Production of controlled architectures of aligned carbon nanotubes by an injection chemical vapour deposition method," *Carbon,* vol. 41, pp. 359-368, 2003.
[202] I. Kunadian, R. Andrews, M. P. Menguc, and D. Qian, "Multiwalled carbon nanotube deposition profiles within a CVD reactor: An experimental study," *Chemical Engineering Science,* vol. 64, pp. 1503-1510, 2009.
[203] A. Morancais, B. Caussat, Y. Kihn, P. Kalck, D. Plee, P. Gaillard, *et al.*, "A parametric study of the large scale production of multi-walled carbon nanotubes by fluidized bed catalytic chemical vapor deposition," *Carbon,* vol. 45, pp. 624-635, 2007.
[204] T. Kyotani, L.-f. Tsai, and A. Tomita, "Formation of ultrafine carbon tubes by using an anodic aluminum oxide film as a template," *Chemistry of Materials,* vol. 7, pp. 1427-1428, 1995.
[205] T. Kyotani, L.-f. Tsai, and A. Tomita, "Preparation of ultrafine carbon tubes in nanochannels of an anodic aluminum oxide film," *Chemistry of Materials,* vol. 8, pp. 2109-2113, 1996.
[206] C. R. Martin, "Membrane-based synthesis of nanomaterials," *Chemistry of Materials,* vol. 8, pp. 1739-1746, 1996.
[207] P. L. Chen, J. K. Chang, C. T. Kuo, and F. M. Pan, "Field emission of carbon nanotubes on anodic aluminum oxide template with controlled tube density," *Applied Physics Letters,* vol. 86, 2005.
[208] K. Choy, "Chemical vapour deposition of coatings," *Progress in Materials Science,* vol. 48, pp. 57-170, 2003.
[209] J. H. Han, S. H. Choi, T. Y. Lee, J. B. Yoo, C. Y. Park, H. J. Kim, *et al.*, "Effects of growth parameters on the selective area growth of carbon nanotubes," *Thin Solid Films,* vol. 409, pp. 126-132, 2002.
[210] Y. C. Sui, D. R. Acosta, J. A. Gonzalez-Leon, A. Bermudez, J. Feuchtwanger, B. Z. Cui, *et al.*, "Structure, thermal stability, and deformation of multibranched carbon nanotubes synthesized by CVD in the AAO template," *Journal of Physical Chemistry B,* vol. 105, pp. 1523-1527, 2001.
[211] S. H. Jeong, H. Y. Hwang, S. K. Hwang, and K. H. Lee, "Carbon nanotubes based on anodic aluminum oxide nano-template," *Carbon,* vol. 42, pp. 2073-2080, 2004.

[212] M. J. Kim, J. H. Choi, J. B. Park, S. K. Kim, J. B. Yoo, and C. Y. Park, "Growth characteristics of carbon nanotubes via aluminum nanopore template on Si substrate using PECVD," *Thin Solid Films*, vol. 435, pp. 312-317, 2003.
[213] P. Ciambelli, D. Sannino, M. Sarno, A. Fonseca, and J. Nagy, "Hydrocarbon decomposition in alumina membrane: an effective way to produce carbon nanotubes bundles," *Journal of Nanoscience and Nanotechnology*, vol. 4, pp. 779-787, 2004.
[214] P. Ciambelli, L. Arurault, M. Sarno, S. Fontorbes, C. Leone, L. Datas, *et al.*, "Controlled growth of CNT in mesoporous AAO through optimized conditions for membrane preparation and CVD operation," *Nanotechnology*, vol. 22, p. 265613, 2011.
[215] M. Sarno, D. Sannino, C. Leone, and P. Ciambelli, "CNTs tuning and vertical alignment in anodic aluminium oxide membrane," *Journal of Natural Gas Chemistry*, vol. 21, pp. 639-646, 2012.
[216] D. Mattia, H. H. Ban, and Y. Gogotsi, "Wetting of CVD carbon films by polar and nonpolar liquids and implications for carbon nanopipes," *Langmuir*, vol. 22, pp. 1789-1794, 2006.
[217] G. Crawford, L. Steele, R. Ondris-Crawford, G. Iannacchione, C. Yeager, J. Doane, *et al.*, "Characterization of the cylindrical cavities of Anopore and Nuclepore membranes," *The Journal of Chemical Physics*, vol. 96, p. 7788, 1992.
[218] T. Hertel, R. E. Walkup, and P. Avouris, "Deformation of carbon nanotubes by surface van der Waals forces," *Physical Review B*, vol. 58, p. 13870, 1998.
[219] A. Pantano, D. M Parks, and M. C. Boyce, "Mechanics of deformation of single- and multi-wall carbon nanotubes," *Journal of the Mechanics and Physics of Solids*, vol. 52, pp. 789-821, 2004.
[220] M. P. Rossi, Y. Gogotsi, and K. G. Kornev, "Deformation of carbon nanotubes by exposure to water vapor," *Langmuir*, vol. 25, pp. 2804-2810, 2009.
[221] R. S. Ruoff, J. Tersoff, D. C. Lorents, S. Subramoney, and B. Chan, "Radial deformation of carbon nanotubes by van der Waals forces," *Nature*, vol. 364, pp. 514-516, 1993.
[222] P. Delhaes, "Chemical vapor deposition and infiltration processes of carbon materials," *Carbon*, vol. 40, pp. 641-657, 2002.
[223] S. Marinković and S. Dimitruević, "Carbon/carbon composites prepared by chemical vapour deposition," *Carbon*, vol. 23, pp. 691-699, 1985.
[224] X.-T. Yan and Y. Xu, *Chemical Vapour Deposition: An Integrated Engineering Design for Advanced Materials*: Springer, 2010.
[225] J. S. Lee, G. H. Gu, H. Kim, K. S. Jeong, J. Bae, and J. S. Suh, "Growth of carbon nanotubes on anodic aluminum oxide templates: fabrication of a tube-in-tube and linearly joined tube," *Chemistry of Materials*, vol. 13, pp. 2387-2391, 2001.
[226] Y. Sui, B. Cui, R. Guardian, D. Acosta, L. Martınez, and R. Perez, "Growth of carbon nanotubes and nanofibres in porous anodic alumina film," *Carbon*, vol. 40, pp. 1011-1016, 2002.
[227] H. Morrison, "The analysis of curved arrhenius plots in diffusion experiments," *Philosophical Magazine*, vol. 31, pp. 243-254, 1975.
[228] D. G. Truhlar and A. Kohen, "Convex Arrhenius plots and their interpretation," *Proceedings of the National Academy of Sciences*, vol. 98, pp. 848-851, 2001.

[229] G. D. Towell and J. J. Martin, "Kinetic data from nonisothermal experiments: Thermal decomposition of ethane, ethylene, and acetylene," *AIChE Journal*, vol. 7, pp. 693-698, 1961.
[230] C. E. Morosanu, *Thin films by chemical vapour deposition*: Elsevier Amsterdam, 1990.
[231] D. S. Knight and W. B. White, "Characterization of diamond films by Raman spectroscopy," *Journal of Materials Research*, vol. 4, pp. 385-393, 1989.
[232] P. Lespade, R. Al-Jishi, and M. Dresselhaus, "Model for Raman scattering from incompletely graphitized carbons," *Carbon*, vol. 20, pp. 427-431, 1982.
[233] G. A. Zickler, B. Smarsly, N. Gierlinger, H. Peterlik, and O. Paris, "A reconsideration of the relationship between the crystallite size L_a of carbons determined by X-ray diffraction and Raman spectroscopy," *Carbon*, vol. 44, pp. 3239-3246, 2006.
[234] M. Nakamizo, R. Kammereck, and P. Walker Jr, "Laser Raman studies on carbons," *Carbon*, vol. 12, pp. 259-267, 1974.
[235] R. Dash, J. Chmiola, G. Yushin, Y. Gogotsi, G. Laudisio, J. Singer, *et al.*, "Titanium carbide derived nanoporous carbon for energy-related applications," *Carbon*, vol. 44, pp. 2489-2497, 2006.
[236] K. Yum, N. Wang, and M.-F. Yu, "Nanoneedle: A multifunctional tool for biological studies in living cells," *Nanoscale*, vol. 2, pp. 363-372, 2010.
[237] S. Bonde, K. R. Rostgaard, T. K. Andersen, T. Berthing, and K. L. Martinez, "Exploring arrays of vertical one-dimensional nanostructures for cellular investigations," *Nanotechnology*, vol. 25, p. 362001, 2014.
[238] Y. Alapan, K. Icoz, and U. A. Gurkan, "Micro-and nanodevices integrated with biomolecular probes," *Biotechnology advances*, vol. 33, pp. 1727-1743, 2015.
[239] K. R. Rostgaard, R. S. Frederiksen, Y.-C. C. Liu, T. Berthing, M. H. Madsen, J. Holm, *et al.*, "Vertical nanowire arrays as a versatile platform for protein detection and analysis," *Nanoscale*, vol. 5, pp. 10226-10235, 2013.
[240] V. Krivitsky, L.-C. Hsiung, A. Lichtenstein, B. Brudnik, R. Kantaev, R. Elnathan, *et al.*, "Si nanowires forest-based on-chip biomolecular filtering, separation and preconcentration devices: nanowires do it all," *Nano Letters*, vol. 12, pp. 4748-4756, 2012.
[241] S. Pogodin and V. A. Baulin, "Can a carbon nanotube pierce through a phospholipid bilayer?," *Acs Nano*, vol. 4, pp. 5293-5300, 2010.
[242] T. Berthing, C. B. Sørensen, J. Nygård, and K. L. Martinez, "Applications of nanowire arrays in nanomedicine," *Journal of Nanoneuroscience*, vol. 1, pp. 3-9, 2009.
[243] X. Xie, A. M. Xu, M. R. Angle, N. Tayebi, P. Verma, and N. A. Melosh, "Mechanical model of vertical nanowire cell penetration," *Nano Letters*, vol. 13, pp. 6002-6008, 2013.
[244] Y.-R. Na, S. Y. Kim, J. T. Gaublomme, A. K. Shalek, M. Jorgolli, H. Park, *et al.*, "Probing enzymatic activity inside living cells using a nanowire–cell “sandwich” assay," *Nano Letters*, vol. 13, pp. 153-158, 2012.
[245] A. Hai, J. Shappir, and M. E. Spira, "In-cell recordings by extracellular microelectrodes," *Nature Methods*, vol. 7, pp. 200-202, 2010.

[246] M. Golshadi, L. K. Wright, I. M. Dickerson, and M. G. Schrlau, "High-Efficiency Gene Transfection of Cells through Carbon Nanotube Arrays," *Small,* vol. 12, pp. 3014-3020, 2016.
[247] K. S. Brammer, C. Choi, S. Oh, C. J. Cobb, L. S. Connelly, M. Loya, *et al.*, "Antibiofouling, sustained antibiotic release by Si nanowire templates," *Nano Letters,* vol. 9, pp. 3570-3574, 2009.
[248] J. Wang, "Carbon-nanotube based electrochemical biosensors: A review," *Electroanalysis,* vol. 17, pp. 7-14, 2005.
[249] M. A. Bucaro, Y. Vasquez, B. D. Hatton, and J. Aizenberg, "Fine-tuning the degree of stem cell polarization and alignment on ordered arrays of high-aspect-ratio nanopillars," *Acs Nano,* vol. 6, pp. 6222-6230, 2012.
[250] C. J. Bettinger, R. Langer, and J. T. Borenstein, "Engineering substrate topography at the micro-and nanoscale to control cell function," *Angewandte Chemie International Edition,* vol. 48, pp. 5406-5415, 2009.
[251] T. Berthing, S. Bonde, K. R. Rostgaard, M. H. Madsen, C. B. Sørensen, J. Nygård, *et al.*, "Cell membrane conformation at vertical nanowire array interface revealed by fluorescence imaging," *Nanotechnology,* vol. 23, p. 415102, 2012.
[252] L. Hanson, Z. C. Lin, C. Xie, Y. Cui, and B. Cui, "Characterization of the cell–nanopillar interface by transmission electron microscopy," *Nano Letters,* vol. 12, pp. 5815-5820, 2012.
[253] H. Persson, C. Købler, K. Mølhave, L. Samuelson, J. O. Tegenfeldt, S. Oredsson, *et al.*, "Fibroblasts cultured on nanowires exhibit low motility, impaired cell division, and DNA damage," *Small,* vol. 9, pp. 4006-4016, 2013.
[254] X. Yang, D.-P. Kim, D.-S. Um, G.-H. Kim, and C.-I. Kim, "Temperature dependence on dry etching of Al2O3 thin films in BCl3/Cl2/Ar plasma," *Journal of Vacuum Science & Technology A,* vol. 27, pp. 821-825, 2009.
[255] X. Yang, J.-C. Woo, D.-S. Um, and C.-I. Kim, "Dry Etching of Al 2 O 3 Thin Films in O 2/BCl 3/Ar Inductively Coupled Plasma," *Transactions on Electrical and Electronic Materials,* vol. 11, pp. 202-205, 2010.
[256] K. R. Williams, K. Gupta, and M. Wasilik, "Etch rates for micromachining processing-Part II," *Microelectromechanical Systems, Journal of,* vol. 12, pp. 761-778, 2003.
[257] J. Yeon, W. Lim, J. Park, N. Kwon, S. Kim, K. Min, *et al.*, "Removal of Anodic Aluminum Oxide Barrier Layer on Silicon Substrate by using Cl2/BCl3 Neutral Beam Etching," *Journal of the Electrochemical Society,* vol. 158, pp. D254-D258, 2011.
[258] X. Yang and D. S. Um, "Regular Paper: Dry Etching of Al2O3 Thin Films in O2/BCl3/Ar Inductively Coupled Plasma," *Trans. Electr. Electron. Mater.(TEEM),* vol. 11, pp. 202-205, 2010.
[259] K. Tokunaga, F. Redeker, D. Danner, and D. Hess, "Comparison of aluminum etch rates in carbon tetrachloride and boron trichloride plasmas," *Journal of the Electrochemical Society,* vol. 128, pp. 851-855, 1981.
[260] M. Golshadi and M. G. Schrlau, "Template-Based Synthesis of Aligned Carbon Nanotube Arrays for Microfluidic and Nanofluidic Applications," *ECS Transactions,* vol. 50, pp. 1-14, 2013.

[261] K. R. Williams and R. S. Muller, "Etch rates for micromachining processing," *Microelectromechanical Systems, Journal of,* vol. 5, pp. 256-269, 1996.
[262] J. K. Holt, H. G. Park, Y. Wang, M. Stadermann, A. B. Artyukhin, C. P. Grigoropoulos, *et al.*, "Fast mass transport through sub-2-nanometer carbon nanotubes," *Science,* vol. 312, pp. 1034-1037, 2006.
[263] M. Majumder, N. Chopra, R. Andrews, and B. J. Hinds, "Nanoscale hydrodynamics: enhanced flow in carbon nanotubes," *Nature,* vol. 438, pp. 44-44, 2005.
[264] F. White, "Viscous fluid flow. 2006," ed: McGraw-Hill, 2006.
[265] S. S. Ray, P. Chando, and A. L. Yarin, "Enhanced release of liquid from carbon nanotubes due to entrainment by an air layer," *Nanotechnology,* vol. 20, p. 095711, 2009.
[266] S. Sinha, M. P. Rossi, D. Mattia, Y. Gogotsi, and H. H. Bau, "Induction and measurement of minute flow rates through nanopipes," *Physics of Fluids (1994-present),* vol. 19, p. 013603, 2007.
[267] D. A. Dean, "Cell-specific targeting strategies for electroporation-mediated gene delivery in cells and animals," *J Membr Biol,* vol. 246, pp. 737-44, Oct 2013.
[268] A. Pfeifer and I. M. Verma, "Gene therapy: promises and problems," *Annu Rev Genomics Hum Genet,* vol. 2, pp. 177-211, 2001.
[269] J. A. O'Brien and S. C. Lummis, "Biolistic transfection of neuronal cultures using a hand-held gene gun," *Nat Protoc,* vol. 1, pp. 977-81, 2006.
[270] E. Brailoiu, D. Churamani, X. Cai, M. G. Schrlau, G. C. Brailoiu, X. Gao, *et al.*, "Essential requirement for two-pore channel 1 in NAADP-mediated calcium signaling," *The Journal of cell biology,* vol. 186, pp. 201-209, 2009.
[271] G. Becattini, L. S. Mattos, and D. G. Caldwell, "A fully automated system for adherent cells microinjection," *IEEE J Biomed Health Inform,* vol. 18, pp. 83-93, Jan 2014.
[272] A. K. Shalek, J. T. Robinson, E. S. Karp, J. S. Lee, D.-R. Ahn, M.-H. Yoon, *et al.*, "Vertical silicon nanowires as a universal platform for delivering biomolecules into living cells," *Proceedings of the National Academy of Sciences,* vol. 107, pp. 1870-1875, 2010.
[273] S. C. Egea and I. M. Dickerson, "Direct interactions between calcitonin-like receptor (CLR) and CGRP-receptor component protein (RCP) regulate CGRP receptor signaling," *Endocrinology,* vol. 153, pp. 1850-1860, 2012.
[274] D. S. Auerbach, J. Jones, B. C. Clawson, J. Offord, G. M. Lenk, I. Ogiwara, *et al.*, "Altered cardiac electrophysiology and SUDEP in a model of Dravet syndrome," *Plos One,* vol. 8, p. e77843, 2013.
[275] Z. Orynbayeva, R. Singhal, E. A. Vitol, M. G. Schrlau, E. Papazoglou, G. Friedman, *et al.*, "Physiological validation of cell health upon probing with carbon nanotube endoscope and its benefit for single-cell interrogation," *Nanomedicine: Nanotechnology, Biology and Medicine,* vol. 8, pp. 590-598, 2012.
[276] R. Langer, "Drug delivery and targeting," *Nature,* vol. 392, pp. 5-10, 1998.
[277] D. B. Peckys and N. de Jonge, "Visualizing gold nanoparticle uptake in live cells with liquid scanning transmission electron microscopy," *Nano Letters,* vol. 11, pp. 1733-1738, 2011.

[278] S. Bhattacharyya, R. Bhattacharya, S. Curley, M. A. McNiven, and P. Mukherjee, "Nanoconjugation modulates the trafficking and mechanism of antibody induced receptor endocytosis," *Proceedings of the National Academy of Sciences,* vol. 107, pp. 14541-14546, 2010.
[279] M. Kwak, L. Han, J. J. Chen, and R. Fan, "Interfacing Inorganic Nanowire Arrays and Living Cells for Cellular Function Analysis," *Small,* vol. 11, pp. 5600-5610, 2015.
[280] C. N. Prinz, "Interactions between semiconductor nanowires and living cells," *Journal of Physics: Condensed Matter,* vol. 27, p. 233103, 2015.
[281] L. ten Siethoff , M. Lard, J. Generosi, H. k. S. Andersson, H. Linke, and A . Mårnsson, "Molecular motor propelled filaments reveal light-guiding in nanowire arrays for enhanced biosensing," *Nano Letters,* vol. 14, pp. 737-742, 2014.
[282] W. Hällström, M. Lexholm, D. B. Suyatin, G. Hammarin, D. Hessman, L. Samuelson, *et al.*, "Fifteen-piconewton force detection from neural growth cones using nanowire arrays," *Nano Letters,* vol. 10, pp. 782-787, 2010.
[283] Z. Li, J. Song, G. Mantini, M.-Y. Lu, H. Fang, C. Falconi, *et al.*, "Quantifying the traction force of a single cell by aligned silicon nanowire array," *Nano Letters,* vol. 9, pp. 3575-3580, 2009.
[284] D. B. Suyatin, W. Hällström, L. Samuelson, L. Montelius, C. N. Prinz, and M. Kanje, "Gallium phosphide nanowire arrays and their possible application in cellular force investigations," *Journal of Vacuum Science & Technology B,* vol. 27, pp. 3092-3094, 2009.
[285] M. Lard, L. Ten Siethoff , J. Generosi, A. Månsson, and H. Linke, "Molecular motor transport through hollow nanowires," *Nano Letters,* vol. 14, pp. 3041-3046, 2014.
[286] X. Duan, T.-M. Fu, J. Liu, and C. M. Lieber, "Nanoelectronics-biology frontier: From nanoscopic probes for action potential recording in live cells to three-dimensional cyborg tissues," *Nano Today,* vol. 8, pp. 351-373, 2013.
[287] J. T. Robinson, M. Jorgolli, A. K. Shalek, M.-H. Yoon, R. S. Gertner, and H. Park, "Vertical nanowire electrode arrays as a scalable platform for intracellular interfacing to neuronal circuits," *Nature Nanotechnology,* vol. 7, pp. 180-184, 2012.
[288] C. Xie, Z. Lin, L. Hanson, Y. Cui, and B. Cui, "Intracellular recording of action potentials by nanopillar electroporation," *Nature Nanotechnology,* vol. 7, pp. 185-190, 2012.
[289] W. Hällström, C. N. Prinz, D. Suyatin, L. Samuelson, L. Montelius, and M. Kanje, "Rectifying and sorting of regenerating axons by free-standing nanowire patterns: a highway for nerve fibers," *Langmuir,* vol. 25, pp. 4343-4346, 2009.
[290] C. Prinz, W. Hällström, T. Mårtensson, L. Samuelson, L. Montelius, and M. Kanje, "Axonal guidance on patterned free-standing nanowire surfaces," *Nanotechnology,* vol. 19, p. 345101, 2008.
[291] S. Bonde, T. Berthing, M. H. Madsen, T. K. Andersen, N. Buch-Månson, L. Guo, *et al.*, "Tuning InAs nanowire density for HEK293 cell viability, adhesion, and morphology: Perspectives for nanowire-based biosensors," *ACS applied materials & interfaces,* vol. 5, pp. 10510-10519, 2013.

[292] S.-W. Kuo, H.-I. Lin, J. H.-C. Ho, Y.-R. V. Shih, H.-F. Chen, T.-J. Yen, *et al.*, "Regulation of the fate of human mesenchymal stem cells by mechanical and stereo-topographical cues provided by silicon nanowires," *Biomaterials,* vol. 33, pp. 5013-5022, 2012.
[293] S. Qi, C. Yi, S. Ji, C.-C. Fong, and M. Yang, "Cell adhesion and spreading behavior on vertically aligned silicon nanowire arrays," *ACS applied materials & interfaces,* vol. 1, pp. 30-34, 2008.
[294] B. Wehrle-Haller and B. A. Imhof, "Actin, microtubules and focal adhesion dynamics during cell migration," *The international journal of biochemistry & cell biology,* vol. 35, pp. 39-50, 2003.
[295] B. Wehrle-Haller and B. A. Imhof, "Integrin-dependent pathologies," *The Journal of pathology,* vol. 200, pp. 481-487, 2003.
[296] F.-H. Lee, C. Haskell, I. F. Charo, and D. Boettiger, "Receptor-ligand binding in the cell-substrate contact zone: a quantitative analysis using CX3CR1 and CXCR1 chemokine receptors," *Biochemistry,* vol. 43, pp. 7179-7186, 2004.
[297] D. Cuvelier, M. Théry, Y.-S. Chu, S. Dufour, J.-P. Thiéry, M. Bornens, *et al.*, "The universal dynamics of cell spreading," *Current biology,* vol. 17, pp. 694-699, 2007.
[298] S. Nir and M. Andersen, "Van der Waals interactions between cell surfaces," *The Journal of membrane biology,* vol. 31, pp. 1-18, 1977.
[299] S. J. Son, X. Bai, and S. B. Lee, "Inorganic hollow nanoparticles and nanotubes in nanomedicine: Part 1. Drug/gene delivery applications," *Drug Discovery Today,* vol. 12, pp. 650-656, 2007.
[300] S. J. Son, X. Bai, and S. B. Lee, "Inorganic hollow nanoparticles and nanotubes in nanomedicine: Part 2: Imaging, diagnostic, and therapeutic applications," *Drug Discovery Today,* vol. 12, pp. 657-663, 2007.
[301] S. McLenachan, J. P. Sarsero, and P. A. Ioannou, "Flow-cytometric analysis of mouse embryonic stem cell lipofection using small and large DNA constructs," *Genomics,* vol. 89, pp. 708-720, 2007.
[302] V. F. Van Tendeloo, P. Ponsaerts, F. Lardon, G. Nijs, M. Lenjou, C. Van Broeckhoven, *et al.*, "Highly efficient gene delivery by mRNA electroporation in human hematopoietic cells: superiority to lipofection and passive pulsing of mRNA and to electroporation of plasmid cDNA for tumor antigen loading of dendritic cells," *Blood,* vol. 98, pp. 49-56, 2001.
[303] M. A. Kotterman, T. Vazin, and D. V. Schaffer, "Enhanced selective gene delivery to neural stem cells in vivo by an adeno-associated viral variant," *Development,* vol. 142, pp. 1885-1892, 2015.
[304] M. A. Kay, J. C. Glorioso, and L. Naldini, "Viral vectors for gene therapy: the art of turning infectious agents into vehicles of therapeutics," *Nature Medicine,* vol. 7, pp. 33-40, 2001.
[305] M. T. Lin, L. Pulkkinen, J. Uitto, and K. Yoon, "The gene gun: current applications in cutaneous gene therapy," *International journal of dermatology,* vol. 39, pp. 161-170, 2000.
[306] K. A. Whitehead, R. Langer, and D. G. Anderson, "Knocking down barriers: advances in siRNA delivery," *Nature Reviews Drug Discovery,* vol. 8, pp. 129-138, 2009.

[307] J. S. Wadia and S. F. Dowdy, "Protein transduction technology," *Current Opinion in Biotechnology*, vol. 13, pp. 52-56, 2002.
[308] Z. Liu, M. Winters, M. Holodniy, and H. Dai, "siRNA delivery into human T cells and primary cells with carbon-nanotube transporters," *Angewandte Chemie International Edition*, vol. 46, pp. 2023-2027, 2007.
[309] J. L. Gori, P. D. Hsu, M. L. Maeder, S. Shen, G. G. Welstead, and D. Bumcrot, "Delivery and Specificity of CRISPR/Cas9 Genome Editing Technologies for Human Gene Therapy," *Human gene therapy*, vol. 26, pp. 443-451, 2015.
[310] P. D. Hsu, E. S. Lander, and F. Zhang, "Development and applications of CRISPR-Cas9 for genome engineering," *Cell*, vol. 157, pp. 1262-1278, 2014.
[311] A. Aalipour, A. M. Xu, S. Leal-Ortiz, C. C. Garner, and N. A. Melosh, "Plasma membrane and actin cytoskeleton as synergistic barriers to nanowire cell penetration," *Langmuir*, vol. 30, pp. 12362-12367, 2014.
[312] E. P. Papapetrou, N. C. Zoumbos, and A. Athanassiadou, "Genetic modification of hematopoietic stem cells with nonviral systems: past progress and future prospects," *Gene Ther*, vol. 12 Suppl 1, pp. S118-30, Oct 2005.
[313] J. Fergus, R. Quintanilla, and U. Lakshmipathy, "Characterizing Pluripotent Stem Cells Using the TaqMan® hPSC Scorecard TM Panel," *Human Embryonic Stem Cell Protocols*, pp. 25-37, 2016.
[314] A. M. Tsankov, V. Akopian, R. Pop, S. Chetty, C. A. Gifford, L. Daheron, *et al.*, "A qPCR ScoreCard quantifies the differentiation potential of human pluripotent stem cells," *Nature biotechnology*, 2015.
[315] G. Dontu and M. S. Wicha, "Survival of mammary stem cells in suspension culture: implications for stem cell biology and neoplasia," *Journal of mammary gland biology and neoplasia*, vol. 10, pp. 75-86, 2005.
[316] S. K. Singh, I. D. Clarke, M. Terasaki, V. E. Bonn, C. Hawkins, J. Squire, *et al.*, "Identification of a cancer stem cell in human brain tumors," *Cancer research*, vol. 63, pp. 5821-5828, 2003.
[317] T. Akerstrom, K. Vedel, J. Needham, P. Hojman, E. Kontou, Y. Hellsten, *et al.*, "Optimizing hyaluronidase dose and plasmid DNA delivery greatly improves gene electrotransfer efficiency in rat skeletal muscle," *Biochemistry and Biophysics Reports*, vol. 4, pp. 342-350, 2015.
[318] H. Jansen, H. Gardeniers, M. de Boer, M. Elwenspoek, and J. Fluitman, "A survey on the reactive ion etching of silicon in microtechnology," *Journal of micromechanics and microengineering*, vol. 6, p. 14, 1996.
[319] J. Hopwood, "Review of inductively coupled plasmas for plasma processing," *Plasma Sources Science and Technology*, vol. 1, p. 109, 1992.
[320] O. Instruments. (2016). *Inductively Coupled Plasma (ICP) Etching*. Available: http://www.oxford-instruments.com/products/etching-deposition-and-growth/plasma-etch-deposition/icp-etch
[321] A. Beltrán-Langarica, D. López-Contreras, and W. Kuri-Harcuch, "A simple procedure for washing and sterilizing plastic tissue culture dishes for reuse," *Journal of tissue culture methods*, vol. 8, pp. 173-176, 1983.
[322] M. P. Petkov, "Non-Destructive Cleaning of Carbon Nanotube Surfaces: Removal of Organic Contaminants and Chemical Residue with Oxygen Radicals," *Microscopy and Microanalysis*, vol. 11, pp. 1928-1929, 2005.

[323] L. M. Fujimoto, R. Roth, J. E. Heuser, and S. L. Schmid, "Actin assembly plays a variable, but not obligatory role in receptor-mediated endocytosis in mammalian cells," *Traffic,* vol. 1, pp. 161-71, Feb 2000.
[324] E. P. Kilsdonk, P. G. Yancey, G. W. Stoudt, F. W. Bangerter, W. J. Johnson, M. C. Phillips, *et al.*, "Cellular cholesterol efflux mediated by cyclodextrins," *J Biol Chem,* vol. 270, pp. 17250-6, Jul 21 1995.
[325] S. K. Rodal, G. Skretting, O. Garred, F. Vilhardt, B. van Deurs, and K. Sandvig, "Extraction of cholesterol with methyl-beta-cyclodextrin perturbs formation of clathrin-coated endocytic vesicles," *Mol Biol Cell,* vol. 10, pp. 961-74., 1999.
[326] P. A. Orlandi and P. H. Fishman, "Filipin-dependent inhibition of cholera toxin: evidence for toxin internalization and activation through caveolae-like domains," *J Cell Biol,* vol. 141, pp. 905-15, May 18 1998.
[327] D. Dutta, C. D. Williamson, N. B. Cole, and J. G. Donaldson, "Pitstop 2 is a potent inhibitor of clathrin-independent endocytosis," *PLoS One,* vol. 7, p. e45799, 2012.
[328] M. Hamasaki, N. Araki, and T. Hatae, "Association of early endosomal autoantigen 1 with macropinocytosis in EGF-stimulated A431 cells," *Anat Rec A Discov Mol Cell Evol Biol,* vol. 277, pp. 298-306, Apr 2004.
[329] M. A. West, M. S. Bretscher, and C. Watts, "Distinct endocytotic pathways in epidermal growth factor-stimulated human carcinoma A431 cells," *J Cell Biol,* vol. 109, pp. 2731-9, Dec 1989.
[330] I. M. Anton, S. P. Saville, M. J. Byrne, C. Curcio, N. Ramesh, J. H. Hartwig, *et al.*, "WIP participates in actin reorganization and ruffle formation induced by PDGF," *J Cell Sci,* vol. 116, pp. 2443-51, Jun 15 2003.
[331] S. Lee, Y. Sato, and R. A. Nixon, "Lysosomal proteolysis inhibition selectively disrupts axonal transport of degradative organelles and causes an Alzheimer's-like axonal dystrophy," *J Neurosci,* vol. 31, pp. 7817-30, May 25 2011.
[332] A. P. Bevan, A. Krook, J. Tikerpae, P. J. Seabright, K. Siddle, and G. D. Smith, "Chloroquine extends the lifetime of the activated insulin receptor complex in endosomes," *Journal of Biological Chemistry,* vol. 272, pp. 26833-26840, 1997.
[333] D. Koley and A. J. Bard, "Triton X-100 concentration effects on membrane permeability of a single HeLa cell by scanning electrochemical microscopy (SECM)," *Proceedings of the National Academy of Sciences,* vol. 107, pp. 16783-16787, 2010.
[334] T. Kumeria, A. Santos, and D. Losic, "Nanoporous anodic alumina platforms: engineered surface chemistry and structure for optical sensing applications," *Sensors,* vol. 14, pp. 11878-11918, 2014.
[335] R. S. Balaban, S. Nemoto, and T. Finkel, "Mitochondria, oxidants, and aging," *Cell,* vol. 120, pp. 483-95, Feb 25 2005.
[336] X. J. Huang and Y. K. Choi, "Chemical sensors based on nanostructured materials," *Sensors and Actuators B-Chemical,* vol. 122, pp. 659-671, Mar 26 2007.
[337] J. X. Wang, M. X. Li, Z. J. Shi, N. Q. Li, and Z. N. Gu, "Direct electrochemistry of cytochrome c at a glassy carbon electrode modified with single-wall carbon nanotubes," *Analytical Chemistry,* vol. 74, pp. 1993-1997, May 1 2002.

[338] Y. Tu, Y. H. Lin, W. Yantasee, and Z. F. Ren, "Carbon nanotubes based nanoelectrode arrays: Fabrication, evaluation, and application in voltammetric analysis," *Electroanalysis,* vol. 17, pp. 79-84, Jan 2005.
[339] G. D. Liu, Y. H. Lin, Y. Tu, and Z. F. Ren, "Ultrasensitive voltammetric detection of trace heavy metal ions using carbon nanotube nanoelectrode array," *Analyst,* vol. 130, pp. 1098-1101, 2005.
[340] R. C. Mani, X. Li, M. K. Sunkara, and K. Rajan, "Carbon nanopipettes," *Nano Letters,* vol. 3, pp. 671-673, May 2003.
[341] S. Miserendino, J. Yoo, A. Cassell, and Y. C. Tai, "Electrochemical characterization of parylene-embedded carbon nanotube nanoelectrode arrays," *Nanotechnology,* vol. 17, pp. S23-S28, Feb 28 2006.
[342] R. L. McCreery, "Advanced carbon electrode materials for molecular electrochemistry," *Chem. Rev,* vol. 108, pp. 2646-2687, 2008.
[343] K. T. Kawagoe, P. A. Garris, and R. M. Wightman, "pH-Dependent processes at Nafion¬Æ-coated carbon-fiber microelectrodes," *Journal of Electroanalytical Chemistry,* vol. 359, pp. 193-207, 1993.
[344] Y. Lee and J. Kim, "Simultaneous electrochemical detection of nitric oxide and carbon monoxide generated from mouse kidney organ tissues," *Analytical Chemistry,* vol. 79, pp. 7669-75, Oct 15 2007.
[345] C. Amatore, S. Arbault, M. Guille, and F. Lemaitre, "Electrochemical monitoring of single cell secretion: vesicular exocytosis and oxidative stress," *Chemical Reviews,* vol. 108, pp. 2585-2621, 2008.
[346] B. S. Harrison and A. Atala, "Carbon nanotube applications for tissue engineering," *Biomaterials,* vol. 28, pp. 344-353, Jan 2007.
[347] D. L. Shi, J. Lian, W. Wang, G. K. Liu, P. He, Z. Y. Dong, *et al.*, "Luminescent carbon nanotubes by surface functionalization," *Advanced Materials,* vol. 18, pp. 189-+, Jan 19 2006.
[348] A. K. Gupta and M. Gupta, "Synthesis and surface engineering of iron oxide nanoparticles for biomedical applications," *Biomaterials,* vol. 26, pp. 3995-4021, Jun 2005.
[349] R. Singh, D. Pantarotto, L. Lacerda, G. Pastorin, C. Klumpp, M. Prato, *et al.*, "Tissue biodistribution and blood clearance rates of intravenously administered carbon nanotube radiotracers," *Proceedings of the National Academy of Sciences of the United States of America,* vol. 103, pp. 3357-3362, Feb 28 2006.
[350] M. C. Denis, U. Mahmood, C. Benoist, D. Mathis, and R. Weissleder, "Imaging inflammation of the pancreatic islets in type 1 diabetes," *Proceedings of the National Academy of Sciences of the United States of America,* vol. 101, pp. 12634-12639, Aug 24 2004.
[351] H. I. Jung, M. I. Kettunen, B. Davletov, and K. M. Brindle, "Detection of apoptosis using the C2A domain of synaptotagmin I," *Bioconjugate Chemistry,* vol. 15, pp. 983-987, Sep-Oct 2004.
[352] M. Zhao, D. A. Beauregard, L. Loizou, B. Davletov, and K. M. Brindle, "Non-invasive detection of apoptosis using magnetic resonance imaging and a targeted contrast agent," *Nature Medicine,* vol. 7, pp. 1241-1244, Nov 2001.

[353] E. A. Schellenberger, F. Reynolds, R. Weissleder, and L. Josephson, "Surface-functionalized nanoparticle library yields probes for apoptotic cells," *Chembiochem,* vol. 5, pp. 275-279, Mar 5 2004.

[354] P. M. Winter, A. M. Morawski, S. D. Caruthers, R. W. Fuhrhop, H. Y. Zhang, T. A. Williams, *et al.*, "Molecular imaging of angiogenesis in early-stage atherosclerosis with alpha(v)beta(3)-Integrin-targeted nanoparticles," *Circulation,* vol. 108, pp. 2270-2274, Nov 4 2003.

[355] A. H. Schmieder, P. M. Winter, S. D. Caruthers, T. D. Harris, T. A. Williams, J. S. Allen, *et al.*, "Molecular MR imaging of melanoma angiogenesis with alpha(nu)beta(3)-targeted paramagnetic nanoparticles," *Magnetic Resonance in Medicine,* vol. 53, pp. 621-627, Mar 2005.

[356] Z. Xu, X. Chen, X. H. Qu, J. B. Jia, and S. J. Dong, "Single-wall carbon nanotube-based voltammetric sensor and biosensor," *Biosensors & Bioelectronics,* vol. 20, pp. 579-584, Oct 15 2004.

[357] R. Singh, D. Pantarotto, D. McCarthy, O. Chaloin, J. Hoebeke, C. D. Partidos, *et al.*, "Binding and condensation of plasmid DNA onto functionalized carbon nanotubes: Toward the construction of nanotube-based gene delivery vectors," *Journal of the American Chemical Society,* vol. 127, pp. 4388-4396, Mar 30 2005.

[358] R. J. Chen, H. C. Choi, S. Bangsaruntip, E. Yenilmez, X. W. Tang, Q. Wang, *et al.*, "An investigation of the mechanisms of electronic sensing of protein adsorption on carbon nanotube devices," *Journal of the American Chemical Society,* vol. 126, pp. 1563-1568, Feb 11 2004.

[359] J. Wang and M. Musameh, "Electrochemical detection of trace insulin at carbon-nanotube-modified electrodes," *Analytica Chimica Acta,* vol. 511, pp. 33-36, May 24 2004.

[360] Y. Z. Xian, Y. Y. Zhou, H. T. Wang, L. H. Zhou, F. Liu, and L. T. Jin, "Nanostructured electrode based on multi-wall carbon nanotubes/Pt microparticles nanocomposite for electrochemical determination of thiols in rat striatum by high performance liquid chromatography separation," *Journal of Chromatography B-Analytical Technologies in the Biomedical and Life Sciences,* vol. 817, pp. 239-246, Mar 25 2005.

[361] X. C. Tan, M. J. Ll, P. X. Cai, L. J. Luo, and X. Y. Zou, "An amperometric cholesterol biosensor based on multiwalled carbon nanotubes and organically modified sol-gel/chitosan hybrid composite film," *Analytical Biochemistry,* vol. 337, pp. 111-120, Feb 1 2005.

[362] M. Kaempgen and S. Roth, "Transparent and flexible carbon nanotube/polyaniline pH sensors," *Journal of Electroanalytical Chemistry,* vol. 586, pp. 72-76, Jan 1 2006.

[363] A. Abarrategi, M. C. Gutierrez, C. Moreno-Vicente, M. J. Hortiguela, V. Ramos, J. L. Lopez-Lacomba, *et al.*, "Multiwall carbon nanotube scaffolds for tissue engineering purposes," *Biomaterials,* vol. 29, pp. 94-102, Jan 2008.

[364] V. Lovat, D. Pantarotto, L. Lagostena, B. Cacciari, M. Grandolfo, M. Righi, *et al.*, "Carbon nanotube substrates boost neuronal electrical signaling," *Nano Letters,* vol. 5, pp. 1107-1110, Jun 2005.

[365] M. A. Correa-Duarte, N. Wagner, J. Rojas-Chapana, C. Morsczeck, M. Thie, and M. Giersig, "Fabrication and biocompatibility of carbon nanotube-based 3D

networks as scaffolds for cell seeding and growth," *Nano Letters*, vol. 4, pp. 2233-2236, Nov 2004.

[366] A. V. Melechko, R. Desikan, T. E. McKnight, K. L. Klein, and P. D. Rack, "Synthesis of vertically aligned carbon nanofibres for interfacing with live systems," *Journal of Physics D-Applied Physics*, vol. 42, Oct 7 2009.

[367] S.-H. Yeom, O.-G. Kim, B.-H. Kang, K.-J. Kim, H. Yuan, D.-H. Kwon, *et al.*, "Highly sensitive nano-porous lattice biosensor based on localized surface plasmon resonance and interference," *Optics express*, vol. 19, pp. 22882-22891, 2011.

[368] T. Kumeria and D. Losic, "Controlling interferometric properties of nanoporous anodic aluminium oxide," *Nanoscale research letters*, vol. 7, pp. 1-10, 2012.

CHAPTER 10

Appendices

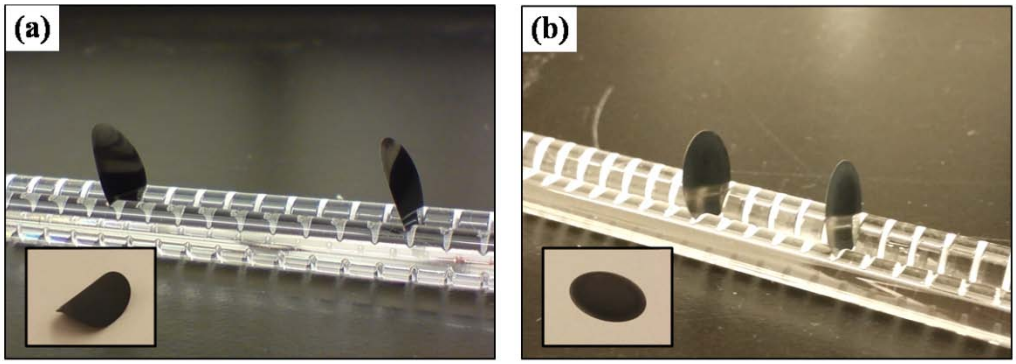

Figure S1: Flat and curled membranes after the CVD process. The membranes (a) without pre-process annealing will curl after the CVD, while the (b) annealed membranes remain flat.

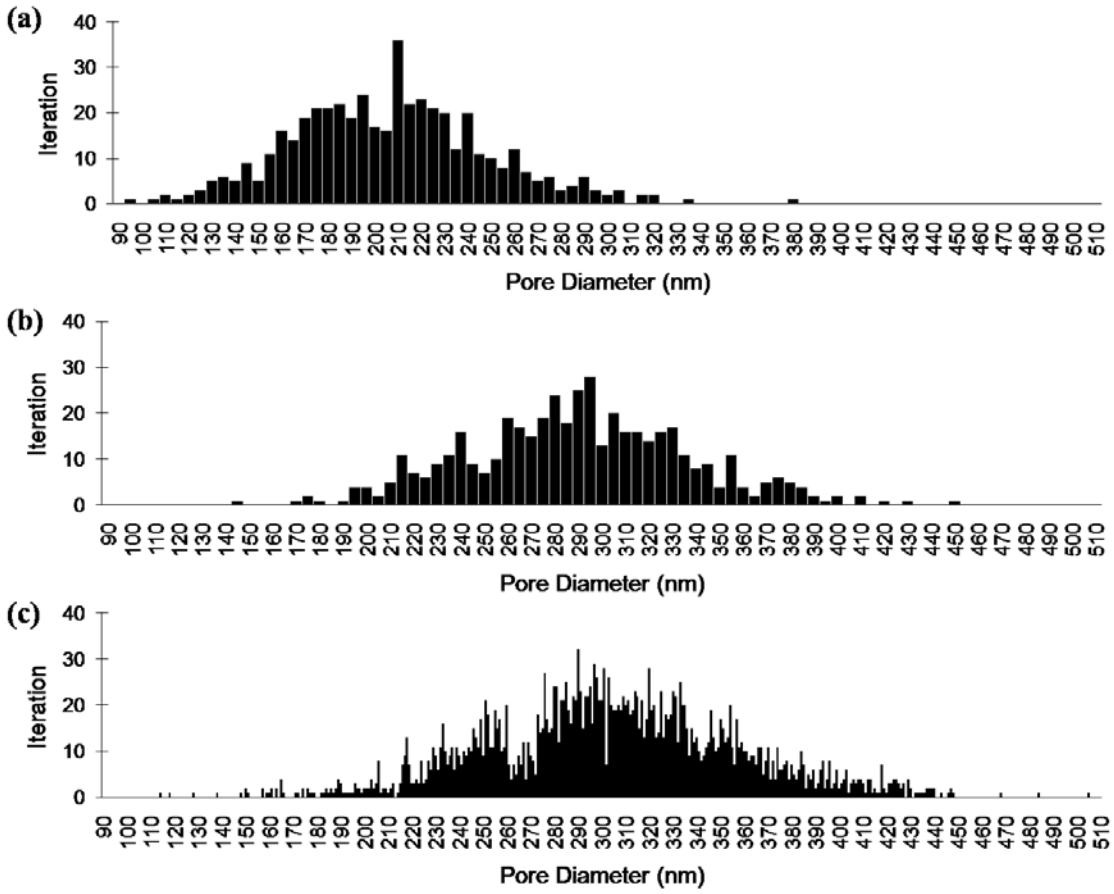

Figure S2: Histograms of the template pore diameter measurement using (a, b) SEM micrographs of the surface of the Whatman 200 nm AAO membranes, and (c) TEM micrographs of the resultant CNTs.

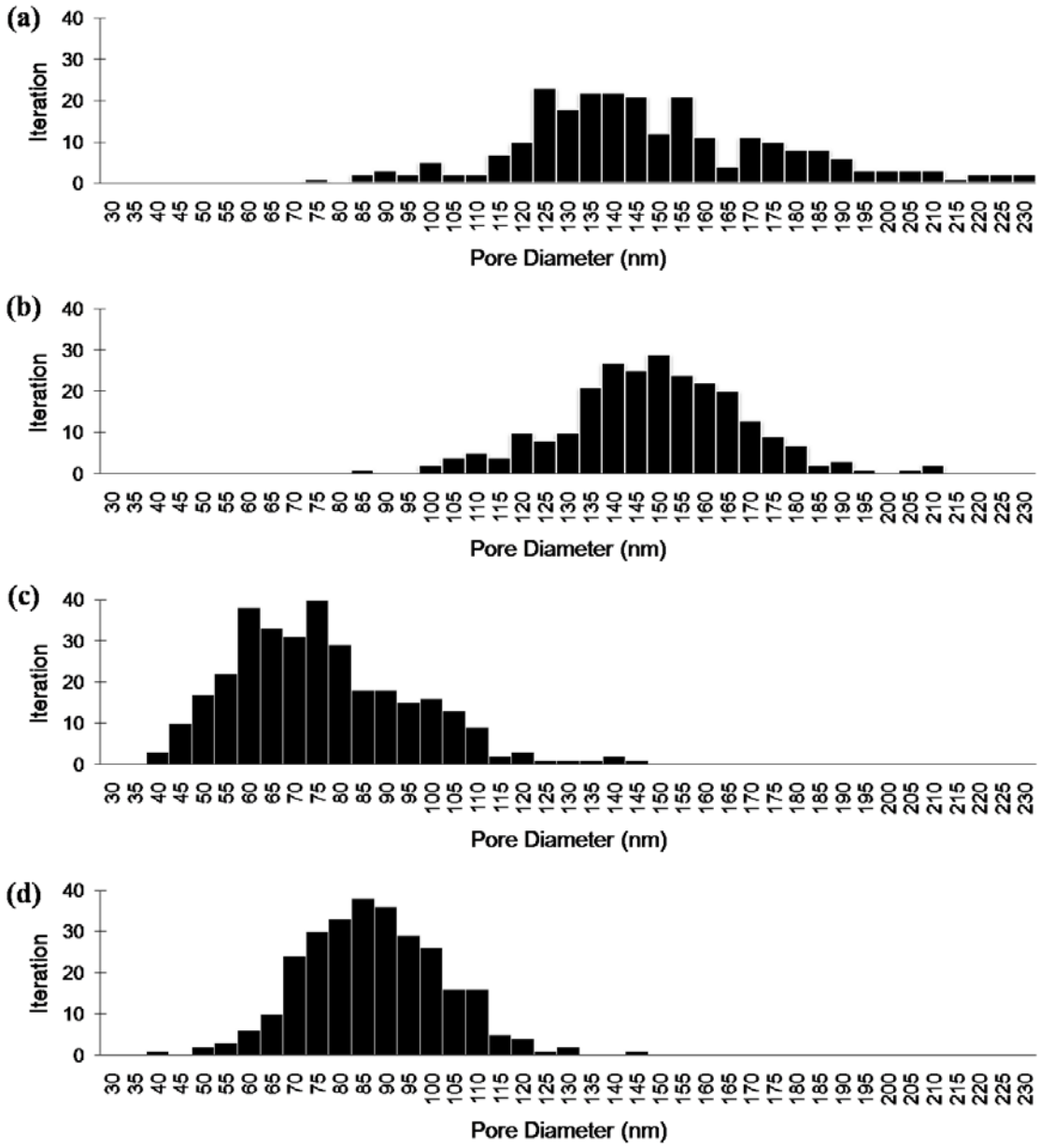

Figure S3: Histograms of the template pore diameter measurement using SEM micrographs of the AAO surfaces for (a, b) Synkera 150 nm and (c, d) Synkera 100 nm membranes.

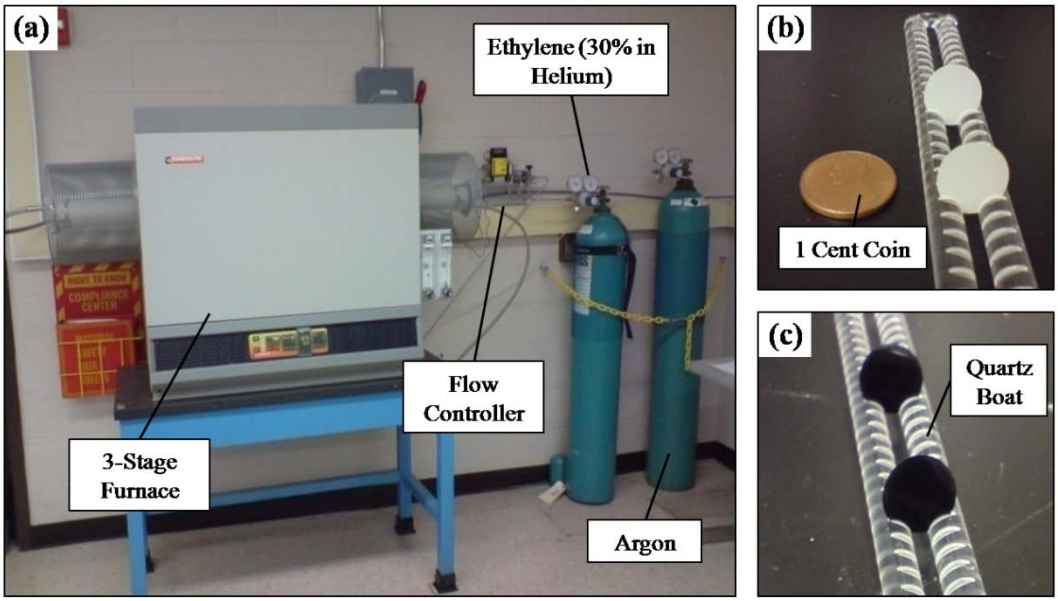

Figure S4: (a) Chemical vapor deposition (CVD) experimental setup, and the AAO membranes (b) before and (c) after carbon deposition using CVD. The dark black color indicates deposited carbon over the AAO surfaces.

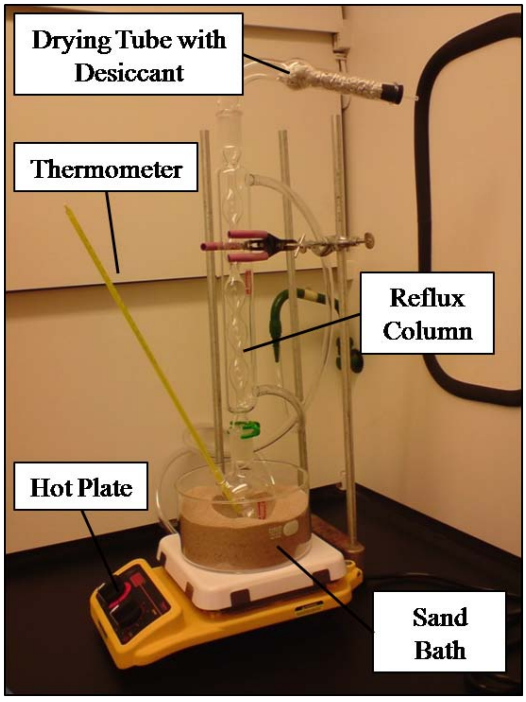

Figure S5: The reflux column setup for wet chemical etching of AAO membranes with controlled etchant temperature and molarity.

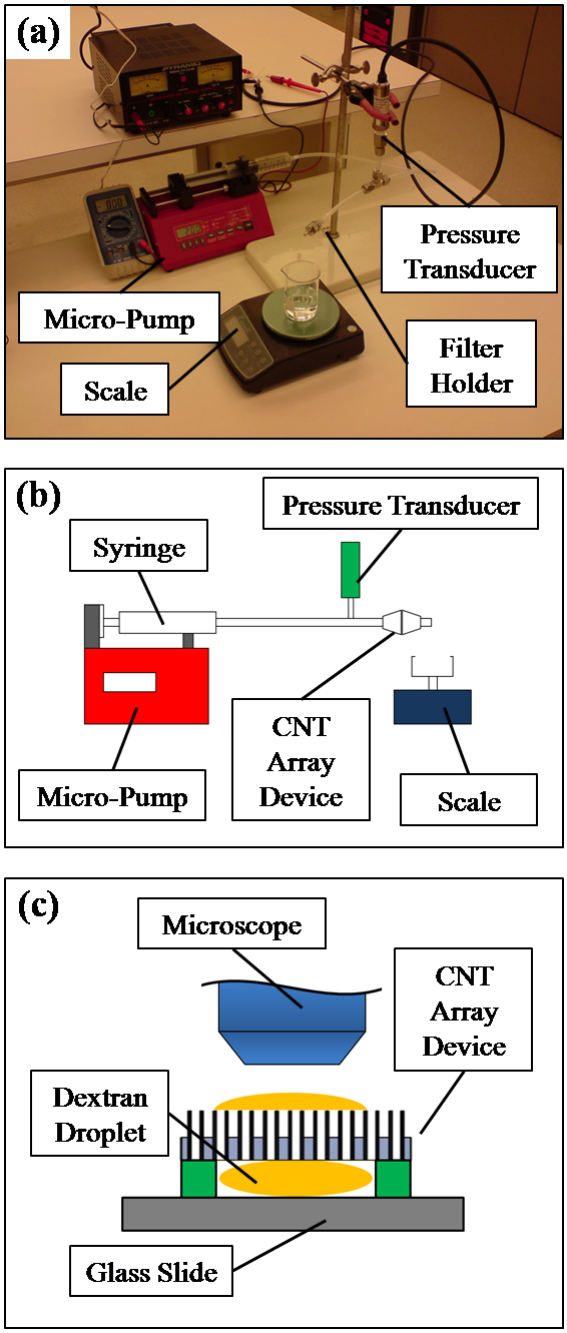

Figure S6: Fluid transportation through CNT array device. (a) Experimental setup and (b) schematics of fluid transportation system using pressure gradient. (c) Schematic illustration of the experimental setup for fluid transportation through CNT array device using concentration gradient.

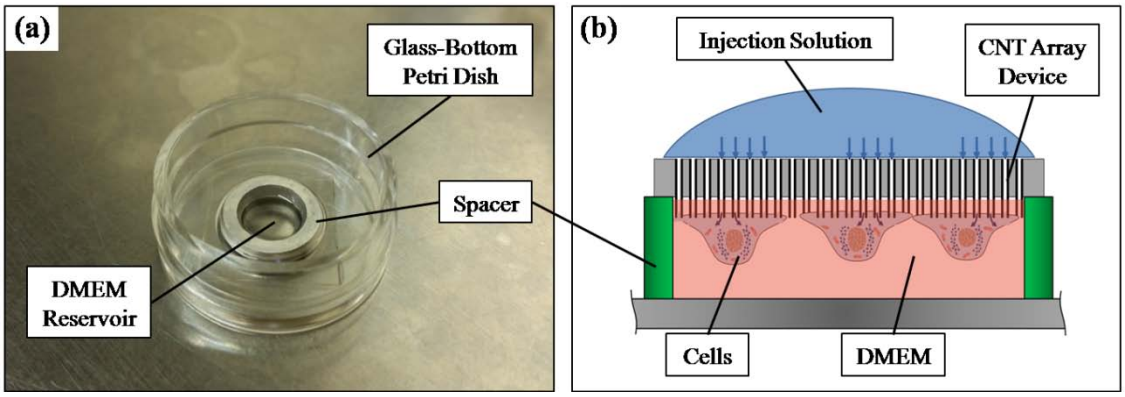

Figure S7: (a) Experimental and (b) schematic illustration of intracellular transfection setup.

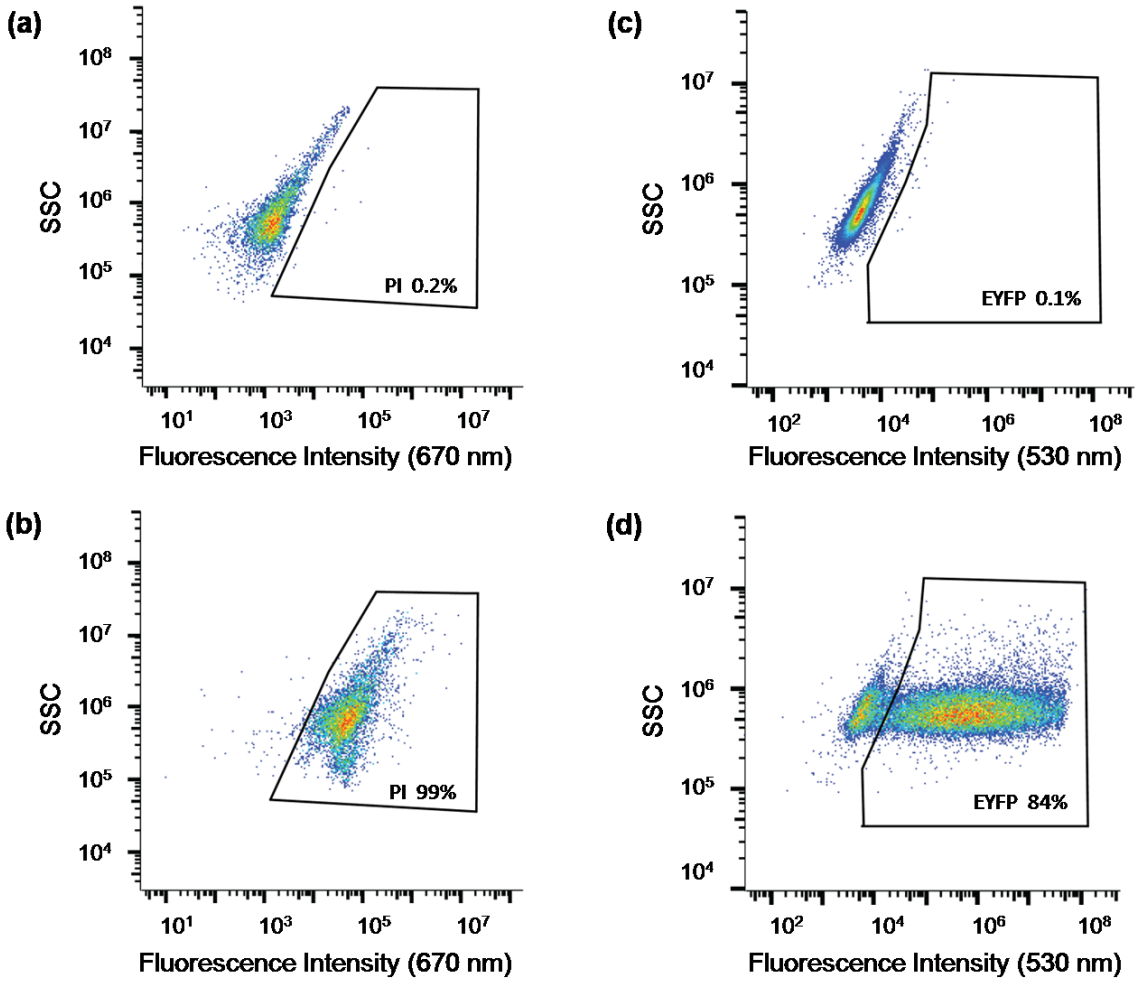

Figure S8: Flow cytometry gates. (a) Gate for PI dye was set for 0.2% (PI) spillover of positive control untransfected L6 cells. (b) Gate defined in (a) applied to L6 cells transfected with PI. (c) Gate for EYFP fluorescence was set for 0.1% (EYFP) spillover of positive control untransfected HEK293 cells. (d) Gate defined in (c) applied to HEK293 cells transfected with plasmid DNA encoding EYFP.

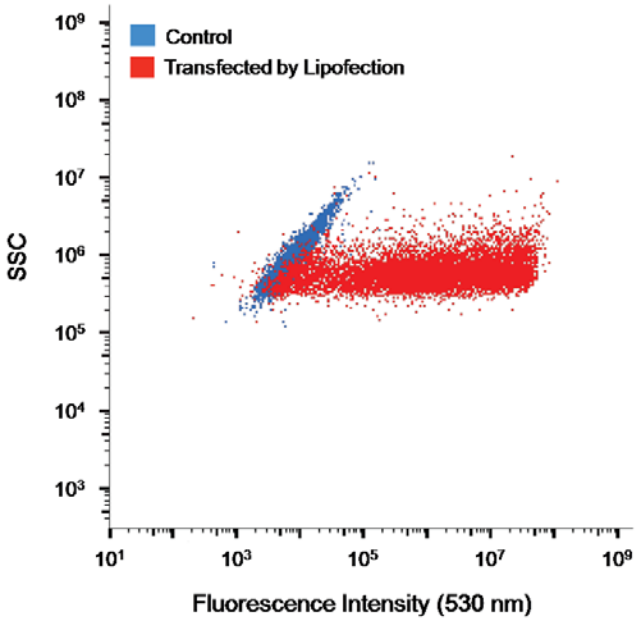

Figure S9: Flow cytometry results of HEK293 cells transfected with plasmid DNA encoding EYFP by lipofection. Transfection indicated by rightward shift in the 530 nm fluorescence intensity of injected cell population (red) compared to control uninjected (blue) cells. Thirty thousand cells were counted for each sample population.

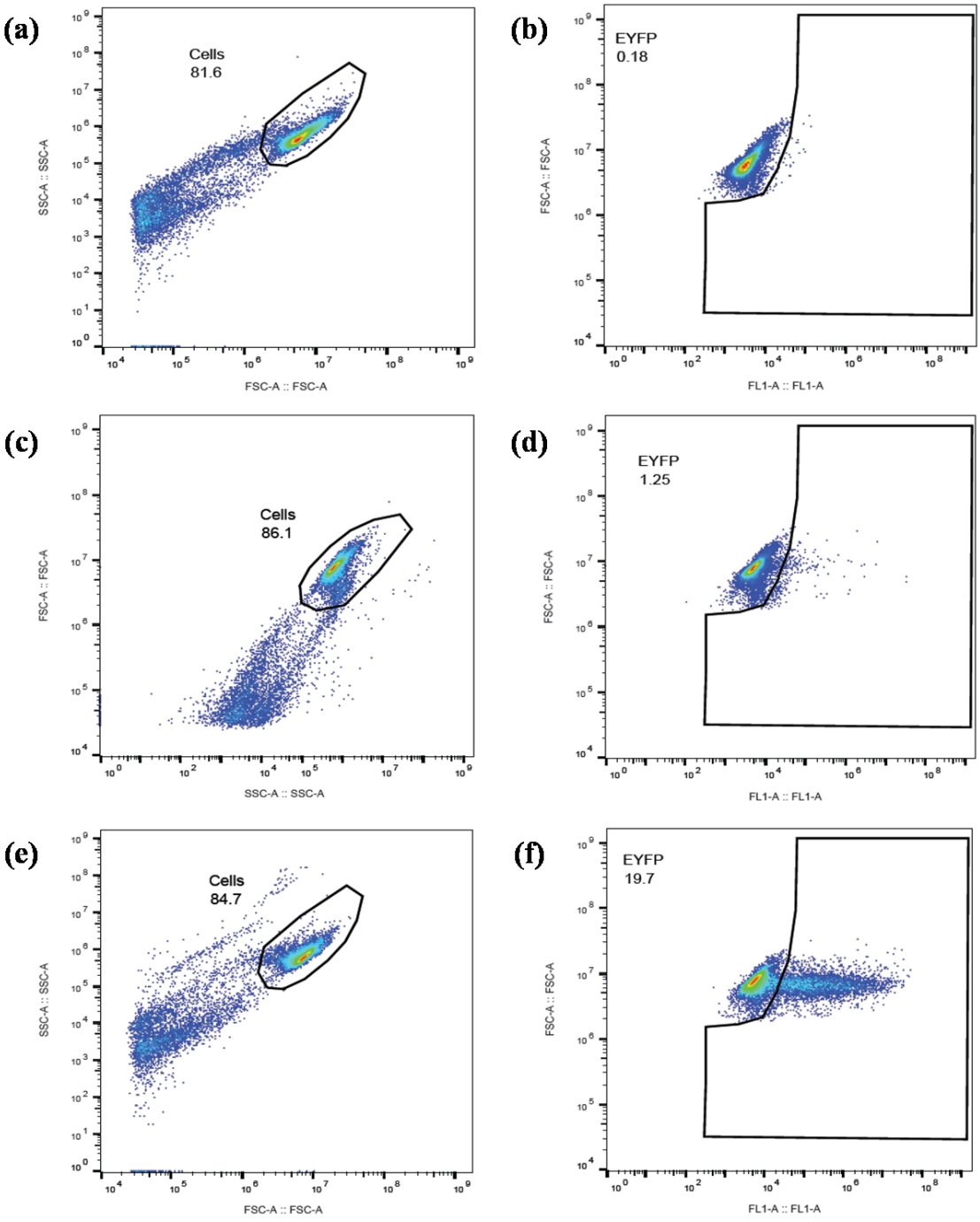
(a)
Cells
81.6
SSC-A :: SSC-A
FSC-A :: FSC-A
(b)
EYFP
0.18
FSC-A :: FSC-A
FL1-A :: FL1-A
(c)
Cells
86.1
FSC-A :: FSC-A
SSC-A :: SSC-A
(d)
EYFP
1.25
FSC-A :: FSC-A
FL1-A :: FL1-A
(e)
Cells
84.7
SSC-A :: SSC-A
FSC-A :: FSC-A
(f)
EYFP
19.7
FSC-A :: FSC-A
FL1-A :: FL1-A

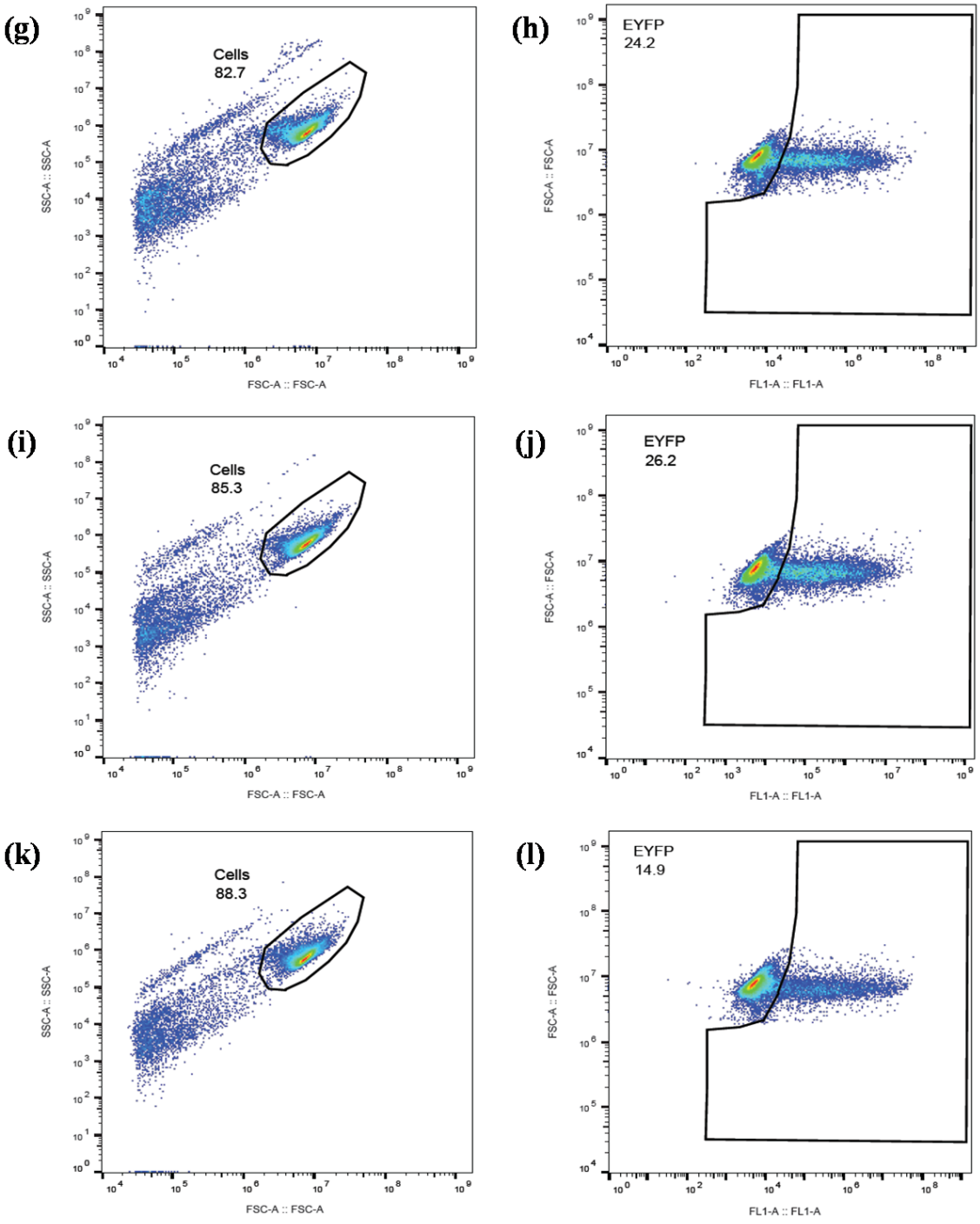
(g)
Cells
82.7
SSC-A :: SSC-A
FSC-A :: FSC-A
(h)
EYFP
24.2
FSC-A :: FSC-A
FL1-A :: FL1-A
(i)
Cells
85.3
SSC-A :: SSC-A
FSC-A :: FSC-A
(j)
EYFP
26.2
FSC-A :: FSC-A
FL1-A :: FL1-A
(k)
Cells
88.3
SSC-A :: SSC-A
FSC-A :: FSC-A
(l)
EYFP
14.9
FSC-A :: FSC-A
FL1-A :: FL1-A

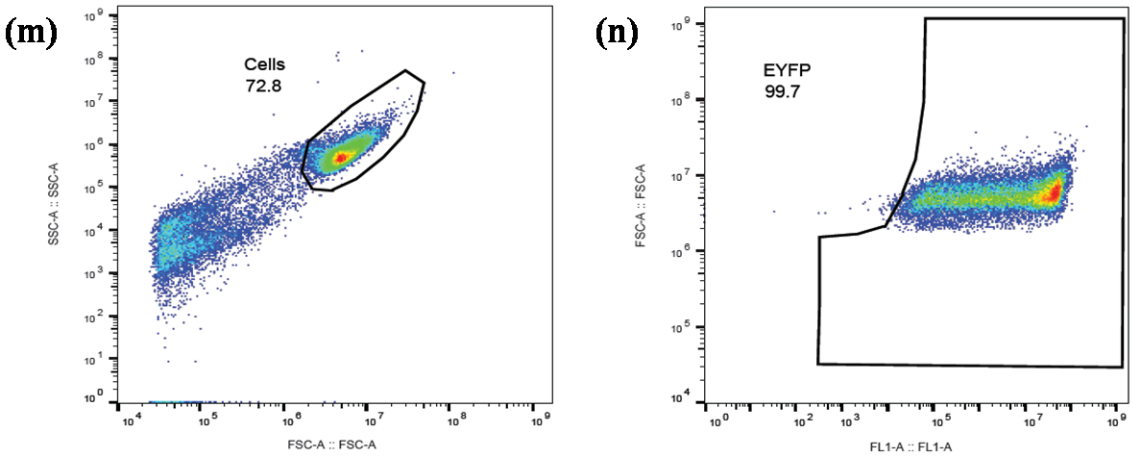

Figure S10: Flow cytometry gates. Gates for (a) Live cells and (b) for EYFP fluorescence set for 0.2% (EYFP) spillover of positive control untransfected HEK293 cells. Gates defined in a and b applied to HEK293 cells transfected with plasmid DNA encoding EYFP using CNT array device after the first reactive ion etching (RIE) process in 1-step manufacturing protocol for RIE etching times of (c, d) 2 hours, (e, f) 2.5 hours, (g, h) 3 hours, (i, j) 3.5 hours and (k, l) 4 hours, and also for (m, n) lipofection control experiment.

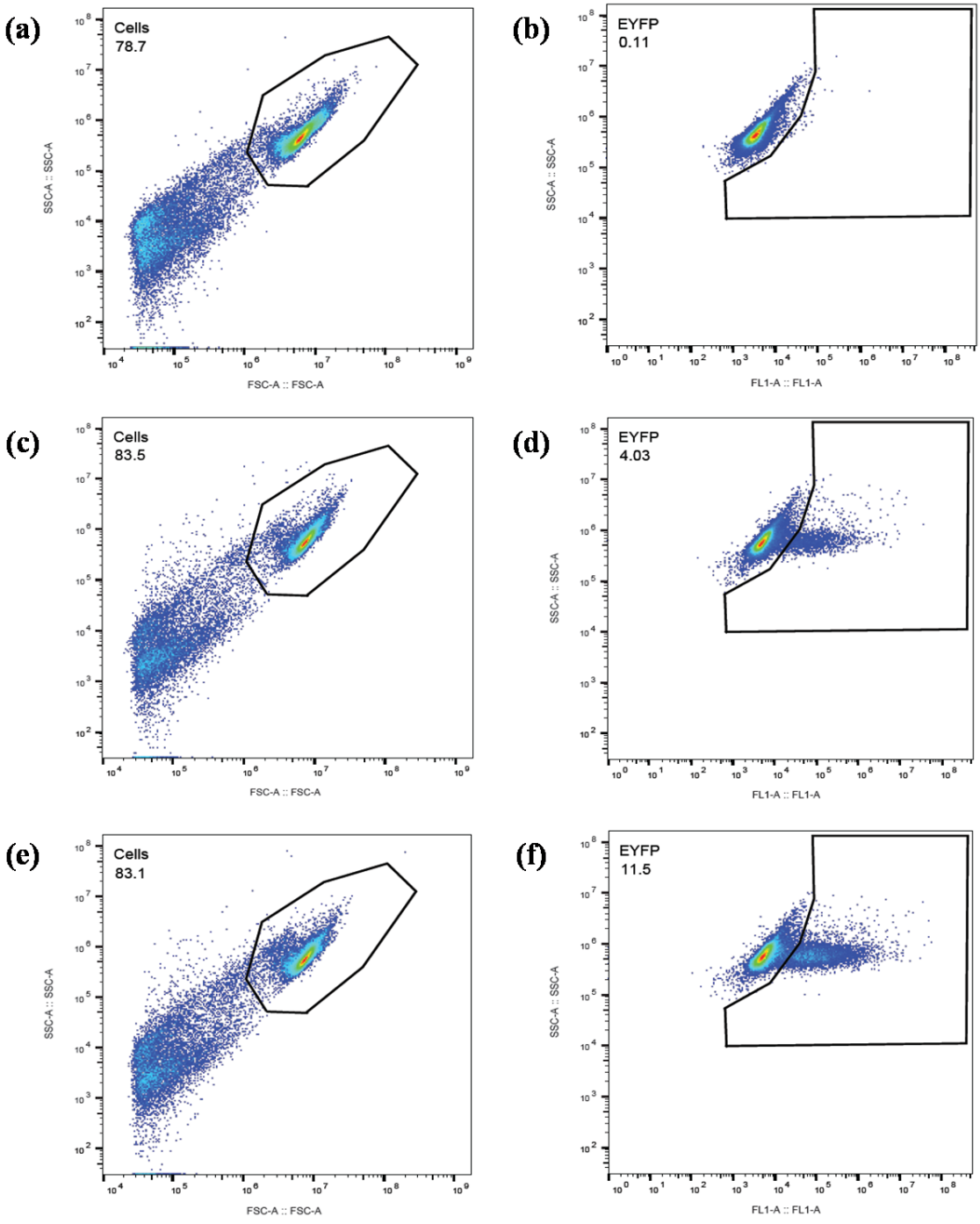
(a)
Cells
78.7
SSC-A :: SSC-A
FSC-A :: FSC-A
(b)
EYFP
0.11
SSC-A :: SSC-A
FL1-A :: FL1-A
(c)
Cells
83.5
FSC-A :: FSC-A
(d)
EYFP
4.03
SSC-A :: SSC-A
FL1-A :: FL1-A
(e)
Cells
83.1
SSC-A :: SSC-A
FSC-A :: FSC-A
(f)
EYFP
11.5
SSC-A :: SSC-A
FL1-A :: FL1-A

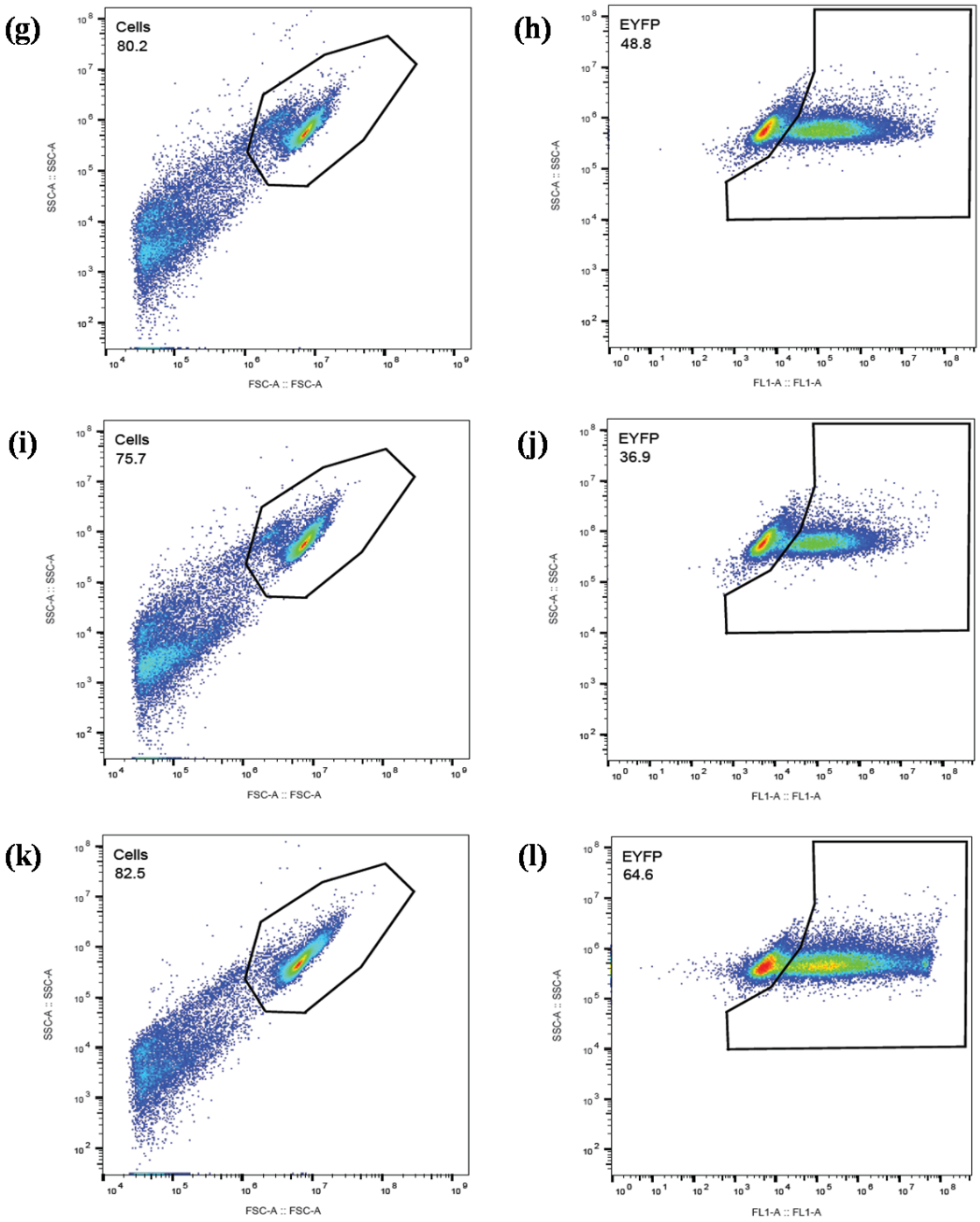

Figure S11: Flow cytometry gates. Gates for (a) Live cells and (b) for EYFP fluorescence set for 0.1% (EYFP) spillover of positive control untransfected HEK293 cells. Gates defined in a and b applied to HEK293 cells transfected with plasmid DNA encoding EYFP using CNT array device after the second reactive ion etching (RIE) process in 2-steps manufacturing protocol for RIE etching times of (c, d) 0 hours, (e, f) 2 hours, (g, h) 4 hours and (i, j) 6 hours, and also for (k, l) lipofection control experiment.

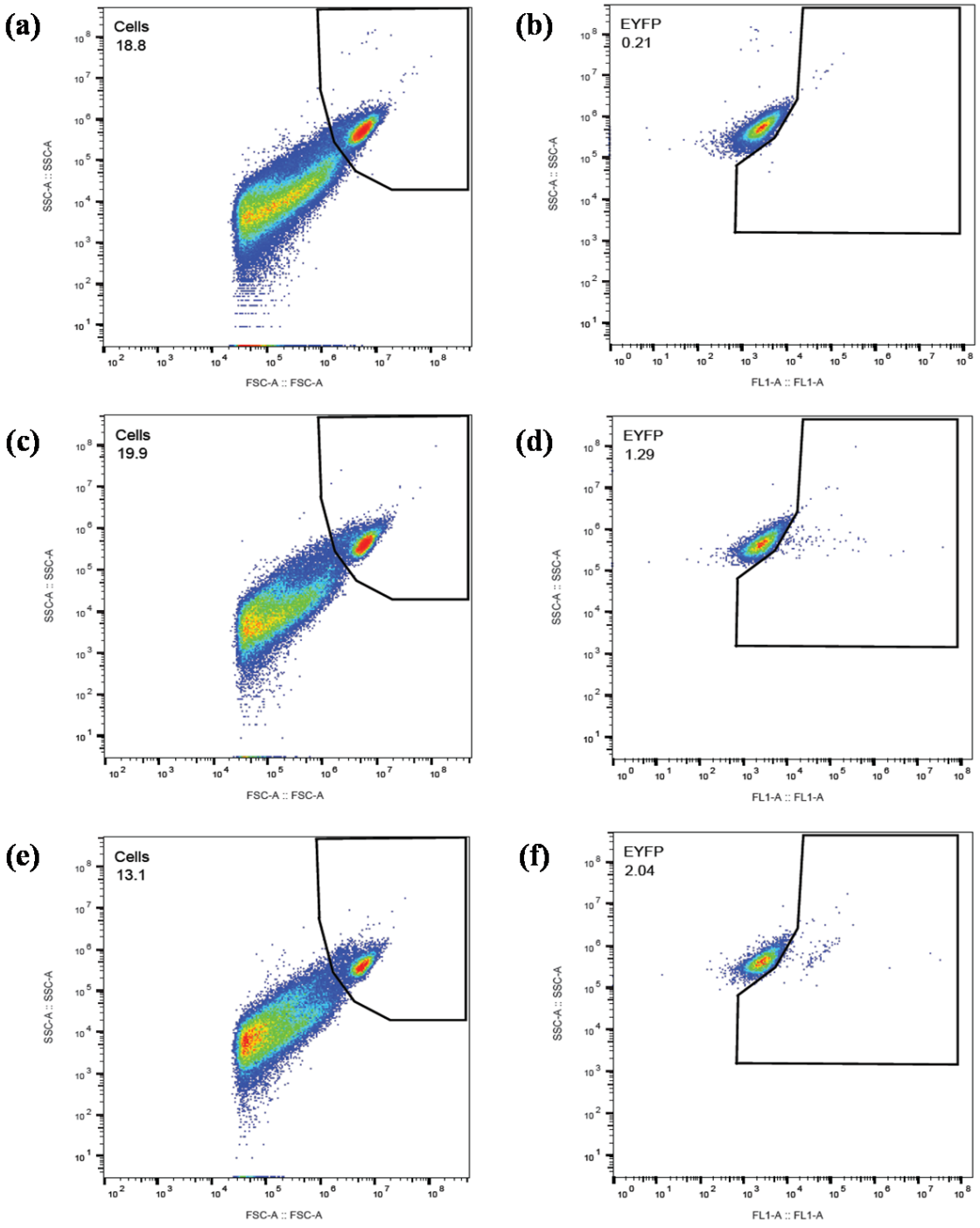
(a)
Cells
18.8
SSC-A :: SSC-A
FSC-A :: FSC-A
(b)
EYFP
0.21
SSC-A :: SSC-A
FL1-A :: FL1-A
(c)
Cells
19.9
SSC-A :: SSC-A
FSC-A :: FSC-A
(d)
EYFP
1.29
SSC-A :: SSC-A
FL1-A :: FL1-A
(e)
Cells
13.1
SSC-A :: SSC-A
FSC-A :: FSC-A
(f)
EYFP
2.04
SSC-A :: SSC-A
FL1-A :: FL1-A

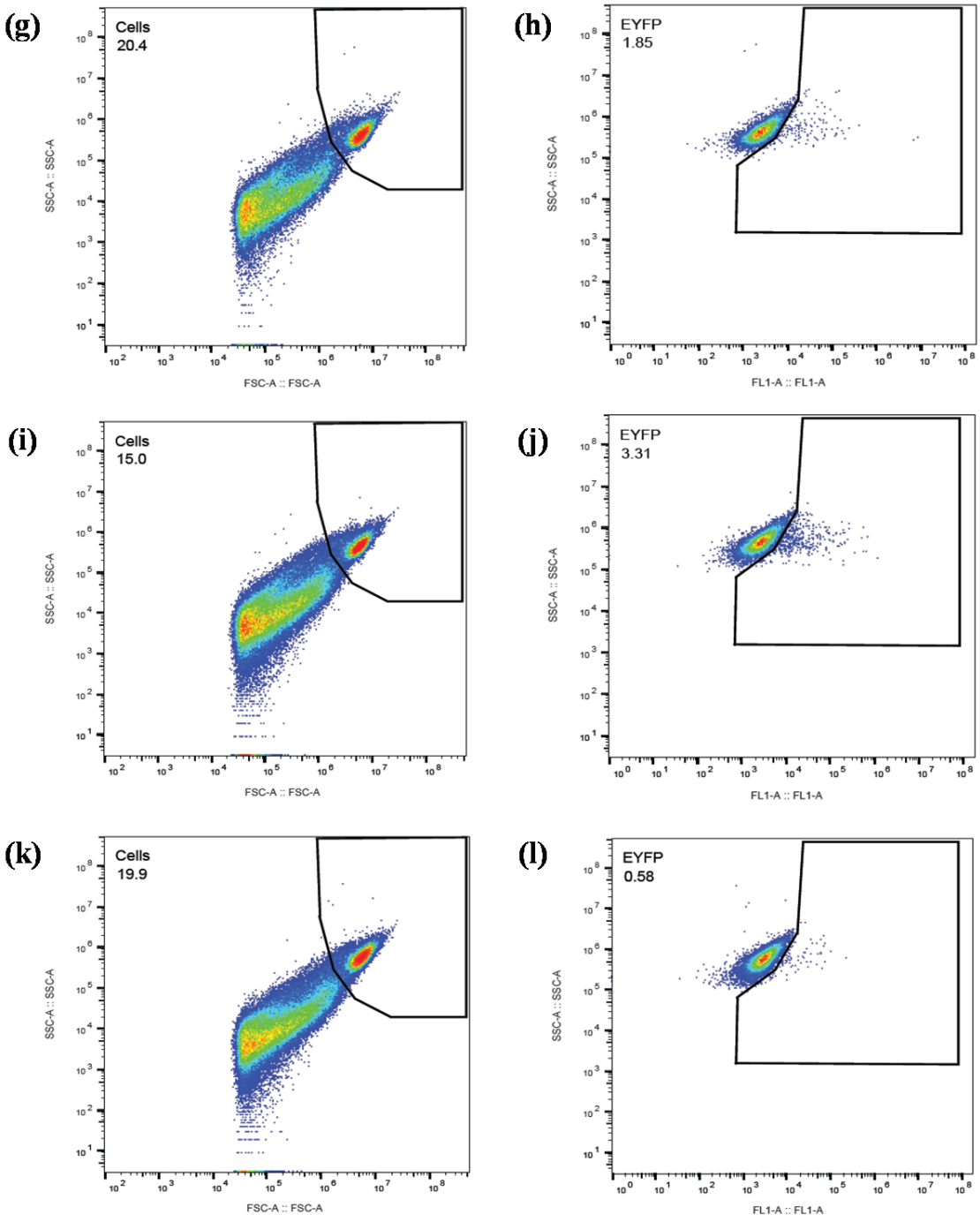

Figure S12: Flow cytometry gates. Gates for (a) Live cells and (b) for EYFP fluorescence set for 0.2% (EYFP) spillover of positive control untransfected H7 human embryonic stem cells. Gates defined in a and b applied to H7-hESCs transfected with plasmid DNA encoding EYFP using CNT array device after the second reactive ion etching (RIE) process in 2-steps manufacturing protocol for RIE etching times of (c, d) 0 hours, (e, f) 2 hours, (g, h) 4 hours and (i, j) 6 hours, and also for (k, l) lipofection control experiment.

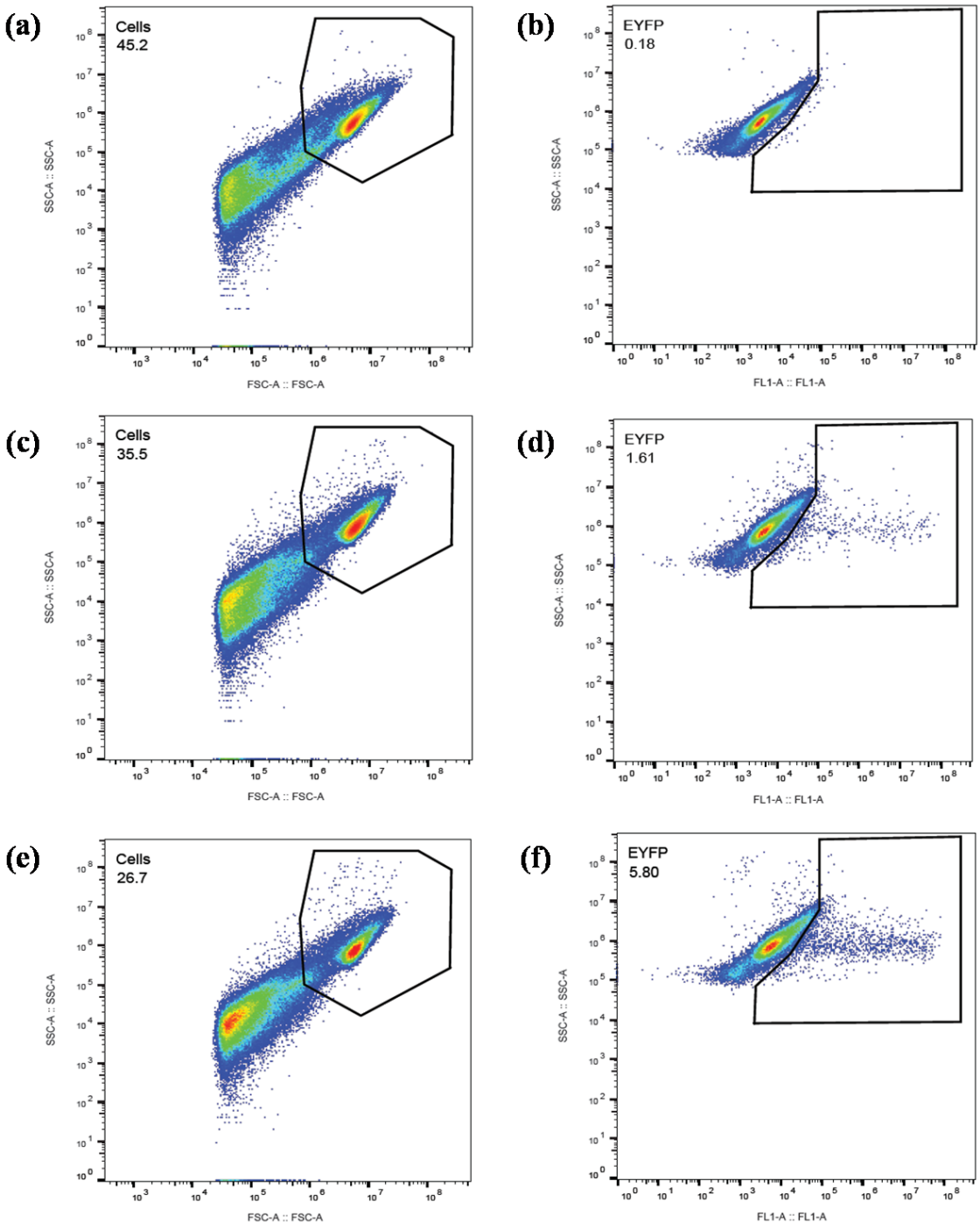
(a)
Cells
45.2
SSC-A :: SSC-A
FSC-A :: FSC-A
(b)
EYFP
0.18
SSC-A :: SSC-A
FL1-A :: FL1-A
(c)
Cells
35.5
SSC-A :: SSC-A
FSC-A :: FSC-A
(d)
EYFP
1.61
SSC-A :: SSC-A
FL1-A :: FL1-A
(e)
Cells
26.7
SSC-A :: SSC-A
FSC-A :: FSC-A
(f)
EYFP
5.80
SSC-A :: SSC-A
FL1-A :: FL1-A

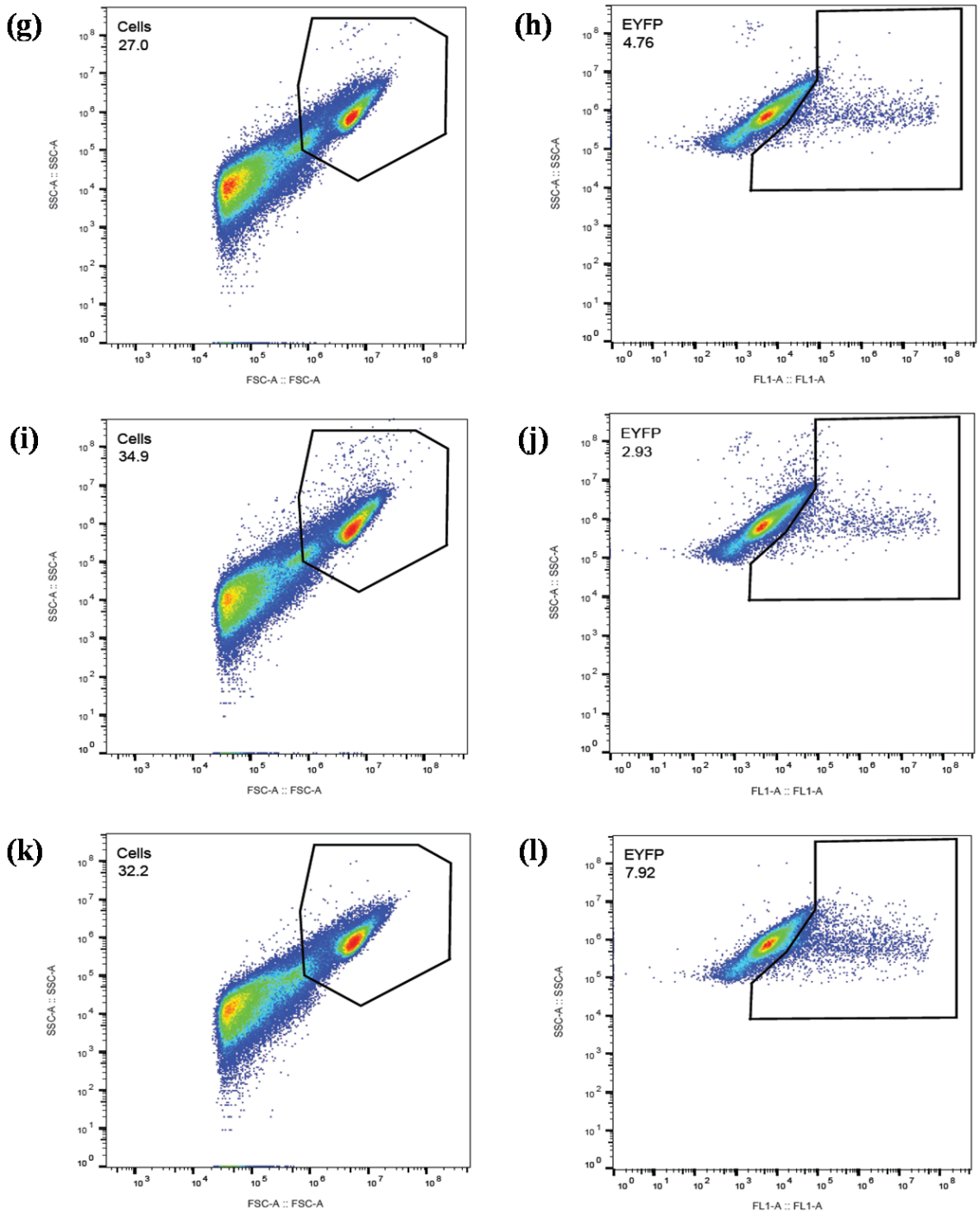

Figure S13: Flow cytometry gates. Gates for (a) Live cells and (b) for EYFP fluorescence set for 0.2% (EYFP) spillover of positive control untransfected primary human skin cells. Gates defined in a and b applied to primary human skin cells transfected with plasmid DNA encoding EYFP using CNT array device after the second reactive ion etching (RIE) process in 2-steps manufacturing protocol for RIE etching times of (c, d) 0 hours, (e, f) 2 hours, (g, h) 4 hours and (i, j) 6 hours, and also for (k, l) lipofection control experiment.

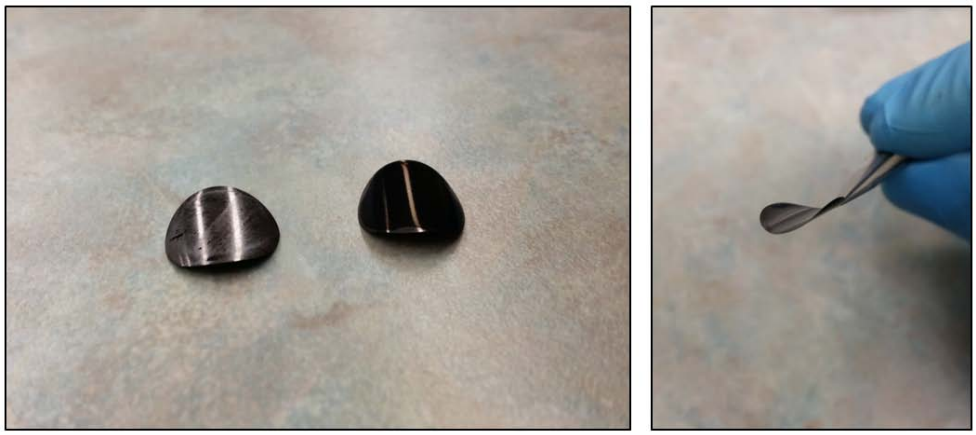

Figure S14: CNT array devices after cleaning in high temperature furnace at 700 °C for 4 hours, indicating the curled devices.

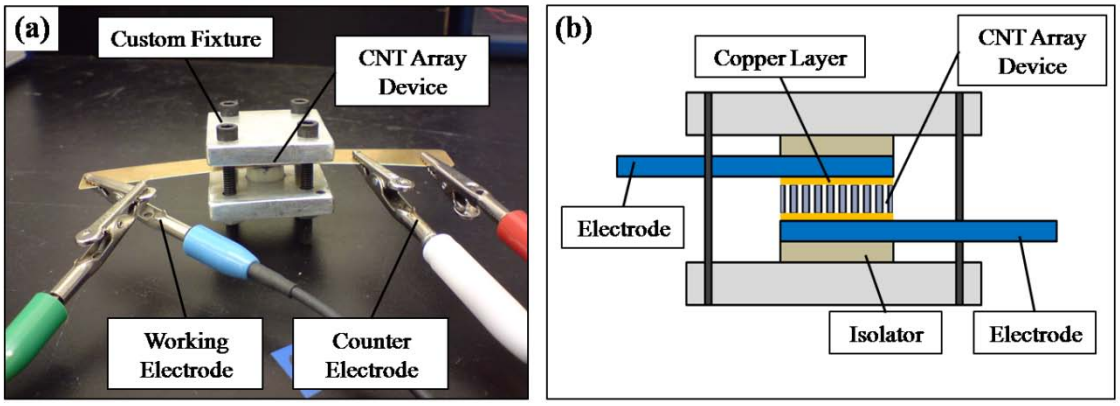

Figure S15: (a) The exprimental setup and (b) its schematic illustartion for measuring the electrical resistivity of the CNT array devices.

Publication List

Refereed Journal Articles

- **Golshadi M**, Nguyen L, Dickerson IM, Schrlau MG; Template-Based Fabrication of Vertically Aligned Carbon Nanotube Arrays. (Nanotechnology, *Under Review*)
- **Golshadi M**, Wright LK, Dickerson IM, Schrlau MG; High Efficiency Gene Transfer through Carbon Nanotube Arrays. *Small* 12:2014-3020. (2016)
- **Golshadi M**, Maita J, Lanza D, Zeiger M, Presser V, Schrlau MG; Effects of Synthesis Parameters on Carbon Nanotubes Manufactured by Template-Based Chemical Vapor Deposition. *Carbon* 80:28-39. (2014)

Articles in Preparation

- **Golshadi M**, Dickerson IM, Schrlau MG; Effect of Geometrical Properties of Carbon Nanotube Arrays on Intracellular Gene Transfection. (*Under Preparation*)

Conference Proceedings

- **Golshadi M**, Schrlau MG, Template-Based Synthesis of Aligned Carbon Nanotube Arrays for Microfluidic and Nanofluidic Applications. ECS Transactions 50.33:1-14. (2013)

Book Chapters

- **Golshadi M**, Schrlau MG; Carbon Nanostructures in Biomedical Applications. Carbon Nanomaterials, Second Edition, Edited by Yury Gogotsi and Volker Presser, Taylor and Francis/CRC Press, Boca Raton, Chapter 7, pp 217-232. ISBN 9781439897812. (2013)

Patent

- Dickerson IM, Schrlau MG, **Golshadi M**; Delivery of Biomolecules into Cells through Carbon Nanotube Arrays, US Provisional Patent 62/235,386. (2015)

Oral Presentations

- **Golshadi M**, Dickerson I, Schrlau MG; Carbon nanotube array for intracellular gene delivery. Department of Mechanical Engineering, Rochester Institute of Technology, March 3, Rochester, NY. (2016)
- **Golshadi M**, Schrlau MG; Tailoring the Geometrical and Structural Features of Carbon Nanotubes for Biomedical Applications. 2015 MRS Fall Meeting & Exhibit, November 29-December 4, Boston, MA. (2015)
- **Golshadi M**, Schrlau MG; Template-Based Synthesis of Aligned Carbon Nanotube Arrays for Microfluidic and Nanofluidic Applications. 222nd ECS Meeting and PRIME, October 7-12, Honolulu, HI. (2012)

Poster Presentations

- **Golshadi M**, Schrlau MG; Template-Based Synthesis of Aligned Carbon Nanotube Arrays for Microfluidic and Nanofluidic Applications. RIT 4th Annual Graduate Research and Creativity Symposium, July 17, Rochester, NY. (2012)